Structure and Conformational Dynamics of 3D DNA Origami Objects Probed by Small-Angle X-Ray Scattering

Linda Karoline Brützel

München 2017

Structure and Conformational Dynamics of 3D DNA Origami Objects Probed by Small-Angle X-Ray Scattering

Linda Karoline Brützel

Dissertation
an der Fakultät für Physik
der Ludwig–Maximilians–Universität
München

vorgelegt von
Linda Karoline Brützel
aus Hamburg

München, den 13.10.2017

Erstgutachter: Prof. Dr. Jan Lipfert
Zweitgutachter: Prof. Dr. Hendrik Dietz
Tag der mündlichen Prüfung: 13.12.2017

Zusammenfassung

Seit mehreren Jahrzenten verfolgen Forscher das Ziel, künstliche molekulare Maschinen zu erschaffen, die eigens definierte biologische Funktionen ausführen können. Ein vielversprechender Ansatz basiert auf der Verwendung von Desoxyribonukleinsäure (DNA), dem Träger der Erbinformation. Die im Jahre 2006 veröffentlichte DNA-Origami Technik, welche die spezifische Watson-Crick-Basenpaarung von DNA mit dem Konzept der Selbstassemblierung verbindet, stellt ein neues Designparadigma in der DNA-Nanotechnologie mit potenziellen Anwendungen in Bereichen der Biotechnik, Biosensorik oder Medizin dar. Während der anfängliche Fokus auf der Konstruktion von statischen dreidimensionalen (3D) Objekten lag, wurden jüngst dynamische Strukturen entwickelt, die ihre Konformation in Abhängigkeit von bestimmten Umgebungsbedingungen verändern können. Eine einwandfreie Funktion dieser ‚Nanomaschinen' erfordert jedoch eine spezifische räumliche Organisation der jeweiligen Komponenten, die stark von äußeren Faktoren wie Temperatur, Salz oder pH-Wert abhängt. Detaillierte Kenntnisse der Struktur synthetischer Nano-Objekte sind daher Schlüsselvoraussetzung für die Charakterisierung ihrer Funktionsweisen sowie für die Etablierung neuer DNA-Origami Designstrategien. Bisher erfolgte die strukturelle Charakterisierung von DNA-Origami Objekten meist mittels Rasterkraftmikroskopie (AFM) oder Elektronenmikroskopie (EM), wobei jedoch Strukturänderungen aufgrund von Wechselwirkungen zwischen der Probe und der Oberfläche auftreten können. Eine sinnvolle Alternative bietet die Kleinwinkel-Röntgenstreuung (SAXS). Diese Technik ermöglicht es sowohl die Struktur als auch die Wechselwirkungen von biologischen Makromolekülen und ihren Komplexen unter diversen Lösungsbedingungen zu analysieren, wobei weder eine Oberflächenimmobilisierung noch eine chemische Markierung der Moleküle benötigt werden. In dieser Arbeit konnte ich zeigen, dass mit SAXS Konformationsänderungen von DNA-Origami Strukturen unter verschiedenen Lösungsbedingungen quantitativ ermittelt werden können. Im Fokus dieser Arbeit stand dabei die Strukturanalyse konfigurierbarer 3D DNA-Origami Objekte, die über Stapelbindungen zwischen Nukleobasen an formkomplementäre Oberflächen interagieren können. SAXS Messungen an einem DNA-Origami Schalter (Switch), der reversibel zwischen einem X-förmigen offenen und einem rechteckigen geschlossenen Zustand in Abhängigkeit der Ionenstärke wechseln kann, konnten diesen Übergang als einen Zwei-Zustands Prozess identifizieren. Zudem konnte gezeigt werden, dass atomistische Strukturmodelle des Origami Schalters durch Kombination von experimentellen SAXS Daten und einer Methode der Normal-Moden-Analyse präzesierter werden können. Dieser erstmalig auf eine DNA-Origami Struktur angewendete Ansatz, deckte Deformationen der internen Struktur des Origami Schalters im Ångstrom Bereich auf. Durch zeitaufgelöste SAXS Messungen konnte ich die außergewöhnlich schnellen Übergangskinetiken des DNA-Origami Schalters aufdecken, die im Millisekunden-Bereich liegen und nahe des theoretischen Diffusionslimit erfolgen. Zudem wurde in dieser Arbeit ein heteromeres DNA-Origami Block-System, das zwei Monomer Blöcke umfasst, die unter bestimmten Salzbedingungen dimerisieren können, hinsichtlich der Struktur und der Dimerisierungsdynamiken bei unterschiedlichen Salz- und Temperaturbedingen charakterisiert. SAXS Messungen an Block-Monomeren und Dimeren zeigten Ionenart- und konzentrationsabhängige strukturelle Deformationen wobei ein Temperatureffekt nicht festgestellt wurde. Zeitaufgelöste SAXS Messungen von Dimerisierungskinetiken, ergaben 10-mal schnellere Kinetiken in Gegenwart von einwertigen Ionen im Vergleich zu zweiwertigen Ionen, während eine Temperaturerhöhung nur zu einem geringfügig schnelleren Ablauf führte. Als weiteres Projekt wird ein labor-basierter SAXS Aufbau, der SAXS Messungen an unterschiedlichen Makromolekülen ermöglicht und während dieser Arbeit entwickelt wurde, vorgestellt.

Preface

Living cells have evolved a plethora of highly sophisticated macromolecular assemblies, formed by proteins, nucleic acids or lipids. These complexes can be thought of as molecular machines that perform tasks such as reading the genetic code, producing metabolic energy or generating cell locomotion, critical for sustaining cellular structure and function. Formation of these machineries often relies on molecular self-assembly, a process in which molecules spontaneously form higher order structures without any external guidance. The concept of self-assembly has attracted considerable interest from many researchers intrigued by the idea to create artificial molecular machines that can carry out user-defined functions. A promising approach uses DNA, Nature's designated molecule for storing and transmitting genetic information, as building block for nanoconstruction. In this context, the DNA origami technique, which combines the predictable Watson-Crick base pairing of DNA with the concept of self-assembly, has become a new design paradigm in DNA nanotechnology for many potential applications in e.g. bioengineering, biosensing, or drug delivery. While an initial focus was on designing static three-dimensional (3D) objects, recent developments yielded dynamic structures that can change their conformation in response to changes in environmental conditions.

However, proper function of these nanomachines requires a precisely defined spatial organization of constituent components, which strongly depends on environmental factors, such as temperature, salt or pH-value. Thus, detailed knowledge of molecular structure is a key prerequisite for characterizing the performance of synthetic nano-objects and for establishing new DNA origami design principles. So far, structural characterization of DNA origami objects mostly relies on structural techniques like atomic force microscopy (AFM) or electron microscopy (EM), potentially biasing the overall structure due to interactions with the surface. A valuable complementary tool is small-angle X-ray scattering (SAXS), which can probe the structure and interactions of biological macromolecules and their complexes under a broad range of solution conditions without the need for surface immobilization or labeling.

Within this thesis, I demonstrated that SAXS can quantitatively monitor conformational changes of DNA origami structures under varying solution conditions. Thereof, I could show that 'idealized' atomistic models of DNA origami objects can be refined against solution-based SAXS data. I further exploited the possibilities of SAXS to monitor conformational kinetics of DNA origami objects proceeding on timescales of millliseconds to minutes. Of special interest were reconfigurable 3D DNA origami objects featuring shape-complementary interfaces, which can interact via short-ranged nucleobase stacking bonds and serve as binding motives.

An introduction to small-angle X-ray scattering and DNA nanotechnology is provided in Chapters 1 - 2, presenting theoretical concepts and recent developments and applications. The results of this thesis are described in Chapters 3 - 6, where each Chapter provides a separate introduction and is accompanied by its own Materials and Methods section.

In Chapter 3 the design and performance of an in-house SAXS setup is described, which was developed in collaboration with the group of Bert Nickel at the LMU. In contrast to most common in-house SAXS setups that are based on copper anodes, we employed a molybdenum-anode-based source. Here, both technical aspects and SAXS measurements on biological macromolecules with different scattering properties are presented, based on Bruetzel *et al.* [1].

Chapter 4 focuses on the characterization of conformational states of a dynamic DNA origami switch device, which is designed to reversibly switch between an x-shaped open and a rectangular-shaped closed state as a function of ionic strength, by using SAXS. The results are compared to data obtained from other structural techniques. In addition, a computational approach based on an elastic network model is presented, which allows for refinement of 3D atomistic models of the switch device against scattering data. This Chapter is adapted from Bruetzel *et al.* [2].

In Chapter 5 time-resolved SAXS studies on conformational kinetics of the DNA origami switch device are presented. Using a stopped-flow kinetic mixer, conformational changes of the switch object are induced upon rapid mixing with different divalent concentrations. We could demonstrate that, remarkably, the dynamic switch undergoes large scale open to closed conformational transitions on the time scale of milliseconds. This Chapter is submitted as an article to *Nature Nanotechnology* by Bruetzel *et al.* [3].

Chapter 6 illustrates SAXS experiments on assembly kinetics of a DNA origami brick system, involving two monomeric brick variants with shape-complementary patterns that can form a dimer depending on ambient cation concentrations. Beside the structural analysis of monomeric and dimeric brick objects, we monitor dimer assembly kinetics as a function of monovalent or divalent ions and for two different temperatures.

SAXS measurements on DNA origami structures were performed in collaboration with the group of Prof. Hendrik Dietz at the TUM, Munich.

A conclusion and suggestions for future research directions are presented in Chapter 7.

Publications

Publications that are part of this thesis and presented in Chapters 3 - 5:

1. Linda K. Bruetzel, Stefan Fischer, Annalena Salditt, Steffen M. Sedlak, Bert Nickel, and Jan Lipfert, **'A Mo-anode-based in-house source for small-angle X-ray scattering measurements of biological macromolecules'**, *Review of Scientific Instruments* 87(2), 025103 (2016)
DOI:10.1063/1.4940936

2. Linda K. Bruetzel, Thomas Gerling, Steffen M. Sedlak, Philipp U. Walker, Wenjun Zheng, Hendrik Dietz, and Jan Lipfert, **'Conformational changes and flexibility of DNA devices observed by small-angle X-ray scattering'**, *Nano Letters* 16(8), 4871–4879 (2016)
DOI:/10.1021/acs.nanolett.6b01338

3. Linda K. Bruetzel*, Philipp U. Walker*, Thomas Gerling, Hendrik Dietz, and Jan Lipfert, **'Time-resolved SAXS reveals millisecond transitions of a DNA origami switch'**, *submitted.*
*contributed equally to this work

Further publications, which have not been included as main results in this thesis:

4. Jochen P. Müller, Salomé Mielke, Achim Löf, Tobias Obser, Christoph Beer, Linda K. Bruetzel, Diana A. Pippig, Willem Vanderlinden, Jan Lipfert, Reinhard Schneppenheim, and Martin Benoit, **'Force sensing by the vascular protein von Willebrand factor is tuned by a strong intermonomer interaction'**, *Proceedings of the National Academy of Sciences* 113(5), 1208–1213 (2016),
DOI: 10.1073/pnas.1516214113

5. Jochen P. Müller, Achim Löf, Salomé Mielke, Tobias Obser, Linda K. Bruetzel, Willem Vanderlinden, Jan Lipfert, Reinhard Schneppenheim, and Martin Benoit, **'pH-dependent interactions in dimers govern the mechanics and structure of von Willebrand factor'**, *Biophysical Journal* 111(2), 312–322 (2016),
DOI: 10.1016/j.bpj.2016.06.022

6. Steffen M. Sedlak, Linda K. Bruetzel, and Jan Lipfert, **'Quantitative evaluation of statistical errors in small-angle X-ray scattering measurements'**, *Journal of Applied Crystallography* 50, 621-630 (2017),
DOI: 10.1107/S1600576717003077

7. Nadine Harrer*, Christina E. M. Schindler*, Linda K. Bruetzel, Ignasi Forné, Johanna Ludwigsen, Axel Imhof, Martin Zacharias, Jan Lipfert, and Felix Mueller-Planitz **'Structural architecture of the nucleosome remodeler ISWI determined from cross-linking, mass spectrometry, SAXS and modeling'**, *resubmitted to: Structure, (2017)*
*contributed equally to this work

Contents

Part I

Introduction

Chapter 1

Small-Angle X-ray Scattering to Study Biological Macromolecules in Solution

1.1 Introduction

Function arises from structure, whether on a macromolecular level within living cells or within synthetic objects. Obtaining structural information about macromolecules and their assemblies and deciphering the interactions and dynamics between molecules, is crucial to understand biological mechanisms. In addition, this knowledge can promote and inspire research in nanotechnology, which aims to create synthetic objects that can mimic functions of biological macromolecular complexes. Today's structural analysis approaches employ and combine a vast array of advanced techniques which cover several ranges of resolution, starting from X-ray crystallography, solution-based nuclear magnetic resonance (NMR) and cryo-electron microscopy (cryo-EM), providing resolutions of a few Ångstroms [4, 5], to atomic force microscopy (AFM) imaging and small-angle X-ray scattering (SAXS) with resolutions of $\sim 1\,\mathrm{nm}$ [6, 7].

Since its introduction in the late 1930's, SAXS has become a well established tool for structural analysis of proteins, nucleic acids and macromolecular complexes. As a solution technique, SAXS offers the potential for obtaining information about macromolecular shape and conformations under virtually arbitrary solution conditions, free of potential biases and perturbations due to surface interactions as it can occur in EM or AFM. Moreover, SAXS allows for probing macromolecules with sizes ranging from a few kilo Dalton (kDa) up to several GDa, spanning the ranges that limit NMR and EM methods [7]. Today, SAXS is often synergistically combined with both complementary structural characterization techniques and computational approaches. The following sections provide a short description of the underlying physics of SAXS and give an overview of structural information derived by SAXS. Further, potential application to structural biology and recent developments in experimental setups are presented.

1.2 Basic principles of SAXS

The basic principle of biological SAXS experiments is to scatter X-ray photons elastically off molecules, which are randomly oriented in solution, and to record the scattering intensity as a function of the scattering angle (Figure 1.1). The macromolecules are homogeneously diluted in a buffer solution at moderate sample concentrations (usually several mg/ml but depending on the molecular weight of the macromolecule) [8] and exposed to a collimated monochromatic X-ray beam. The X-rays are generated either by a synchrotron facility or a laboratory-based setup (see section 1.6). The incident X-rays interact with the electrons of the atomic shells and X-rays scattered into a small angular range (typically $\sim 0.01°$ - $2°$) are recorded by a detector. The elastic scattering of randomly oriented monodisperse particles results in an isotropic, radially symmetric scattering pattern as a function of scattering angle. It represents the average scattering of all possible particle orientations relative to the X-ray beam. The scattering data are circular averaged resulting in a one-dimensional scattering intensity profile as a function of scattering vector q (see Figure 1.1 and section 1.2.1), containing information about the three-dimensional shape of the macromolecules. In order to compensate for the scattering contribution from the buffer, the scattering profile obtained from a separate measurement of only the buffer solution, is subtracted from the SAXS profile of the sample (i.e. macromolecules in solution):

$$I(q) = I(q)_{sample} - I(q)_{buffer} \tag{1.1}$$

where *I(q)* denotes the final scattering profile that is used for data analysis. To obtain structural information of the studied macromolecules, a homogeneous sample solution with non-interacting identical particles is an important prerequisite for SAXS measurements.

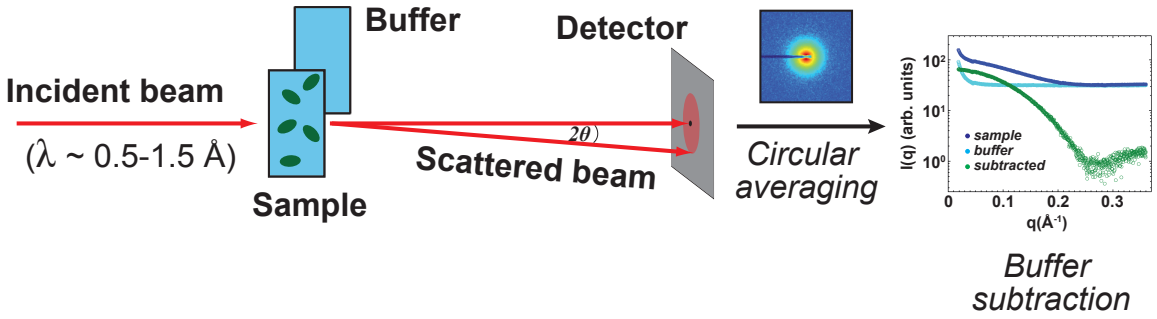

Figure 1.1: Schematic representation of a biological SAXS experiment. A monochromatic, focused X-ray beam with a wavelength of $\lambda \sim 0.5 - 1.5$ Å hits the sample and is elastically scattered by the macromolecules dissolved in a buffer. The scattered X-rays are recorded by a detector and the scattering pattern is circularly averaged yielding a one-dimensional scattering intensity profile as a function of scattering vector q. The whole process is repeated for only the buffer and the resulting scattering profile is subtracted from the scattering profile of the sample.

1.2.1 Scattering theory

SAXS experiments are typically performed with X-rays in the energy regime of 8 - 25 keV, where the dominant interaction processes between the incident X-ray photons and matter are the photoelectric effect, Compton scattering and Rayleigh scattering [9]. The former are inelastic processes, where the photoelectric effect describes absorption of photons and the Compton effect results in a reduction of energy of the scattered photon, delivering no structural information. Rayleigh scattering describes the elastic scattering of photons by particles and is considered for small-angle X-ray scattering experiments. Following the classical description for an elastic scattering process, illumination of matter with monochromatic X-rays described by the wave vector $|\mathbf{k_0}| = 2\pi/\lambda$ forces the electrons in the material to resonate with the frequency of the X-rays resulting in the emission of spherical waves. The intensity of the scattered wave by a single electron at a distance r from an arbitrarily chosen origin is given by the Thomson formula:

$$I_s(\Theta) = \frac{r_e^2}{r^2}\left(\frac{1 + cos^2(2\Theta)}{2}\right) I_0 \tag{1.2}$$

where r_e is the classical electron radius, I_0 the intensity of the primary beam and the term in brackets is referred to as polarization factor, which is close to 1 for small angles ($2\Theta < 5°$) [10]. Here, 2Θ is commonly referred to as scattering angle and describes the angle between the wave vectors of the incident $\mathbf{k_0}$ and the scattered beam $\mathbf{k}'$ (Figure 1.2). As for elastic scattering $|\mathbf{k_0}| = |\mathbf{k}'|$, it is convenient to introduce the scattering vector $\mathbf{q}$, which can be considered as a measure of the directional momentum change of the X-ray photons [7]:

$$\mathbf{q} = \mathbf{k_0} - \mathbf{k}' \tag{1.3}$$

with the amount $q = 4\pi/\lambda\ sin(\Theta)$, typically in $Å^{-1}$ or nm^{-1}. The scattering vector is defined in the so-called 'reciprocal' space.

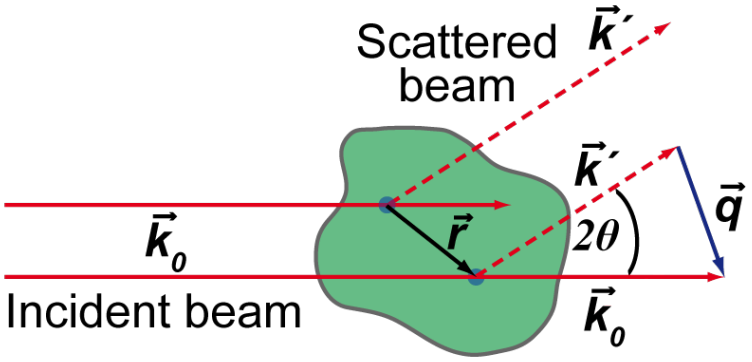

Figure 1.2: Illustration of elastic scattering of X-rays. In a SAXS experiment the incident beam is elastically scattered by electrons within the macromolecule (green area). Here, only two electrons (blue circles), which are separated by a distance $\mathbf{r}$, are shown for simplicity. The scattering vector $\mathbf{q}$ is the difference between the incident wave vector $\mathbf{k_0}$ and the scattered wave vector $\mathbf{k}'$. Graphical representation was inspired by Fig. 1.2 of Ref. [11].

In order to determine the scattering from an assembly of atoms one has to add the amplitudes of the scattered waves originating from each electron in the irradiated volume taking into account the phase difference (Figure 1.2). The macromolecule is represented by a continuous distribution of electrons, where it is of practical use to define the scattering length density distribution $\rho(\mathbf{r})$ [11], which corresponds to the electron density distribution multiplied by the scattering length of a single electron (r_e = 2.82 x 10^{-15} m). The scattering amplitude of the macromolecule is given by:

$$A(\mathbf{q}) = \int_V \Delta\rho(\mathbf{r})\ exp(i\mathbf{qr})d\mathbf{r} \tag{1.4}$$

which corresponds to the Fourier transform of the distribution of electrons, where V denotes the particle volume and $\Delta\rho(\mathbf{r})$ the excess scattering length density. The latter is given by the scattering length density difference between the particles and the solvent. The square of the scattering amplitude divided by the particle volume is often referred as form factor *P(q)*.

In a SAXS experiment one is not able to measure the amplitude but only the scattered intensity as a function of scattering vector **q**:

$$I(q) = \langle |A(\mathbf{q}) \cdot A^*(\mathbf{q})| \rangle_\Omega = \left\langle \int |\Delta\rho(\mathbf{r}) exp(i\mathbf{qr}) d\mathbf{r}|^2 \right\rangle_\Omega = 4\pi \int_0^\infty r^2 \gamma(r) \frac{sin(qr)}{qr} \tag{1.5}$$

where $\langle\ \rangle_\Omega$ denotes the spherical averaging, as the scattering molecules can take all orientations relative to the X-ray beam in solution. Therefore, the phase factor yields $\langle exp(i\mathbf{qr}) \rangle_\Omega = \frac{sin(qr)}{qr}$. In the last part of Equation 1.5, $\gamma(r)$ is the autocorrelation function, indicating how much the excess scattering density spatially correlates with itself and will be discussed in more detail in section 1.4. Equation 1.5 highlights that SAXS data are recorded in reciprocal space.

1.2.2 Contrast and resolution

From the previous equations it becomes evident that SAXS is inherently a contrast based method, as the scattering signal is mainly determined by the difference in the average electron density between the macromolecules in solution $\rho(\mathbf{r})$ and that from the bulk solvent ρ_s. The latter can be approximated with ~ 0.33 e^-/ Å^3 (pure water), while proteins and nucleic acids have an average electron density of ~ 0.44 e^-/ Å^3 [7] and ~ 0.55 e^-/ Å^3 [12], respectively. Thus, the resulting excess electron density is rather small, making an appropriate buffer selection essential. For instance, elevated salt concentrations in the buffer (e.g. 1 M NaCl), often required to reduce interparticle effects such as repulsion, or the addition of protein stabilizers like sucrose [13] will reduce the contrast by ~ 20% and ~ 40% (for 50% (w/v) sucrose), respectively [11]. The high sensitivity to electron density requires that macromolecules should always be diluted in the identical buffer solution used for buffer measurements, in order to ensure accurate buffer subtraction.

Moreover, the scattering intensity usually drops off rapidly for higher q-values ($I(q) \sim sin(qr)/(qr)$ (Equation 1.5)). Together, these facts commonly result in a small difference in scattering signal between sample and buffer at higher q-values (Figure 1.1) which also has an impact on the resolution. For SAXS the nominal resolution is estimated by $\Delta = 2\pi/q_{max}$, where q_{max} denotes the maximum detectable q-value.

However, due to spherical averaging of the scattering intensity, it is not possible to uniquely derive structural models at the theoretical resolution.

Nevertheless, in the SAXS community one often refers to the resolution limit in terms of the smallest achievable q-value (q_{min}). The latter is directly related to the maximum dimension of the macromolecule D_{max} (see section 1.4) via the reciprocal relation $q_{min} = 2\pi/D_{max}$. Thereof, it is more appropriate to describe SAXS as a high precision technique for macromolecular size and shape determination [14].

1.3 Initial analysis and quality assessment of solution scattering data

SAXS profiles of macromolecules have to be carefully evaluated regarding sample monodispersity and absence of interparticle interactions in order to assure a reliable structural analysis and interpretation of the scattering data. Concentration effects and radiation damage of the sample are most prominent phenomena occurring in SAXS experiments that can cause misinterpretation of the data and incorrect structural models. Both effects will be briefly discussed in the following.

1.3.1 Concentration effects

In order to obtain scattering data of a signal-to-noise ratio sufficient for structural analysis, molecular sample concentrations are usually in the range of several mg/ml. For instance, SAXS measurements on BSA ($MW \sim 66$ kDa) are commonly performed at sample concentrations $\sim$ 5 mg/ml and a 24 base-pair DNA duplex requires concentrations $\sim$ 2 mg/ml. These comparably high sample concentrations can result in sample aggregation or interparticle interference effects. The former results in an increase in molecular weight, causing an increase in scattering intensity at the lowest q-values and is often identified by performing a Guinier analysis (section 1.4.1).

Interparticle interference describes the repulsive or attractive interactions among particles in solution and modulates the scattering profile of isolated particles (denoted by the form factor *P(q)*) by the so-called structure factor (*S(q)*). The latter reflects the distribution of the particles in solution [11]. Interference effects become noticeable in a SAXS profile by a decrease in scattering intensity at low angles (Figure 1.4). These effects often scale linearly with sample concentration and can be avoided by extrapolation to infinite dilution [15]. Alternatively, increasing the ionic strength of the buffer solution to screen electrostatic interactions or in case of proteins, setting the pH closer to the isoelectric point can eliminate interference effects. However, the structure factor has proven quite useful for quantifying interaction potentials of isolated DNA structures [16] or proteins [17] in solution.

In general, it is recommendable to perform concentration series of the macromolecular sample ranging from high to low concentrations to exclude these effects. This also allows (if necessary) to merge scattering data from high and low sample concentrations for the low- and high q-regime, respectively, to improve the signal-to-noise ratio.

1.3.2 Radiation damage

X-ray induced damage of macromolecules in solution is an undesired but very often inevitable effect in synchrotron-based biological SAXS experiments. It arises from bond breakage and free radical formation, such as free hydroxyl (OH^-) or hydroperoxyl (HO_2^-) radicals. They are produced from the photolysis of water and can be considered as main source of radiation damage [18]. In proteins, these highly reactive species rapidly attach to the backbone and/or side chains resulting in a fast radical activation ($10^9 - 10^{10}$ M^{-1} s^{-1}) of the protein [19]. Radiation sensitivity strongly depends on the macomolecular composition and structure, where nucleic acids tend to be more radiation resistant than proteins [20]. In SAXS, systematic changes of the scattering profile in a series of exposures are a sign of radiation damage, which manifests itself as irreversible aggregation, unfolding or fragmentation of the sample. While attempts have been made to characterize radiation damage effects in more detail on a molecular level, for instance by analyzing the irradiated sample subsequently after the experiment [21], conclusive explanations are still missing.

Dose calculations

Radiation damage effects in macromolecules depend on the absorbed dose defined as [22]:

$$Dose = \frac{\Phi\, t\, A\, E_{ph}}{\rho l} \tag{1.6}$$

where Φ is the photon flux density of the incident beam (ph s^{-1} μm^{-2}) with a photon energy E_{ph}, A denotes the fraction of incident energy absorbed, t is the exposure time, ρ is the sample density and l is the X-ray path length through the sample. For synchrotron-based SAXS measurements on biological samples with photon fluxes $\sim 10^{12}$ (ph s^{-1}), X-ray beam energies commonly around 10 - 12 keV and beam sizes ~ 500 μm, the upper dose limit before damage occurs varies from several hundred Gray (Gy) to several kGy, depending on the sample [22].

However, Equation 1.6 requires some corrections, which have to be considered for accurate dose calculations. Macromolecules can diffuse into and out of the irradiated volume, with the additional complexity that a non-uniform beam profile (typically approximated by a gaussian shape) will cause different flux densities within that volume [22]. Thus, the absorbed X-ray beam energy will be spread over a larger volume, reducing the dose. As the timescale for molecular diffusion out of the beam is proportional to the beam size, it becomes shorter as the beam size gets smaller. Therefore, downsizing the beam size without changing the beam intensity reduces the dose. Molecular diffusion is especially relevant for static SAXS measurements, where both beam position and sample volume are fixed in place, and it should be considered when choosing the exposure time (and possible dead times between images). Further details in this context can be found in Ref. [18, 19, 22] Moreover, a software tool has been introduced allowing for dose calculations in biological SAXS experiments [23].

Detecting and quantifying radiation damage

The most straightforward way to detect radiation damage effects in a series of exposures, is to examine the scattering profiles for systematic changes. An increase or decrease in scattering intensity at low q-values are usually a sign of radiation damage (Figure 1.3). Further, structural parameters like the radius of gyration and the forward scattering intensity, which are discussed in more detail in section 1.4.1 can be applied as a metric for radiation damage. Statistical approaches and software tools assessing the onset of radiation damage for subsequent exposure times in a SAXS experiment are also available and are implemented in most biological SAXS beamlines [23, 24].

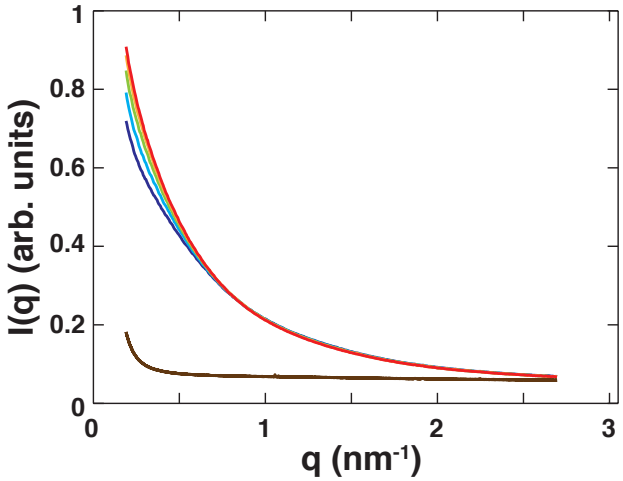

Figure 1.3: Radiation damage effects on scattering profiles. SAXS profiles of a 24-bp DNA duplex obtained from five subsequent 1.0 s exposure times and corresponding buffer profiles. Adapted from [20].

Limiting radiation damage in biological SAXS experiments

Direct measures to reduce radiation damage in synchrotron-based SAXS experiments include adjustments of the buffer solutions. For instance, higher buffer concentrations of MOPS (3-(*N*-morpholino) propanesulfonic acid) or Tris (tris(hydroxymethyl) aminomethane) tend to confer some protection from radiation damage [20]. In addition, buffer solutions can be supplied with so-called radical scavengers, like dithiothreitol (DTT), glycerol, ascorbate or sucrose. However, free radical absorbers should be carefully selected, as some of them reduce the scattering contrast leading to a higher noise level, or may alter the conformation of the macromolecule [25, 26]. For instance, addition of DTT can reduce disulfide bridges in a protein that is otherwise kept in an oxidized state. As radiation damage also depends on sample concentration [19, 27] it is advisable to perform concentration series for a given set of sample conditions.

Technical approaches to limit radiation damage include a reduction of the exposure time, beam attenuation by using appropriate filters or the use of flow-through capillaries, where the sample is translated through the capillary while the X-ray beam is kept at a fixed position.

A far more sophisticated alternative to reduce radiation damage is to employ cryo-SAXS, where the macromolecules are rapidly cooled into vitrified glass (e.g. by plunge freezing into liquid nitrogen) applying cryo-protectants and preserved in a vitrified state during data

collection [28]. While this method allows for higher doses and requires smaller sample volumes ($\sim$ 20μl (SAXS) vs. $\sim$ 20 nl (cryo-SAXS)) further methodological development is required. Cryo-SAXS is technically challenging, requiring highly specialized instrument setups and more elaborate sample preparation. The latter implies the intricacy to obtain homogeneous and monodisperse vitrified samples while preserving the macromolecular structure and an adequate signal-to-noise level.

1.4 Key structural parameters and analysis methods in SAXS

The scattering profile from monodisperse, non-interacting particles provides information about the global structure and conformation of the studied molecule. Some key parameters that can be determined from SAXS data are the molecular weight (MW), the radius of gyration (R_g), and the maximum intramolecular distance (D_{max}). While these parameters are often applied in initial data inspection (as discussed in section 1.3), they are essential for evaluating macromolecular states and conformational transitions, as in protein or RNA folding.

1.4.1 Guinier analysis: Evaluating sample quality and characterizing molecular size

The very low q-region of a scattering profile allows for the calculation of the radius of gyration (R_g) providing information about the mass distribution within a particle. It is defined as the sum of root-mean-squared distances of all elemental scattering volumes from their centre of mass weighted by their scattering densities [15]. The R_g can be obtained by the Guinier-approximation [29], which is valid only within a q-range of $qR_g < 1.3$ [10]. The derivation is based on the power series expansion of the sinc-function of the scattering intensity I(q) (see Equation 1.5):

$$\frac{sin(qr)}{qr} = 1 - \frac{(qr)^2}{3!} + \frac{(qr)^4}{5!} - O((qr)^6) \tag{1.7}$$

Further simplification and rewriting (see Refs. [29, 30]) results in:

$$I(q) = I(0)\left(1 - \frac{q^2R_g^2}{3} + O(q^4)\right) \tag{1.8}$$

which can be rewritten into the Guinier formula:

$$I(q) \approx I(0)exp\left(\frac{-q^2R_g^2}{3}\right) \tag{1.9}$$

By fitting a line to the natural logarithm of the intensity as a function of q^2 yields the R_g from the slope. The y-intercept gives the intensity at zero angles *I(0)*. For monodisperse, non-interacting particle solutions, where the scattering data are measured to q-values that are low enough to reliably characterize their largest dimensions, the scattering pattern should be a linear function within the Guinier regime (Figure 1.4b). A considerable amount of sample

aggregation or interparticle repulsion results in an upswing or downswing of the scattering data in Guinier representation, respectively (Figure 1.4b).

Additionally, the molecular weight (MW) of the sample can be determined based on the following relation:

$$I(0) = \kappa c(\Delta\rho)^2(MW)^2 \tag{1.10}$$

where κ is a proportionality constant that can be determined from a measurement of a molecular weight standard (e.g. a protein of known molecular weight and concentration) and c is the concentration of the macromolecule [31]. Due to the dependency of the scattering intensity on the concentration and molecular weight, SAXS data are often normalized by *I(0)*.

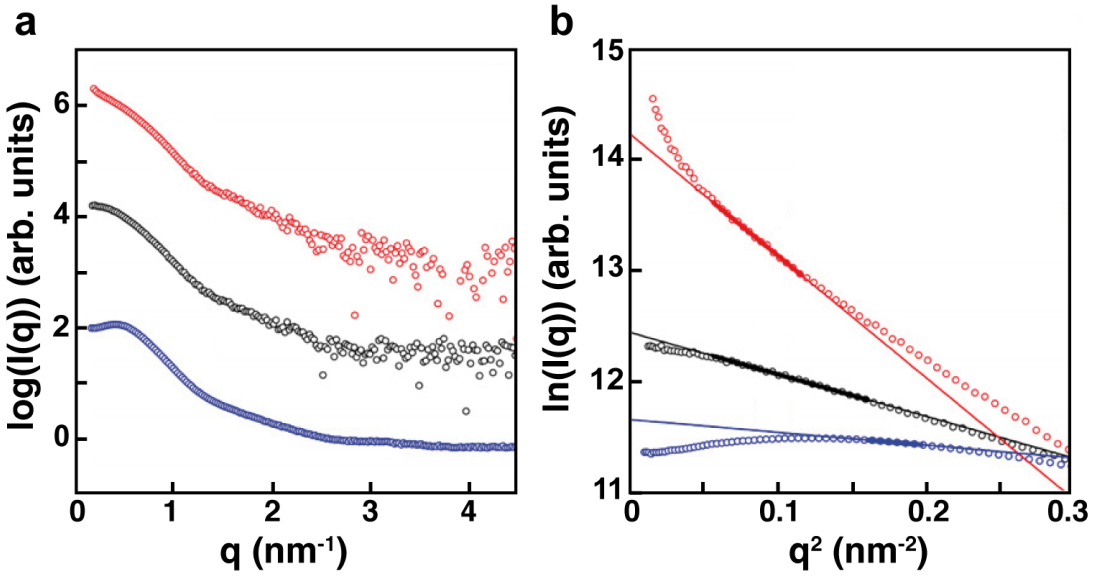

Figure 1.4: Example SAXS profiles and corresponding Guinier graphs for BSA. **a** BSA scattering profiles showing aggregation (red circles, top), good data (black circles) and inter-particle repulsion (blue circles, bottom). **b** Corresponding SAXS curves in Guinier representation with Guinier fits (thick lines) within the q-range $qR_g < 1.3$. Adapted from [32] with permission from Elsevier. Copyright ©2010 Elsevier Inc.

1.4.2 The pair distance distribution function: Representing scattering data in real space

Small-angle X-ray scattering data are represented in reciprocal space as the intensity is a function of the scattering vector q. The scattering intensity can be Fourier transformed to obtain the pair distance distribution function *P(r)* measured in real space [11]:

$$P(r) = \frac{r^2}{2\pi^2}\int_0^\infty I(q)\,\frac{sin(qr)}{qr}\,q^2dq \tag{1.11}$$

As SAXS data can be measured only at a finite number of data points (q_i) within a certain q-range [q_{min}, q_{max}] and with errors [30], a direct calculation of the Fourier transform of the experimental data is not possible. A more conventional way is to compute the *P(r)* function by an 'indirect Fourier transform', first introduced by Glatter *et al.* [33]:

$$I(q) = 4\pi\int_0^{D_{max}} P(r)\frac{sin(qr)}{qr}dr \tag{1.12}$$

with D_{max} as maximum particle distance. Therefore the *P(r)* function is approximated by a limited series of functions ($\varphi_i(r)$) and coefficients (c_i) for $0 \leq r \leq D_{max}$:

$$P(r) = \sum_{i=1}^{n} c_i \varphi_i(r) \tag{1.13}$$

where n denotes the number of functions. The coefficients are determined by fitting Equation 1.12 to the experimental scattering data. By now, there exist several approaches based on indirect Fourier transform [33–35].

In practice, the *P(r)* function describes the distribution of distances between all pairs of points inside a particle weighted by the excess electron density distribution [30]:

$$P(r) = r^2 \gamma(r) = r^2 \left\langle \int \Delta\rho(\mathbf{r}' + \mathbf{r}) \Delta\rho(\mathbf{r}') d\mathbf{r}' \right\rangle_{\omega} \tag{1.14}$$

where $\gamma(r)$ is the autocorrelation function introduced in section 1.2.1. Figure 1.5 shows examples of the *P(r)* function for proteins of different shapes.

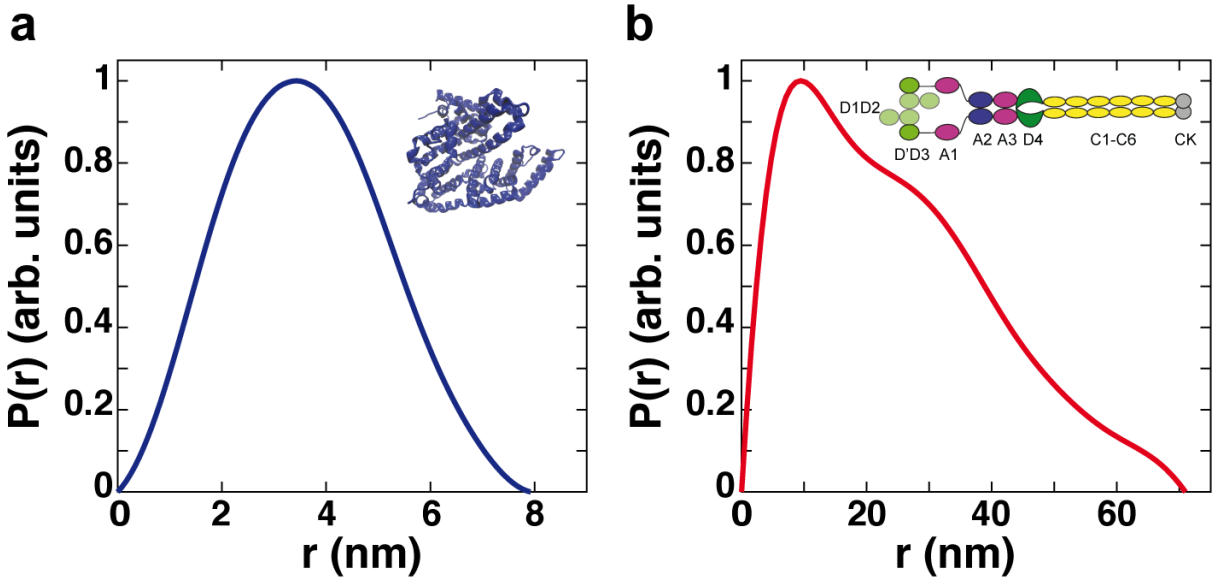

Figure 1.5: Pair distance distribution (*P(r)*) functions calculated for proteins of different geometric shapes. **a** *P(r)* function for BSA ($MW \sim 66$ kDa), representative for a protein with globular shape, and corresponding crystal structure (PDB code: 4F5S). **b** *P(r)* function for the large glycoprotein von Willebrand factor (vWF) ($MW \sim 500$ kDa) with an elongated rod-like shape, illustrated by the schematic of its overall structure (letters indicate single domains). *P(r)* data are normalized by their maximum value.

Also, the *P(r)* function can be used to determine the radius of gyration:

$$R_g^2 = \frac{1}{2} \cdot \frac{\int_0^{D_{max}} P(r) r^2 dr}{\int_0^{D_{max}} P(r) dr} \tag{1.15}$$

1.4.3 Assessing conformational states of macromolecules based on Kratky representation of SAXS data

Using SAXS as an analytical tool to dissect the conformational states and transitions of biological macromolecules dates back to the work of Glatter and Kratky in the 1950s [36]. To qualitatively study the folding or unfolding behavior of proteins [37] or nucleic acids (especially RNA) [38] the scattering data are commonly represented in a Kratky plot, where the scattering intensity multiplied by the square of the scattering vector ($I(q) \cdot q^2$) is plotted against q (Figure 1.6) [39]. As shown by Kratky [36], the scattering intensity of a folded globular protein typically decays as $\sim q^{-4}$ for higher q-values, resulting in a bell-shaped curve with a well-defined peak in a Kratky plot. Unfolded molecules or random coils display a much slower intensity decay $\sim q^{-2}$, so that the corresponding Kratky curve displays a plateau in the lower q-regime followed by a linear rise of the intensity.

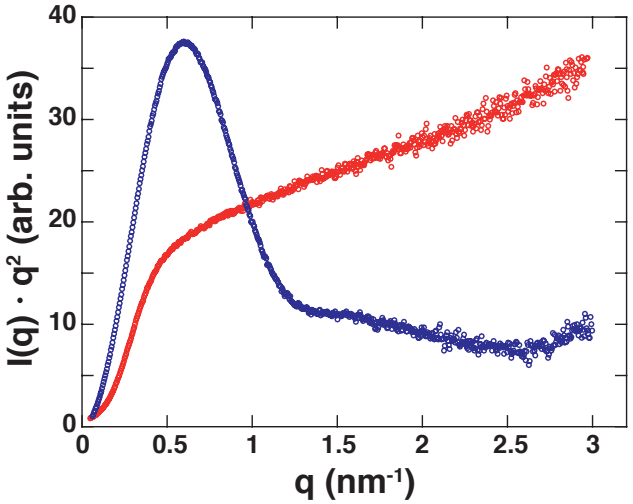

Figure 1.6: Kratky representation of scattering profiles from the globular protein BSA (blue) and synthetic elastin-like polypeptides (ELPs) (red). SAXS data were measured at beamline BM29, ESRF, Grenoble at sample concentrations of 5 mg/ml (BSA) and 8 mg/ml (ELPs).

1.5 Small-angle X-ray scattering as an important complementary technique in structural biology

The previous section introduced methods to obtain structural information from SAXS data requiring no further input. To obtain a more complete picture of macromolecular conformations, SAXS can be easily combined with high-resolution structural techniques and/or with bioinformatic approaches. In addition, SAXS data can be used to reconstruct the three-dimensional shape of macromolecules, particularly useful to identify relative orientations of individual domains and subunits in multidomain proteins or macromolecular complexes if high-resolution models are available. Here, a brief overview of related methods and recent developments is given.

1.5.1 High-resolution structure validation based on theoretical scattering profiles

Combining data from solution scattering with atomic resolution structures to validate structural conformations of macromolecules and their assemblies has evolved into a powerful approach in structural biology [7, 40, 41]. Atomistic structures of macromolecules are commonly determined by X-ray crystallography, NMR, or electron microscopy. However, these technique can deliver ambiguous results for macromolecules with functional flexibility or intrinsic disorder, which play an important role in cellular processes like transport or signaling [42]. For instance, crystal packing forces or cryogenic temperatures can promote a single conformer among a structural ensemble. Thus, to perceive how the structure of a molecule is related to its biological function, a synergistic approach delivering both flexibility, as seen by SAXS, and detail, as provided by high-resolution structural techniques is preferable.

To validate atomic models of macromolecules, theoretical SAXS profiles from the models are commonly calculated. There are several software tools available [43–46], which mainly differ in the underlying formulas to calculate the theoretical scattering intensity, the treatment of excluded volume effects and the description of the solvation shell. The latter consists of layers of ordered water molecules that surround macromolecules in solution and is often referred to as hydration shell (Figure 1.7) [44].

Computation of theoretical scattering patterns

Accurate calculation of the scattering intensity from an atomistic structure requires the scattering from the particle and the solvent, including an adequate description of the hydration shell, (Figure 1.7) and can be expressed as follows [11]:

$$I(q) = \left\langle |A_p(q) - \rho_s A_s(q) + (\rho_h - \rho_s)A_h(q)|^2 \right\rangle_\Omega \tag{1.16}$$

$A_p(q)$ describes the scattering amplitude from the particle *in vacuo*. $A_s(q)$ is the scattering amplitude from the excluded volume, arising from the displacement of solvent by the macromolecule, so that the second term in Equation 1.16 can be considered as buffer subtraction, where ρ_s denotes the scattering density of the solvent. The last term contains the scattering amplitude $A_h(q)$ from the hydration shell with the scattering density ρ_h. As the water molecules are more ordered and densely packed in this layer, the scattering density ρ_h differs from ρ_s [46]. The amplitudes can be calculated using the Debye formula or spherical harmonics expansions. The former is implemented in the program *FOXS*, where the theoretical scattering profile is given by [44]:

$$I(q) = \sum_{i=1}^{N} \sum_{j=1}^{\mathrm{N}} f_i(q) f_j(q) \frac{sin(qd_{ij})}{qd_{ij}} \tag{1.17}$$

Here, N denotes the number of atoms in the molecule, q is the scattering vector, $f_i(q)$ and $f_j(q)$ represent the isotropic atomic form factors of the atoms i and j taking into account the displaced solvent as well as the hydration layer, and d_{ij} is the Euclidean distance between these atoms.

CRYSOL, another standard program in this context uses spherical harmonics expansions to calculate the amplitude of a particle [46]:

$$A_p(q) = \sum_{i=n}^{N} f_n(q) exp(i\mathbf{qr_n}) = 4\pi \sum_{l=0}^{l_{max}} \sum_{m=-l}^{l} i^l Y_{lm}^*(\Omega) \sum_{n=1}^{N} f_n(q) j_l(qr_n) Y_{lm}(\omega_n) \tag{1.18}$$

where $j_l(qr)$ are spherical Bessel functions of order l, $f_n(q)$ is the atomic form factor and $Y_{lm}^*(\Omega)$ are spherical harmonics of order (l;m). While this method improves computational efficiency due to orthogonality of the spherical harmonics, it is limited in accuracy for complex shapes, like molecules with internal cavities [47].

In both cases the computed profile is fitted to an experimental SAXS profile by minimizing the reduced χ^2-function with respect to a scale factor c:

$$\chi^2 = \frac{1}{N} \sum_{i=1}^{N} \left(\frac{I_{exp}(q_i) - cI_{theo}(q_i)}{\sigma(q_i)} \right)^2 \tag{1.19}$$

where $I_{exp}(q)$ and $I_{theo}(q)$ are the experimental and theoretical scattering profiles, respectively, $\sigma(q)$ is the experimental error of the measured profile at each q-value, and N is the number of data points in the SAXS profile.

Modeling the hydration shell

The hydration layer surrounding proteins and nucleic acids highly influences their structure and function. Adequate description of the hydration shell is a non-trivial task, as the composition and properties vary for different macromolecules (Figure 1.7). For instance, the hydration shell around proteins often has a non-uniform electron density [48, 49]. X-ray scattering studies on proteins with known atomic structures revealed that the hydration layer density is on average 1.05–1.20 times higher than that of the bulk [50], mainly attributed to changes in water structure such as higher coordination numbers [7]. Further, the hydration layer is highly dynamic with a thickness depending on the chemical properties of the protein surface [51, 52]. The picture of the hydration shell for nucleic acids is often even more complex, as their interactions with the surrounding is stronger than for proteins of similar molecular weight due to their highly negative charge [49]. For DNA the water density of the hydration layer can be up to six times higher than bulk density and can span a range of up to 1 nm from the surface of the DNA [49]. In addition, structural studies on nucleic acids often require the presence of ions, which will create a so-called ‘ion atmosphere’ around the nucleic acid structure resulting in an increased amount of dissolved salt ions in proximity to the DNA or RNA surface [53]. Modeling of the ion atmosphere can become quite cumbersome as their composition, dynamics and range strongly depends on the ion species [53, 54].

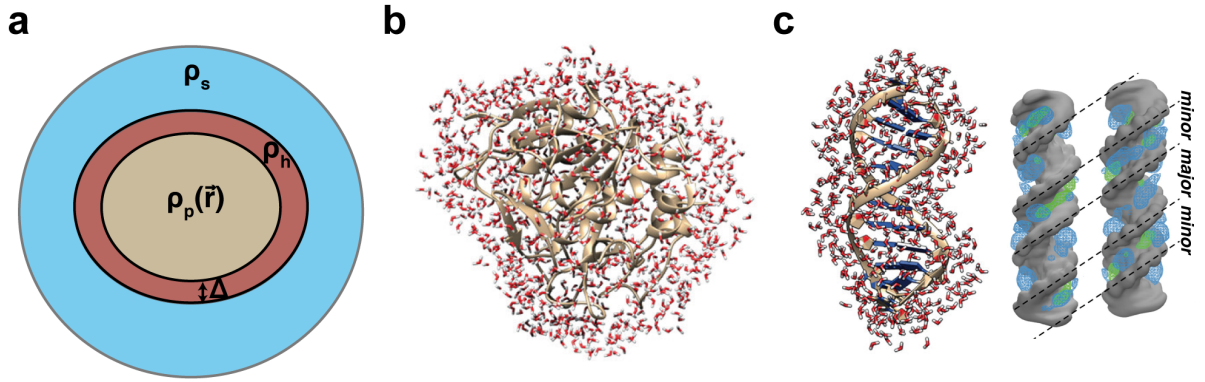

Figure 1.7: Illustrations of the hydration shell for macromolecules in solution. **a** A molecule (brown area) with the scattering length density $\rho_p(\mathbf{r})$ is surrounded by the hydration shell (red area) with a thickness Δ and a density ρ_h that differs from the density of the bulk solvent ρ_s (cyan area). **b** Simulated hydration shell of a protein. Adapted from [52]. **c** Simulated hydration shell of a DNA double strand (left). Adapted from [52]. (Right) Binding of Mg^{2+} and Na^+ ions to the minor and major grooves of a DNA double strand, where the DNA duplex (gray), Mg^{2+} (blue), and Na^+ (green) are shown as isosurfaces of 0.5 and 0.02 $Å^{-3}$ atom number density, respectively. DNA molecules are shown from opposite sides [55]. Reprinted with permission from [55]. Copyright (2012) American Chemical Society.

Most programs used for calculating theoretical scattering patterns represent the hydration shell as a continuous layer with a thickness of 3 Å [56]. The electron density of the hydration layer can be varied within a certain range, depending on the program [46, 56]. While a theoretical scattering pattern can be calculated omitting the contribution from the hydration shell, better fits to the experimental scattering data are often obtained when the hydration layer is included [46, 56]. However, scattering contributions from the ordered hydration layer are still several orders of magnitude lower than the scattering from the solute and the excluded volume [7]. Examples of theoretical scattering profiles calculated for different macromolecules and further discussion of the related outputs are provided in chapters 3 and 4.

1.5.2 *Ab-initio* shape reconstruction based on SAXS data allows for the determination of low-resolution morphologies

Small-angle X-ray scattering offers the possibility to reconstruct a three-dimensional (3D) molecular shape from the one dimensional SAXS profile, known as *ab initio* shape reconstruction, where *ab initio* refers to the absence of a pre-defined input structure [7]. Due to great advances in reconstruction algorithms, *ab initio* models have become a valuable tool for model building, in particular for flexible systems or protein–DNA (RNA) complexes (see section 1.5.3). However, an important prerequisite for reliable *ab initio* modeling is the use of scattering data from a monodisperse sample that does not suffer from significant radiation damage or concentration effects.

The first method for *ab initio* shape determination from scattering data was introduced by Stuhrmann [57] in 1970, where the molecular shape was represented by an angular envelope function describing the molecular surface by spherical harmonics expansion [11]. However, this approach was limited to globular molecules, having no cavities or multiple domains. More sophisticated models could be obtained by shape-reconstruction algorithms, which were proposed in the late 1990's [58, 59] and further developed in the 2000's [60, 61]. Here, the shape

of the macromolecule is represented by a large number (up to thousands) of finite-volume elements, which are either densely packed beads (dummy atoms) [59] or dummy residues [62]. Thereof, a bead (or dummy residue) configuration is searched whose accumulated scattering coincides with the experimental data.

Ab initio reconstruction based on bead models

Representative programs for *ab initio* shape determination using finite-volume elements are the programs *DAMMIN* [59] and *DAMMIF* [61], which employ a simulated annealing protocol. Both programs start from a search volume with dimensions given by the maximum dimension (D_{max}) or the R_g-value of the particle, determined from the SAXS data. The search volume is filled with closely packed beads of radius $r_0 \ll D_{max}$ ($\ll R_g$). The beads are assigned to a certain phase belonging either to the particle or to the solvent (Figure 1.8a). It is important to note that the beads do not represent positions of specific residues or nucleotides. The shape of the resulting dummy atom model (DAM) is described by a binary configuration vector X, from which a scattering profile is calculated using spherical harmonics (see Equation 1.18).

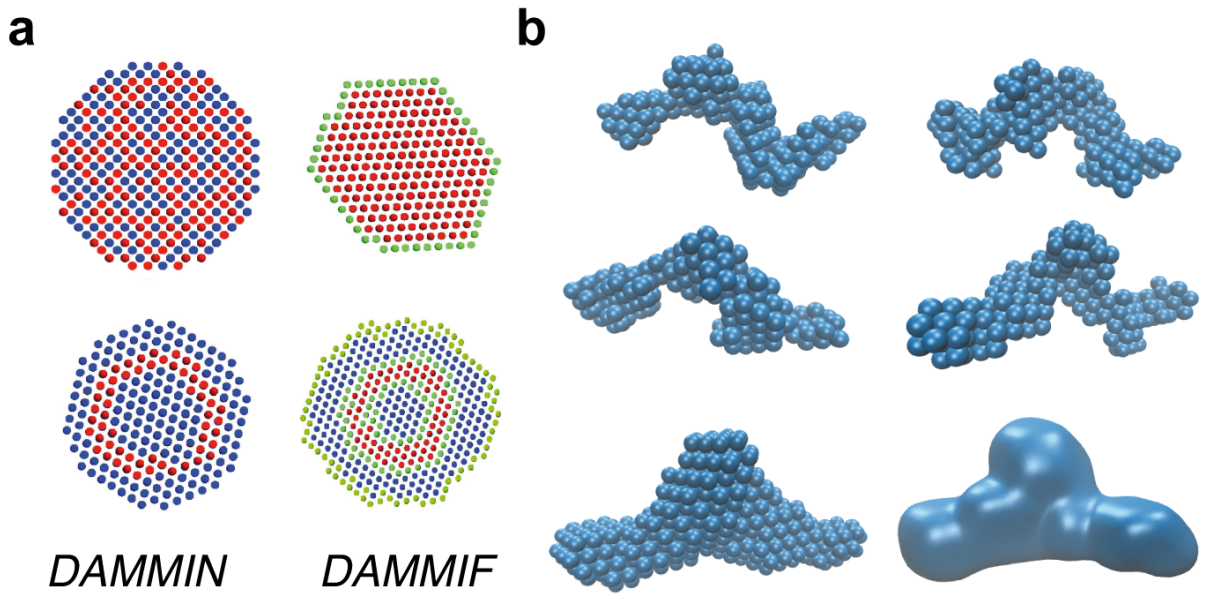

Figure 1.8: Overview of dummy atom based *ab initio* shape reconstructions from scattering data. **a** Cross sections of dummy atom models of *DAMMIN* (left) and *DAMMIF* (right). In the top row initial models are shown: In *DAMMIN* the search volume is usually defined by a sphere with diameter of D_{max}, whereas *DAMMIF* starts from an isometric object with the radius of gyration. The bottom row displays the final models of both programs. The phases of the dummy atoms are indicated by different colors: red corresponds to particle and turquoise, blue and green to solvent. *DAMMIN* allows phase transitions anywhere in the search volume. In *DAMMIF*, only red and turquoise beads are subject to phase changes. Here, the actual, extensible border of *DAMMIF*'s mapped area is indicated by green solvent beads. Reproduced from [61] with permission of the International Union of Crystallography. **b** First two rows display models restored by *DAMMIF* for the HSS domain of the chromatin-remodeling protein ISWI. Bottom row shows the average model from 20 runs and the corresponding density map converted with the software SITUS [63].

To find a configuration that fits the experimental SAXS data best, a simulated annealing protocol is applied that aims to find a configuration *X*, which minimizes a goal function *F(X)* [61]:

$$F(X) = \chi^2 + \sum_{i=1} \alpha_i P_i(X) \tag{1.20}$$

where χ^2 is the difference between experimental and calculated scattering data (see Equation 1.19) and $P_i(X)$ describes penalty terms each weighted by $\alpha_i > 0$ that enforce physical constraints (e.g. interconnectivity and compactness) or can take into account additional structural information (e.g. contacts between specific residues) [64]. The minimization process starts from an initial random configuration X_0 at the so-called annealing temperature $T = F(X_0)$ and runs through the following steps [59]:

1.) A bead from configuration X_0 is randomly selected and its phase (particle or solvent) is changed to obtain a new configuration X.
2.) The difference between both configurations is calculated: $\Delta = F(X) - F(X_0)$.
3.) For $\Delta < 0$, X is chosen and for $\Delta > 0$, X is chosen with the probability $\exp(\Delta/T)$; step 2 is repeated for the chosen configuration.

The process is iterated for a defined number of reconfigurations ($\sim 100 \times N$, with N as number of beads) or a certain number of successful reconfigurations (i.e. $F(X') < F(X)$) at a constant annealing temperature. Next, the annealing temperature is slightly reduced, making reconfigurations that increase *F(X)* less probable, and the minimization procedure is terminated when no further minimization of *F(X)* can be achieved. While in *DAMMIN* the search volume is fixed during the search procedure, *DAMMIF* allows for volume variations if required (Figure 1.8 a) [11].

In contrast to pure Monte Carlo search algorithms, simulated annealing algorithms prevent the system from getting trapped in local minima by accepting also configurations increasing the goal function *F(X)* with a certain probability [11]. Presently, these shape determination programs require hours of CPU time, where *DAMMIF* is up to 40 times faster on a single CPU than *DAMMIN* [61]. Moreover, symmetry restrictions for the particle shape can be imposed, which can improve the reliability of the *ab inito* model and speed up the computation time [30], but can produce reconstruction artefacts in case of misapplication.

The normalized spatial discrepancy value: a measure of uniqueness of *ab initio* models

Reconstruction of a 3D model from a 1D scattering pattern is an ill-posed problem, implying that several models with equally good fits to the same scattering profile can be obtained [65]. Thus, it advisable to perform multiple reconstruction runs and evaluate the outcomes. For this purpose, the normalized spatial discrepancy (NSD) value [66] enabling quantitative comparison of similarities between models, is a useful parameter. In brief, the NSD value for two models is obtained as follows: each 3D model is represented as a set of points (S1 and S2). For each point from S1 the minimum value among distances between a point from S1 and and all points from S2 is determined and vice versa. The resulting distances are added and normalized against the average distances between neighboring points from both sets. For ideally superimposed similar

objects, the NSD value tends to be 0 and it exceeds 1 if the objects systematically differ from one another. A more detailed description of the NSD value can be found in Ref. [66]. The NSD value is implemented in several programs that can be used to superimpose, filter and classify structurally similar models and to generate an average structure from each class (Figure 1.8b) [66, 67]. The final bead model can be converted into standard density map formats by using the software *SITUS* [63] (Figure 1.8b).

1.5.3 SAXS-based hybrid approaches for structural studies on macromolecules and their complexes

The focus of structural biology has recently shifted to structural investigations on dynamic macromolecular assemblies composed of nucleic acids and/or protein complexes, as they are fundamental for many cellular processes. Due to their large size and inherent flexibility, high-resolution structures of the whole complex are hard to obtain and are often only partially available. In this context, comprehensive use of high-resolution techniques, SAXS and bioinformatic methods has become a powerful approach toward understanding the functional roles and interaction mechanisms of these large complexes (Figure 1.9) [37, 41].

To refine an atomic model against SAXS data, fitting can be performed based on normal mode analysis (NMA) or elastic network models (ENM) [68, 69]. In NMA, the molecular structure is represented by a 3D elastic network, where each residue (nucleotide) in the protein (nucleic acid) is reduced to one point and linked to its neighbors in space by springs of the same strength. Global, slow collective motions of the system can be concisely described as a linear combination of the lowest frequency normal modes [70, 71]. For structural refinement theoretical scattering patterns are commonly calculated and the molecule is refined with the aim to fit the calculated profile to the experimental SAXS curve. An example for NMA-based refinement against SAXS data is provided in chapter 4.

When atomic resolution structures or suitable homology models are available, simple fitting of high resolution structures into *ab initio* shapes can be achieved by using the software SITUS, that uses vector quantization of the high and low resolution structures to achieve a best fit between these (see chapter 3 for examples) [72]. However, *ab initio* reconstructions can also serve as a suitable structural framework for model building when only the secondary structure is available. For instance, Lipfert *et al.* [73] could develop a structural model for the VS ribozyme (Figure 1.9), which is the largest known nucleolytic ribozyme consisting of several sub-components and where high resolution information was not available at that time. They calculated SAXS-based *ab inito* models in which they placed cylindrical elements corresponding to individual helical components given by the secondary structure. Conversion of the resulting cylindrical model to a residue specific model in combination with an energy minimization refinement procedure yield an atomistic solution model of the entire VS ribozyme. It was in good agreement with the previously determined crystal structure of VS ribozyme [74].

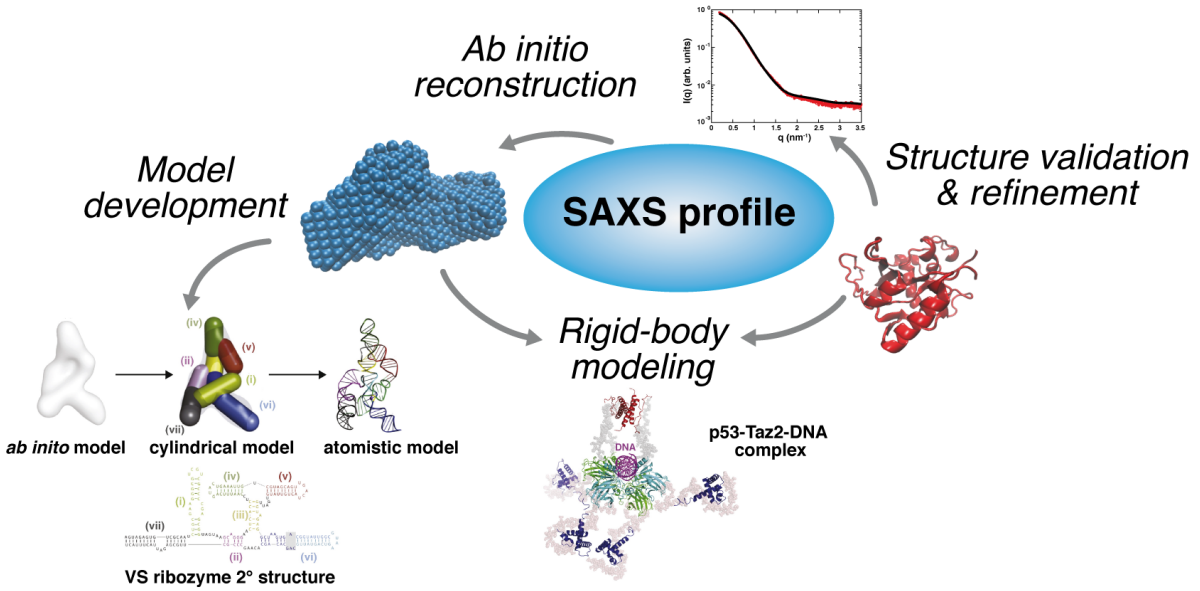

Figure 1.9: Examples of structural analysis approaches combining SAXS with high-resolution data and bioinformatic methods. Graphics on the lower left illustrate the model development of the VS ribozyme solution structure, as described in [73].(Reprinted from [41] with permission from Elsevier Ltd.) In the middle, the rigid-body model of the tumor suppressor protein p53 complex (cyan and green; tetramerization domain (red)) with its Taz2 binding domains (blue) and DNA (magenta), which was deduced by Wells *et al.* [75], reprinted from [41] with permission from Elsevier Ltd.. The atomistic model on the right side was taken from the Protein database [76] (PDB code: 1MO8).

A further hybrid approach is the so-called rigid-body modeling, which has become an attractive concept for quaternary structure analysis of macromolecular complexes or multidomain proteins [7, 65]. Here, atomic models of only individual subunits or domains are available and combined with low-resolution data. For rigid-body modeling, the domains or subunits are oriented such that they either fit best into the low-resolution envelope determined by *ab initio* reconstructions, or that their conformations yield a theoretical scattering profile that best matches the experimental data [77]. As rigid-body refinement can be prone to over-parametrization and multiple non-unique solutions, it is often performed in combination with distance and symmetry constraints obtained from cross-linking or FRET data [15]. The combination of rigid-body modeling and *ab initio* reconstruction has also proven to be advantageous in the refinement of high resolution or homology models, where parts of the structure like flexible linkers or loops are missing. The program *BUNCH* [78] allows for rigid-body refinement by optimizing the position and orientation of domains or subunits and the missing parts, which are represented as interconnected chains composed of dummy residues. An impressive example for rigid-body modeling is the work of Wells *et al.* [75], where the authors employ a combined approach of NMR, X-ray crystallography, and SAXS to deduce a structural model of the multifunctional tumor suppressor protein p53 in complex with DNA (Figure 1.9).

Furthermore, low-resolution information derived from SAXS can be effectively applied in combination with protein-protein docking, a computational modeling approach that aims to predict the 3D structure of a protein-protein complex. Docking itself only produces plausible candidate structures, which have to be filtered, clustered and evaluated [79]. Over the past few

years several integrative docking methods with SAXS have been developed, where the docking models are evaluated based on a χ^2-value of the model scattering profile and the experimental SAXS data [80, 81].

1.6 Experimental SAXS setups

Having discussed the main structural information provided by small-angle X-ray scattering and the diverse possible application of this technique, technical aspects of experimental SAXS setups will be presented.

Small-angle X-ray scattering experiments can be performed either at in-house setups or synchrotron facilities. Over the past few decades a tremendous progress in synchrotron technology and in-house setups, in particular with regard to X-ray sources and detectors, could be observed. Although the majority of biological X-ray data are primarily collected at dedicated synchrotron beamlines, there is still a demand for laboratory-based systems due to limited availability of measurement time at synchrotron facilities and associated logistic challenges concerning sample stability and transportation.

1.6.1 Laboratory-based SAXS

During this thesis I was involved in the construction of a laboratory-based SAXS setup. A detailed description of the setup is provided in chapter 3. Here, only the main important components and their functions are introduced and recent developments of in-house SAXS sources are presented (Figure 1.10).

X-ray sources and focusing optics

Regardless of the type of X-ray sources, the generation of X-rays in the laboratory follows the same principle: in a vacuum tube a high voltage (e.g. 50 kV) is applied to accelerate electrons that are released by a hot cathode, towards a metal target (anode). Collision of the electrons with the metal results in the generation of heat ($\sim$ 99%) [82] and X-rays. The resulting X-ray spectrum is a superposition of a continuous spectrum and a sharp line spectrum. The broad continuous part is related to the deceleration of electrons in the metal resulting in the emission of photons known as 'Bremsstrahlung' with an energy maximum corresponding to the applied voltage.

Upon collision with the target atoms, electrons with a sufficiently high energy can knock a bound orbital electron out of an inner shell of a metal atom. The resulting vacancy is subsequently filled with an electron from an outer shell producing a photon with a characteristic energy corresponding to the energy difference between the two shells. Highly pronounced peaks occur in the so-called 'characteristic spectrum' and which are named after the inner shell (K, L, M) and the distance between the shells (α for neighboring shells, β for next-neighbors). As the K_α-line has the highest intensity, the corresponding wavelength is used for experiments requiring a monochromatic beam. Available anode materials include chromium (Cr; K_α = 2.29 Å), copper (Cu; K_α = 1.54 Å), molybdenum (Mo; K_α = 0.71 Å), silver (Ag; K_α = 0.56 Å) and tungsten (W; K_α = 0.02 Å) [83], where Cu-anodes are most commonly used.

Since the first in-house-based SAXS experiments, X-ray tube anodes and appropriate focusing optics have been under an ongoing development. Early sealed-tube instruments suffering from the problem of low power and anode melting were replaced by rotating anodes often in combination with perfect-crystal monochromators and long curved mirrors for beam focusing [84]. Although these configurations yield a higher brilliance, a quantity that describes the photon flux considering also the beam dimensions (Table 1.1), and source sizes in the mm-regime (Table 1.1), rotating anodes require high maintenance and are prone to failure [85].

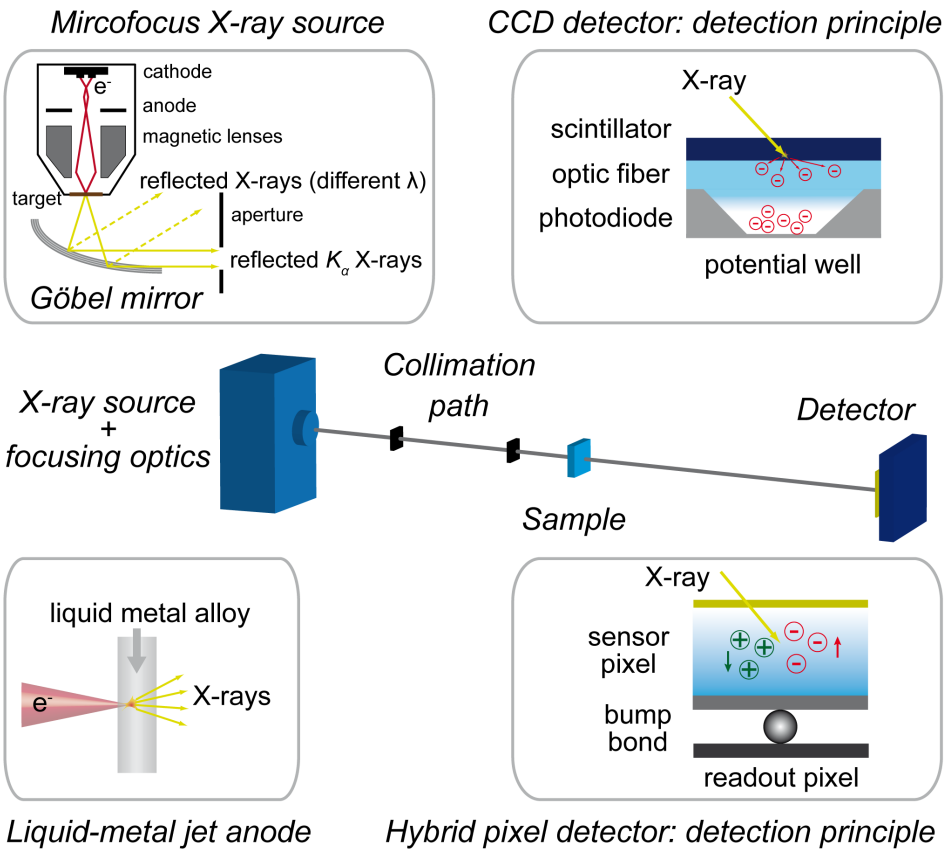

Figure 1.10: Layout of an laboratory-based SAXS setup and its most relevant components. (Top left) Schematic of a microfocus X-ray source in combination with a Göbel mirror. Electrons are accelerated by a high voltage bias towards an anode. The passing electrons are focused by magnetic lenses to the target. K_α-X-rays are parallelized and focused by Bragg-reflection at the parabolic multilayers of the Göbel mirror, while X-rays of other wavelengths (λ) are blocked by an aperture. (Bottom left) Operating principle of a liquid-metal jet anode, where a focused electron beam hits a circulating liquid-metal stream resulting in the generation of X-rays. (Top right) Detection principle of a CCD detector shown for one pixel. Incidence of an X-ray photon gives rise to its conversion into several visible photons achieved by a scintillator material (e.g. phosphorus). These photons are then converted to a current in the photodiode. Potential wells store the generated charges (electrons), which are transferred from well to well followed by amplification and digitization. (Bottom right) Detection principle of a hybrid pixel detector shown for one pixel. The incident X-ray photon is directly converted into a current in the sensor pixel. The so-called 'bump-bonding' technique allows for the collection of electrons, which are then transformed into an electric impulse that is subsequently amplified and discriminated before being counted in the readout pixel [86].

The introduction of microfocus X-ray sources and Göbel mirrors [87], which are parabolically bent multilayers with a thickness varying along the parabola, could reduce the beam focus spot size to several tens of μm (Table 1.1, Figure 1.10) and a reduction in power requirements [85]. However, these systems are still limited in performance due to melting of the anode material above their actual power load capacity [85]. A recent innovation from Excillum circumvents the melting-problem by using a liquid-metal jet as anode material (Figure 1.10) [82, 88]. Current sources employ a liquid gallium (K_α = 1.34 Å) or indium (K_α = 0.51 Å) alloy that is pumped in a closed circuit and hit by an electron beam in an evacuated chamber, delivering significantly higher brilliances (Table 1.1) while withstanding higher electron beam power. In combination with multilayer focusing optics, the device performance is comparable to second generation bending magnet synchrotron beamlines [85].

System	Power (W)	Spot size on anode (μm)	Brilliance (photons / s mm^2 mrad^{-1})
Standard sealed tube	2000	10000 × 1000	0.1×10^9
Standard rotating anode	3000	3000× 300	0.6×10^9
Microfocus sealed tube	50	150 × 30	2.0×10^9
Excillum Metal Jet D2+ 160 kV	up to 250	5 - 30	up to 6.5×10^{11}

Table 1.1: Comparison of technical properties of different X-ray sources. Values were quoted from [85] and Excillum (http://www.excillum.com).

Collimation

In order to collimate the X-ray beam, controlling beam size and divergence, apertures like pinholes and slits are integrated in SAXS instruments [84]. First SAXS setups relied on line-collimation, where the X-ray beam is well collimated in the direction of the scattering vector, but not in the perpendicular direction [36], resulting in smearing effects of the recorded scattering intensities [84]. Development of slit systems led to the use of pinhole collimation, obviating desmearing procedures but causing lower flux and an increased background due to so-called parasitic scattering from the slits [89]. Great improvement in data quality could be achieved by the invention of hybrid metal-single-crystal slits, where a rectangular single-crystal substrate is bonded to a metal base with a large tapering angle away from the beam producing almost no observable slit scattering [90].

Detectors

For a long period of time scattering data were collected based on X-ray films. It was in the 1980's and 1990's that first electronic detectors comprising multiwire proportional counters and electronically controlled imaging plates were introduced. This enabled the connection to computers making data collection much faster [85]. Despite detector type specific advantages, such as detection area size or a high dynamic range, drawbacks like slow readout times (~ min) let to extended measurement times. The latter could be improved with charge-coupled device (CCD) based detectors with readout times ~ seconds, but where the performance is affected by thermal noise known as dark current [86]. Today, recently developed hybrid-pixel photon counting devices [91] have become standard detectors at most synchrotron SAXS beamlines

and have become more and more established for in-house setups. Here, an active area of sensor pixels, usually made from silicon (Si), cadmium telluride (CdTe) or gallium arsenide (GaAs) [86], absorbs every photon generating electron-hole pairs. The electrons are collected via a so-called 'bump-bonding' into a readout chip. This technique results in a wide dynamic range, high count-rates (up to 10^7 photons/s/pixel) and short readout times (~ ms) in the absence of readout noise and dark current.

1.6.2 Synchrotron-based SAXS

Synchrotron radiation is the electromagnetic radiation emitted by electrons (or other charged particles) moving close to the speed of light in an external magnetic field that forces them to follow curved trajectories. In modern synchrotron sources, a linear accelerator (LINAC) in combination with a booster ring serves to accelerate electrons to several giga electron volts (GeV) (Figure 1.11). The electrons are then injected into an evacuated storage ring containing arrays of different magnets that focus and bend the electron beam. Arced sections of the ring are equipped with bending magnets while straight sections contain so-called insertion devices. As the magnets force the electrons to stay on a circular path, which can be considered as a form of acceleration, the electrons loose energy by emitting synchrotron radiation. The energy loss during each turn is compensated by radio frequency (RF) supply. As the synchrotron radiation is emitted tangentially to the plane of the electron beam when the electrons pass the magnets, beamlines, containing optics and an experimental station (Figure 1.11), are located close to the magnets and run off tangentially to the storage ring. The beamline optics are designed to deliver an intense X-ray beam that can be fine-tuned in energy, beam-size, bandwidth, and flux to deliver the appropriate conditions for a particular experiment.

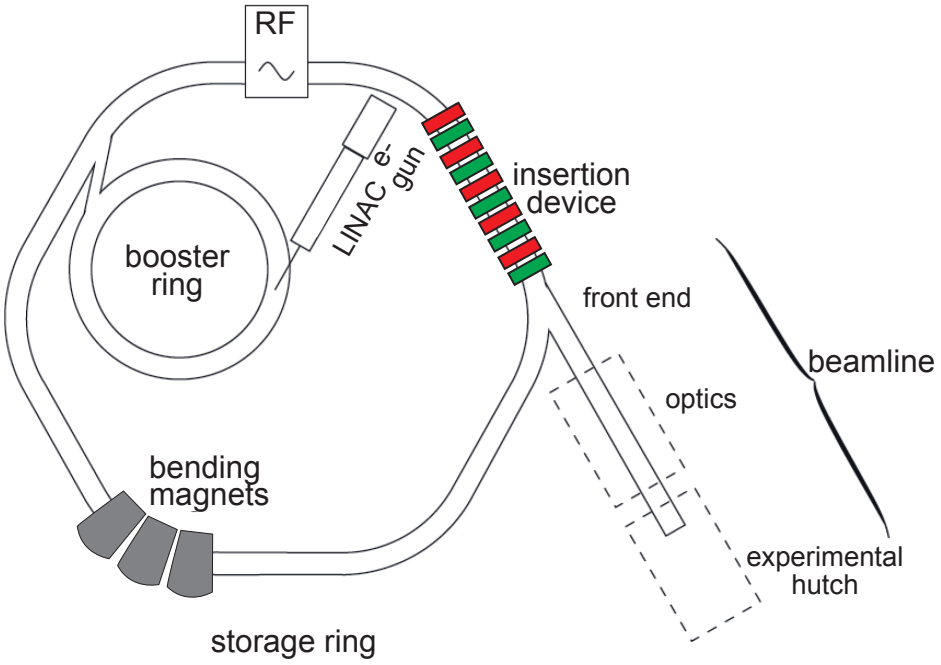

Figure 1.11: Sketch of the main components of a synchrotron. Adapted from [92] with permission from Wiley. Copyright ©2011 John Wiley & Sons, Ltd..

The ESRF in Grenoble is one of the world's largest synchrotron facility in Europe with a storage ring circumference of 844 m and 49 different beamlines. The beam is usually kept at current of 100 mA and brought to an operating energy of 6 GeV (see *www.esrf.eu*).

Since the first observation of synchrotron light in 1947, three generations of synchrotron radiation sources have been established until now. While during the 1960's so-called *first generation* synchrotron radiation facilities served only to perform high energy physics experiments, *second generation* sources, equipped with bending magnets and magnetic structures known as wigglers, were totally dedicated to synchrotron radiation studies (Figure 1.12). Improvements in insertion device technology has allowed to conceive current *third-generation* synchrotron light sources optimized for synchrotron radiation of much higher brilliance (section 1.6.2) with small beam sizes and tunable energies (Figure 1.12). Thereof, synchrotron radiation has found an extensive use in varying disciplines of fundamental and applied research, illustrated by the fact that ~ 77% of the total number of structure depositions in the Protein Data Bank (PDB) were based on the use of synchrotron radiation in 2016 [93]. However, a new generation of synchrotron sources has already been introduced with the development of free electron lasers (FELs) that can produce very short coherent light pulses (~ 10^{-15} s) with even higher peak intensities than the most powerful synchrotrons.

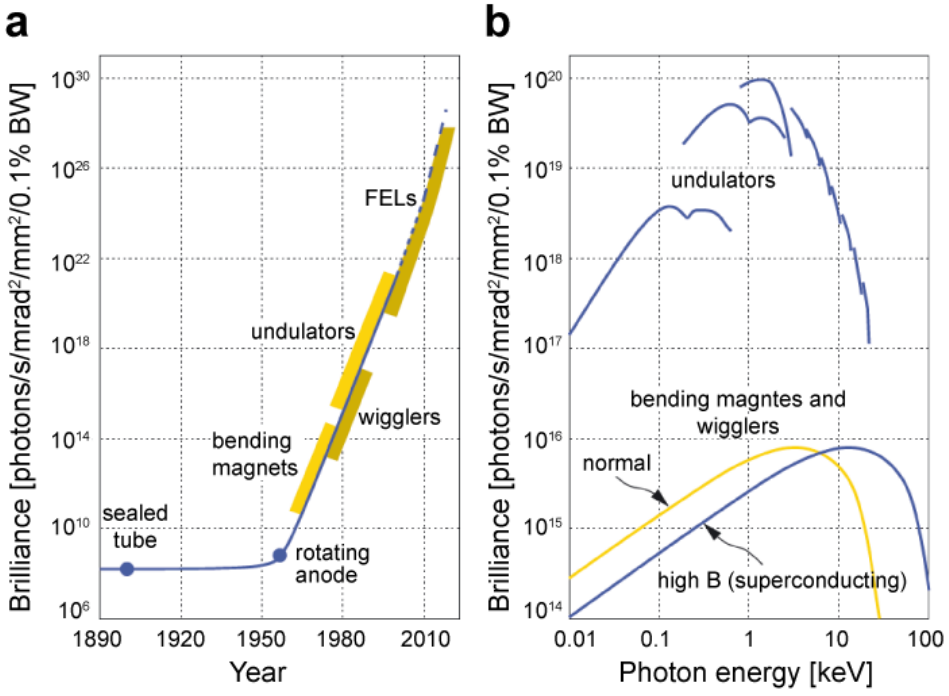

Figure 1.12: Overview of the brilliance of different X-ray sources. **a** Chronological development of X-ray sources and corresponding brilliances. **b** Spectral brilliance curves for different magnet types frequently applied in 3^{rd} generation synhcrotron facilities. Reused from [92] with permission from Wiley. Copyright ©2011 John Wiley & Sons, Ltd..

Properties of synchrotron radiation

The radiation pattern emitted by electrons circulating in a storage ring close to the speed of light, is confined to a narrow cone in the direction of motion [9]. The opening angle θ of the cone is given by:

$$\theta \approx \frac{mc^2}{E} = \gamma^{-1} \tag{1.21}$$

where m denotes the electron rest mass, c the velocity of light, E the storage ring energy, and γ the Lorentz factor. For typical energies E of 1–8 GeV the opening angle is in the order of 0.5–0.06 mrad [92]. For many experiments the photon beam has to be focused down to a very small spot which is quantified by a highly relevant synchrotron radiation property termed brilliance. The latter essentially describes the spatial and angular distribution of the photon flux and is given by [92]:

$$Brilliance = \frac{photons/second}{(mrad)^2(mm^2\ sourcearea)(0.1\%bandwidth)} \tag{1.22}$$

For modern synchrotron facilities optimization of photon flux and brilliance is of major concern. These quantities are considerably influenced by the magnet type.

Bending magnets

Synchrotron radiation from a bending magnet (BM) is confined to a flattened cone (Figure 1.13a) and covers a continuous spectrum extending from the X-ray to infrared region. It is linearly polarized when observed in the bending plane and elliptically polarized out of this plane [94]. The spectrum is characterized by a critical energy E_c, that divides the spectrum into two parts of equal radiated power (i.e. half of the total power is radiated at energies below E_c and the other half at energies above E_c) (Figure 1.13b). The critical energy is determined by the properties of the synchrotron source [92]:

$$E_c[keV] = 0.665 \cdot E^2[GeV] \cdot B[T] \tag{1.23}$$

where E is the energy of the electron beam and B the magnetic field of the bending magnet. Figure 1.13b depicts BM spectra for different storage energies, illustrating the shift of E_c towards higher values for increasing storage ring energies. The maximum achievable photon energy is a few times its critical energy.

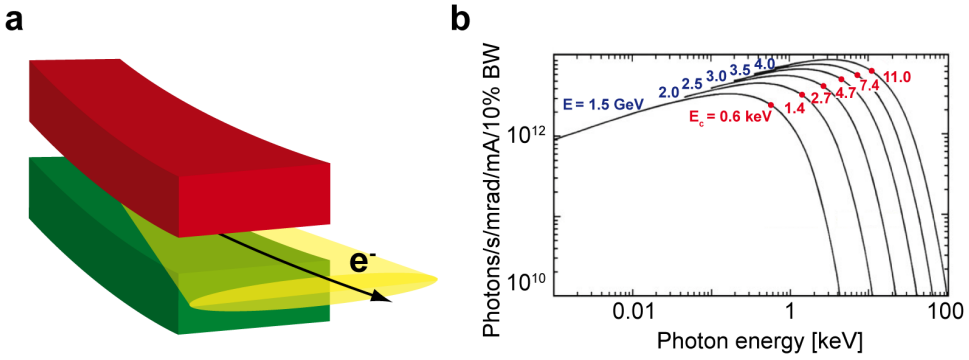

Figure 1.13: Schematic view of the radiation fan and corresponding emission spectrum generated by a bending magnet (BM). **a** Sketch of the synchrotron emission spectrum generated when the electron beam passes the BM. **b** Spectral distribution of the emitted photons for different storage ring energies (written in blue). Red circles display the critical energy (E_c) and the corresponding values are noted below. Adapted from [94], with permission from Springer. Copyright ©Springer-Verlag Berlin Heidelberg 2015.

Insertion devices

Inclusion of insertion devices (ID) in storage rings designating second and third generation synchrotron facilities, has allowed for the production of significantly higher flux and brilliance than realized by BM (Figure 1.14). In ID the magnets are periodically arranged producing an alternating magnetic field, which forces the electrons on an oscillatory trajectory. There exist two types of ID known as wiggler and undulator. In the following only the main characteristics of undulators will be discussed. Undulators generate a "quasi-monochromatic" radiation spectrum where the photons emitted by the oscillating electrons interfere. Constructive interference occurs only for a particular wavelength and its harmonics (Figure 1.14). The resulting spectral lines are equally separated in energy ΔE by [92]:

$$\Delta E = \frac{2hc\gamma^2}{\lambda_u \left(1 + \frac{K^2}{2}\right)} \tag{1.24}$$

with h as Planck constant, λ_u as undulator period and K as dimensionless parameter, which depends on the ID properties and is typically ~ 1 for undulators. The angle of the radiation cone of the n-th harmonic is compressed by a factor of $1/\sqrt{N}$ (where N is the number of periods in the undulator) in comparison to the opening angle of the radiation from a BM [9]. Moreover, for an undulator with N periods, the brilliance can be up to a factor of N^2 more than a for bending magnet. The polarization of the emitted radiation can be controlled by laterally shifting the relative positions of the magnet poles, resulting in a linear polarization if the oscillations are confined to a plane, or a circular polarization, if the oscillation trajectory is helical.

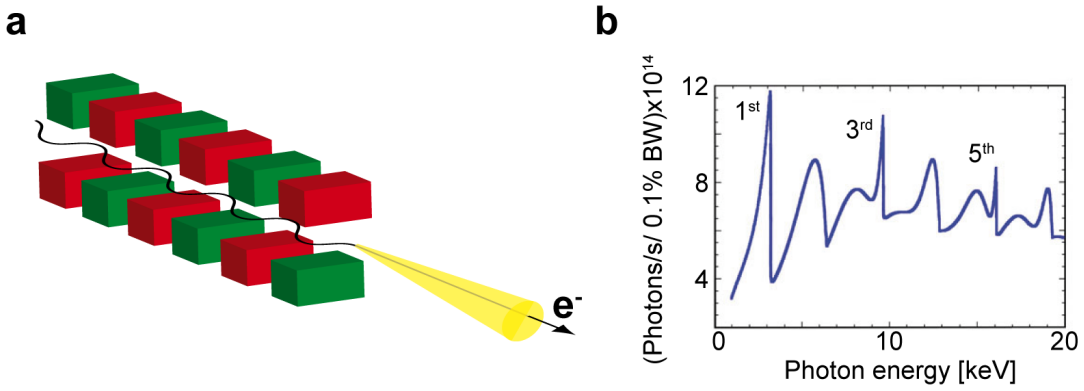

Figure 1.14: Schematic view of the radiation fan and corresponding emission spectrum generated by an undulator. **a** Sketch of the synchrotron radiation emission from a multipole undulator. **b** Calculated flux spectrum of the APS (Advanced Photon Source (7 GeV)-Argonne (Illinois)) undulator A, optimized to generate X-ray photons in a wide energy range, using the first, third and fifth radiation harmonics (sharp peaks) [94]. The electron beam current was 100 mA. Adapted from [94] with permission from Springer. Copyright ©Springer-Verlag Berlin Heidelberg 2015.

1.6.3 Example for a biological SAXS beamline

Synchrotron-based SAXS experiments are conducted in the so-called 'experimental hutch' of a beamline (Figure 1.11) A typical layout of a synchrotron beamline is illustared in Figure 1.15 showing the BioSAXS beamline BM29 at the ESRF in Grenoble [95], where most SAXS experiments during this PhD thesis were conducted. The X-rays generated from a BM are first masked then monochromated and calibrated to the desired energy and further shaped in a fully evacuated beam path. The experimental hutch is equipped with an automated sample loader [96], where a robot loads the sample from a PCR tube into a quartz capillary (diameter ~ 1.5 mm). Commonly, the sample is passed through the capillary at a constant flow velocity and the beam hits the sample at a defined position. Typical sample volumes for one run are in the order of 20 - 30 μl. The scattered X-rays pass an evacuated flight tube and hit the detector, which is placed ~ 3 m behind the sample environment. A beamstop in front of the detector blocks the direct beam in order to prevent damage of the detector array. A more detailed description of the measurement procedures can be found in the Materials and Methods section of chapter 4.

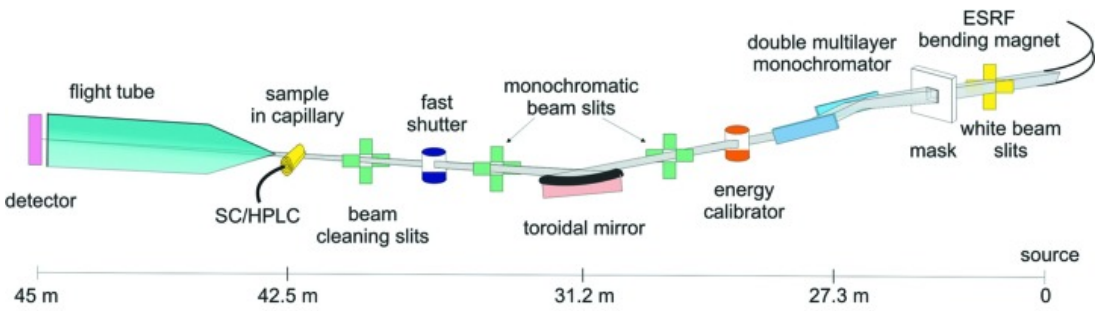

Figure 1.15: Schematic view of the BioSAXS beamline BM29 at the ESRF. Adapted from [95].

Moreover, SAXS experiments described in chapter 5 were carried out at beamline ID02 at the ESRF, where two undulators deliver a higher photon beam than at beamline BM29 (Table 1.2). The beamline layout is comparable to the one of beamline BM29 and main characteristics of both beamlines are summarized and compared to the in-house SAXS source at the LMU (see chapter 3) in Table 1.2.

Parameter	**ID02**	**BM29**	**in-house source LMU**
Energy (keV)	7.7-17.0 (12.4*)	7.0-15.0 (12.4*)	17.4
Maximum flux (photons/s)	$\sim 10^{14}$	$\sim 10^{12}$	2.5×10^{6}
Standard beam size (mm × mm)	0.2×0.4	0.5×0.5	1.2×1.2
Divergence (mrad)	0.02×0.04	0.13	0.16
Sample-detector distance (m)	0.6 - 30.0	2.9	1.1 - 2.5
q-range (nm^{-1})	0.001 - 60	0.03 - 5	0.09 - 3.8
Sample volume (μl)	20	30	80
Exposure time	$\sim$ 10 - 20 ms	$\sim$ 1 s	2 h

Table 1.2: Comparison of the main X-ray beam characteristics of beamline ID02 and BM29 at the ESRF in Grenoble and the in-house source at the LMU. * denotes the optimum energy.

Chapter 2
DNA Nanotechnology

2.1 Introduction

The concept of nanotechnology was first formulated by the physicist Richard Feynman in his famous seminal talk entitled 'There's plenty of room at the bottom' in 1959 [97]. He envisioned the possibility to precisely manipulate individual atoms and molecules and this idea was further developed by the engineer Eric Drexler, presenting a bottom-up manufacturing approach to create artificial molecular machines ('molecular assemblers') that are able to direct chemical reactions or to build copies of themselves and other molecular machines 'atom-by-atom' [98]. Another way to design molecular structures employs molecular self-assembly, describing the process in which individual molecules spontaneously assemble in a highly parallel manner into a defined target structure requiring no external guidance. The final structure is programmed in the shape and functional groups of the molecules.

In 1980 the crystallographer Nadrian Seeman proposed to utilize DNA molecules as a programmable building material [99], where one takes advantage of the predictable properties of Watson-Crick base pairing to encode the global target shape. He originally intended to construct three-dimensional (3D) DNA lattices enabling to orient proteins and study their structure with X-ray crystallography making the delicate crystallization process redundant. Early attempts resulted in complex DNA nanostructures with symmetric shapes like a cube [100] or a truncated octahedron [101]. A conceptual breakthrough was achieved with the introduction of the 'DNA-origami' technique, laid out by Paul Rothemund in 2006 [102]. This approach has allowed for the creation of both two- and three-dimensional nanoscale objects with increasing structural complexity and applicability [103–117]. The following sections give an overview of the DNA origami technique and created nanostructures as well as possible applications.

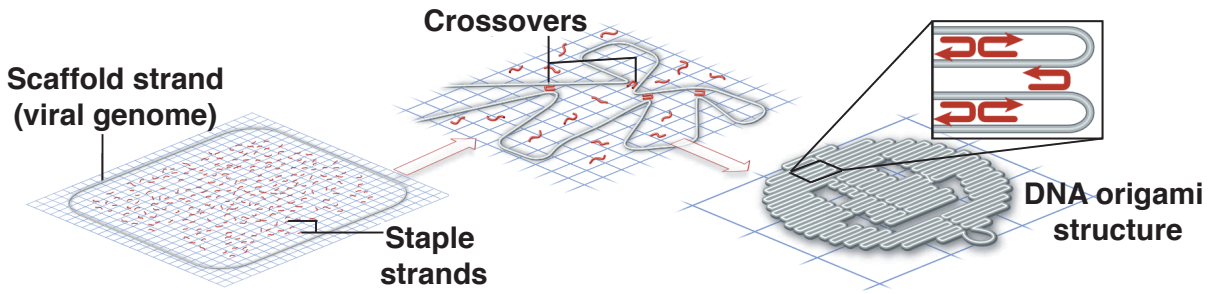

Figure 2.1: Schematic representation of DNA origami-based self-assembly. A long viral circular single-stranded DNA strand (scaffold strand) is mixed with hundreds of short 'staple' strands that bind sequence specifically to the scaffold strand forcing the scaffold into the designed target shape. Adapted from [118] with permission from Nature Publishing Group, copyright 2010.

2.2 DNA origami-based self-assembly

The DNA origami technique employs a long (~ 7000 - 8000 bp) circular single-stranded DNA template strand, typically derived from the M13 bacteriophage genome and known as 'scaffold strand', which is folded into a prescribed target shape by hundreds of short synthetic DNA oligonucleotides ('staple strands'), typically 20 - 60 bp long (Figure 2.1) [119]. The latter are designed to be complementary to specific segments along the scaffold strand allowing for the hybridization between staples and the scaffold strand. As a result spatially distant regions are brought together and a parallel-array of double helices is formed. Adjacent helices are held in place by double crossovers in the form of holliday junctions, which are covalent phosphate links between two DNA double helices.

The self-assembly of DNA origami objects proceeds in one-pot reaction mixtures containing the required DNA strands and cations (generally divalent magnesium ions, but monovalent sodium ions can also be used [120]). The reaction mixtures are subjected to a thermal annealing ramp, starting with a thermal denaturation step in order to render all DNA in solution single-stranded. Next, the sample is continuously cooled over a narrow, object-specific temperature interval [121], where the staples attach to their complementary parts on the scaffold strand. This process is highly cooperative. The final solution contains the target objects, excess staple strands and some unintended by-products, such as misfolded or defective structures, and higher-order multimeric aggregates that can form during the reaction [122]. Thus, purification procedures are required to extract only the target DNA origami objects from the folding reaction mixture (see Refs. [122, 123] for details). Scaffolded DNA origami enables the creation of a variety of complex objects reaching over 100 nm in size and molecular masses in the megadalton regime [102, 124, 125].

2.3 Static DNA origami structures of complex 2D- and 3D shapes

First DNA origami objects were of planar, arbitrary two dimensional shapes including a triangle, a star and a smiley face (Figure 2.2a) [102]. Due to the ability to functionalize DNA nanostructures with nanometer precision, 2D origami structures have been successfully applied as templates to organize molecules, proteins or nanoparticles into specified geometries [126] or for visualization of chemical reactions [127]. Expanding DNA origami structures to the third dimension was mainly achieved by Shih and coworkers [124] in 2009. Their design concept is based on a flat array of parallel helices that can be folded into 3D structures with double helices constrained to a honeycomb lattice (Figure 2.2a). The almost simulatenous development of the open-source software caDNAno [128] could facilitate the design of 3D DNA origami nanostructures and has become a standard design tool. Subsequent work allowed for even more sophisticated 3D DNA origami structures [129]. Here, site-directed insertions and deletions of base pairs in DNA bundles, allows for creating twisted and curved 3D DNA origami objects of varying geometries (Figure 2.2a). Further design concepts, deviating from the honeycomb lattice framework were introduced a few years later (Figure 2.2a) [125, 130, 131].

Due to the great interest in DNA nanotechnology and rapid advances in the development of design rules and assembly methods, DNA origami has emerged as a versatile toolset for constructing well-defined, arbitrarily shaped nanostructures with applications in a variety of fields. Examples include 3D DNA origami nanostructures applied for biosensing [132], super-resolution microscopy [133], NMR-based structure determination of membrane proteins [117] or as structural framework for the spatial organization of synthetic nanomaterials to tailor surface plasmon resonances [134, 135] and to create artificial light-harvesting complexes [136] (Figure 2.2b).

2.4 Dynamic DNA nanostructures: state of the art and general concepts

Despite the diversity of static DNA origami objects, functional nanostructures that can be used as targeted drug delivery vehicle or as artificial nanomachines with defined and controllable functionalities will likely require the ability to undergo reconfigurable conformational changes. In general, conformational transitions of dynamic DNA devices are triggered and controlled by external stimuli. In this context a reaction known as toehold-mediated strand displacement where single stranded (ss) DNA strands serve as an external trigger, has become a widely used strategy to direct conformational changes [137, 138]. The first successful realization of this concept was demonstrated in 2000 by Yurke *et al.* [138], who had developed a so-called DNA tweezer. It was further adapted to create dynamic DNA origami nanostructures, such as a DNA origami box with a controllable lid [139] or a DNA nanorobot [110] allowing for molecular payload transport and release in cells (Figure 2.2b). Strand displacement reactions can be considered as a random walk process with reaction rates between $1-10^6\ M^{-1}s^{-1}$ [137] depending on the properties of the toehold domain and the input strand concentration. Conformational transitions of DNA origami devices triggered by ssDNA strands are reported to occur on the timescale of minutes [137].

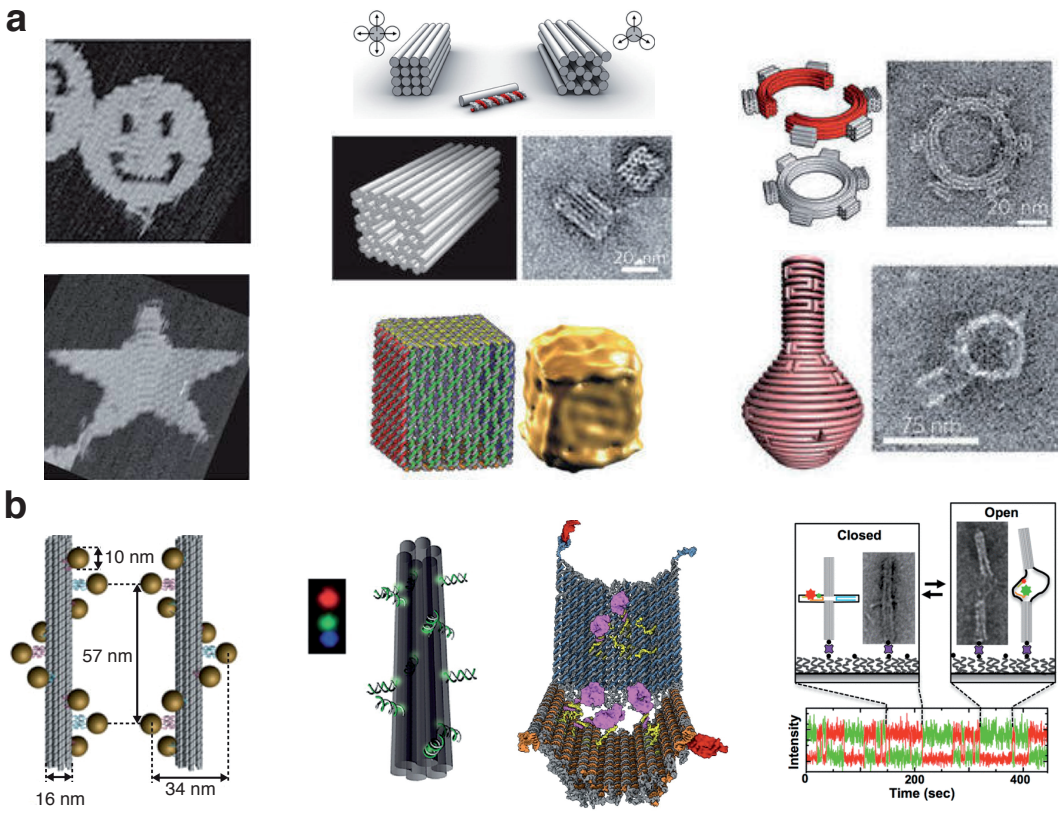

Figure 2.2: Overview of 2D and 3D DNA origami structures. **a** First planar 2D DNA origami structures designed by Paul Rothemund (left). Multilayer DNA origami objects in square lattice (left) and honeycomb lattice (right) packing, based on the design principles from Shih and coworkers [124] (top, middle). Below, a 3D square nut as an example for a multilayer object is shown, followed by a hollow box designed by Andersen *et al.* [139]. On the right: a square-toothed gear (top) and a nanoflask (bottom) as represenatives for curved 3D DNA origami objects. Figures were reused from [140] with permission from Nature Publishing Group, copyright 2011. **b** Chiral plasmonic nanostructures where goldnanoparticles are attached to a DNA origami helix bundle (left). Imaging probes for fluorescence microscopy using fluorescently labeled DNA origami helix bundles. DNA nanorobot that can carry molecular payloads and release them when specific cell surface proteins are present (middle). Figures were adapted from [141] with permission from Elsevier, copyright 2013. Dynamic nanodevice exhibiting a tunable ensemble of states that respond to physical interaction with the local environment (right) [142]. Reused from [142].

An alternative method is to design DNA devices where the conformational transition is initiated by changes in pH, ionic strength, temperature or light irradiation. The latter include azobenzene modified DNA devices [143] and 3D plasmonic DNA origami nanosystems, labeled with gold-nanoparticles [144, 145] that can reversibly switch between two conformational states upon the irradiation with UV and visible light. Castro and coworkers [142] designed a DNA origami nanodevice that can sense and respond to the local environment by changing its conformation (Figure 2.2b).

A very common approach employs the integration of specific DNA sequence motives such as the i-motif [146] or poly(dG-dC) sequences [147] that are sensitive to changes in solution conditions. These structural motives were implemented in a pH-responsive DNA device changing between an open and a closed conformation upon the addition of H^+ or OH^- ions [148] and a DNA origami based rotary motor with a poly(dG-dC) motif as functional site, where a B-Z DNA transition occurs when the magnesium chloride concentration is increased [108].

Using external stimuli other than DNA as trigger offer the advantage that related conformational changes of dynamic DNA nanostructures can occur on faster timescales (~ seconds) [149, 150].

Recently, Gerling *et al.* [112] reported on a framework that allows for the dynamic assembly and disassembly of homo- and heteromultimeric 3D DNA origami objects upon changes in cation concentration or ambient temperature. The objects feature shape-complementary components that interact via short-ranged nucleobase stacking bonds competing against electrostatic repulsion between the involved interfaces. A detailed structural description and kinetic analysis of related DNA origami structures are provided in chapters 4-6.

2.5 Future challenges of DNA origami based nanostructures

The previous sections have illustrated the interdisciplinary character and the rapid growth of DNA nanotechnology. However, the field also faces some challenges that need to be addressed. For instance, broader applicability especially in biomedical applications will require reduction in costs for synthesis and an increase in quantity regarding fabrication of DNA origami structures. Additionally, some applications may require even larger and complex DNA origami objects than currently feasible. As the size is limited by the use of M13 bacteriophage-based DNA, use of longer scaffold strands [151], assembly of pre-formed structures [152] or extended hierarchical assembly approaches [153] have been introduced for size expansion.

Also, the variety of structural analysis techniques might be further exploited for detailed structural characterization of DNA origami objects, which will be helpful for future design strategies or optimization. So far, structural analysis of DNA origami objects mostly rely on AFM or negative-stain TEM imaging, which require surface immobilization of the sample, potentially biasing the conformation of the sample and making it difficult to detect conformational changes upon variation in solution conditions. Here, the application of cryo-EM and SAXS, that both have been succesfully applied in DNA nanotechnology [2, 154–156], can be considered as promising complementary techniques. In combination with computational approaches [157] a more profound structural characterization of large DNA origami objects might be achieved.

Finally, a major obstacle is to enhance the stability of DNA origami structures in cellular environment, where denaturation of DNA due to physiological salt concentrations and structural degradation mediated by nucleases limit their applicability [114]. Improvements in stability and bioavailability have been made by enveloping DNA nanostructures in PEGylated lipid bilayers [158] or oligolysine [114].

Part II

Results

Chapter 3

A Mo-Anode-Based In-House Source for Small-Angle X-Ray Scattering Measurements of Biological Macromolecules

Summary

We demonstrate the use of a Molybdenum-anode-based in-house SAXS setup to study biological macromolecules in solution. Our system consists of a microfocus X-ray tube delivering a highly collimated flux of 2.5×10^6 photons/s at a beam size of 1.2×1.2 mm^2 at the collimation path exit and a maximum beam divergence of 0.16 mrad. The resulting observable scattering vectors q are in the range of 0.38 Å^{-1} down to 0.009 Å^{-1} in SAXS configuration and of 0.26 Å^{-1} up to 5.7 Å^{-1} in wide-angle X-ray scattering (WAXS) mode. To determine the capabilities of the instrument, we collected SAXS data on weakly scattering biological macromolecules including proteins and a nucleic acid sample with molecular weights varying from ~ 12 to 69 kDa and concentrations of 1.5-24 mg/ml. The measured scattering data display a high signal-to-noise ratio up to q-values of ~ 0.2 Å^{-1} allowing for an accurate structural characterization of the samples. Moreover, the in-house source data are of sufficient quality to perform *ab initio* 3D structure reconstructions that are in excellent agreement with the available crystallographic structures. In addition, measurements for the detergent decyl-maltoside show that the setup can be used to determine the size, shape, and interactions (as characterized by the second virial coefficient) of detergent micelles. This demonstrates that the use of a Mo-anode based in-house source is sufficient to determine basic geometric parameters and 3D shapes of biomolecules and presents a viable alternative to valuable beam time at third generation synchrotron sources.

This Chapter was reproduced from Bruetzel *et al.* [1], with the permission of AIP Publishing. Author contributions: L.K.B, S.F., B.N., and J.L. designed the study and wrote the paper, L.K.B. and S.F. constructed the setup and performed experiments with A.S., S. M. S.; all authors analyzed the data.

3.1 Introduction

Small-angle X-ray scattering (SAXS) is a powerful tool to investigate the structure and interactions of biological macromolecules in solution [7, 10, 31]. SAXS has the important advantage of being a solution-based technique, thus obviating the need for sample crystallization and enabling studies of biological macromolecules in a range of solution conditions, from (near-) physiological to highly denaturing [39]. In the past, SAXS data have frequently been used to determine basic parameters of macromolecules in solution, such as the radius of gyration [29, 30] (R_g) and the maximum intermolecular distance [159] ($Dmax$). Determination of e.g. (R_g) under varying solution conditions has provided important insights into protein [39] and RNA folding [160] and into the nature of the unfolded states [161, 162]. Nonetheless, the utility of SAXS data has been tremendously enhanced in the last two decades through the increasing availability of algorithms to determine and to compare the (low resolution) 3D structures of macromolecules from 1D scattering profiles. In particular, a number of algorithms now make it possible to obtain low resolution 3D "bead" models from SAXS data for proteins [59, 60, 62] and for nucleic acids [163] without any other prior information of the sample. In addition, if SAXS data can be combined with prior information from e.g. FRET [73], NMR [164], crosslinking, or known crystal structures [7, 30] even more refined molecular models can be obtained.

Current SAXS measurements often rely on state-of-the-art synchrotron sources, in particular due to their high photon flux and tunability. Nonetheless, in-house anode-based sources remain an important and attractive alternative [84], in particular given the limited availability of measurement time at synchrotron user facilities and the considerable logistic challenges to carry out measurements at an – often far away – off-site location. In principle, it is possible to compensate the reduced flux at lab-sources at least partially by extended counting times, e.g. by increasing exposure times from ~ 1 s typical for biological samples at high-flux synchrotrons to $10^3 - 10^4$ s. However, this approach only works if the signal-to-noise ratio is high, i.e. if the background noise does not increase too much for long integration times. Therefore, the question which energy range is best suited for SAXS measurements of macromolecules in solution is tightly connected to the question which energy range provides the best signal-to-noise ratio for these conditions.

Currently, most in-house based sources employ copper (Cu) anodes with K_α radiation at 8.0 keV, corresponding to a wavelength of 1.54 Å. Their application for solution SAXS measurements on weakly scattering biological samples has been already proven [84] and also *ab initio* reconstructions with the programs *DAMMIF* [61] and *GASBOR* [62] could be performed successfully [165, 166]. An alternative to using Cu anodes are molybdenum (Mo; K_α = 17.4 keV) anode sources, which provide shorter wavelength X-rays compared to Cu, with a characteristic wavelength of 0.71 Å. Mo-anode sources have been employed to investigate macromolecules, powders or thin film alloys by SAXS [167], wide-angle X-ray scattering (WAXS) [167–169], grazing-incidence X-ray scattering (GISAXS) [170], crystallography [171] and diffractometry [172, 173]. However, a detailed description and analysis of a Mo-anode-based in-house setup for SAXS measurements on biological macromolecules in solution is still lacking. Here, we present a comprehensive specification and characterization of a Mo-anode in-house source for SAXS measurements on proteins, nucleic acids, and detergent micelles. The shorter wavelength of Mo has a number of potential advantages: First, since the absorption coefficient for X-rays decreases sharply with increasing energy, higher energies cause less radiation damage in the

sample [19]. Second, scattering from air and window materials in the beam path is also reduced at higher X-ray energies. Third, the reduced absorption coefficient means that the optimal beam path (μ^{-1}) in the sample is longer for higher X-ray energies, e.g. for water $\mu^{-1} \sim 10$ mm for Mo and $\mu^{-1} \sim 1$ mm for Cu radiation, which can be advantageous for samples handling, i.e. for sample environments that benefit from a larger sample dimensions. Fourthly, since the magnitude of the scattering vector q is inversely proportional to the X-ray wavelength λ, a shorter wavelength is highly beneficial to perform WAXS measurements, where high q-values are desired. Thus, a shorter wavelength as given by Mo anodes, facilitates the combination of SAXS and WAXS measurements within a single setup, which can be advantageous for structural studies on biological samples such as proteins or peptides [174, 175].

We test our Mo-anode setup on a panel of typical, weakly scattering biological samples, including several proteins (bovine serum albumin, horse heart cytochrome *c*, and chicken egg white lysozyme), a nucleic acid sample (24 bp DNA duplex), and a micelle forming detergent (decyl-maltoside; DM). These samples have been investigated previously at third generation synchrotron sources and (except for the micelle sample) have known crystallographic structures, enabling a critical comparison and evaluation of our in-house data. The results suggest that our Mo-anode-based source achieves good signal-to-noise even on weakly scattering samples; the data are of sufficient quality to carry out standard SAXS analyses, such as Guinier fitting of the R_g, and to obtain *ab initio* 3D shape reconstructions for the protein and nucleic acid samples that exhibit good agreement with the known crystallographic structures. In addition, the data permit to fit a two-component ellipsoid model to the DM micelle data and to determine the size, shape, and interactions of the detergent micelles in solution.

3.2 The X-ray Setup

In brief, the in-house setup consists of a microfocus X-ray source with multilayer optics corresponding to the K_α line of the target, a collimation path with two scatterless slits, a motorized sample stage, two exchangeable vacuum tubes, and a hybrid pixel detector (Fig. 3.1). The individual components are described in detail in the following sections. The setup is optimized for SAXS measurements, but can also be used for WAXS and diffraction measurements, as shown previously[176] and discussed only briefly here.

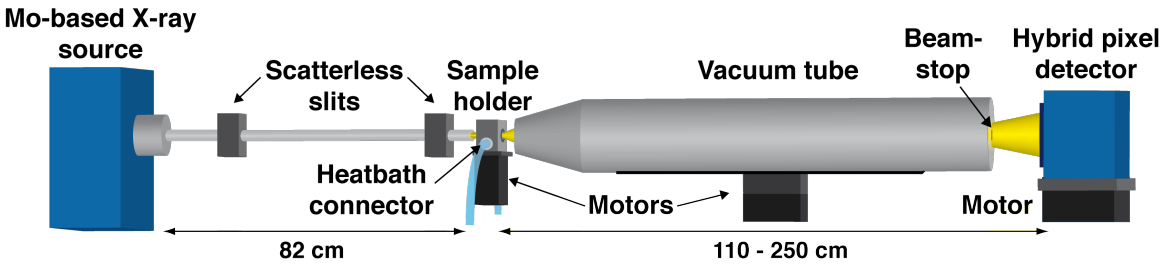

Figure 3.1: Schematic layout of the in-house setup for SAXS measurements. For further details see section 3.2 in the text.

3.2.1 X-ray source and collimation path

Our system consists of a Mo GeniX^{3D} microfocus X-ray tube (Xenocs SA, Sassenage, France) combined with FOX2D single reflection optics delivering a monochromatic and highly stable beam with an X-ray energy of 17.4 keV. The flux is typically around 2.5×10^6 photons per second at the sample stage. For collimation the beam enters an 82 cm long, fully evacuated collimation path closed by a 25 μm thick Kapton foil at the end. Collimation is achieved by integrating two partially motorized scatterless aperture slits (Xenocs SA, Sassenage, France) [90], one upstream right at the mirror and the second at the tube exit. The scatterless slits consist of a rectangular single Ge-crystal substrate bonded to a metal base with a large tapering angle away from the beam, which significantly reduces parasitic scattering and enhances resolution compared to conventional X-ray apertures [90]. Moreover, their insertion leads to a simplified optical design in comparison to previous implementations, which required three apertures [177]. With this optical configuration we achieve a highly collimated (horizontal divergence: 0.12 mrad, vertical divergence: 0.16 mrad FW20%M) beam with a size of approximately $1.2 \times 1.2\,\mathrm{mm}^2$ at the collimation path exit.

3.2.2 Sample cell and sample stage

The sample stage is positioned 5 cm in front of the collimation path exit. It consists of a fully motorized platform where six stepper motors allow moving the stage in horizontal and vertical directions with 5 μm and 0.1 μm precision, respectively, and enable rotation of the stage about all three axes with 0.005° precision. A rectangular aluminum sample holder with two slots for sample chambers (adapted from [178]) is connected to the platform for successive automated measurements of sample and buffer solution (Supplementary Fig. 3.7). The bottom part of the sample holder is connected to a circulating heat bath (F12-MA, Julabo, Germany) via rubber tubes enabling temperature control of the sample cells in the range of 4 - 70 °C (± 0.8 °C). For SAXS measurements conducted at room temperature, we used polyvinyl chloride (PVC) based sample chambers. The cylindrical observation volume of the chambers is filled with sample solution via two small inlets with a diameter of 0.6 mm from the top. This design prevents the formation of air bubbles and minimizes evaporation during measurements.

In order to achieve the optimum scattering signal, the chamber length corresponds to the absorption length of Mo in water, equal to the absorption coefficient, which is approximately 10 mm [179]. The diameter of the cylindrical observation volume is 3 mm so that parasitic scattering due to interactions of the incoming beam with the PVC is avoided and the opening angle is large enough so that scattering events happening at the beginning of the chamber can still be detected. The overall sample volume is roughly 80 μl. The windows of the sample chamber are made of 25 μm thick potassium aluminosilicate (muscovite mica) sheets (Goodfellows Cambridge Ltd., UK) that are glued on both openings of the cell with two-component epoxy (UHU Ltd., Germany). The use of mica as window material only introduces $\sim$ 6% attenuation (assuming an attenuation length of 800 μm for mica [179]) and it suppresses evaporation of sample solution during measurements. Furthermore, the windows do not cause a detectable background signal (Supplementary Note 1 in section 3.7.1 and Supplementary Fig. 3.8). For temperature-controlled experiments, we used sample chambers made from aluminum for improved thermal coupling. The sample holder can be removed to perform calibration measurements with glassy carbon, silver behenate (AgBe), and lanthanum hexaboride (LaB_6).

AgBe and LaB_6 are stored in aluminum chambers closed by 25 μm thick Kapton foils. The glassy carbon sample is fixed in an aluminum holder and mounted directly below the AgBe chamber. The calibration materials can be placed into the beam by a motor.

3.2.3 Evacuated flight path and beamstop

Our setup for SAXS measurements can be switched between two sample-detector distances of 110 cm and 250 cm, corresponding to q-ranges of 0.014 - 0.38 Å^{-1} and 0.009 - 0.15 Å^{-1}, respectively. A distance of 250 cm corresponds to more pixels covering the low q-range. For the two measurement modes, vacuum tubes with lengths of 95 cm and 180 cm, respectively, are placed between the sample stage and the detector in order to reduce air scattering (Fig. 3.1). A detailed analysis of various sources of background signals and in particular of the influence of air scattering on the SAXS data is given in Supplementary Note 1 in section 3.7.1 and Supplementary Fig. 3.8. Kapton foils with a thickness of 25 μm at the front and 50 μm at the end seal the ends of each vacuum tube. The vacuum tube has a diameter of 3 cm at the front and 10 cm at the back. We integrate beamstops at the end of the vacuum tubes by gluing circular lead tapes with diameter of 3 mm (for the 95 cm vacuum tube) and 4 mm (for the 180 cm vacuum tube) at the center of the Kapton foil inside the vacuum tube. The entire vacuum tube can be moved by two stepper motors in vertical and horizontal directions allowing for accurate alignment of the beamstop. This configuration is advantageous, as it does not introduce any additional shadow effects from a beamstop holder, and as it avoids air scattering compared to a beamstop positioned outside of the vacuum. Moreover, the lead tape is slightly transparent to the beam so that fluctuations in the beam position can be detected. In the WAXS geometry the sample-to-detector distance is set to 32 cm resulting in a q-range of 0.26 - 5.7 Å^{-1}. Due to the relatively short sample-to-detector distance we do not employ an evacuated flight path.

3.2.4 Detector

For X-ray detection we use a CMOS hybrid pixel detector (Pilatus 100K, Dectris Ltd, Switzerland) with a sensor thickness of 1000 μm yielding a quantum efficiency at Molybdenum K_α-energy of 76%, which is limited by the absorption of silicon (μ^{-1} (Mo) $\sim$ 700 μm for silicon). The detector area consists of 487 x 195 pixels with a pixel size of 172 μm in both directions, which leads to a total size of 83.8 $\times$ 33.5 mm^2 (width $\times$ height). The dynamic range is 20 bits, corresponding to 1048576 photons. Hybrid pixel detectors are single photon counters with the advantage of low background and the absence of dark noise [180]. For the SAXS configuration with the short vacuum tube, the detector is attached to a stepper motor that moves the detector in vertical direction. This stepper motor is fixed to a custom-made focusing rail, which can be moved manually in order to align the detector in the horizontal direction. For the configuration with the long sample-detector distance the detector is fixed in vertical position such that the beam is centered and can be adjusted manually in the horizontal dimension. For WAXS measurements the detector is placed on a motorized stage (BiSlide, Velmex Inc.). The motorized stage can be moved in horizontal and vertical direction with a travel range of 25.4 cm for automated scanning and stitching of the detector images.

3.2.5 Software

We control the instrument components and perform data acquisition using the UNIX-based software package 'spec' (Certified Scientific Software, Cambridge, USA) which is widely used for X-ray scattering and diffraction experiments at synchrotrons and laboratory systems. 'spec' can directly communicate with the Pilatus detector via macros (downloaded from the Dectris website: www.dectris.com). Furthermore, a custom-written Matlab routine displays the live image of the detector for fast and easy adjustment.

3.3 Materials and Methods

3.3.1 Calibration standards

We utilize silver behenate (AgBe; VWR International, Germany) to calibrate the beam center position and sample-to-detector distance for all small-angle measurements (Supplementary Fig. 3.9) [181]. In addition, we use a pre-calibrated 1 mm thick glassy carbon sample (kindly provided by Dr Jan Ilavsky, APS, Argonne National Laboratory, USA) for the calibration of the recorded intensity to absolute scattering cross section units [182] of cm^{-1} and sr^{-1}, which enables the comparison of scattering data from different instruments. For the calibration of the wide-angle configuration we use lanthanum hexaboride (LaB_6; SRM 660c, NIST) (Supplementary Fig. 3.9).

3.3.2 Sample preparation

A 24 bp DNA duplex sample was assembled from chemically synthesized oligonucleotides (Metabion, Germany) and prepared as described previously [183]. BSA, cytochrome *c* and lysozyme were purchased from Sigma-Aldrich and used without further purification. Detailed information about the employed buffers and sample concentrations are listed in Table 3.1. For concentration series a stock solution of the highest concentration was prepared by weighing out the lyophilized protein powder and diluted to the required concentrations. Both buffer and sample solutions were filtered through 0.22 μm syringe filters (Thermo scientific, USA). Prior to the measurements, sample solutions were centrifuged at 13500 rpm for 10 min in a tabletop centrifuge (Eppendorf, Germany). Sample and buffer solutions were degased in a desiccator at a pressure level of 30 mbar for 20 min to avoid the formation of air bubbles in the sample chamber during measurements. For each measurement 80 μl of sample or buffer solution were loaded into the sample chambers.

3.3.3 Measurement procedures

Prior to each experimental run, scattering curves of AgBe and glassy carbon were measured to determine the sample-detector distance with mm-accuracy and to calibrate the scattering curves on an absolute scattering scale. Sample chambers were placed in the sample holder and aligned such that the incoming X-ray beam penetrates the chamber at its center as follows: The sample stage is scanned vertically and horizontally in a range of 5 mm. At each position a 1 s exposure is recorded with the beamstop removed and the intensity is integrated. The intensity stays

approximately constant when the X-ray beam penetrates the observation volume and drops off rapidly when the beam is clipped by the sides of the sample chamber, allowing for an accurate determination of the center position. Biological SAXS measurements were performed at room temperature and exposure times were set to 1 - 3 h with 3 to 6 repeats each, resulting in a total exposure time of up to 24 h for each measurement. Matching SAXS profiles of each repeat were used for data averaging as described in the following section. For concentration series, we used the same chamber, which was rinsed with deionized water and buffer solution before filling it with fresh sample solution. Matching buffer profiles were collected using identical settings and procedures. For selected SAXS experiments, dynamic light scattering measurements on a NANO-flex 180° instrument (Particle Metrics GmbH, Germany) were performed to test for possible aggregation. No aggregation was observed for any of the tested samples.

Sample	**Number of residues / nucleotides**	**Molecular weight (kDa)**	**Concentrations (mg/ml)**	**Buffer**
BSA	583	69.0	5	50 mM HEPES, pH = 7.5, 50 mM KCl
Cytochrome *c*	104	12.4	2, 8, 24	100 mM acetate buffer, pH = 4.6, 0.5 M guanidinium hydrochloride
Lysozyme	129	14.3	5, 10, 20	40 mM acetate buffer, pH = 4.5, 150 mM NaCl
24 bp DNA duplex	48	~ 14.6	1.5, 4.4	50 mM sodium 3-(N-morpholino) propanesulfonic acid, pH = 7.0, 150 mM NaCl

Table 3.1: Overview of samples with corresponding concentrations and buffers used for SAXS measurements.

3.3.4 Data processing and evaluation

The two-dimensional detector images were processed with a macro including the command 'remove outliers' of the software ImageJ (National Institutes of Health, USA) in order to remove artefacts, which appear as small bright spots of only a few pixels in the detector image, due to background radiation as for instance cosmic rays. The 'remove outliers' algorithm replaces a pixel value by the median of adjacent pixel values if it deviates from the median by more than the threshold value. We used a radius of 7 for the pixel area to calculate the median and a threshold value of 50. By setting 'which outlier' to 'bright' only pixels that are brighter than the median of the surrounding are replaced. Next, we used the Igor Pro plugin NIKA [184] to reduce the 2D detector data into a one-dimensional scattering intensity. First, the sample-to-detector distance and the beam center were refined based on the AgBe scattering data. Then, circular averaging of both sample and buffer images was performed without any additional corrections. We further used custom-written MATLAB scripts (The MathWorks, Inc., MA, USA) to inspect the scattering data for aggregation or radiation damage, to perform data averaging,buffer subtraction, to define the usable q-range and for calibration of the data to exposure time, concentration, and absolute intensity. In addition, the MATLAB scripts performed a Guinier analysis to determine the radius of gyration R_g by iterative linear regression within the q-range of the data limited by $qR_g < 1.3$. Unless otherwise noted, the profiles shown represent averaged scattering data resulting from 3 repeats of 2 h exposures.

3.3.5 Theoretical scattering curves and *ab initio* low resolution reconstructions

For comparison of the experimental SAXS data, we calculated theoretical scattering profiles for our panel of scattering standards based on their atomic coordinates using the program *CRYSOL* [46] in default mode. The crystallographic structures of the protein samples were obtained from the protein data bank [76], with PDB accession codes 4F5S for BSA, 1HRC for cytochrome *c* and 6LYZ for lysozyme. For the 24 bp DNA a PDB file with the atomic coordinates was generated using the 3DNA package [185]. We used the program *DAMMIF* [61] to generate *ab initio* three-dimensional models from the scattering data. *DAMMIF* represents the particle as an assembly of identical beads inside a search volume. It employs a simulated annealing protocol to determine a compact interconnected model whose scattering pattern fits the experimental data. The particle distance distribution function *P(r)* generated from the ATSAS software [186] was used as input file. For each tested molecule, 20 independent runs in the 'slow' mode were performed using default parameters and assuming no symmetry. Next, we averaged the 20 models for each molecule using *DAMAVER* [67] comprising a sequence of programs: first, the low resolution models from *DAMMIF* were aligned based on their axes of inertia using a normalized spatial discrepancy (NSD) criterion [66]. The NSD value provides a quantitative measure of similarity between different models. A NSD value of zero corresponds to identical objects and values exceeding 1 refer to objects that systematically differ from one another. If pairwise NSD values are in the range between zero and one then the models are classified as structurally similar. The aligned bead models were averaged and filtered by removing loosely connected beads. For the next steps the reconstructed file with the lowest NSD value was chosen. We used the pdb2vol program from the *SITUS* [63] package (version 2.7.2) to convert aligned bead models to electron density maps. Finally, we aligned the models to the corresponding crystal structures [76], again by minimizing the NSD value between both structures. Molecular graphics were prepared using VMD [187].

3.4 Results and Discussion

To explore the capabilities of our setup, we conducted a number of test measurements using a panel of biological macromolecules as measurement standards that comprise horse heart cytochrome *c*, chicken egg white lysozyme, bovine serum albuminum (BSA) and a 24 bp DNA construct (Table 3.1). The selected macromolecules all have known high-resolution structures, have been thoroughly characterized and used as scattering standards previously [163, 188–190]. They span a range of molecular weights but in general have relatively small sizes and, consequently, scatter weakly. Therefore, they are ideally suited to characterize our setup within the described q-range and constitute rigorous test cases for typical biological samples for SAXS measurements.

3.4.1 Exposure time and concentration analysis

We initially carried out a set of test measurements to determine concentration requirements, optimal exposure times, and possible radiation damage effects. We performed concentration- and exposure time series on the scattering standard samples listed in Table 3.1 (except for BSA). Fig. 3.2a shows SAXS profiles for three different concentrations (5 mg/ml, 10 mg/ml and 20 mg/ml) of lysozyme, which has been previously characterized in synchrotron based SAXS experiments [162, 190]. The concentration scaled data are superimposable and exhibit no evidence of radiation damage or interparticle effects such as aggregation or interparticle interference. Kratky plots, where the scattering intensity weighted by q^2 is plotted against q, are shown for all concentrations (Fig. 3.2b). The Kratky representation is frequently used to represent scattering data of macromolecular ensembles [39], where a well-folded homogeneous particle will exhibit a parabolic curve and an unfolded particle will give rise to a hyperbolic curve.

For all three concentrations of lysozyme the scattering profiles display a pronounced peak indicating that the protein is well-behaved in its folded state. Although the signal-to-noise ratio decreases for lower concentrations, we still obtain reasonable quality data at the lowest concentration of 5 mg/ml. In addition, we examined different exposure times and number of repeats for the highest and lowest concentration used for our test molecules (Fig. 3.2c). We found that for lysozyme (c = 20 mg/ml) six exposures of 30 min each lead already to decent signal for q-values below 0.2 $Å^{-1}$.

However, we observed an improvement in data quality when using three repeats of 2 h, resulting in a signal-to-noise ratio suitable for structural analysis as described in section 3.4.3. Even longer exposure times were tested for the lowest concentration, but did not increase the data quality. This is probably due to a higher level of background noise attributed to background radiation, which is also integrated over time. Similar results were obtained for cytochrome *c* measured at concentrations of 2, 8, and 24 mg/ml (Supplementary Fig. 3.10).

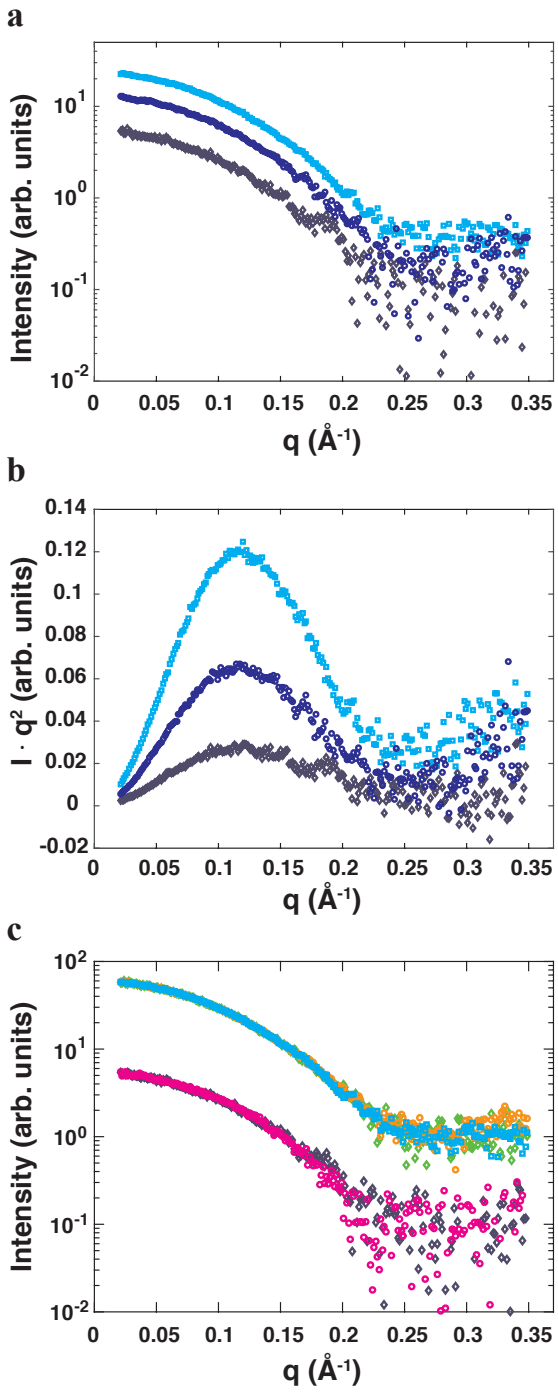

Figure 3.2: Effects of protein concentration and exposure time on scattering profiles. Scattering profiles shown are for lysozyme (see Table 3.1 for details). **a** Averaged scattering data at concentrations of 20 mg/ml (cyan, squares), 10 mg/ml (blue, circles) and 5 mg/ml (grey, diamonds) for three repeats of 2h. **b** Kratky plots ($q^2 \times I$ vs. q) for the data from panel **a**. **c** Averaged scattering data of lysozyme at a concentration of 20 mg/ml for six repeats of 0.5 h (green, diamonds), three repeats of 1 h (orange, circles) and two repeats of 2 h (cyan, squares) and a concentration of 5 mg/ml with exposure times of 2 h for three repeats (grey, diamonds) and 3 h for two repeats (magenta, circles). Data are scaled by exposure time.

3.4.2 Comparison of in-house data and synchrotron data

We compared the data obtained at our in-house source with data collected at the beamline BM29 at the ESRF in Grenoble (for proteins) and at the beamline 12-ID-B of the Advanced Photon Source (APS), Argonne, Illinois (for the 24bp DNA), both third generation synchrotron light sources with instruments designed for biological SAXS measurements in solution (Fig. 3.3). ESRF data were collected in the 'flow' mode at room temperature with an exposure time of one second. APS data were collected in a static sample cell at room temperature with an exposure time of one second. Matching data from ten runs were averaged. For q-values < 0.2 Å^{-1} the synchrotron scattering profiles are closely approximated by those acquired on the in-house setup. However, for larger q-values, the signal-to-noise ratio decreases faster for the in-house data, as one would expect.

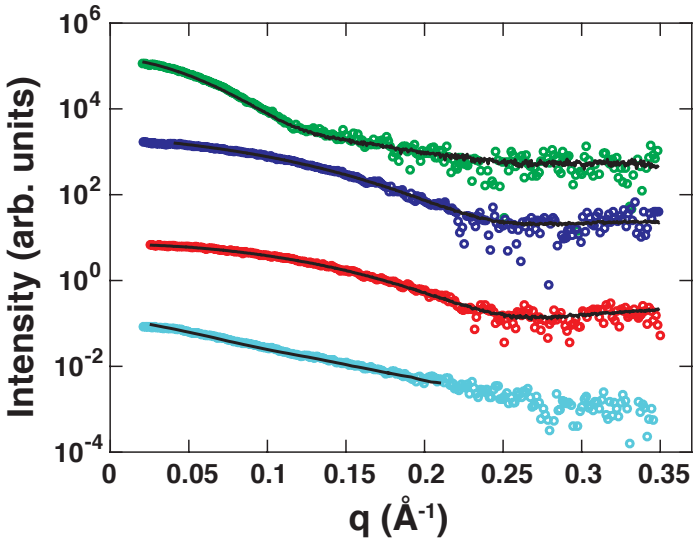

Figure 3.3: Comparison of in-house source and synchrotron-based SAXS data. Scattering profiles acquired at our in-house source (shown in color) and measured at synchrotron sources (shown as black lines) for BSA (green, top), lysozyme (blue), cytochrome *c* (red) and 24 bp DNA (cyan, bottom) with concentrations from Table 3.2. In-house data correspond to averaged data from three repeats with 2 h exposure time. Synchrotron data were averaged from 10 runs with 1 s exposure time. The synchrotron data for lysozyme had to be cut at a q-value of 0.04 Å^{-1} due to problems with the flow cell. DNA data were taken at another beamline with a maximum q-value of 0.21 Å^{-1}. Profiles are vertically offset for clarity.

3.4.3 Structural characterization and *ab initio* modeling of proteins and nucleic acids

The radius of gyration (R_g) and forward scattering intensity at zero angle (*I(0)*) are two parameters routinely extracted from SAXS data by Guinier analysis, where a straight line is fitted to the logarithm of the scattering intensity plotted as a function of q^2 for the lowest scattering angles. The R_g gives an overall measure for the size of the molecule; (*I(0)*) is used to calculate the molecular weight (MW) and to evaluate sample monodispersity [30, 31]. We performed Guinier analyses of the scattering profiles for every concentration and exposure time (see Fig. 3.4 for examples). For the molecular weight determination we employed BSA as reference sample. The Guinier plots for all of our test samples exhibit good linearity (Fig. 3.4) and the forward scattering intensities scale linearly with sample concentration, indicating the absence of interparticle interference effects or aggregation. We obtained radii of gyration from our experimental data that are consistent with literature values reported for the native state of each tested macromolecule (Table 3.2).

Molecular weight estimates from the forward scattering (Table 3.2) are in good agreement (within experimental error) with the molecular weights expected from the primary structure of the monomeric samples. The error of the molecular weight determination in (Table 3.2) is dominated by uncertainties in the macromolecular concentrations of approximately 10% relative error.

Sample	PDB used	Concentration (mg/ml)	R_g(Å)^a	R_g(Å)^b	R_g(Å)^c	R_g(Å)^d	MW (kDa)^a	MW (kDa)^b
BSA	4F5S	5	29.0 (±0.8)	29.9 (± 0.8)[190]	27.3	28.1	-	69.0
Cytochrome *c*	1HRC	8	13.4 (± 0.1)	13.8 (± 0.3)[189]	12.6	13.2	11.5 (± 1.1)	12.4
Lysozyme	6LYZ	10	14.6 (± 0.4)	14.3 (± 0.4)[190]	14.6	14.7	14.8 (± 1.3)	14.3
24 bp DNA duplex	-	1.5	23.3 (± 2.7)	24.2 (± 0.5)[163]	24.8	21.8	15.5 (± 2.5)	14.6

Table 3.2: Values for radii of gyration and molecular weights determined in this study (^{a}), taken from experimental data reported in the literature (^{b}), calculated from the theoretical scattering profiles (^{c}) and from the reconstruction fit files (^{d}).

For further comparison, we calculated theoretical scattering profiles from the crystal structures (Fig. 3.5a-d) for each tested molecule and determined the radius of gyration from the predicted scattering profiles based on the crystal structures (Table 3.2). The experimental data are in excellent agreement with the theoretical scattering profiles and the overall scattering features of each molecule are observable. The resulting chi-squared values (χ^2), which characterize the "goodness-of-fit", are all around 0.1. Moreover, the theoretically predicted R_g values are in the range of the experimental and literature values for all test samples.

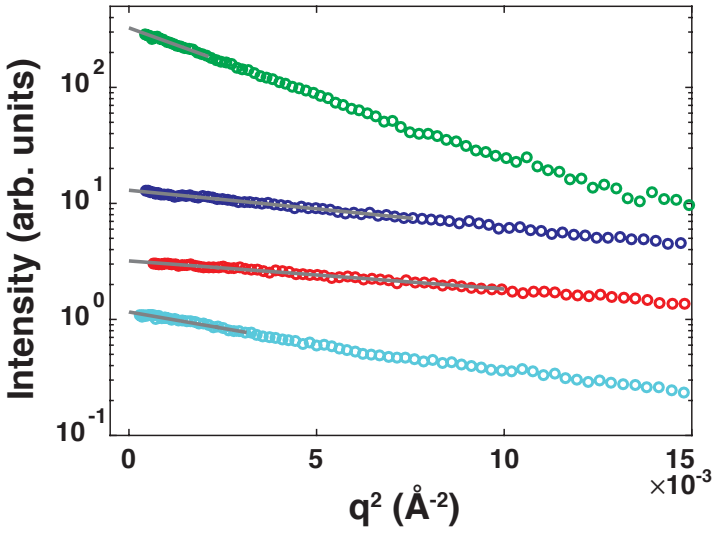

Figure 3.4: Guinier analysis of biological samples. Guinier representation of the experimental scattering data for BSA (green, top), lysozyme (blue), cytochrome c (red) and 24 bp DNA (cyan, bottom). The Guinier fits are indicated by grey lines covering a q-range of $qR_g < 1.3$. Profiles are vertically offset for clarity.

Over the last two decades the development of algorithms for *ab initio* reconstructions of low resolution three-dimensional electron density maps from one-dimensional scattering profiles has significantly enhanced the capabilities of SAXS measurements [59, 60, 62, 191]. In addition, *ab initio* reconstructions can be combined with atomistic structures derived by NMR or X-ray crystallography or other sources of structural information to enhance or validate models for both proteins and nucleic acids [77, 163, 192]. To determine whether the data collected at our Mo-based in-house source are of sufficient quality to obtain 3D structure reconstructions of typical biological macromolecules, we performed *ab initio* modeling for all macromolecules of our test panel using the software *DAMMIF* (see section 3.3). The reconstructions converged to solutions that fit the experimental scattering profiles very well (Fig. 3.5a-d). The scattering profiles from the models are in very good agreement with the experimental data over the whole q-range with χ^2 values below 0.1. However, they slightly deviate from the theoretical scattering profiles of the crystal structures for q-values above 0.25 Å^{-1}. For all reconstructions the pairwise NSD values for independent reconstruction runs never exceeded 1, indicating that the reconstruction algorithm is stable and converges onto similar structures in each run.

The final *ab initio* generated models were compared and aligned to corresponding crystal structures. Figs. 3.5e-h show the bead models of each molecule rendered as smooth transparent surfaces and the superimposed crystal structures as black ribbons (proteins) and stick (24 bp DNA duplex) representations. The overall shapes and sizes of the proteins were reproduced well. For BSA (Fig. 3.5e) the reconstructed density fits nicely to the triangular-like shape of the protein. The surface of the density map is rough with several small indentations reproducing the high amount of alpha-helices present in native BSA. For lysozyme and cytochrome *c* (Fig. 3.5f,g) we obtained reconstructions representing their globular shape, which are in good agreement with the protein sizes.

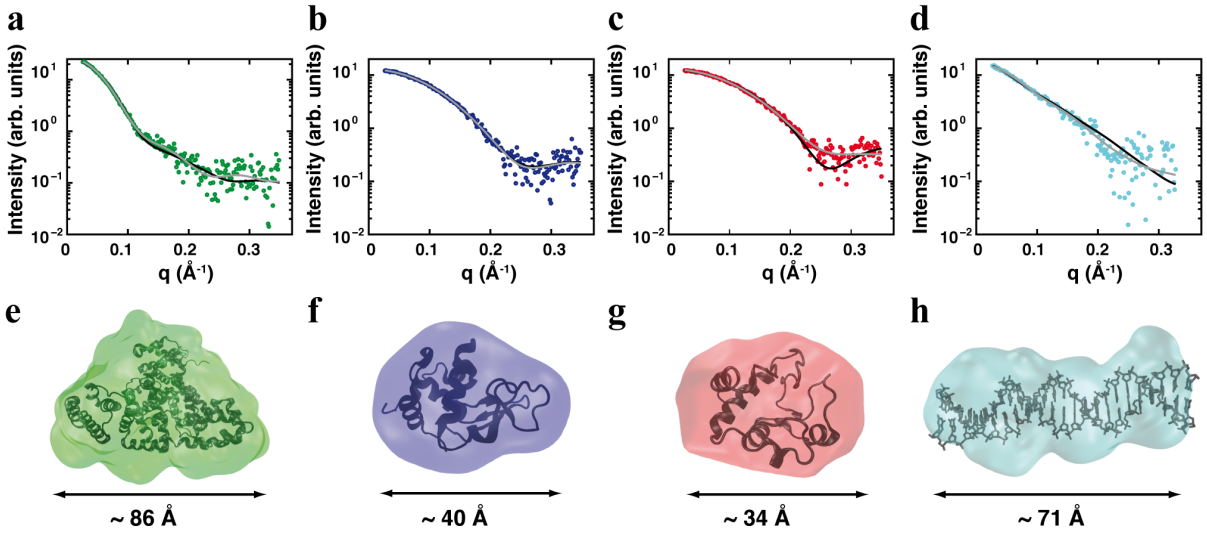

Figure 3.5: Comparison of crystal structures and *ab initio* 3D shape reconstructions for protein and DNA samples. **a-d** Comparison of experimental (colors; same color code as in Fig. 3.3 and 3.4) and theoretical scattering profiles that were predicted from the crystal structures (black lines) and fitted scattering profiles from *ab initio* 3D reconstructions (grey lines). **e-h** Models obtained from *ab initio* 3D structure reconstructions for BSA (green), lysozyme (blue), cytochrome *c* (red) and 24 bp DNA (cyan). The maximum dimension D_{max} of each molecule is indicated below each molecule and was derived by calculating the pair distance distribution function *P(r)* from the experimental scattering profiles.

The reconstructed density of the 24 bp DNA duplex (Fig.3.5h) corresponds reasonably to the overall cylindrical shape of a duplex. The length of the duplex gets reproduced well, whereas small deviations for the diameter of the reconstructions are observable. However, the periodicity of the major and minor grooves is visible in the reconstruction.

3.4.4 Determining the shape, size, and interactions of detergent micelles

Micelles are aggregates of amphiphilic molecules in aqueous solution where the hydrophilic head groups face outward and hydrophilic tail groups are segregated in the interior (Fig. 3.6a). Micelle forming detergents are employed in a large range of biochemical and industrial applications. In particular, detergents are commonly used as mimetics of the cell membrane for the solubilization and structural characterization of membrane proteins [193, 194]. However, the choice of a suitable detergent for membrane protein solubilization still remains a major hurdle [195–197]. SAXS has been used extensively to characterize the size and shapes of both membrane protein-detergent complexes – formed by a membrane protein surrounded by detergents – and of "empty" micelles [198–202].

To test to what extent our in-house source is capable of revealing the shape and size of detergent micelles, we recorded scattering profiles at different concentrations of n-decyl-β-D-maltoside (DM), a detergent featuring a maltose head group and a ten carbon single-chain alkyl tail (Fig. 3.6a), which is routinely used for membrane protein solubilization and has been characterized by SAXS in several previous studies [201, 203]. We obtain decent signal-to-noise down to a concentration of 12.5 mM DM (Fig. 3.6b). The scattering profiles are well described

by a two-component ellipsoid model (Fig. 3.6b,d), which features a core corresponding to the hydrophobic portion of the micelles formed by the tail groups and of a shell corresponding to the hydrated head groups (Fig. 3.6a; see Supplementary Note 2 in section 3.7.1 for details of the model). The size parameters obtained from the fits of the two-component ellipsoid model reveal oblate micelles with the short axis of the core of ~ 12.8 Å and the long axes of ~ 22.2 Å and a thickness of the hydrophilic shell of ~ 7 Å, in excellent agreement with previous work [201, 203]. In addition, we performed a Guinier analysis of the data (Fig. 3.6c) and determined apparent aggregation numbers (i.e. the number of detergent monomers per micelle) from the fitted forward scattering intensities by comparison with a scattering standard as described by Lipfert *et al.* [201] (see Supplementary Note 2 in section 3.7.1 for details).

For the measured concentrations we find radii of gyration in the range of 25.5 Å (± 0.4 Å) and aggregation numbers from the forward scattering intensity in the range of ~ 90 for the lowest concentration (Fig. 3.6d), in excellent agreement with the number calculated from the size of the hydrophic core volume of ~ 26 nm^3 determined from the two-component ellipsoid fit and with previous measurements, which indicate aggregation numbers in the range of 85-95 monomers per micelle [201, 203]. The apparent aggregation numbers show a small, but systematic decrease with increasing detergent concentration (Fig. 3.6d). This decrease in apparent aggregation number could be indicative of DM micelles shrinking with increasing detergent concentrations, which is however unlikely, or due to interparticle interference effects. The latter results in particular from repulsive interactions of the micelles in solution, e.g. due to excluded volume effects, that become more relevant at higher concentrations. Similar decreases in the apparent aggregation number with increasing detergent concentrations had been seen for a range of uncharged and in particular charged detergents previously [201].

Here, we present a new model that describes the apparent aggregation number as a function of detergent concentration in terms of intrinsic, true aggregation number and of the second virial coefficient, a parameter that characterizes the interparticle interactions in solution (see Supplementary Note 2 in section 3.7.1 and Supplementary Fig. 3.11). Our DM data are well described by the model (Fig. 3.6d, solid line), with a fitted intrinsic aggregation number of $N(c_0) = 92$ and a fitted second virial coefficient of $A_2 = 5.6 \times 10^{-5}$ mol × ml/g^2, which indicates weak repulsive interactions. In summary, the DM data suggest that our in-house setup is fully able to reveal the size, shape, and overall interactions of typical detergent micelles.

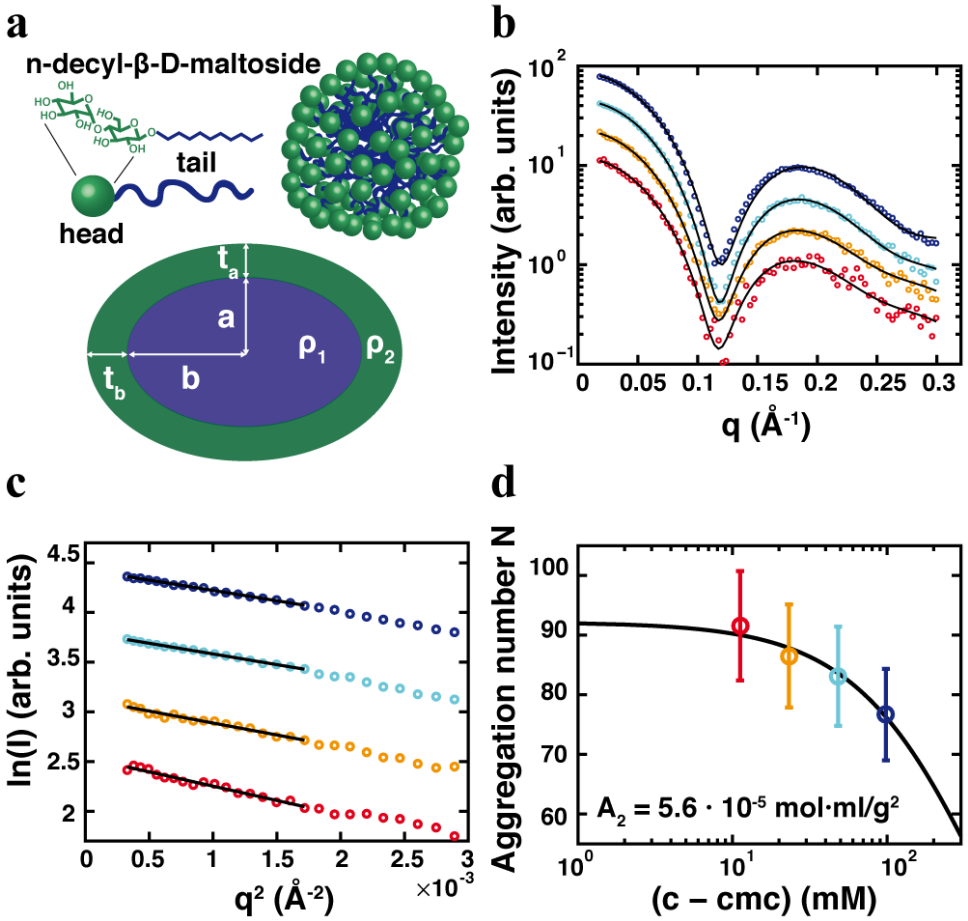

Figure 3.6: Characterization of the size, shape, and interactions of DM micelles. **a** Chemical structure of n-decyl-β-D-maltoside forming micelles and the schematic of the two-component ellipsoid model. a and b are the dimensions and ρ_1 the electron density of the hydrophobic core. t_a and t_b are the thicknesses and ρ_2 the electron density of the head group region. The figure shows the case of an oblate ellipsoid with $a < b$. **b** Experimental data for different DM concentrations of 100 mM (blue, top), 50 mM (cyan), 25 mM (orange) and 12.5 mM (red, bottom) and the corresponding fits (black lines). **c** Guinier analysis for DM data shown in **b**. **d** Apparent aggregation numbers N obtained from the extrapolated forward scattering intensity and Eqn. 3.2 in the Supplementary Note 2 in section 3.7.1 (circles, same color code as in **b**. The solid line is a fit to the model of Eqn. 3.6 and A_2 is the fitted second virial coefficient determined from the fit, indicative of weak repulsive interactions between the DM micelles in solution at higher concentrations.

3.5 Conclusion

We have presented a Mo-anode-based in-house SAXS setup for structural analysis of macromolecules covering a broad range of sizes, shapes, compositions (proteins/DNA/micelles) and scattering properties. Our system contains a Mo-based microfocus X-ray tube with an integrated multilayer mirror delivering a stable monochromatic beam. By using two scatterless slits for collimation, a highly collimated X-ray beam of low beam divergence is generated. The typical flux at the sample stage is around 2.5×10^6 photons per second. Due to the reduced air scattering for Mo-radiation, the sample chambers do not have to be placed in vacuum. Our sample holder contains two sample chambers with observation volumes of 80 μl allowing subsequent automated SAXS measurements of sample and buffer. In addition, the sample chambers can be temperature controlled within a temperature range of 4 – 70 °C (± 0.8 °C). By using the hybrid pixel detector PILATUS 100K, weakly scattering signals can be detected. Our system allows us to perform SAXS measurements on a broad range of weakly scattering biological macromolecules at concentrations comparable to synchrotron based SAXS measurements within 2 h. The achievable scattering vectors for SAXS measurements cover a range of 0.009 - 0.38 $Å^{-1}$, such that macromolecules with a size of up to ~ 30 nm can be structurally characterized. By performing in-house SAXS measurements on a test set of molecules including several proteins and DNA, we demonstrate that the data are of adequate quality to determine *ab initio* low resolution 3D structures of the macromolecules, which were in very good agreement with previously reported structures.

Our scattering data were also consistent with theoretical data calculated from the atomic structures of our test molecules. In addition, we demonstrate the instrument's ability to obtain high quality data for detergent micelles commonly used in membrane protein studies and we describe a novel simple model that enables us to determine the micelle aggregation number and second virial coefficient from SAXS data at different detergent concentrations. In general, the significantly lower flux (at least five orders of magnitude) of current Mo-based in-house sources compared to synchrotron sources necessitates much longer integration times (hours compared to seconds, respectively) and limits the practically achievable signal-to-noise ratio in particular at larger q-values. However, these disadvantages are partially offset by the much greater availability and reduced measurement logistics of an in-house instrument. In summary, our results suggest that Mo-anode-based in-house SAXS experiments are a viable alternative to other anode materials and allow studying many aspects of weakly scattering biological samples.

3.6 Acknowledgments

We thank Dr. Adam Round for support at beamline BM 29 at the ESRF in Grenoble, Dr. Jan Ilavsky (APS) for the calibrated glassy carbon specimen, Dr. Sönke Seifert for support with measurements at beamline 12ID at Argonne National Lab, Dr. Linda Columbus for discussions and for providing detergent samples, and Julian Nguyen for help with the fitting of the micelle data. Use of the Advanced Photon Source was supported by the U. S. Department of Energy, Office of Science, Office of Basic Energy Sciences. The authors acknowledge the Center for Nanoscience (CeNS), DFG-SFB 1032 (Nanoagents) and the Nanosystems Initiative Munich (NIM) for financial support.

3.7 Supplementary Material

3.7.1 Supplementary Notes

Supplementary note 1: Analysis of contributions to the background signal in Molybdenum-anode-based SAXS experiments

When performing SAXS experiments the reduction of the overall background, mainly caused by detector noise, natural background radiation and parasitic scattering, is of major concern. The latter originates from apertures, window materials and air in the beam path. For our in-house setup the main contribution of parasitic scattering can be related to windows and air scattering, as the collimation of the beam employs scatterless slits. The correct choice of window material and the evacuation of the flight path can reduce the amount of parasitic scattering. In order to estimate the overall background, we performed SAXS measurements using mica and Kapton as window materials commonly used for X-ray scattering experiments (both with window thicknesses of 25 μm), under conditions when the flight path between the sample and detector was either fully evacuated or in air. To mimic the regular measurement conditions of a SAXS experiment, we used deionized water as a sample solution. Moreover, we measured the natural background when the X-ray tube is turned off. For all measurements exposure times were set to 2 h with three repeats and circular integrated data were averaged. The intensity was transformed to counts per second. The natural background level recorded by the detector is $\sim 10^{-4}$ counts/s (Supplementary Fig. 3.8a), which is well (by at least a factor of three) below the intensity level obtained from SAXS measurements on the water sample, suggesting that despite the increased sensor thickness of our detector ($\sim$ three times higher than the sensor thickness of the Pilatus 100 K detector (i.e. 320 μm) commonly used for Cu-anode based SAXS measurements), the natural background radiation recorded by the detector do not limit our measurements. Comparing the results obtained for SAXS measurements on the water sample with the flight path (95 cm) either in air or fully evacuated (Supplementary Fig. 3.8a), we find significant deviations of the scattering curvature for the non-evacuated measurement, in the low q-region. The q-dependence of the air scattering is influenced by two effects. If the flight path is not evacuated, air molecules along the entire flight path will contribute to the scattering signal. However, scattering by molecules close to the beamstop will only contribute to the signal at high q, since their low q contribution is blocked by the beamstop (Supplementary Fig. 3.8b). This shadowing effect of the beamstop leads to the decrease of the scattering intensity in the low q-region for the air measurements (Supplementary Fig. 3.8). The mean background levels for the higher q-range are in the range of $\sim 3.3 \times 10^{-4}$ and $\sim 4.5 \times 10^{-4}$ counts/s for the air measurements and the evacuated experiments, respectively. The difference between both datasets is $\sim 2.9 \times 10^{-3}$ counts/s, implying that per cm of non-evacuated distance the background due to parasitic scattering is increased by $\sim 3 \times 10^{-5}$ counts/s. This relatively low level of air scattering suggests that a few cm of non-evacuated flight path result in a background level in the order of the natural background. Therefore, it is for instance not necessary to evacuate the sample environment, as it is done for some Cu-anode-based SAXS setups. Additionally, we find no significant change in parasitic scattering for the different window materials.

Supplementary note 2: Determination of detergent micelle size, shape, and interactions from SAXS measurement

Two-component ellipsoid model for detergent micelles

In the absence of significant interparticle interference effects (as is the case for our lowest detergent concentrations), the scattering intensity profile from monodisperse micelles can be well approximated by the scattering form factor of a two-component ellipsoid model (Fig.3.6a) that features a core with electron density ρ_1, symmetry axis of length a and orthogonal axes of length b and a shell of electron density ρ_2 and thicknesses along the a and b dimensions of t_a and t_b, respectively [201]. For micelles, the electron density of the core, which corresponds to the region occupied by the hydrophobic tail groups, is typically less than the electron density of the solvent ρ_s, i.e. $\rho_1 < \rho_s$. In contrast, the electron density of the outer shell, which corresponds to the hydrated head groups, is usually larger than that of the solvent, such that $\rho_2 > \rho_s$. For $a < b$ the micelle is oblate and for $a > b$ it is prolate. The form factor of the two component ellipsoid model is given by:

$$P(q) = \int_0^1 \left(3V_1(\rho_1 - \rho_2)\frac{j_1(u_1)}{u_1} + 3(V_1 + V_2)(\rho_2 - \rho_s)\frac{j_1(u_2)}{u_2} \right)^2 dx \tag{3.1}$$

with $u_1 = q\left(a^2x^2 + b^2(1-x^2)\right)^{\frac{1}{2}}$, $u_2 = q\left((a+t_a)^2x^2 + (b+t_b)^2(1-x^2)\right)^{\frac{1}{2}}$, the core volume $V_1 = \frac{4\pi ab^2}{3}$, the total volume $V_1 + V_2 = \frac{4\pi(a+t_a)(b+t_b)^2}{3}$, and j_1 being the first order spherical Bessel function. We fitted Eqn. 3.1 to the experimental scattering data (Fig. 3.6b) using custom written Matlab routines as described in Lipfert *et al.* [201]. In the fits, we held the solvent density and the density of the hydrophobic core fixed at $\rho_s = 0.34\ e^-/\ \text{Å}^3$, the approximate electron density of water with 150 mM NaCl added at room temperature, and $\rho_1 = 0.273\ e^-/\ \text{Å}^3$, the electron density of the hydrophobic core computed from the Tanford volume of the hydrocarbon chain [201]. In addition, we assumed equal thicknesses of the outer shell in all dimensions, i.e. kept $t_a = t_b$ in the fits. Consequently, the free fitting parameters were a, b, t_a, ρ_2, as well as an overall scaling constant and a constant offset. The fits yielded values for the density of the outer shell of $\rho_2 \approx 0.45\ e^-/\ \text{Å}^3$, which is slightly less then the theoretical value from the chemical composition and the density of the head group alone (= $0.52\ e^-/\ \text{Å}^3$) [201], as would be expected, since ρ_2 represents the average electron density of the hydrated head group layer. The fitted values for a, b, t_a are given in section 3.4.4.

Determination of micelle aggregation numbers from the forward scattering intensity

The forward scattering intensity determined from Guinier analysis (Fig. 3.6c) can be related to a scattering standard and to the expected intensity from a monomer to determine the (apparent) aggregation numbers of micelles, i.e. the number of detergent monomers in a micelle [201, 203]:

$$N = \frac{I(0)_{det}}{I(0)_{mon}} = \frac{I(0)_{det}}{\kappa c\left(\rho_{det} - \rho_s\right)^2 V_{mon}^2} \tag{3.2}$$

$I(0)_{det}$ is the experimentally determined forward scattering intensity obtained from Guinier analysis of the data (Fig. 3.6 c), c the detergent monomer concentration corrected for the

critical micelle concentration $c = c_{mon} - cmc$ (cmc = 1.8 mM for DM [201]), V_{mon} and ρ_{det} are the molecular volume of a detergent monomer and its average electron density, both computed from the published specific densities as described [201]. κ is a proportionality constant determined from measurements of our protein molecular weight standards of known concentration, electron density, and molecular mass (Table 3.1). Applying Eqn. 3.2, we find the apparent aggregation numbers N for DM as a function of detergent concentration (Fig.3.6d, symbols).

Determination of true micelle aggregation numbers and second virial coefficients from the concentration dependence of the apparent aggregation numbers

In the N vs. concentration data, we observe a change in the apparent aggregation number with increasing detergent concentration (see Fig. 3.6d and similar observations for a range of detergents in Refs. [201, 203]). *A priori*, there are two possible reasons for a change of apparent aggregation number with detergent concentration: i) the actual aggregation number might change with increasing detergent concentration or ii) interparticle interference effects might influence the scattering profiles at higher concentrations, in particular at low q, which in turn would influence the extrapolated forward scattering intensity and thus the measured apparent aggregation number. In cases where the apparent aggregation number decreases with increasing concentration, as is the case for DM (Fig. 3.6d), the second explanation is much more likely, since it is unlikely that micelles would shrink with increasing detergent concentration and it is plausible that micelles repel in solution, via excluded volume and (for charged detergent head group) electrostatic interactions.

Here, we present an analysis framework to fit apparent aggregation number vs. detergent concentration data to determine the aggregation number in the absence of interparticle interference effects and the second virial coefficient due to micelle-micelle interactions. The second virial coefficient is the first term in an expansion describing deviations from non-interacting "ideal gas-like" particles. Positive values of the second virial coefficient correspond to repulsive interactions between the particles and negative values are characteristic of attractive interactions. Generally, the solution structure factor is the change of the concentration-normalized scattering intensity compared to the scattering intensity obtained at a concentration c_0 ("infinite dilution") at which interparticle interference is negligible (see e.g. Equation 31 of Ref. [30]):

$$S(q,c) = \frac{(c_0 \cdot I(q,c))}{(c \cdot I(q,c_0)} \tag{3.3}$$

The solution structure factor at $q = 0$ is related to the second virial coefficient A_2 (see e.g. Equation 35 of Ref. [30]):

$$\frac{1}{S(q=0,c)} = 1 + 2 \cdot M \cdot A_2 \cdot c \tag{3.4}$$

to first order in the concentration c, where M is the molecular mass of the of the solute. Combining Equations 3.3 and 3.4, the change in concentration normalized forward scattering intensity (again to first order in c) is given by:

$$I(0,c) = \frac{\frac{c}{c_0} \cdot I(q,c_0)}{(1 + 2 \cdot M \cdot A_2 \cdot c)} \tag{3.5}$$

For the apparent aggregation numbers determined from the forward scattering intensity (see Equation 4 of Ref. [201]) this implies:

$$N(c) = \frac{N(c_0)}{(1 + 2 \cdot M \cdot A_2 \cdot c)} \tag{3.6}$$

where *N(c)* is the apparent aggregation number determined at concentration *c* and $N(c_0)$ is the "true" aggregation number determined in the absence of interparticle effects. We again take the concentration c as the monomer concentration corrected for the critical micelle concentration *cmc*, i.e. $c = c_{mon} - cmc$. If we take the concentration in g/ml and the molecular weight in Daltons (g/mol), A_2 has units of mol×ml/g^2. For proteins in solution, A_2 tends to have a magnitude in the range of 10^{-3} to 10^{-5} mol × ml/g^2 and can have a positive or negative sign, depending on solution conditions. Values of A_2 of approximately -5 × 10^{-4} mol × ml/g^2 are characteristic of the so-called "crystallization slot", typical of solution conditions that promote crystal formation [204]. Eqn. 3.6 can be directly fit to experimental data of aggregation number vs. concentration, treating $N(c_0)$ and A_2 as free parameters. The model of Eqn. 3.6 provides an excellent description of our DM data (Fig. 3.6 d, solid line) with $N(c_0)$ = 92 and $A_2 = 5.6 \times 10^{-5}$ mol × ml/g^2.

In order to test the general applicability of the model derived above, we analyzed aggregation number vs. concentration data published previously by Lipfert *et al.* [201] for all detergents for which a decrease of apparent aggregation number with increasing concentration was observed (Supplementary Fig. 3.11)). The model of Eqn. 3.6 provides an excellent description of the observed behaviors. In most cases, the fitted values for $N(c_0)$ are in close agreement with the previously reported values that were simply based on the lowest measured concentrations. In some cases, the fitted numbers for $N(c_0)$ actually match better with the values determined from the two-component ellipsoid models than the previously determined numbers from the forward scattering, in particular for the detergents n-decylphosphocholine (FC-10) and n-dodecylphosphocholine (FC-12). The fitted values of the second virial coefficient are well within the range of values determined for proteins in solution under conditions that are not conducive for crystallization. It is noticeable that the second virial coefficient for n-decyl-β-D-maltoside (DM) and n-dodecyl-β-D-maltoside (DDM) with their non-ionic maltose head groups are significantly smaller than those determined for the ionic 1-palmitoyl-2-hydroxy-sn-glycero-3-[phosphor-rac-(1-glycerol)] (LPPG) or zwitterionic detergents (FC-10, FC-12, DHPC), suggesting that in the latter cases electrostatic repulsion plays an important role.

3.7.2 Supplementary figures

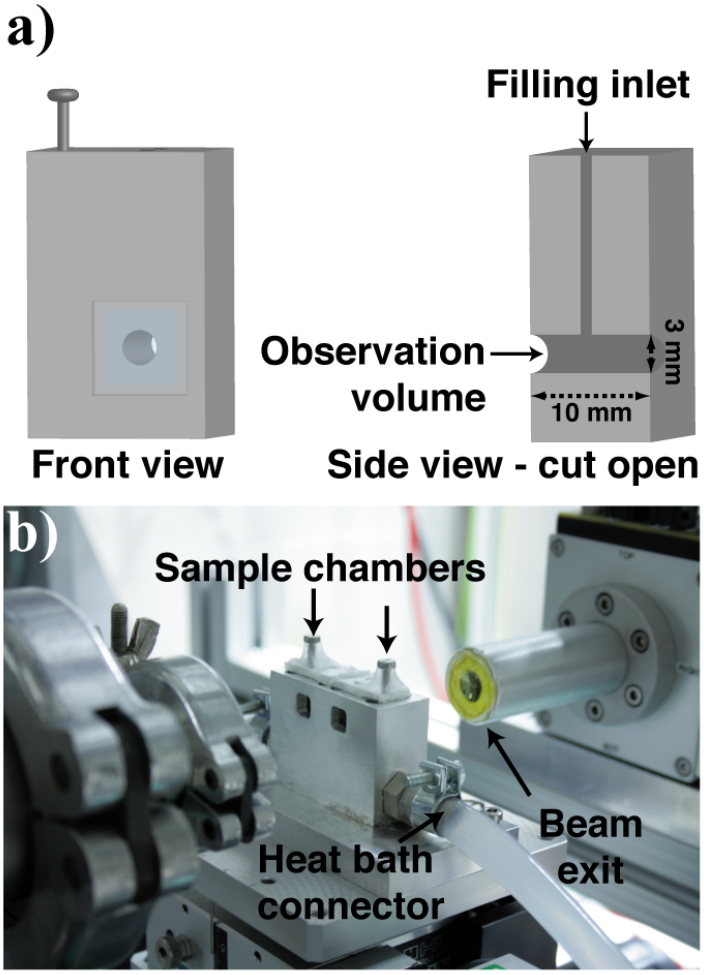

Figure 3.7: Sample chamber and sample stage of the in-house SAXS setup. **a** Schematic front and side view of the sample chamber with an observation volume of 71 mm^3. **b** Image of the sample stage with heat bath connectors containing two sample chambers.

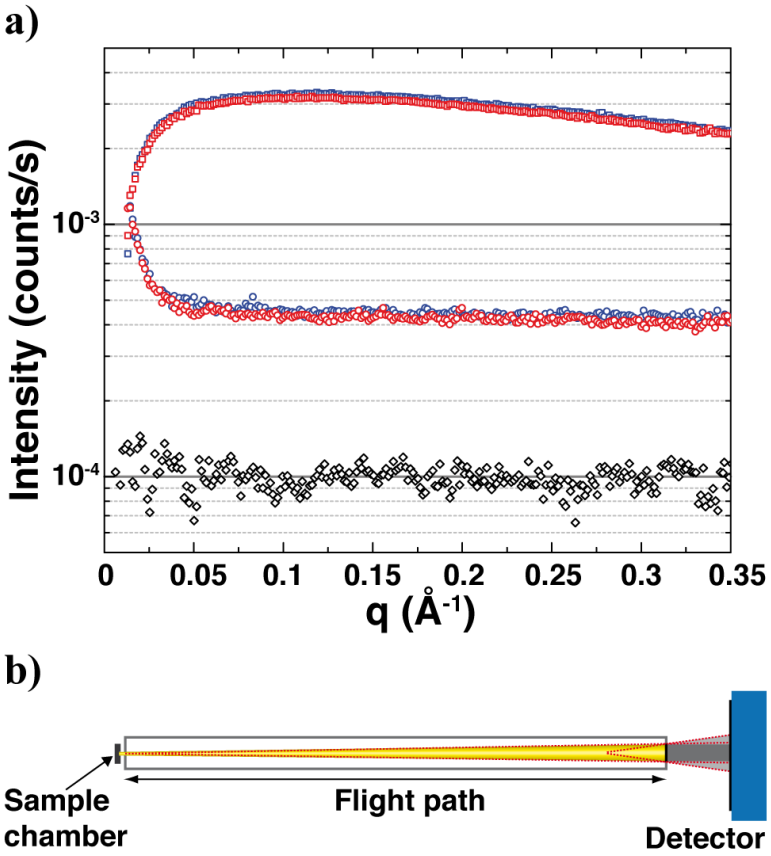

Figure 3.8: Background measurements to estimate parasitic scattering in SAXS experiments. **a** Black diamonds (bottom) indicate the natural background level, measured with the Pilatus 100 K detector when the X-ray tube is turned off. Scattering curves (middle) of a deionized water sample when the flight path is fully evacuated using mica (red dots) and Kapton (blue dots) as window materials. Scattering curves (top) for the same samples described previously when the flight path is in air (mica: red squares; Kapton: blue squares). Data correspond to averaged scattering profiles from three runs with an exposure time of 2 h each. **b** Schematic layout of the sample-to-detector setup for background measurements. When the flight path is fully evacuated only the primary beam (yellow) is blocked by the beamstop resulting in a beamstop shadow in the detector image (dark grey area). For a non-evacuated flight path, scattering from air molecules (illustrated by the red dashed lines) leads to an additional effect of partial shading in the detector image (light grey area) explaining the intensity decrease in (**a**, top) in the low q-region.

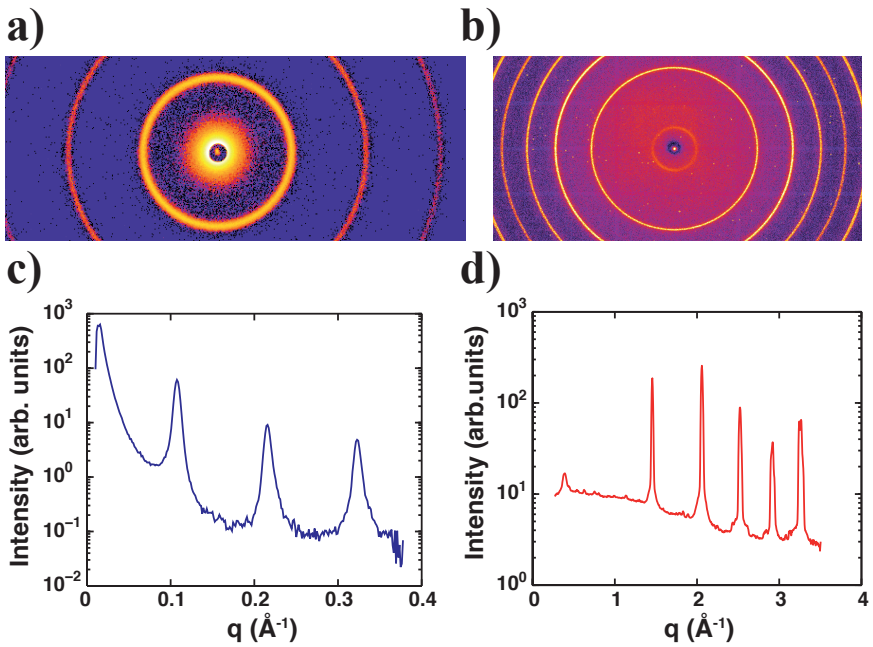

Figure 3.9: Calibration standards for SAXS and WAXS measurements. **a,b** Detector images for measurements of the calibration standards silver behenate (AgBe)(**a**) and lanthanum hexaboride (LaB_6) (**b**) for SAXS and WAXS, respectively. **c,d** Measured diffraction curves for the AgBe (**c**) and LaB_6 (**d**) measurements. The first small peak in the LaB_6 diffraction pattern results from the Kapton foil used as window material.

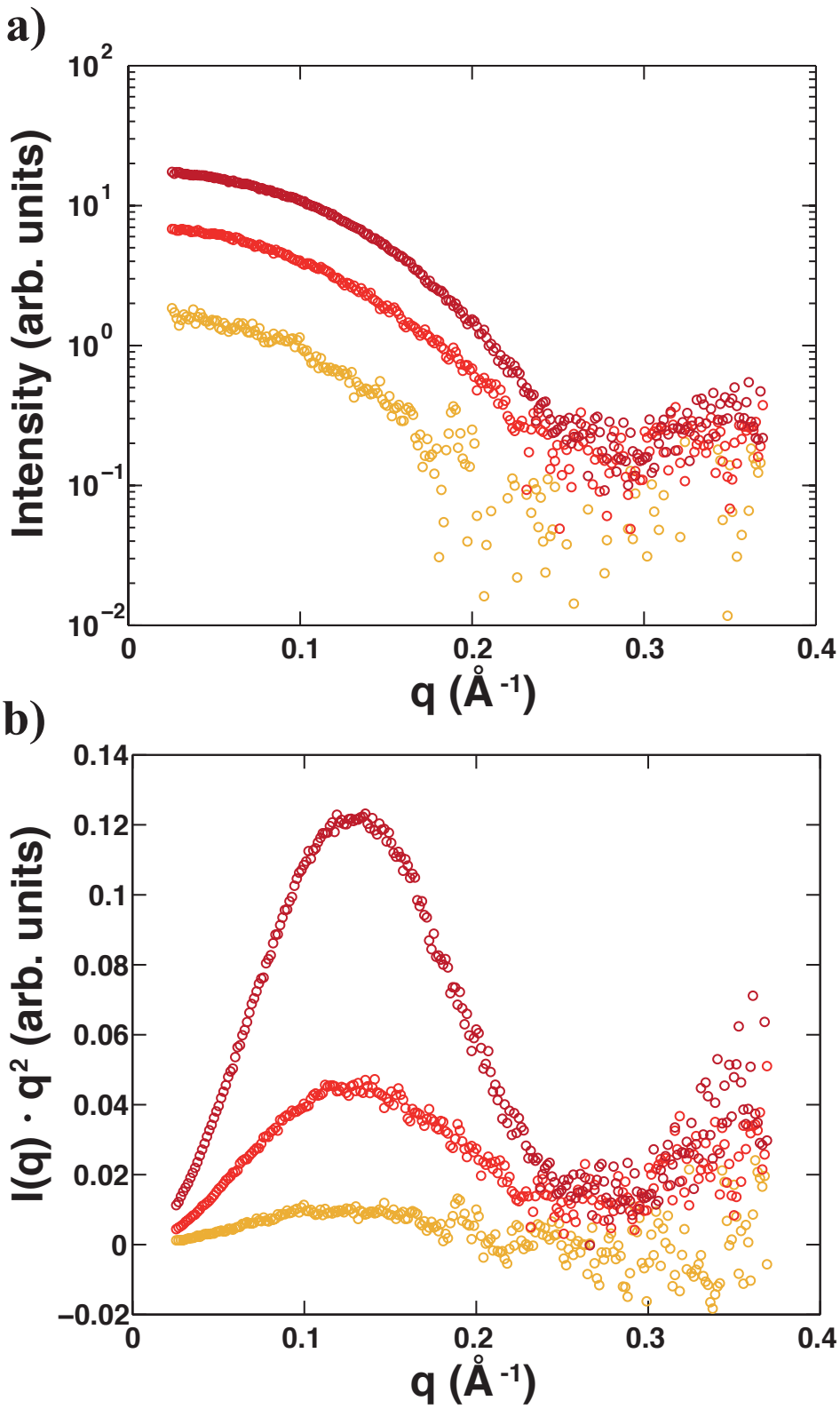

Figure 3.10: Scattering profiles for horse heart cytochrome *c* at different protein concentrations. **a** Scattering profiles for protein concentrations of 24 mg/ml (dark red, top), 8 mg/ml (red, middle) and 2 mg/ml (orange, bottom), averaged from three repeats of 2 h each. **b** Kratky representation of the data from **a**.

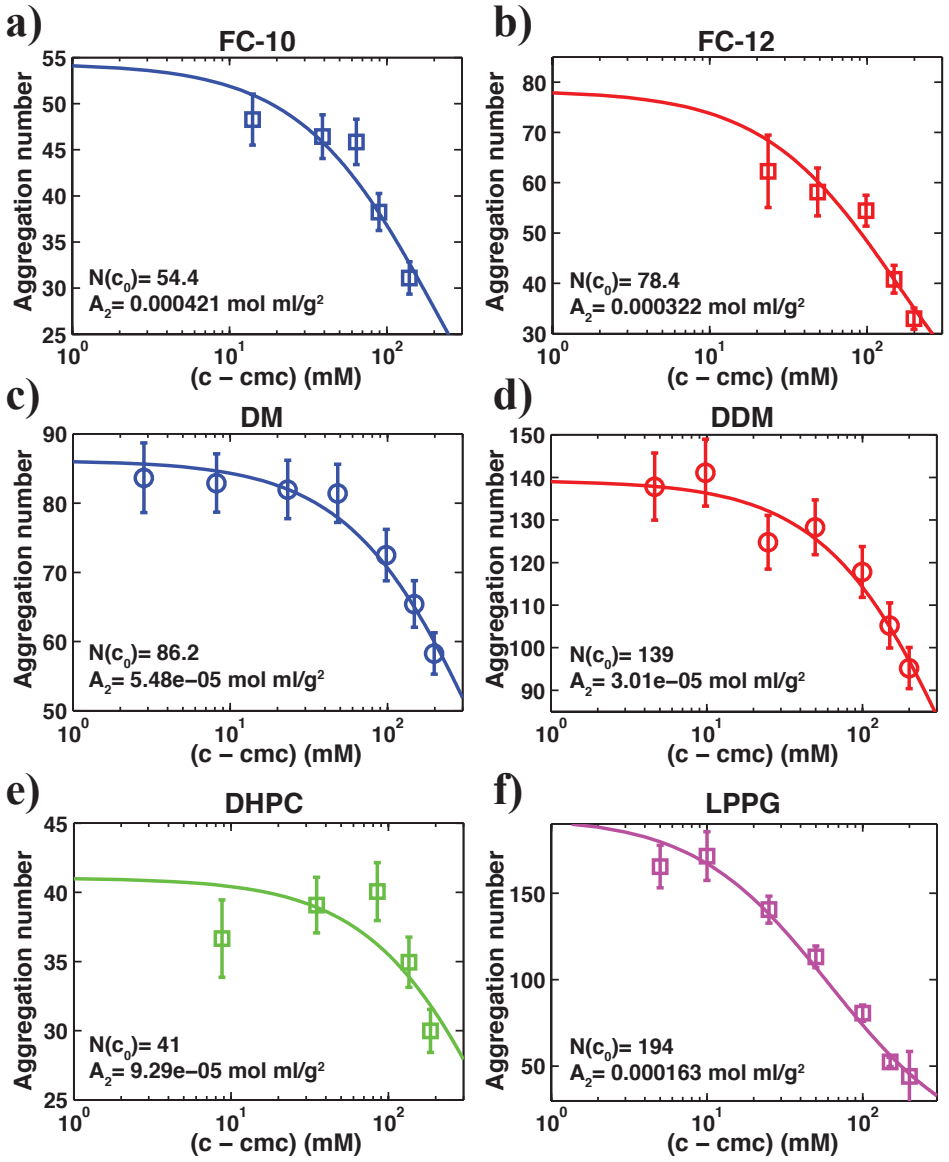

Figure 3.11: Determination of the true aggregation number $N(c_0)$ and the second virial coefficient A_2 from fits of the apparent aggregation number vs. concentration for different detergents. Symbols are aggregation numbers determined from the forward scattering intensity in SAXS measurements taken from Lipfert *et al.* [201] Solid lines are fits of the model in Eqn. 3.6 to the data. The fitted values for $N(c_0)$ and A_2 are shown as insets in each panel. Data are for FC-10 (panel **a**), FC-12 (panel **b**), DM (panel **c**), DDM (panel **d**), DHPC (panel **e**), and LPPG (panel **f**).

Chapter 4

Conformational Changes and Flexibility of DNA Devices Observed by Small-Angle X-ray Scattering

Summary

Self-assembled DNA origami nanostructures enable the creation of precisely defined shapes at the molecular scale. Dynamic DNA devices that are capable of switching between defined conformations could afford completely novel functionalities for diagnostic, therapeutic, or engineering applications. Developing such objects benefits strongly from experimental feedback about conformational changes and 3D structures, ideally in solution, free of potential biases from surface attachment or labeling. Here we demonstrate that small-angle X-ray scattering (SAXS) can quantitatively resolve the conformational changes of a DNA origami two-state switch device as a function of the ionic strength of the solution. In addition, we show how SAXS data allow for refinement of the predicted idealized 3D structure of the DNA object using a normal mode approach based on an elastic network model. The results reveal deviations from the idealized design geometries that are otherwise difficult to resolve. Our results establish SAXS as a powerful tool to investigate conformational changes and solution structures of DNA origami and we anticipate our methodology to be broadly applicable to increasingly complex DNA and RNA devices.

4.1 Introduction

A fundamental aim of nanotechnology is to design synthetic objects that can adopt specific conformational states and carry out functions at the molecular scale, e.g. in transport, signal

This Chapter was published by Bruetzel *et al.* [2] in *Nano Letters* and adapted with permission from the American Chemical Society.

Author contributions: L.K.B., T.G., H.D., and J.L. designed the study; T.G. assembled and purified samples; L.K.B., S.M.S., and P.W. performed SAXS measurements; W.Z. performed structure refinement. All authors analyzed data and contributed to writing the paper.

transduction, or molecular circuitry. Molecular self-assembly of DNA is a particularly successful approach towards creating versatile structures at the nanometer scale [102, 205–207].

When using the DNA origami technique, a several kilobase long circular single-stranded scaffold strand is folded into custom target shapes with the assistance of hundreds of short single-stranded staple strands. By exploiting the specificity of DNA base pairing, precisely controlled shapes reaching over 100 nm in size and molecular weights of several MDa can be created [102, 124, 125, 129, 208].

While an important initial focus in the design of self-assembled DNA structures was to create static objects of well-defined shapes [102, 129, 205, 206], more complex functions require dynamic 3D nanostructures that can undergo controlled conformational changes. Examples of dynamic DNA origami structures include a DNA box with a closable lid [139], a DNA nanorobot [110], a reconfigurable plasmonic nanostructure [209], or a DNA tweezers [210]. Such dynamic DNA structures are promising candidates for applications ranging from nano-engineering [137, 211] to medical diagnostics and therapeutics [212, 213]. An important challenge in this context is the precise control over the 3D shape and mechanical flexibility of the target design in solution to achieve desired functionality.

So far, structural characterization of DNA origami structures has predominantly relied on atomic force microscopy (AFM) imaging [211, 214, 215] and negative-stain transmission electron microscopy (TEM) [129, 131, 144, 216]. While these techniques are well suited to image static structures, they both rely on immobilizing samples on a surface and involve steps such as drying or staining the samples, which renders the solution conditions far from physiological. Cryo-electron microscopy provides less harsh conditions and has recently been successfully applied to DNA origami structures [139, 154] but still requires immobilized samples embedded in vitrified ice, potentially biasing the conformation of the sample and making it difficult to detect conformational changes upon variation in solution conditions.

In contrast, small-angle X-ray scattering (SAXS) can probe molecular conformations and transitions and provides low-resolution structural information on molecules and molecular assemblies in solution [10, 31]. As SAXS can operate under virtually arbitrary solution conditions [7, 217], the technique is ideally suited to detect conformational changes triggered by changes in solution environment, such as ionic strength, denaturant, temperature, or ligand binding. SAXS has proven very powerful to detect the large structural changes associated with the folding of proteins [39, 188, 218] and nucleic acids [38, 160, 219], but can also readily detect more subtle conformational changes, e.g. triggered by the binding of small-molecule ligands [37, 220–222].

Recently, Gerling *et al.* [112] established a framework based on shape-complementary recognition for the programmable and reversible assembly and disassembly of complex 3D shapes built from DNA. One important example involves a dynamic “switch” device, where multiple weak base stacking interactions were exploited to change conformations between a closed and an open state as a function of temperature or ionic strength of the solution. Here we use small-angle X-ray scattering (SAXS) to probe the structure and conformational changes of the switch device in solution. In particular, we detect and evaluate the conformational changes upon variations in solution conditions and observe quantitative agreement with solution Förster resonance energy transfer (FRET) measurements. In addition, we refine the 3D structure of the switch objects against the scattering data using a normal mode based flexible fitting procedure and find evidence for swelling and structural rearrangements away from idealized DNA helix

geometries. Together, our results establish SAXS as a powerful technique to probe the structures and conformations of DNA devices.

4.2 DNA origami switch samples based on base stacking interactions

We performed SAXS measurements on three different variants of a DNA origami switch object that is based on shape-complementarity and base stacking interactions [112]. A dynamic variant of the switch (switch D) can undergo conformational changes between an x-shaped open and a rectangular-shaped closed state (Figure 4.1; see Materials and Methods (4.9) and Supplementary Figures 4.6-4.8 for details).

This variant consists of two rigid bundles of DNA double helices arranged in a honeycomb lattice that form the two arms of the structure. The arms are connected in the middle of the structure by a single Holliday junction that acts as a pivot point for the rotational degree of freedom (Figure 4.1). The structure of the closed state is prescribed by shape-complementary patterns of double helical protrusions (red domains, Figure 4.1) and recessions (blue domains, Figure 4.1) that can precisely dock into each other when the two arms of the switch object come close together. The closed state is stabilized by up to 16 short-range stacking interactions of the terminal bases of shape-complementary surface topographies. The conformational equilibrium sensitively depends on ambient conditions such as the salt concentration or the temperature of the solution [112].

TEM images of the switch D variant show that at low salt concentrations the great majority of structures assume the open state, while at high salt concentrations switch D particles predominantly populate the closed state [112]. As reference structures, we employed two static variants of the switch object that are permanently locked in the open and closed states, respectively. In the static closed variant (switch C) stacking interactions are replaced by stronger hybridization interactions of 3-bases-long single-stranded overhangs of corresponding staple strands holding the two arms of the switch object in the closed conformational state (Figure 4.1, right). In the static open variant (switch O) all stacking interactions are deactivated and the two arms are connected by additional crossovers holding them at an opening angle of $\sim 90^\circ$ (Figure 4.1, left).

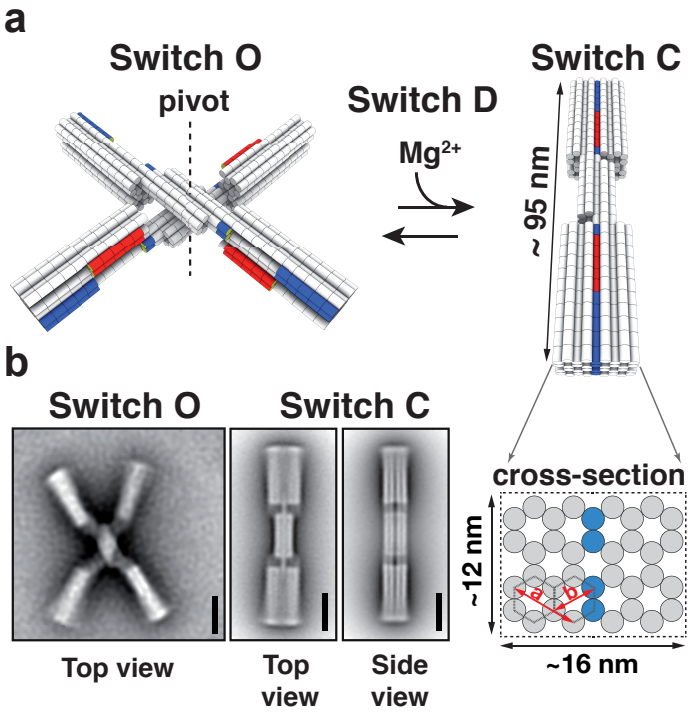

Figure 4.1: Illustrations of static and dynamic switch devices. **a** Schematics of the switch devices used in this study. The dynamic switch object (switch D) changes from an x-shaped open to a rectangular-shaped closed conformation upon addition of magnesium ions. Shape-complementary protrusions and recessions are indicated by the red and blue DNA double helical domains, respectively. Static switch variants are locked in the open (switch O, left) and closed (switch C, right) state. The schematic of the cross-sectional area of switch C indicates the horizontal and vertical dimensions including interhelical distances of a = 6 nm and b = 4 nm, which give rise to a peak in the scattering profiles of switch C and switch O. **b** Corresponding average negative-stain TEM micrographs of switch O in the presence of 5 mM $MgCl_2$ and of switch C at a $MgCl_2$ concentration of 25 mM. Scale bars, 20 nm.

4.3 DNA origami structures give rise to high signal-to-noise SAXS profiles at 25 - 100 nM concentrations

To estimate the minimum concentrations required for synchrotron-based SAXS measurements on our large (~16000 nucleotides (nt) or ~5 MDa) DNA origami structures, we used prior SAXS data of smaller nucleic acids in combination with extrapolation based on a scaling relationship (see Materials and Methods (4.9)). We analyzed the concentrations used for these SAXS measurements that resulted in a sufficient signal-to-noise ratio for structural analyses (which we loosely define as analyses that go beyond Guinier fitting of the lowest q-values) for a range of nucleic acid samples (Figure 4.2a, blue symbols). The dataset ranges from an 8 nt DNA [161] to a large (~400 nt) ribozyme [38] and includes both RNA [73, 221–223] and DNA samples [183, 224], as well as data for a ~14 knt DNA origami structure [139] recorded at an in-house X-ray source. The data are well described by a scaling relationship of the form $c \sim MW^{-\nu}$, where c is the required concentration, MW the molecular weight, and the scaling exponent ν was fitted to be ν = 1.30 (Figure 4.2a, dashed line, and Supplementary Information (4.10)). The scaling relation predicts that concentrations of ~10-50 nM are sufficient to obtain

a good scattering signal for a ~16 knt DNA structure. Experimentally, we indeed obtained good signal-to-noise scattering profiles for concentrations as low as 25 nM of the DNA origami structures (Figure 4.2b and Supplementary Figure 4.9), in excellent agreement with the predicted scaling relationship (Figure 4.2a, red star).

Additional measurements at 50 and 100 nM concentration display even higher signal-to-noise ratios (especially in the higher q-range) and are superimposable after scaling by concentration, indicating the absence of aggregation, radiation damage or interparticle interference (Figure 4.2b and Supplementary Figure 4.9). Interparticle interference effects occur if the particles in solutions are, on average, sufficiently close to interact, e.g. via excluded volume or electrostatic effects. We note that interparticle interference effects are expected to be (even) weaker for larger macromolecular assemblies as the typical intermolecular distances increase for higher molecular weights due to the lower required concentration (Figure 4.2a, inset). For instance, the average intermolecular distance of a 24 bp DNA sample (radius of gyration $R_g \sim$ 2.4 nm) measured at a concentration of 0.2 mM is around 20 nm, whereas for our DNA origami objects ($R_g \sim 28$ nm, see below) measured at 25 nM it is around 400 nm.

Remarkably, due to their large size, the DNA origami objects give rise to scattering profiles with a dynamic range of ≥ 4 orders of magnitude in intensity, with features identifiable up to $q \approx 3$ nm^{-1}. We note that while the scaling argument and extrapolation shown here only provide a rough estimate of the required sample concentrations, we anticipate that it can provide a useful guideline to other SAXS experiments on nucleic acid assemblies as well.

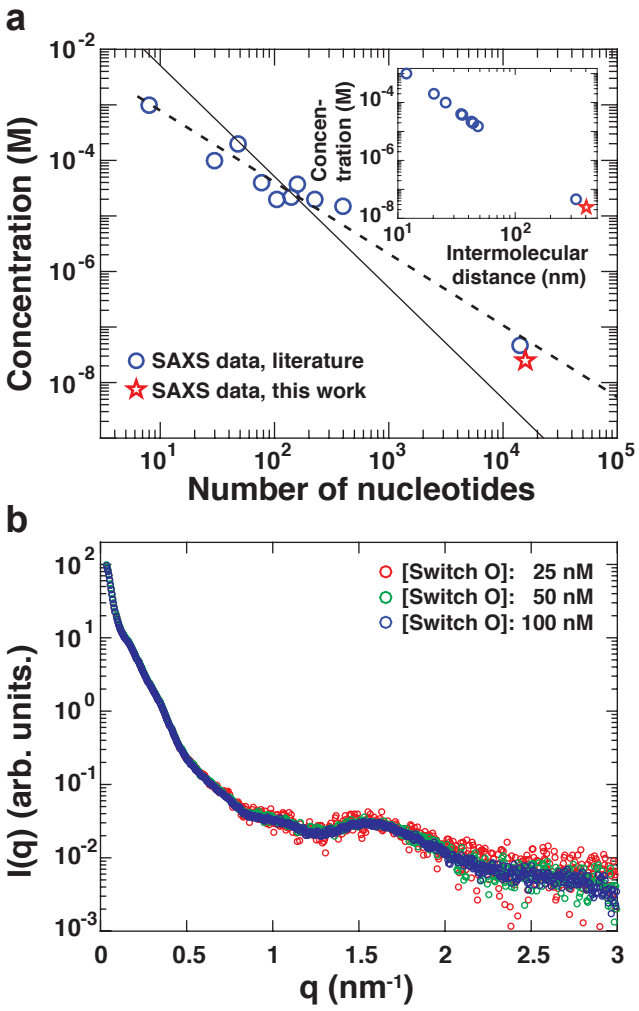

Figure 4.2: Concentration requirements and SAXS signals for large DNA origami structures. *a* Concentrations required to obtain a suitable SAXS signal, as a function of molecule size (in number of nucleotides), for a range of nucleic acid samples investigated previously (blue circles). The solid line is a fit of the relationship a/nt^2, where nt is the number of nucleotides and a is a fitting constant. The dashed line is a fit of the relationship b/nt^{ν} where b and ν are fitting constants. From the best fit we find $\nu \sim 1.30$. The red star corresponds to measurements of the DNA origami switch samples in this study that were guided by the scaling behavior. Inset: Intermolecular distances calculated for the required SAXS concentrations of the different nucleic acid samples. **b** Averaged scattering profiles of the switch O measured at three different concentrations: 25 nM (red circles), 50 nM (green circles), 100 nM (blue circles). Data are scaled by concentration.

4.4 SAXS reveals structural features of DNA origami objects

For a first structural characterization, we analyzed the scattering data from the static switch samples, which serve as reference samples for the dynamic switch variant. When comparing the scattering profiles of the switch O and switch C samples, we observe significant differences in the q-range below $q < 0.5$ nm^{-1} (Figure 4.3a), in line with global structural differences in the open and closed states. For higher q, corresponding to smaller length scales, the scattering curves largely coincide, exhibiting two distinct peaks.

We performed a Guinier analysis of the scattering profiles in the low q-range to determine the overall radii of gyration (R_g) (see Materials and Methods (4.9) and Supplementary Figure 4.10). We obtained an R_g of (27.9 ± 0.1) nm for the switch C (Table 1), which is in excellent agreement with a theoretical R_g of 28 nm, derived from approximating the closed switch as a rectangular beam, with $R_g^{theo} = \frac{1}{3}\left[(\frac{W}{2})^2 + (\frac{H}{2})^2 + (\frac{L}{2})^2\right]^{\frac{1}{2}}$, where W, H and L are the width, height and length of the object, respectively (Figure 4.1). For the switch O sample we found an average R_g of (29.0 ± 0.2) nm (Table 4.1), overall similar to switch C, which is expected as the approximate distances from the center of mass are conserved upon the transition from the closed to the open state.

Sample	R_g **(nm)**	R_c **(nm)**
Switch C	27.9 (± 0.1)	6.7 (± 0.1)
Switch O	29.0 (± 0.2)	4.8 (± 0.0)
Switch D30	28.1 (± 0.1)	6.0 (± 0.1)
Switch D05	27.5 (± 0.2)	4.8 (± 0.0)
CRYSOL (closed)	28.2[a]	6.4
CRYSOL (open)	29.5[a]	4.4

Table 4.1: Comparison of the radius of gyration (R_g) and the cross-sectional R_g (R_c) for the static and dynamic versions of the switch object derived from experimental and theoretical scattering profiles. Experimental data correspond to averaged results from concentration scaled scattering profiles for sample concentrations of 25, 50 and 100 nM. [a] Values were determined from Guinier fits of the predicted scattering profiles in the fitting range $q_{max}R_g < 1.3$.

For elongated rod-like particles, where the axial dimension is much larger than the radial dimension (as is the case for the DNA origami structures investigated in this work) the scattering intensity can be factorized in an axial and radial scattering component [36]. Analysis of the intermediate q-range then permits the calculation of the radius of gyration for the radial cross-section (R_c) (see Materials and Methods (4.9)). We obtained an average R_c value for the switch C of (6.7 ± 0.1) nm corresponding to a radius of the cross-section R ~ 9.4 nm, which is in good agreement with the cross-sectional dimensions of the design model (Figure 4.1). The switch O can be thought of as being assembled from two rods where the cross-section is half of the size as for the switch C sample. Here, a smaller average R_c value of 4.8 nm, corresponding to a radius R ~ 6.8 nm, is fully consistent with the expected reduction of the cross-sectional area when the switch changes from the closed to an open conformation.

A Kratky representation ($q^2 \times I(q)$ vs. q) of the scattering data of switch C and switch O reveals a number of peaks that can be related to structural features (Figure 4.3b). The peak and shoulder at lowest q-values ("1", Figure 4.3b) for the switch O and switch C samples, respectively, at $q \sim 0.06$ nm^{-1} are related to the overall dimensions of the objects (d ~ 100 nm) and to their R_g via $q \approx \sqrt{3}/R_g \approx 0.06$ nm^{-1}. The major peaks ("2", Figure 4.3b) at $q \approx 0.14\,\text{nm}^{-1}$ and at $q \approx 0.19$ nm^{-1} for the switch C and the switch O sample, respectively, are related to the maximum of the cross-sectional intensity expected at $q_{max} = 1/R_c$. The fitted R_c values of 6.7 nm for the switch C and 4.8 nm for the switch O sample (Table 4.1) suggest $q_{max} \sim 0.15\,\text{nm}^{-1}$ and $q_{max} \sim 0.2$ nm^{-1}, in very good agreement with the observed peak positions in the Kratky

plot. In the higher q-range, both scattering profiles display a small and broad peak ("3" , Figure 4.3b) at $q \sim 1.0$ nm^{-1} (d $\sim$ 6.3 nm, Figure 4.1 red arrow a) and a more pronounced peak ("4", Figure 4.3b) at $q \sim 1.6$ nm^{-1} (d $\sim$ 3.9 nm, Figure 4.1 red arrow b), which corresponds to the distances between and within the honeycomb lattice, respectively (Figure 4.1). These values are in approximate agreement with the theoretical values and the relative number of these distances is approximately the same for both conformations, consistent with the similarity of the scattering curves in the higher q-regime. We note that features relating to the structure of single DNA helices (such as their diameter, the minor groove/major groove periodicity, and the spacing between base pairs) occur on even shorter length scales and thus correspond to q-values ≥ 3 nm^{-1}, which have been probed in wide-angle X-ray scattering measurements [225], but are not the focus of the present work.

To more directly visualize the contribution of features on various length scales, we calculated the pair distance distribution function *P(r)* (see Materials and Methods (4.9) and Supplementary Figure 4.11), which describes a histogram of all pairwise distances r within the sample (Figure 4.3c). For both static open and closed structures, we find a maximum pairwise distance D_{max} of 95 nm, in good agreement with the expected maximum distance from the designed structures. The shape of the *P(r)* function obtained for the switch C variant is peaked at low r with a long tail out to higher r, characteristic of an elongated object.

In contrast, the *P(r)* of the switch O exhibits an overall more Gaussian shape, characteristic of a more globular object. In the switch C *P(r)* function, we observe a well-defined peak at an intraparticle distance of 16 nm, which corresponds to the maximum transverse distance of the closed state (Figure 4.1). This peak is not apparent in the *P(r)* function of the switch O sample, as expected, since the opening of the switch reduces the transverse distance to 8 nm. For the open conformation we find a smaller feature at 12 nm that is related to the height of the switch object and also contains contributions from the maximum transverse distance of $\sim$ 8 nm (Figure 4.1), which become more exposed in the open state. The dominant *P(r)* peak for the switch O, however, occurs around 40 nm, the distance associated with the length of each of the two opened arms.

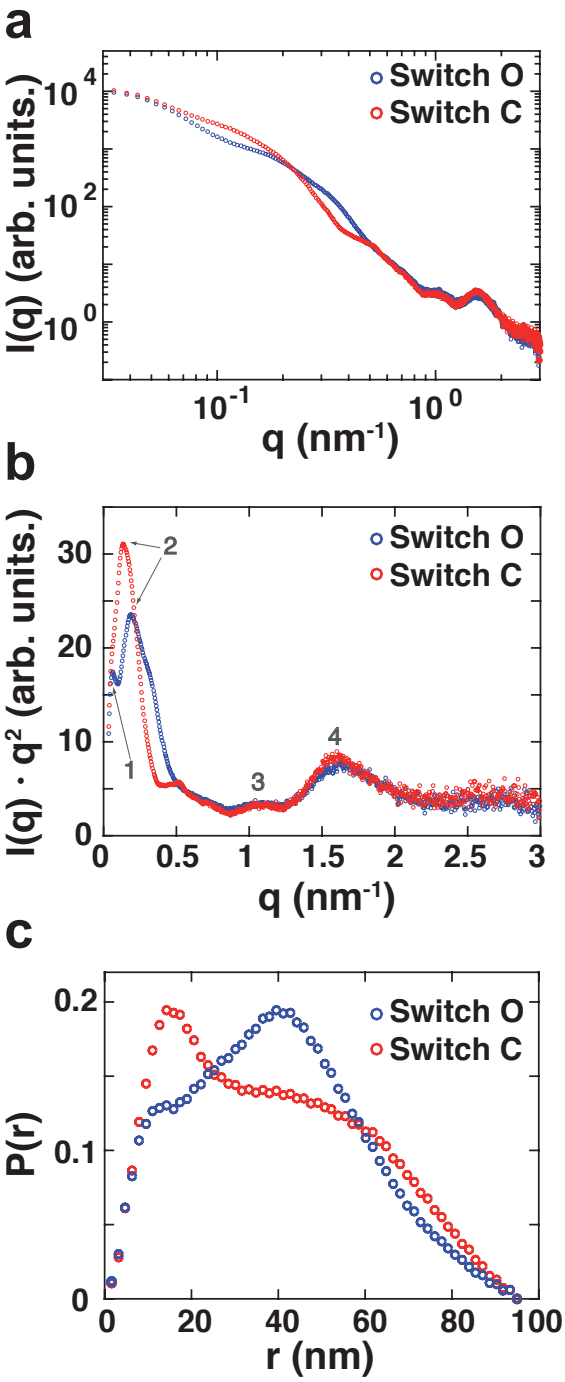

Figure 4.3: SAXS data reveal conformational features for open and closed switch objects. **a** Double-logarithmic representation of scattering intensity profiles obtained from the switch O and switch C sample. **b** Kratky representation of the data from **a** scaled by a constant factor. Numbers indicate peaks, which are described in the main text. **c** Pair distance distribution function *P(r)* calculated from data shown in **a** assuming a maximum particle dimension D_{max} of 95 nm. *P(r)* functions are normalized to equal areas.

4.5 Conformational populations of the dynamic switch variant

Having demonstrated that SAXS clearly reveals the large-scale conformational changes between the open and closed versions of the static switch object, we next analyzed the conformational states of the dynamic version of the switch (switch D) at high (30 mM) and low (5 mM) magnesium chloride ($MgCl_2$) concentrations (Figure 4.4a,b and Supplementary Figure 4.13). In general, the scattering profile from an ensemble is given by the sum of the scattering profiles for the individual components, weighted by their relative occupancy. In the case of a two-state system, the scattering profile can be described by a linear superposition of the two states:

$$I(q) = f_1 \cdot I_1 + f_2 \cdot I_2 \tag{4.1}$$

$I_1(q)$ and $I_2(q)$ are the scattering profiles and the coefficients f_1 and f_2 are fractional occupancies of states *1* and *2*, respectively.

Using the scattering profiles of the switch O and switch C objects for the open and closed states, we fitted the scattering profiles of the dynamic variant at 30 mM $MgCl_2$ (switch D30) and 5 mM $MgCl_2$ (switch D05) as a linear superposition of the two states (Supplementary Figure 4.13). Under both conditions, the two-state fits provide an overall excellent description of the experimental data, suggesting that the conformations of the dynamic switch variant can be well approximated by a two-state model featuring the open and closed states. For both samples slight deviations of the fit become apparent at higher q-values, which might imply that there exist structural differences within the internal honeycomb lattice between the dynamic and static versions. This might be attributed to the different concentrations of $MgCl_2$ in the sample solutions, which have an impact on structural integrity and flexibility owing to its efficacy in screening interhelical repulsion and stabilizing DNA Holliday junctions (see also below) [120, 226]. In addition, previous TEM studies on the switch D05 sample revealed a slightly reduced opening angle compared to the fixed opening angle of 90° for the switch O sample [112], which might cause some additional differences in the scattering profiles.

Complementary to analyzing *I(q)*, we applied a two-state model analogous to Equation 4.1 to the *P(r)* functions (Figure 4.4c). We find that the *P(r)* function of the switch D30 sample can be described very accurately by the two-state model. For the *P(r)* function of the switch D05 sample again slight deviations between the two-state model and the data are observable, but overall the two-state description is still accurate.

The fitted parameters f_1 and f_2 in Equation 4.1 provide a direct measure of the relative populations of the two states. Figure 4.4d shows the relative populations of the closed conformation determined from the scattering intensity and *P(r)* fits (the corresponding populations of the open conformation are the complement to 100%). From the *I(q)* fits, we find a population of $(77 \pm 1)\%$ in the closed state for the switch D30 sample, in agreement with the expectation that screening of electrostatic repulsion at high salt concentration should lead to a predominant population of the closed conformation. In contrast, the occupancies derived for the switch D05 sample are $(3 \pm 2)\%$ for the closed state, in line with the prediction that electrostatic repulsion at lower ionic strength favors the open configuration. The *P(r)* fits gave identical results, within experimental error (Figure 4.4d). These findings are further supported by the fact that the fitted cross-sectional radii of gyrations of the switch D object in 5 and 30 mM $MgCl_2$ are close to values determined for the switch O and switch C conformations, respectively (Table 4.1).

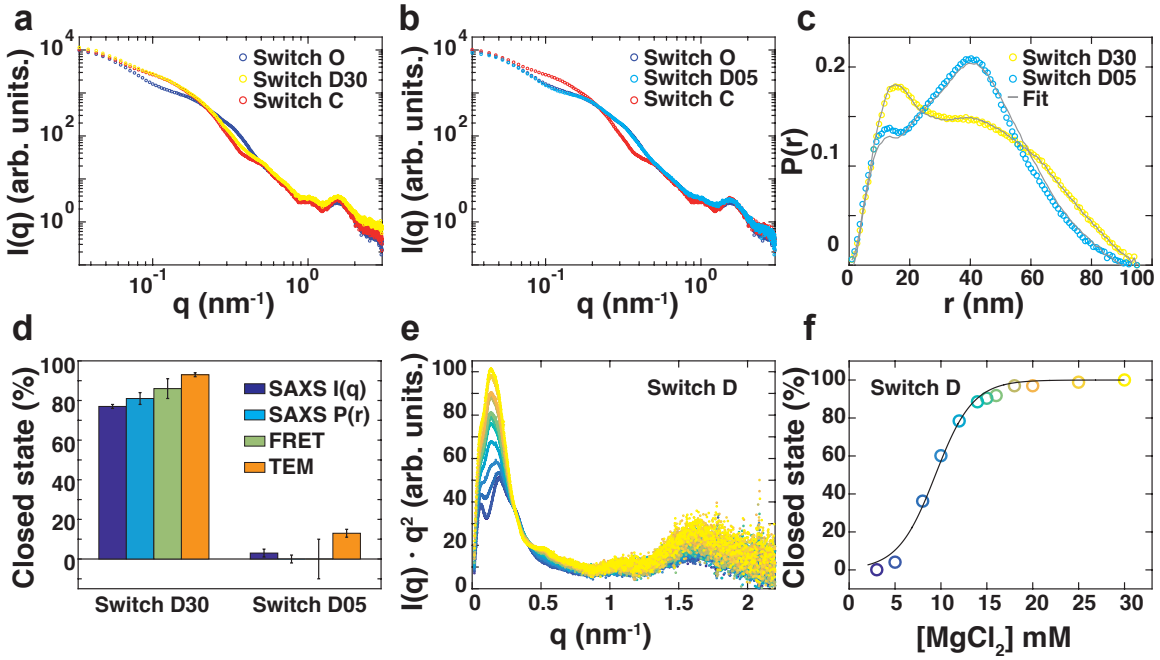

Figure 4.4: Characterization of conformational states of dynamic switch structures. **a** Comparison of the scattering profile from the switch D30 (yellow) to the scattering profiles of the static switch samples switch O (blue) and switch C (red). **b** Scattering profile from the switch D05 sample (cyan) in comparison to scattering curves from the static structures (same color code as in **a**). **c** *P(r)* functions of the dynamic switch variants (cyan, yellow circles) and the resulting two-state model fits (grey lines). **d** Comparison of the relative fractions of the closed states determined from the scattering profiles (blue bars), the *P(r)* functions (cyan bars), ensemble FRET (green bars), and TEM imaging (orange bars) for the switch D30 and switch D05 samples, corresponding to $MgCl_2$ concentrations of 30 mM and 5 mM, respectively. For TEM imaging the highest $MgCl_2$ concentration was 25 mM. **e** Kratky representation of the scattering profiles of switch D samples for varying $MgCl_2$ concentrations: 3 mM (dark blue,bottom), 5 mM, 8 mM, 10 mM, 12 mM, 14 mM, 15 mM, 16 mM, 18 mM, 20 mM, 25 mM and 30mM (light yellow, top). Data are normalized to the intensity at zero scattering angle and scaled by a constant factor. **f** Fraction of closed switch particles for $MgCl_2$ titration experiments shown in **e** , determined from a two-state model. Solid lines represent a two-state model with a free energy term that depends linearly on the $MgCl_2$ concentration.

The results of the SAXS analyses can be compared to data obtained from ensemble FRET measurements and TEM imaging on switch D particles at varying $MgCl_2$concentrations [112] (see Materials and Methods (4.9) and Supplementary Figure 4.6). Data from solution-based ensemble FRET measurements are in good agreement, within experimental errors, with the SAXS results (Figure 4.4d). From TEM imaging data, higher fractional occupancies for the closed state were obtained compared to the solution-based methods: (93 ± 1)% of the objects were identified to be in the closed state at a $MgCl_2$ concentration of 25 mM and (13 ± 2)% of closed particles were found at a $MgCl_2$ concentration of 5 mM. The deviations of the TEM-determined fractions to the solution-based values are modest, but statistically significant for the SAXS derived values (Figure 4.4d) and might be related to several factors: First, for the TEM analysis switch D particles were picked from TEM images for each salt condition and manually assigned to be either open or closed; errors were determined from binomial counting statistics. This process might introduce a slight bias, as overlapping objects could not be classified and as partially closed switch objects were considered as closed. Second, TEM imaging requires immobilization of samples on a surface potentially affecting their conformation. Furthermore,

the staining process for TEM imaging can alter the global shape of the particles [227]. In addition, single-molecule FRET experiments, which likewise require surface immobilization of the switch D particles, gave similar results as the TEM data [112]. Taken together, the data suggest that surface immobilization and/or staining might create a modest bias towards the closed conformation and can give rise to a small population of partially closed conformations, possibly due to direct surface interactions or excluded volume effects.

In order to test whether the transition from the open to the closed state of the dynamic switch variant upon the addition of $MgCl_2$ ions can be described as a two-state process, we performed SAXS experiments on switch D samples for varying $MgCl_2$ concentrations ranging from 3 mM to 30 mM (Figure 4.4e). The scattering profiles at different $MgCl_2$ concentrations exhibit an iso-scattering point around $q \sim 0.3$ nm^{-1} tentatively suggesting that the conformational transition can be described as a two-state process. For a more quantitative analysis, we performed a two-state fit of the scattering profiles at each $MgCl_2$ concentration according to Equation 4.1 and fitted the resulting populations by a thermodynamic model (using Equations 4.9 and 4.10 in Materials and Methods (4.9)) assuming a linear dependence of the free energy ΔG and the ion concentration c. From a least squares fit we obtained for $\Delta G_0 = 1.2$ kcal/mol at the reference ion concentration of 5 mM and the slope $m_c = -0.3$ kcal/(mol $\cdot$ mM) in good agreement with values based on ensemble FRET measurements (Figure 4.4f and Supplementary Figure 4.12). In addition, the two state-fits yield a good fit of the full scattering profiles over the entire range of $MgCl_2$ concentrations (Supplementary Figure 4.13). These findings show that the switch D transition from the open to the closed state can be described adequately, at least at the current level of signal-to-noise, by a two-state model employing a single open and closed conformation, without the need to introduce intermediates states or conformations.

Overall, we find quantitative agreement between SAXS and solution FRET derived population estimates and approximate agreement with the TEM derived values, confirming the switching mechanism in the dynamic switch variant. Our findings highlight the importance of solution-based techniques when performing structural characterization of complex DNA structures.

4.6 Comparison of experimental SAXS data to idealized models and model refinement

In addition to detecting conformational transitions and providing global measures of size and shape (such as R_g, R_c, and D_{max}) SAXS can provide information about the full 3D solution structure of macromolecules and their assemblies [8, 31]. Even though the resolution of SAXS experiments is typically insufficient to compute a unique structure, it is possible to test and refine structural models against experimental SAXS data [43–46]. First, we compared our experimental data to scattering profiles of the switch O and switch C samples predicted from idealized atomistic models generated by CanDo [228] (see Materials and Methods (4.9)). The computed profiles from the CanDo models reproduce the overall shape of the experimental curves and reveal similar characteristic peaks (Figure 4.5a,b; Supplementary Figure 4.14). In addition, we obtain R_g and R_c values from the theoretical scattering curves, which are in good agreement with the experimentally determined values (Table 4.1, Supplementary Table 4.1).

However, small, but systematic deviations between the experimental and theoretical profiles are apparent. There is an additional peak in the theoretical scattering pattern for the open state at $q \sim 0.26$ nm^{-1} and the peaks that are visible in both experimental and theoretical curves are shifted, mostly to higher q in the theoretical curves compared to experiment. Furthermore, the ratios of the peak intensity values at low and high q differ between the experimental and theoretical curves. In addition, we determined the *P(r)* functions from the theoretical data and calculated a histogram of distances directly from the atomistic model coordinates (Supplementary Figure 4.14). In comparison to the experimental data, the peaks are more pronounced and deviations from the experimental peak positions are observable.

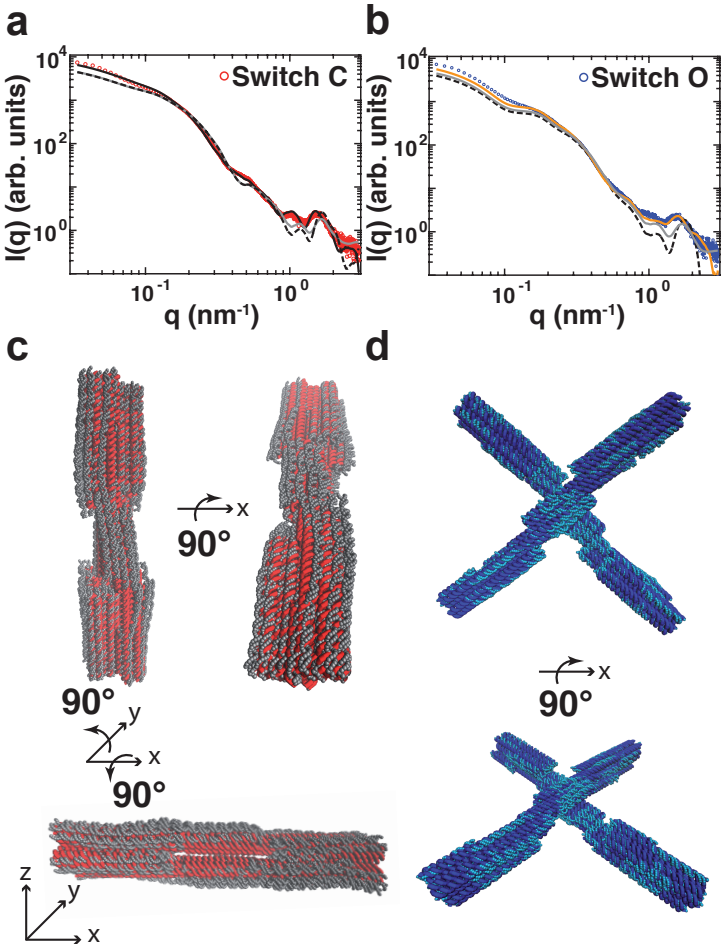

Figure 4.5: Normal mode based refinement of DNA origami structures against SAXS data. **a** shows data for the switch C construct and **b** the corresponding results for the switch O sample. Experimental scattering profiles are shown as red or blue circles. Scattering profiles predicted from the initial, CanDo derived models using all atoms and the software *CRYSOL* are shown as grey lines and using a one-bead-per-base representation as dashed black lines. Scattering profiles for the final models (computed using the one-bead-per-base representation) after normal mode based refinement are shown as black (for switch C) and orange (for switch O) lines. **c** and **d** show the initial models for the switch C and switch O objects as red and blue tubes and the final models after normal mode refinement as orange and cyan spheres, respectively.

We note that even though the different methods to compute scattering profiles from the structures exhibit some differences (see Materials and Methods (4.9) and Supplementary Figure 4.14), they do give overall very similar results and show comparable deviations from the

experimental data, suggesting that the details of the scattering computations are relatively unimportant and can not explain the observed differences to the experimental data. In principle, both the hydration layer of partially ordered water molecules around a macromolecule in solution [46, 50] and the ion atmosphere around charged nucleic acids [53, 229] contribute to the scattering profile. For simple DNA duplexes, the effect of the ion atmosphere has been studied in detail revealing that the ion cloud's contribution to the scattering pattern is relatively minor, typically increasing e.g. the radius of gyration by a few Ångstroms [229, 230]. We have performed electrostatic calculations using linearized Poisson-Boltzmann theory (Materials and Methods (4.9) and Supplementary Figures 4.15 and 4.16) to compare the electrostatic potential in the vicinity of a DNA origami structure with a simple DNA duplex. Our results suggest that the electrostatic potential and, consequently, the ion density around our DNA origami structures is only slightly elevated and overall similar in magnitude and spatial extent compared to a single double-stranded DNA helix (Supplementary Figures 4.15 and 4.16), consistent with previous reports in the literature [231, 232].

Taken together, these observations suggest that for the very large DNA structures considered in this work contributions from the ion atmosphere to the scattering profile are small or negligible. In addition, we tested whether altering the density of the solvent or the contrast of the hydration layer in the range of physically plausible values would explain the observed differences between the CanDo derived models and our experimental data, but again found that while changing the hydration shell gives rise to small changes in the scattering profiles, these changes are insufficient to account for the observed differences (Supplementary Figure 4.17).

Combined, the differences between experimental and predicted scattering profiles indicate that the switch objects adopt conformations in solutions that differ from the idealized models generated by CanDo. Such deviations have been suggested previously: Pan *et al.* [228] found an average root mean square deviation (RMSD) of 3.2 Å between the CanDo derived model and the crystal structure of a DNA tensegrity motif. In general, electrostatic repulsion between adjacent helix bundles or at crossovers resulting in the bowing out of double helical domains [102, 207] can lead to local displacements of nucleobase positions. Theoretical calculations and experimental evidence based on TEM data suggest an important role of flexibility for several DNA origami structures [232–234], indicating maximum root-mean-square fluctuation amplitudes of a few nanometers [233]. In addition, a cryo-EM structure of a DNA origami object observed deviations between the idealized structure and the experimentally determined density map [154].

There is currently no established method to refine DNA origami structures quantitatively against experimental data. A considerable challenge in this regard is the large size of our switch objects that renders refinement e.g. based on all-atom molecular dynamics [157, 232] challenging. As a computationally tractable approach, we turned to normal mode refinement of the CanDo derived model against the experimental SAXS data using an elastic network model. Normal mode analysis [70, 235–238] based on coarse-grained elastic network models has proven to describe large-scale conformational changes surprisingly well as compared to considerably more complex approaches [70] and has been applied to deform macromolecular structures to fit and refine experimental data from cryo-EM [239], X-ray crystallography [237, 240], and SAXS data [68, 69, 241]. We iteratively refined the switch C and switch O structures against the experimental SAXS data by normal mode based deformations (see Materials and Methods (4.9)).

The resulting structures yield significantly better fits to the data (Figure 4.5a,b): the goodness-of-fit statistic χ^2 (defined in Equation 4.5 in the Materials and Methods section (4.9)) is reduced from 0.5% to 0.06% and from 6.7% to 1.9% for the switch C and switch O structures, respectively. We find that for the refined structures the highly symmetric lattice structure is significantly deformed (Figure 4.5c,d). In comparison to the initial models, some parts in the refined closed and opened switch objects swell and bulge out. This effect is especially pronounced in double helices around the center of the structure, where the two arms are connected to each other (Supplementary Figure 4.18). In addition, the refined structures show the helices at the ends and sides of the arms slightly bend outwards (Supplementary Figure 4.18). Interestingly, these effects are more pronounced in the switch C compared to switch O structure. The RMSD for the refined switch C structure compared to the initial model is 22.3 Å; for the switch O, the refined structure has an RMSD of 8.4 Å relative to the starting model. The larger deformations in the switch C object compared to switch O might be due to the more compact structure and, therefore, higher charge density, that would make electrostatic repulsion more relevant for this object. Taken together, these data suggest an important role of flexibility and local deformations in DNA origami objects, which has to be considered when designing complex origami structures.

4.7 Conclusion

In summary, we have demonstrated the ability for SAXS to sensitively monitor conformational changes of self-assembled DNA origami objects in solution. SAXS provides a number of advantages:

First, being a solution-based technique, SAXS is free of potential biases and perturbations from the proximity of a surface. Second, SAXS is a label free method, without the need to chemically modify the structure of interest. Third, SAXS reads out the global conformation of molecules or molecular assemblies in solution, as defined by their electron density, thus avoiding concerns whether e.g. variations in fluorescence might stem from local conformational changes or photophysical effects upon changes in solution condition. Taken together, these advantages render SAXS a very promising novel approach for detecting conformational states of dynamic DNA origami objects and we anticipate that many of the techniques' capabilities that were previously demonstrated in other contexts can be extended towards monitoring conformational changes in DNA nanostructures, including temperature controlled [242] and/or time-resolved SAXS [38, 160, 243] measurements and the detection and characterization of structural intermediates and molecular ensembles [222, 223, 244].

Quantitative comparison of the experimental SAXS data to theoretical profiles derived from 3D models of the DNA objects reveal considerable flexibility and deformations away from the idealized "design" structure. Such deformations will have to be taken into account for high-resolution designs in the future. In addition, this work highlights the ability of SAXS to critically test structural models against solution-based data, even for very large DNA objects, which constitutes a promising approach that is complementary to the more routinely used methods.

4.8 Acknowledgments

We thank Dr. Keyao Pan and Dr. Marc Delarue for helpful discussions and support on atomistic modeling and normal mode analysis, Dr. Adam Round for assistance at beamline BM29 at the ESRF (Grenoble, France), Dr. Alessandro Spilotros and Nelly Hajizadeh for help at beamline P12 at DESY (Hamburg, Germany), Dr. Marianne Liebi at beamline X12SA, cSAXS at the Swiss Light Source (Switzerland), and Florian Praetorius for scaffold DNA preparations.

4.9 Materials and Methods

4.9.1 DNA origami assembly and purification

DNA origami objects were designed using caDNAno v.02. [128]. Three different variants of the switch object were prepared for the SAXS experiments (Supplementary Figures 4.6-4.8): two static variants that were permanently locked either in the open state (switch O) or the closed state (switch C), and a dynamic variant with 16 activated stacking interactions (switch D) (Figure 4.1). Each structure contained 16128 nucleotides. The scaffold DNA (p8064) was prepared as previously described [245]. Staple DNA strands were synthesized by solid-phase chemical synthesis (Eurofins Genomics GmbH, Ebersberg, Germany; HPSF purification). DNA origami objects were self-assembled by subjecting the one-pot reaction mixture to a thermal annealing ramp using a thermal cycling device (TETRAD; MJ Research – now Biorad) [121].

The reaction mixture contained 50 nM scaffold DNA (p8064), 200 nM of each staple DNA strand, folding buffer (1 mM EDTA, 5 mM TrisBase, 5 mM NaCl; pH 8) and 20 mM $MgCl_2$. After a 15 min-long thermal denaturation step at 65 °C, the thermal annealing ramp covered the temperature interval [58 – 55 °C] with a rate of 1 °C/90 min. Excess staple DNA strands were removed from the reaction mixture by performing two rounds of polyethylene glycol (PEG) precipitation [123]. The resulting pellets were dissolved in folding buffer (1 mM EDTA, 5 mM TrisBase, 5 mM NaCl; pH 8) containing 5 mM $MgCl_2$. To allow for equilibration, all samples were incubated at 40 °C and 400 rpm overnight. Residual PEG was removed from the samples by performing three rounds of ultrafiltration (30K Amicon Ultra-0.5mL; Merck Millipore). Filters were equilibrated by adding 500 μl folding buffer containing either 5, 15, or 30 mM $MgCl_2$ at 2000 x g and 25 °C for 2 minutes. Then, 50 μl sample was mixed with 450 μl folding buffer and centrifuged at 8000 x g and 25 °C for 15 minutes. The flow-throw was discarded and 480 μl of folding buffer was added to the recovered sample. The concentration of the different samples was determined using a spectrophotometer (NanoDrop 8000; Thermo Scientific).

All samples were measured at three different DNA origami object concentrations (25 nM, 50 nM, and 100 nM), prepared by dilution using the appropriate buffers. Samples of the switch O and switch C were measured in folding buffer (1 mM EDTA, 5 mM TrisBase, 5 mM NaCl; pH 8) containing 15 mM $MgCl_2$. Samples of the switch D variant were measured in folding buffer containing either 5 mM or 30 mM $MgCl_2$.

4.9.2 Scaling relationship for the concentration requirements for nucleic acid SAXS measurements

For monodisperse solutions and in the absence of interparticle interference effects, the forward scattering intensity *I(0)* scales linearly with sample concentration c and quadratically with the molecular weight MW [20, 30]:

$$I(0) = K \cdot c \cdot (\Delta\rho)^2 \cdot p^2 \cdot (MW)^2 \tag{4.2}$$

$\Delta\rho$ and p are the average electron contrast and the partial specific volume of the molecule and are approximately constant for all nucleic acid molecules [20]. K is an instrument specific constant, which is typically determined from comparison to a molecular weight standard.

Even though Equation 4.2 only strictly holds for the forward scattering intensity, it provides a rough estimate of the scattering signal expected in a SAXS measurement at a given sample concentration and molecular weight. For the set of samples analyzed in this work (Figure 4.2a), the concentrations required for good quality SAXS measurements follows roughly the anticipated $\sim MW^{-2}$ relationship (Figure 4.2a, solid line) from Equation 4.2. Treating the exponent as a free parameter, i.e. fitting the data to a relationship $\sim MW^{-\nu}$, yields a better fit with ν = 1.30 (Figure 4.2a, dashed line). A shallower dependence than $\sim MW^{-2}$ on the number of nucleotides can be rationalized by considering the fact that SAXS profiles for nucleic acids are maximal at low q and fall off for higher q. Importantly, the fall off with increasing q is more rapid for larger structures, suggesting that for these structures higher concentrations than suggested by the simple $\sim MW^{-2}$ scaling are required to obtain a decent signal at higher q-values. Our DNA origami measurements at 25 nM (Figure 4.2a, red star) are in excellent agreement with the extrapolated scaling relationship with ν = 1.30 (Figure 4.2a, dashed line); including the origami data point into the fit yields a nearly identical scaling exponent of ν = 1.36.

4.9.3 SAXS measurements

SAXS measurements were performed at beamline BM29, ESRF, Grenoble [95] at an X-ray wavelength λ of 0.99 Å, using a sample-to-detector distance of 2.87 m and a Pilatus 1M detector, resulting in a q-range of 0.03 to 5 nm^{-1} ($q = \frac{4\pi}{\lambda} sin(\theta)$, where θ is the total scattering angle). For each sample concentration ten runs with an exposure time of 1 s in 'flow' mode were conducted at room temperature. SAXS data of dynamic switch samples for Mg^{2+} titration experiments were collected at beamline P12 (DESY, Hamburg, Germany [246]) at an X-ray wavelength of 1.18 Å and a sample-to-detector distance of 6 m, resulting in a q-range of 0.03 to 2.2 nm^{-1}. Data were acquired in 'flow' mode with an exposure time of 95 ms and 150 frames per sample at room temperature. For each experiment buffer samples were measured using identical procedures before and after each sample measurement. Sample and buffer data from each run were analyzed for radiation damage; no damage was observed in any of the measurements. Matching sample and buffer profiles were averaged and buffer profiles were subtracted for background correction. Unless otherwise noted the scattering profiles shown in this work correspond to data from averaged and buffer subtracted intensity profiles measured at a DNA origami concentration of 100 nM.

4.9.4 SAXS data analysis

We performed Guinier analyses to obtain radii of gyrations for all measured DNA origami structures, by fitting the logarithm of the scattering intensity as a function of q^2 to a straight line for small values of q [29]. Due to the large size of the DNA origami objects, we extended the fitting range criterion to $q_{max}R_g < 1.6$ [192], enabling us to obtain reasonable estimates of the forward scattering intensity and radii of gyration that, nonetheless, should still be treated as approximations (Supplementary Figure 4.10a). In addition to determining the global R_g of the object from the scattering signal at very low q, DNA origami structures investigated in this work can be approximated as rod-like particles with an axial length L (~ 95 nm) and a radial cross section A (~ 20 nm and ~ 14 nm for switch C and switch O, respectively) (Figure 4.1). The total scattering intensity is approximated by [36]:

$$I(q) = I(q)_{axial} \cdot I(q)_{cross} = \frac{\pi L}{q} \cdot A^2 \cdot \Delta\rho^2 \cdot exp\left(-\frac{q^2 R_c^2}{q}\right) = \frac{a}{q} \cdot exp\left(-\frac{q^2 R_c^2}{q}\right) \tag{4.3}$$

where the first factor is related only to the axial component and the remaining part corresponds to the cross-sectional scattering with an electron density contrast $\Delta\rho$. The pre-factors can be combined into a single fitting constant a. Equation 4.3 is valid in the range of $q_{min} = \frac{2\pi}{R_g}$ and $q_{max} = \frac{2\pi}{R_c}$, which corresponds to a q-range of ~ 0.2 – 0.9 nm^{-1} (1.3 nm^{-1}) for the switch C (switch O) object. Values for a and R_c were obtained by performing a least squares analysis in the valid q-range (Supplementary Figure 4.10b,c). The R_c value can be used for calculating the corresponding radius according to $R_c^2 = \frac{R^2}{2}$ when describing the switch object by a cylinder model with R = 10 nm (corresponding to a diagonal D = 20 nm of the cross-sectional area of the closed arm) and R = 7 nm (corresponding to the diagonal $D \approx$ 14 nm of the cross-sectional area of the open arm).

Furthermore, we computed the pair distance distribution function *P(r)* as described by Moore [34] using an indirect Fourier transformation in terms of a sine series expansion, based on the Shannon sampling theorem [247]. The large size of the DNA nanostructure is beneficial in the context of the series expansion, since the maximum number of series coefficients (a_n) is given by $n_{max} = (\frac{q_{max} \cdot D_{max}}{\pi})$, where D_{max} describes the maximum particle dimension. The calculation of *P(r)* requires a fixed value for D_{max}, which we expected to be around 95 nm for the switch object (Figure 4.1). We tested different values for D_{max} ranging from 60 – 130 nm for all switch samples by calculating a *chi*-squared value (χ^2), which describes the discrepancy between the experimental data and the fit, for each D_{max}. The χ^2 values decay approximately exponentially with increasing D_{max}(Supplementary Figure 4.11) until they plateau for D_{max} > 90 nm. For D_{max} values > 95 nm no change in the overall shape of the *P(r)* was observable, thus a D_{max} of 95 nm was taken as the best estimate of D_{max}. *P(r)* functions shown were normalized to give equal surface areas. Structural parameters described above as well as the two-state model fitting (see main text) were calculated from scattering profiles averaged from 10 independent runs for all three sample concentrations. The related errors represent the standard deviation.

4.9.5 Computing SAXS profiles from atomic models of DNA origamis

We generated atomistic models for the open and closed switch object with the CanDo software assuming idealized DNA helix and junction geometries [228]. CanDo simulations were run using the CanDo webserver (http://cando-dna-origami.org); computation time was dependent on the load of the server and the design of the structure, but typically in the range of hours. There are several methods to predict a scattering profile from an atomistic model that differ in various aspects of the computation. We used the programs *CRYSOL* [46] and *FOXS* [44] for calculation of the theoretical scattering curves from atomistic models. *CRYSOL* [46] computes the scattering intensity using a spherical harmonics expansion and scattering contributions from the hydration shell around the molecule are taken into account by assuming a homogenous 3 Å thick border layer with a default density contrast value of 0.03 $e^-/Å^3$. The program *FOXS* [44] evaluates the theoretical scattering profile from the Debye formula and the particle hydration layer is modeled as a function of surface accessibility [56]. As a complementary and more simplistic approach, we utilized a custom written routine in *C*, adapted from the program *SAXS3D* [60], to determine theoretical scattering profiles based on a coarse-grained representation of the switch objects including only scattering centers per DNA base.

For the Debye formula routine, only one particle (placed at the phosphorus position) per base was used and the q-range was set to 0 - 3 nm^{-1} including 300 datapoints. *CRYSOL* was run in interactive mode, setting the order of harmonics to the maximum value of 50, given the large size of the switch object. The number of points in the theoretical curve was fixed to 800 within a q-range from 0 - 3 nm^{-1}; the remaining parameters were set to default values, without fitting the theoretical curve to the experimental data. *FOXS* was executed in default mode using the same number of points and q-range as applied in *CRYSOL*. Calculated scattering profiles were fitted to the experimental data of the switch C and switch O sample by performing a linear fit including a constant offset (Figure 4.5a,b and Supplementary Figure 4.14). To test the influence of the ion shell surrounding the switch object on the shape of the theoretical scattering profiles we investigated solvent density values ranging from 0.334 $e^-/Å^3$ (default, corresponding to the solvent density of water) and 0.344 $e^-/Å^3$ in *CRYSOL* (Supplementary Figure 4.17) and from 0.307 $e^-/Å^3$ (minimum) – 0.388 $e^-/Å^3$ (maximum) in *FOXS* (data not shown). In addition, we varied the contrast of the solvation shell surrounding the DNA origami; i.e. we varied the difference in electron density between the hydration layer and bulk solution, testing values from 0.06 to 0.25 $e^-/Å^3$ (0.03 $e^-/Å^3$ is the default value) in *CRYSOL*. The latter is based on a literature value reported for experiments on Mg^{2+} ions dissolved in water [248]. Increasing the contrast or solvent density to even higher numbers would not correspond to physically plausible solution conditions.

4.9.6 Electrostatic potential calculations and estimates of the ion atmosphere

To estimate the extent of the ion atmosphere around the DNA origami objects used in this work, in particular in comparison to simple double-stranded DNA molecules for which the role of ion scattering has been investigated in detail previously [54, 230, 243, 249], we performed simple electrostatic calculations. We calculated the electrostatic potential with a custom-written MATLAB script based on the Debye-Hückel/Poisson-Boltzmann approximation and on the

atomistic model of a 35 bp DNA and the switch C, including only the positions of the phosphate atoms of the DNA backbone. Each phosphate atom was described by its position (x_i, y_i, z_i) and modeled as a negatively charged point charge. Moreover, we assumed a Debye-Hückel exponential screening factor to account for the ionic screening due to mobile, dissolved ions. The resulting screened electrostatic potential at a certain position r_i is given by the sum of the electrostatic potential over all phosphate atoms:

$$\Phi(r)_{screen} = \sum_i \frac{-q}{4\pi\varepsilon_0\varepsilon_r r_i} \cdot exp\left(\frac{-r_i}{\lambda_D}\right) \tag{4.4}$$

with the charge of $q = 1.602 \times 10^{-19}$ C the vacuum permittivity $\varepsilon_0 = 8.85 \times 10^{-12}$ F m^{-1}, the relative permittivity of water $\varepsilon_r = 80.4$ and a Debye length $\lambda_D = 9.9$ Å corresponding to the high-salt experimental buffer condition for the switch object consisting of 5 mM NaCl and 30 mM $MgCl_2$. We calculated the corresponding ion concentrations around the 35 bp DNA and the switch C assuming the Boltzmann distribution:

$$c^{\pm} = c_0^{\pm} exp\left(\frac{-q\Phi(r)_{screen}}{kT}\right) \tag{4.5}$$

where c_0 correspond to the initial ion concentration , $kT = 4.11 \times 10^{-21}$ J and $\Phi(r)_{screen}$ was computed by Equation 4.4.

4.9.7 Normal mode refinement of models against SAXS data

To refine the initial model against the experimental SAXS data, we employed a flexible fitting method based on a coarse-grained (one-bead-per-residue) nucleic acid representation and a modified elastic network model that allows large-scale conformational changes while maintaining pseudobonds and secondary structures [69]. This method optimizes a pseudoenergy that combines the modified elastic network model energy with a SAXS-fitting score and a collision energy that penalizes steric collisions. The optimization process effectively uses a weighted combination of normal modes to iteratively improve the fitting of SAXS data. To apply this method to a large DNA object, the following modifications and improvements have been made to the methods described previously [69]. First, each DNA nucleotide is represented by a bead located at the C4' atomic position. All pairs of DNA beads within a cutoff distance of 35 Å are linked to build an elastic network model (see Equation 1 of Ref [69]). The coarse-grained form factors for DNA nucleotides are taken from the Fast-SAXS-Pro program [45]. Second, to stabilize the local structure of double-stranded DNA, for nucleotide i and i' that form a base pair, additional springs are added between the following pairs: (i, i'), $(i \pm 1, i')$, $(i, i' \pm 1)$, $(i-1, i+1)$, $(i'-1, i'+1)$. Third, the SAXS fitting score (Equation 10 of Ref. [69]) is modified to the following:

$$E_{SAXS} = f_{SAXS} \cdot N \cdot \chi^2 \tag{4.6}$$

with a chi-squared of:

$$\chi^2 = min_c \left\{ \sum_i \frac{[c \cdot I_m(q_i) - I_t(q_i)]^2}{\sigma_i^2} \Big/ \sum_i \frac{[I_t(q_i)]^2}{\sigma_i^2} \right\} \tag{4.7}$$

The constant pre-factor f_{SAXS} = 30, N is the number of DNA beads and q_i is the scattering vector uniformly sampled between 0 and 3 nm^{-1} with an increment of 0.025 nm^{-1}, I_m is the model SAXS profile, I_t is the target SAXS profile measured experimentally, and σ is the experimental error of I_t. Fourth, no hydration shell is modeled, which is expected to have negligible effect on SAXS fitting especially for large molecular systems [56]. Fifth, to reduce memory usage for the large systems, all Hessian matrices except *HSAXS* in Equation 11 of Ref. [69] are stored in the sparse matrix format, and the *HSAXS* term is omitted. The linear equation in Equation 11 of Ref. [69] is solved using the CHOLMOD suite (http://www.cise.ufl.edu/research/sparse). Normal mode refinement calculations were run on an Intel Xeon Processor L5520 (8M Cache, 2.26 GHz); the full refinement of a structure using 209 q-values required 120 h of computational time.

4.9.8 Ensemble FRET measurements via donor quenching

Ensemble FRET experiments in solution on DNA origami switch objects were conducted and analyzed as described in the Supplementary Information of Gerling *et al.* [112] Fluorescently labeled switch particles exhibit low and high FRET signals upon a conformational change from the open to the closed state, respectively. In order to dissect the populations of the closed and open conformation of the switch D sample as a function of $MgCl_2$ concentration, ensemble FRET measurements were performed on switch C, switch O and switch D samples while titrating $MgCl_2$ concentrations in the range of 5 mM to 25 mM (Supplementary Figure 4.12), as published previously [112]. Ensemble FRET data of the switch C and switch O sample serve as reference samples for the closed and open state, respectively.

To compare the fractions of populations derived from ensemble FRET experiments to the fractions obtained from the two-state model for the switch D sample of the SAXS data, each titration curve was fitted up to a $MgCl_2$ concentration range of 30 mM, assuming a two-state model where the resulting ensemble FRET value (E_{FRET}) is given by:

$$E_{FRET} = f_c \cdot E_c + f_o \cdot E_o \tag{4.8}$$

E_c and E_o correspond to ensemble FRET values and the coefficients f_c and f_o are fractional occupancies of the closed and open state, respectively. From statistical thermodynamics of a two-state system it follows that $f_c + f_o = 1$ where f_c is calculated as follows:

$$f_c = \frac{1}{1 + exp\left(-\frac{\Delta G}{kT}\right)} \tag{4.9}$$

The overall free energy difference between the open and closed state $\Delta G(MgCl_2)$ is given by:

$$\Delta G(MgCl_2) = \Delta G_0 + m_c \cdot c(MgCl_2) \tag{4.10}$$

where ΔG_0 is the free energy difference at a reference $MgCl_2$ concentration of 5 mM, and m_c represents the cation sensitivity parameter. We obtained a ΔG_0 = 1.5 kcal/mol and m_c = -0.4 kcal/(mol · mM) from a least-square fitting of the experimental data. Values from the fitted titration curves at low (5 mM) and high (30 mM) $MgCl_2$ concentrations were used to determine the fraction of closed switch D particles. Analogous to the two-state model approach applied on the SAXS data, the ensemble FRET value of the switch D sample (E_d) can

be described by a linear superposition of the open and closed states represented by ensemble FRET values of switch O (E_{so}) and switch C (E_{sc}), respectively:

$$E_d(MgCl_2) = f_c \cdot E_{sc}(MgCl_2) + f_o \cdot E_{so}(MgCl_2) \tag{4.11}$$

For the evaluation of the conformational state of the switch D sample at low and high $MgCl_2$ concentrations, we averaged fitted ensemble FRET values for each sample taking values at the exact concentration (e.g. E_d(5 mM)) and the values of the precedent and subsequent concentration (i.e. E_d(4 mM) and E_d(6 mM)). Based on these values a least squares fit was performed to determine the closed fraction of the switch D sample at high (30 mM) and low (5 mM) $MgCl_2$ concentrations (Figure 4.4d). Errors were calculated based on a propagation of uncertainty.

4.10 Supplementary Material

4.10.1 Supplementary Table

Sample	R_g **(nm)**	R_c **(nm)**
CRYSOL (closed)	28.2	6.4
FOXS (closed)	28.1	6.3
custom written (closed)	27.6	6.4
CRYSOL (open)	29.5	4.4
FOXS (open)	29.4	4.4
custom written (open)	29.4	4.4

Table 4.2: Comparison of the radius of gyration (R_g) and the cross-sectional R_g (R_c) determined from the theoretical scattering profiles calculated with *CRYSOL*, *FOXS* and a custom written *C* script for the static switch samples. For Guinier analysis the fitting range $q_{max}R_g < 1.3$ was used and for R_c calculations a q-range of $\sim 0.2 - 0.9$ nm^{-1} (1.3 nm^{-1}) for the switch C (switch O) object was defined.

4.10.2 Supplementary figures

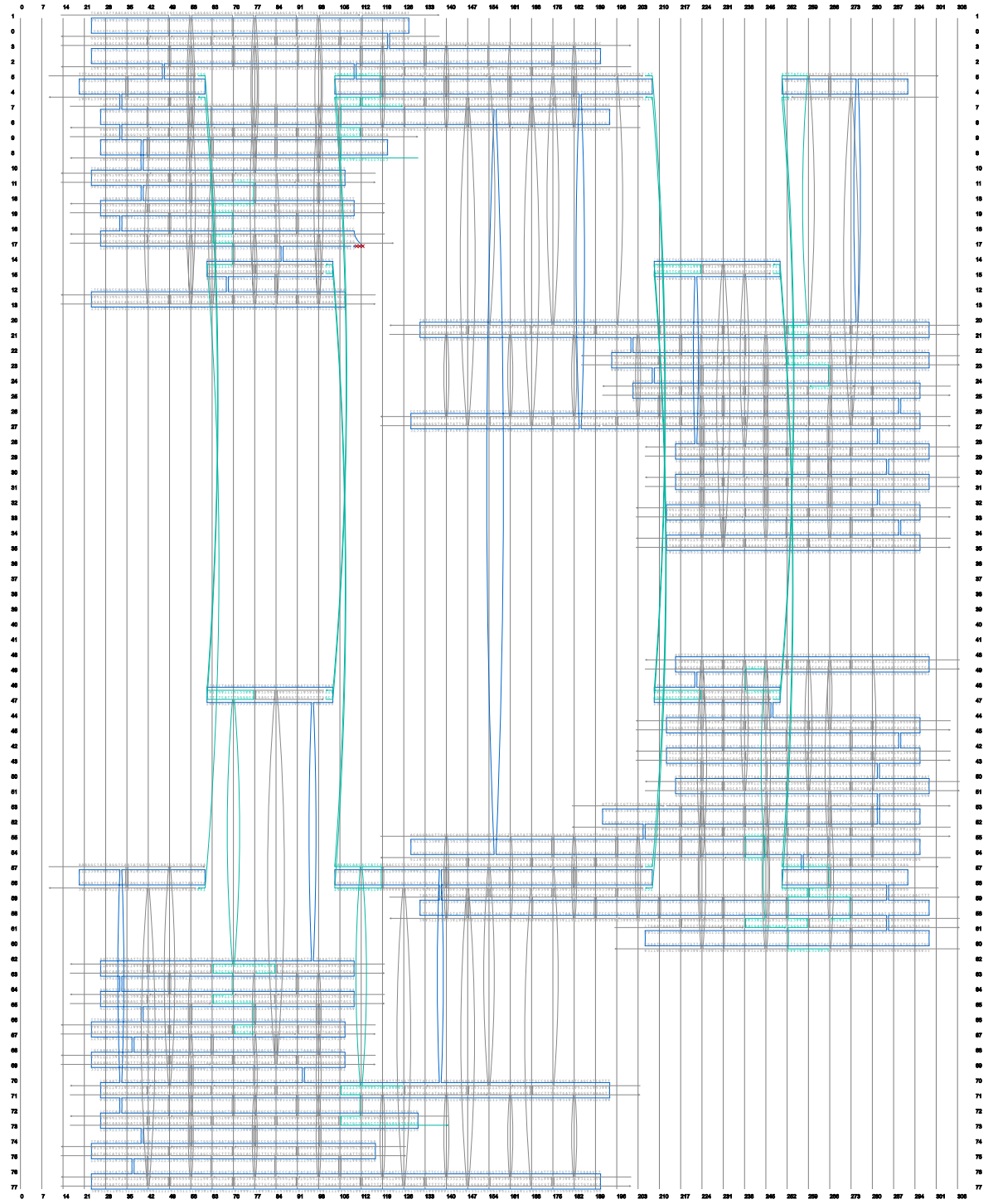

Figure 4.6: Strand diagram of the static closed switch (switch C) variant. Scaffold (shown in blue) and staple layout of the switch C variant. Cyan: 3-bases sticky end. Generated with caDNAno v0.2.

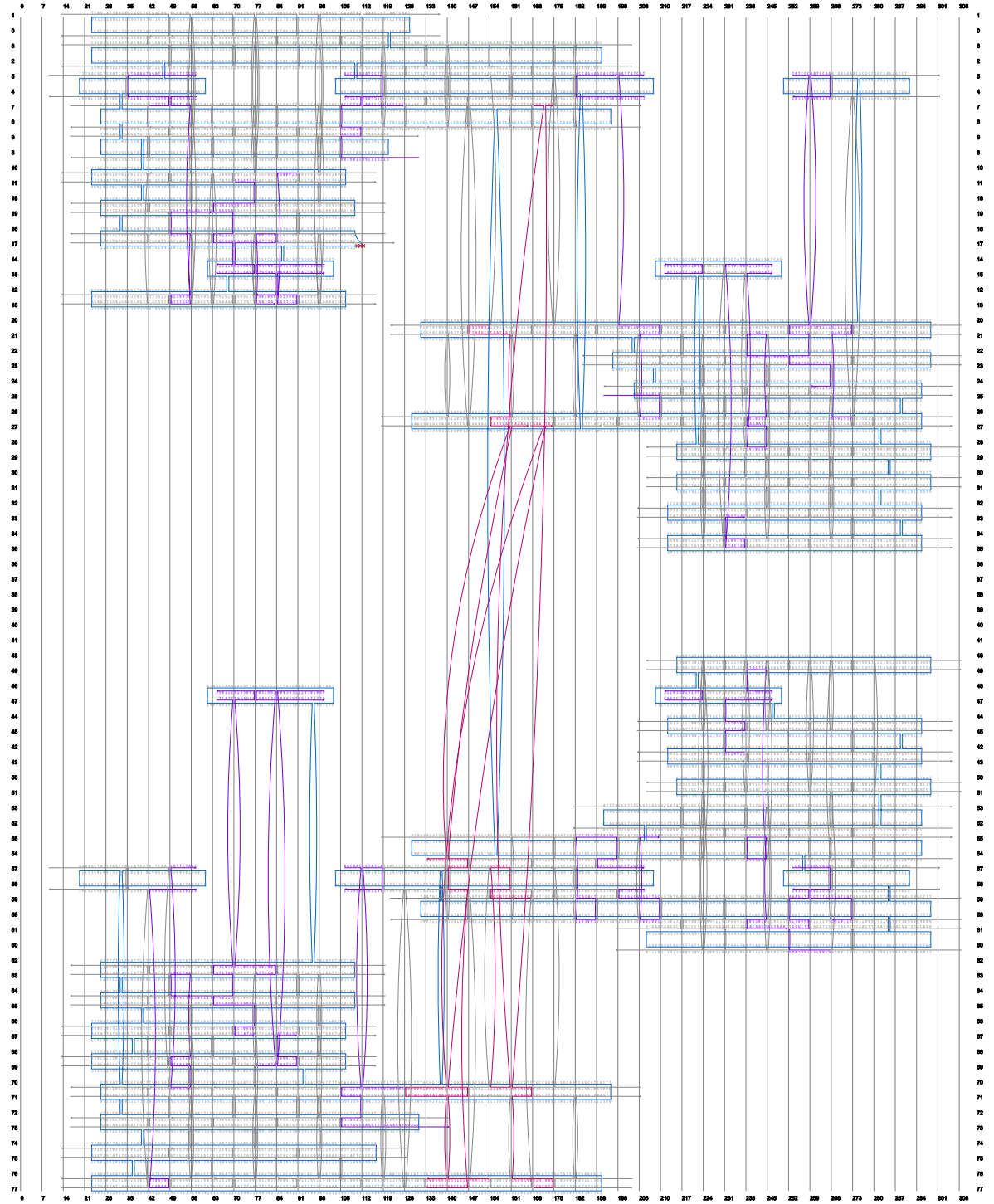

Figure 4.7: Strand diagram of the static open switch (switch O) variant. Scaffold (shown in blue) and staple layout of the switch O variant. Purple: stacking deactivated; Pink: additional connections between the upper and bottom arm. Generated with caDNAno v0.2.

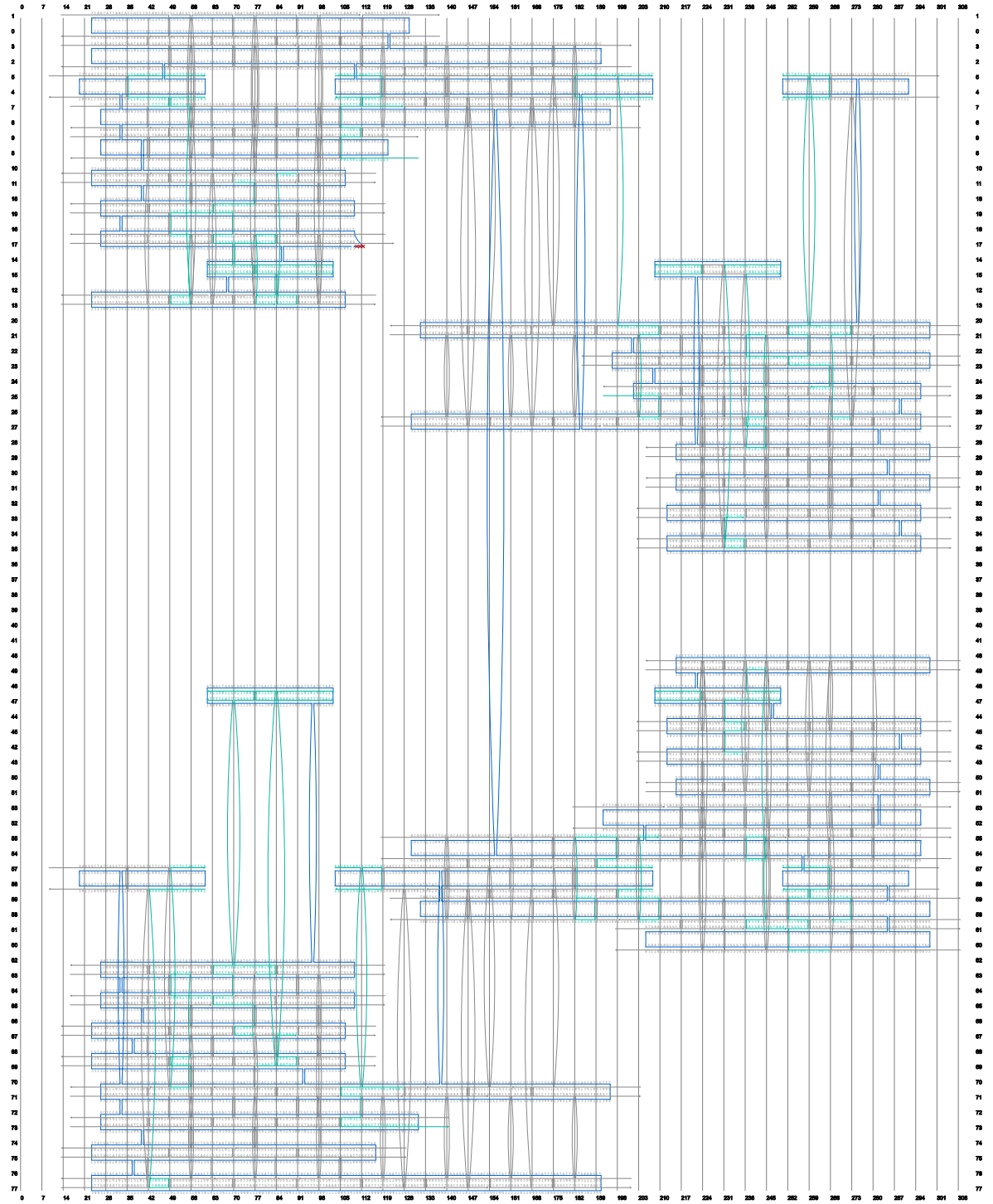

Figure 4.8: Strand diagram of the dynamic (switch D) variant. Scaffold (shown in blue) and staple layout of the dynamic switch variant with 16 activated stacking interactions. Cyan: stacking activated. Generated with caDNAno v0.2.

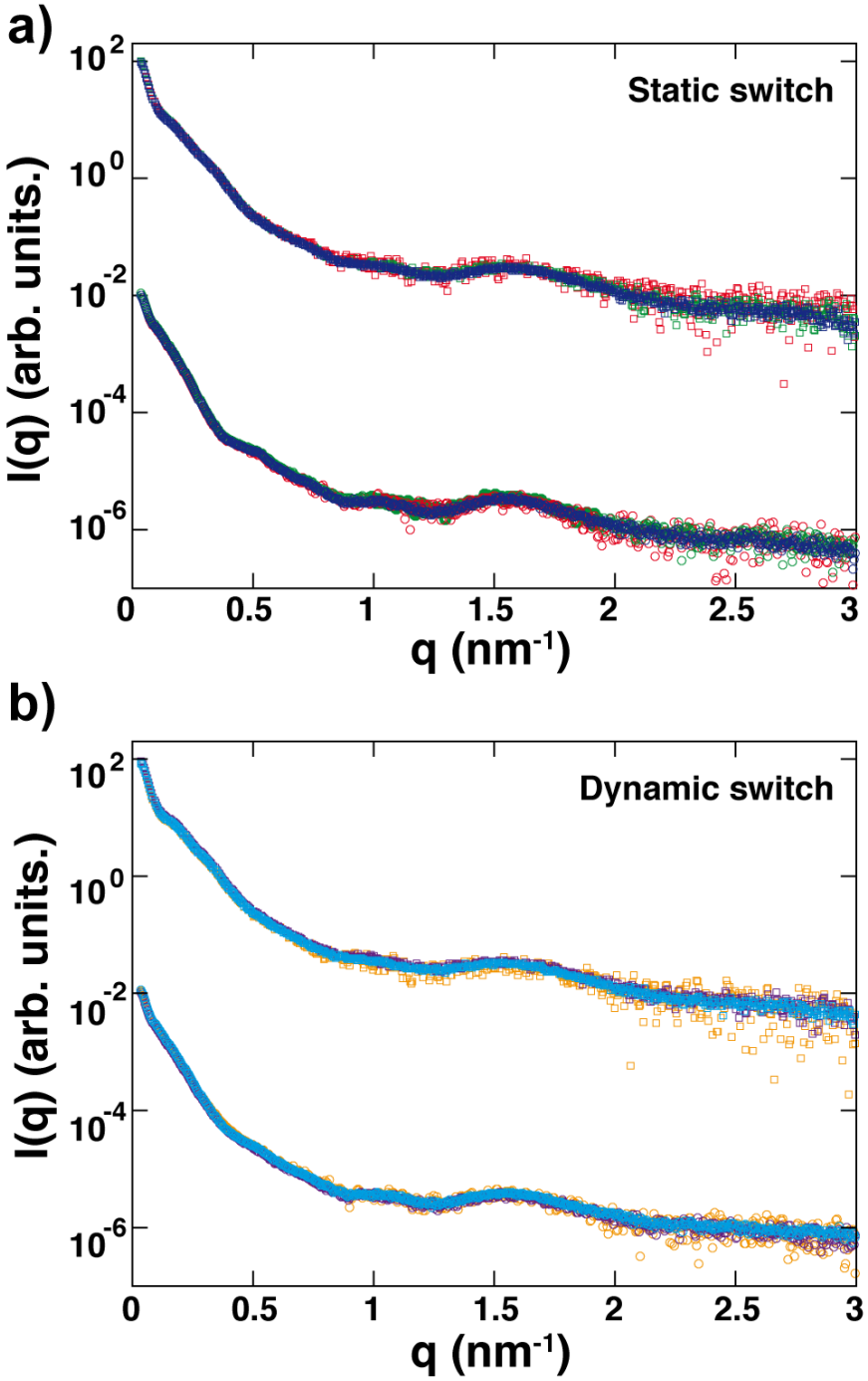

Figure 4.9: Concentration scaled scattering profiles for the static (switch C and switch O, top) and the dynamic (switch D30 and switch D05, bottom) switch variants. **a** Averaged scattering profiles for the switch C (circles, bottom) and switch O (squares, top) measured at varying concentrations: 25 nM (red), 50 nM (green) and 100 nM (blue). **b** Averaged scattering profiles for the switch D30 (circles, bottom) and switch D05 (squares, top) for applied concentrations of 25 nM (orange), 50 nM (purple) and 100 nM (cyan). Profiles are scaled by their concentration and the lower scattering profiles are vertically offset for clarity.

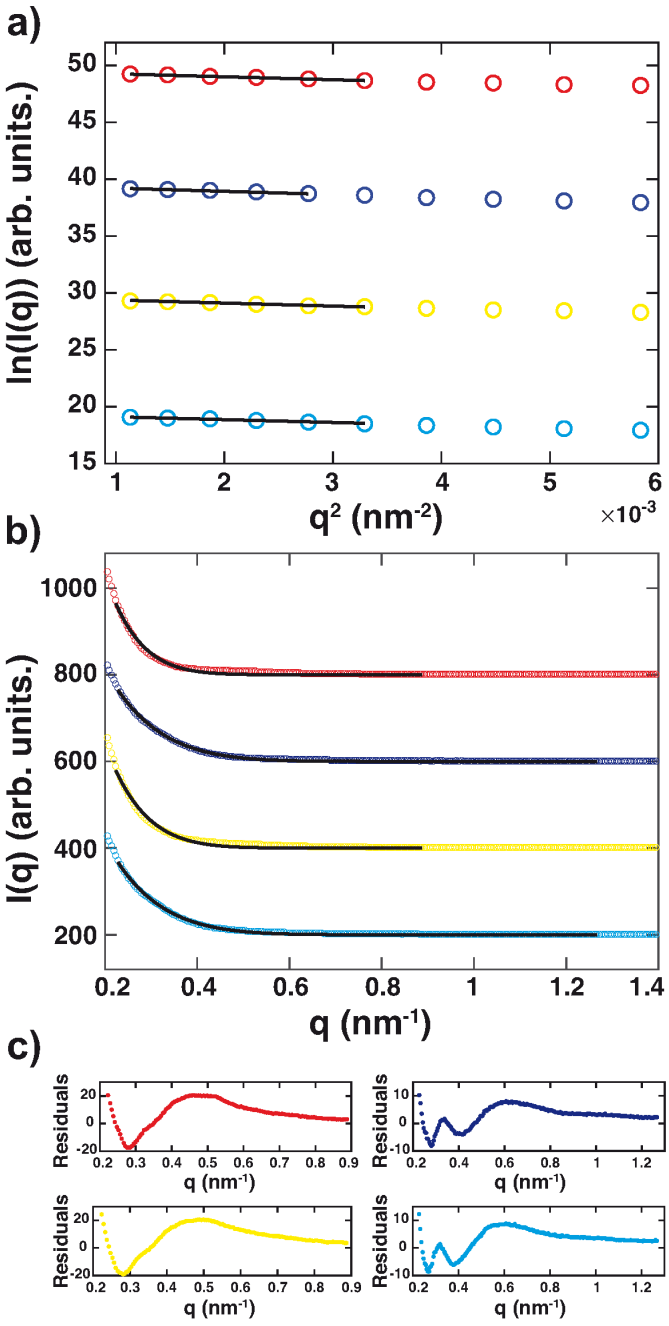

Figure 4.10: Guinier analysis and fits for the cross-sectional scattering intensity of static and dynamic switch samples. **a** Guinier representation of the experimental scattering data for switch C (red, top), switch O (blue), switch D30 (yellow) and switch D05 (cyan, bottom). The Guinier fits are indicated by black lines covering a q-range of $qR_g < 1.6$. Profiles are vertically offset for clarity. **b** Fits of the cross-sectional scattering intensities to experimental data shown in **a** (same color code as in **a**) for the q-range $q_{min} = 2\pi/R_q$ and $q_{max} = 2\pi/R_c$, where the R_c is given by $R_c^2 = R^2/2$. For switch C and switch D30 a radius of R = 10 nm and for switch O and switch D05 a radius of R = 7 nm was assumed for the fit. Profiles are vertically offset for clarity. **c** Residuals for data from **b** (same color code as in **b**).

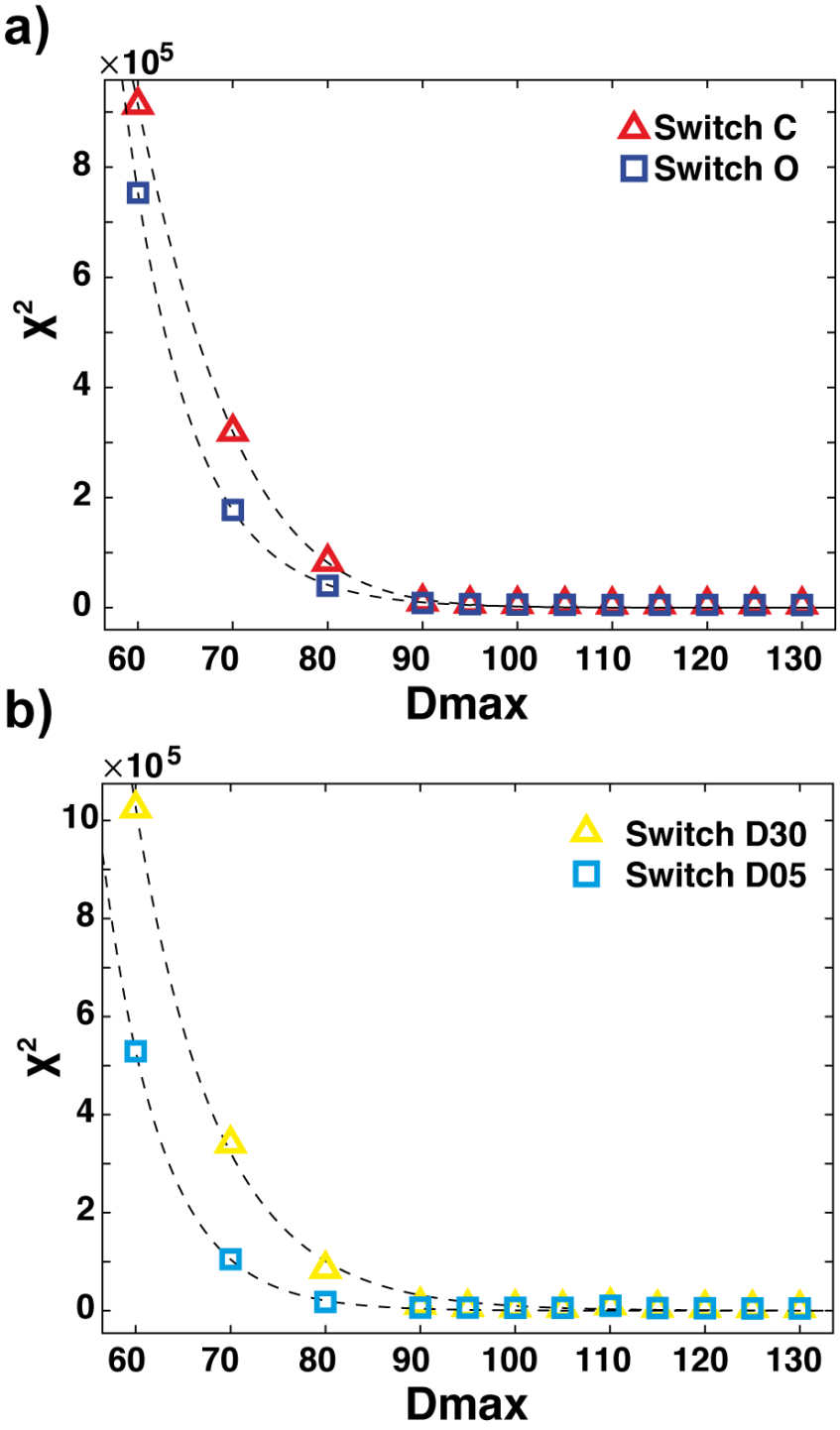

Figure 4.11: Determination of an adequate D_{max} value used for the computation of the pair distance distribution function *P(r)*. **a** χ^2 describing the discrepancy between the experimental data and the fit as a function of different D_{max} values evaluated for the static switch versions switch C and switch O. **b** Corresponding analysis for the dynamic switch versions switch D30 and switch D05. For all samples a mimimun of χ^2 around 95 nm was found, which was applied to calculate the *P(r)* function for each sample.

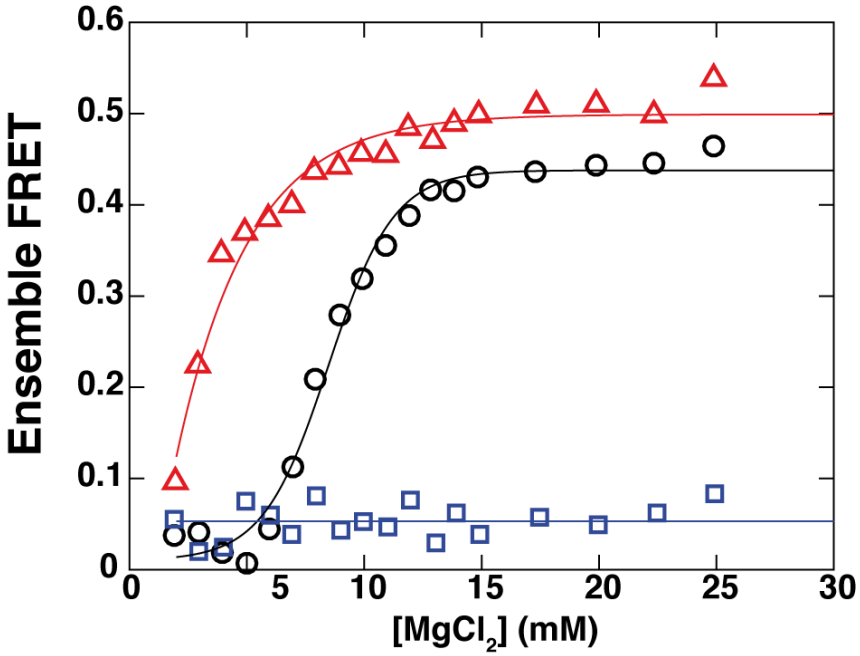

Figure 4.12: Ensemble FRET measured via donor quenching for a titration of $MgCl_2$ in solutions containing switch C (red triangles), switch D (black circles) and the dynamic switch variant with all click contacts deactivated (blue squares). Solid lines represent a two-state model with a free energy term that depends linearly on the $MgCl_2$ concentration (see Equation 4.10).

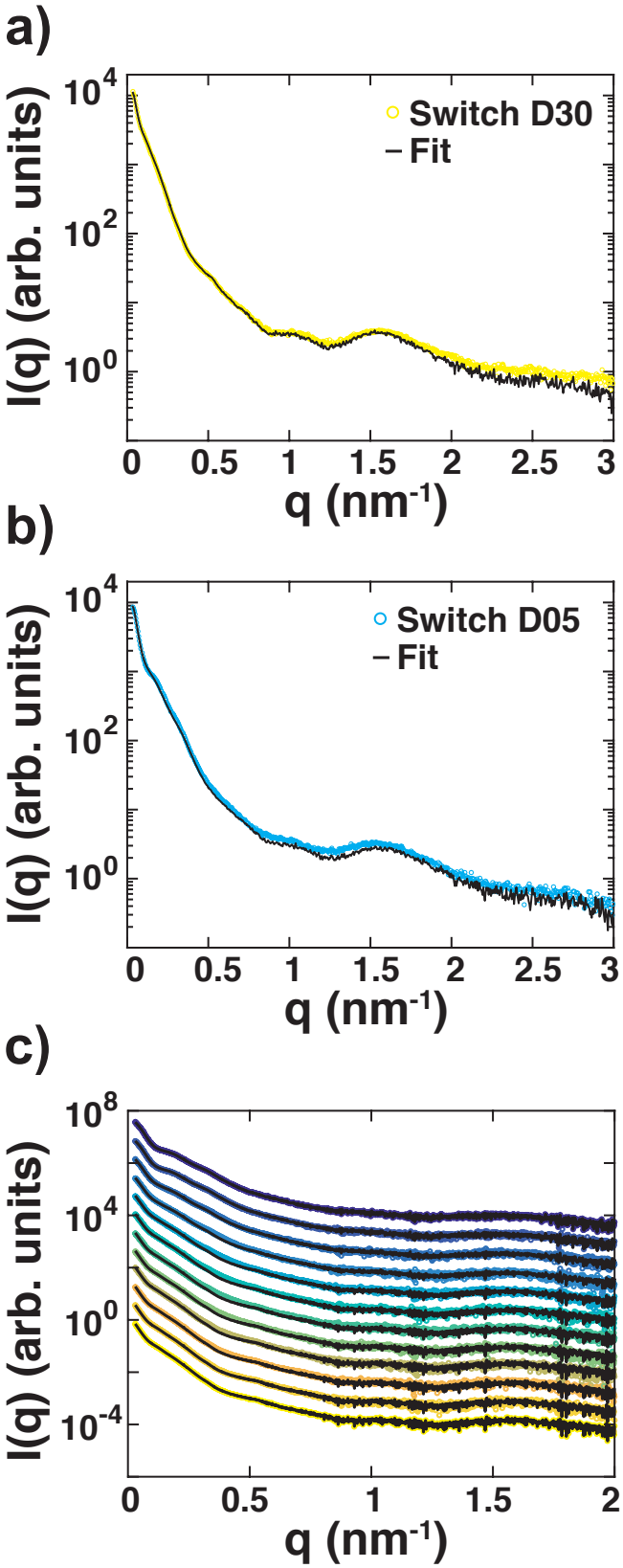

Figure 4.13: Fits of two-state models for the dynamic switch variants (switch D). **a** Scattering profile (yellow) of the switch D30 sample (30 mM $MgCl_2$) and the fitted profile (black) obtained from the two-state model (see main text). **b** Scattering profile (cyan) of the switch D05 sample (5 mM $MgCl_2$) and the fitted profile of the two-state model (black). **c** Scattering profiles of switch D for varying $MgCl_2$ concentrations: 3 (dark blue, bottom), 5, 8, 10, 12, 14, 15, 16, 18, 20, 25 and 30 mM (light yellow, top) and fitted profiles from a two-state model (see main text). Data are vertically offset for clarity.

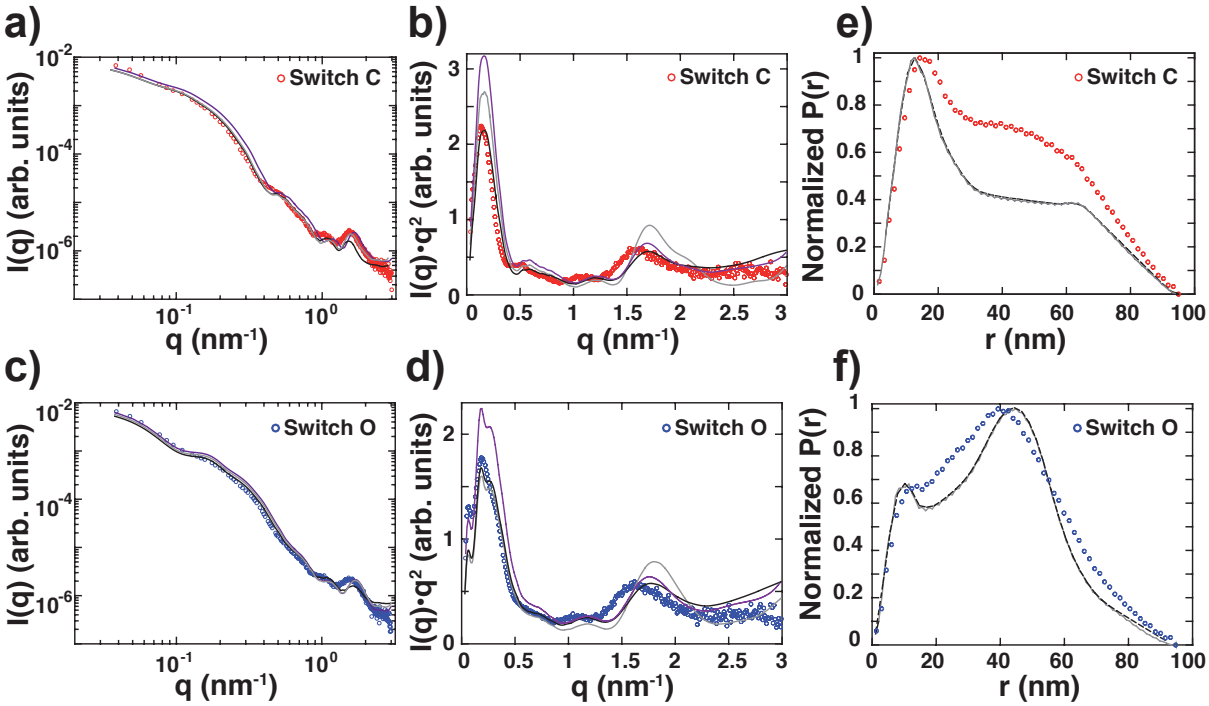

Figure 4.14: Comparison of the experimental and theoretical scattering profiles and P(r) functions that were predicted from the atomistic models derived from CanDo of the static switch samples. **a** Fits including an additional constant in the theoretical scattering profiles calculated with the program *CRYSOL* (black line), *FOXS* (gray line) and a custom written *C* script (purple line) to the experimental data of the switch C sample (red circles). For the custom written routine only one bead per base was assumed. **b** Kratky representation of the data shown in **a** (same color code as in **a**). **c** Fits including an additional constant in the theoretical scattering profiles calculated with the program *CRYSOL*, *FOXS* and a custom written *C* script (same color code and computational settings as in **a**) to the experimental data of the switch O sample (blue circles). **d** Kratky representation of the data shown in **c** (same color code as in **c**). **e,f** *P(r)* functions of switch C (red circles) and switch O (blue circles) based on experimental scattering data and from profiles derived from *FOXS* (gray line). Black dashed lines correspond to histograms of distances calculated directly from the atomistic models. *P(r)* data were normalized to unity.

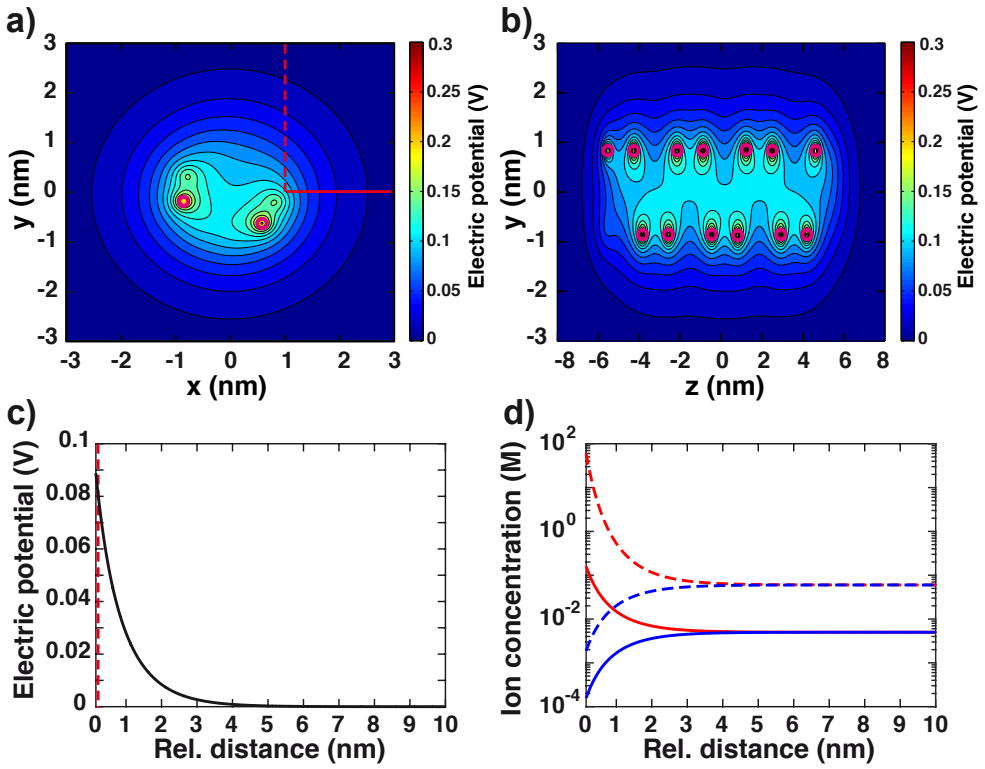

Figure 4.15: Electrostatic potential and ion distribution calculations to estimate the ion atmosphere around a 35bp DNA duplex. **a,b** Contour plots of the screened electrostatic potential for an atomistic model considering only phosphate charges of a 35 bp DNA, showing cross-sections in the x-y plane (**a**) and y-z plane (**b**). Magenta circles indicate positions of phosphate atoms. **c** Electric potential along the x-axis (for y,z = 0 nm) corresponding to a solvent-accessible area outside the 35 bp DNA (indicated by the vertical (dashed) and horizontal red lines). **d** Concentration of mono- and divalent ions for the same area as in **c** corresponding to buffer conditions of 5 mM NaCl and 30 mM $MgCl_2$: Mg^{2+} (red dashed line), $2 \times Cl^-$ (blue dashed line), Na^+ (red line) and Cl^- (blue line).

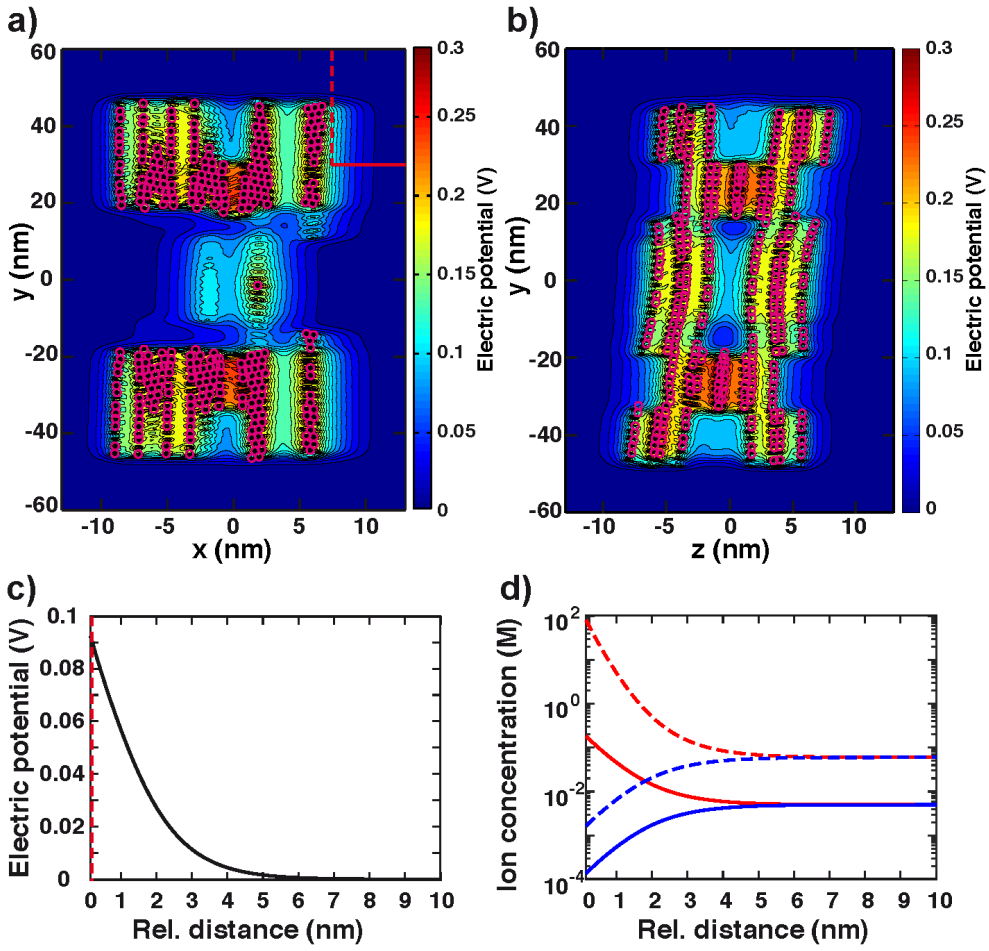

Figure 4.16: Electrostatic potential and ion distribution calculations to estimate the ion atmosphere around the closed switch. **a,b** Contour plots of the screened electrostatic potential for an atomistic model considering only phosphate atoms of switch C, showing cross-sections in the x-y plane **a** and y-z plane **b**. Magenta circles indicate positions of phosphate atoms. **c** Electric potential along the x-axis (for y = 30 nm; z = 0 nm) corresponding to a solvent-accessible area outside the switch C structure (indicated by the vertical (dashed) and horizontal red lines). **d** Concentration of mono- and divalent ions for the same area as in **c** corresponding to buffer conditions of 5 mM NaCl and 30 mM $MgCl_2$: Mg^{2+} (red dashed line), $2 \times Cl^-$ (blue dashed line), Na^+ (red line) and Cl^- (blue line).

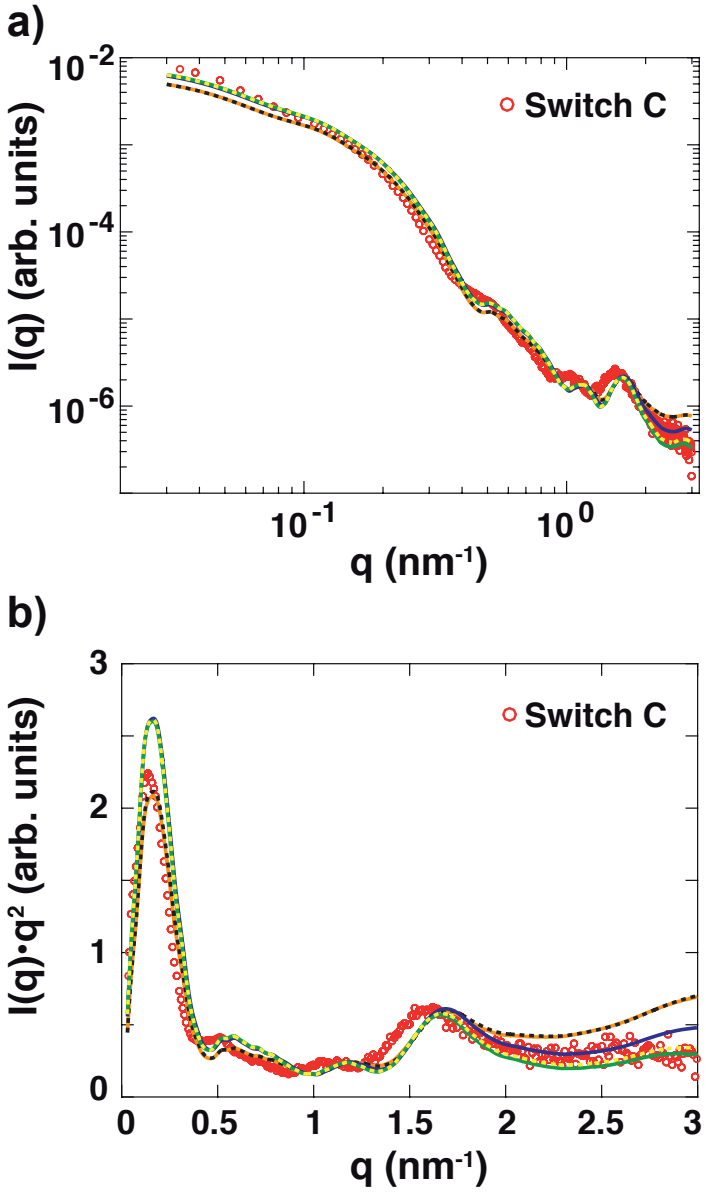

Figure 4.17: Computations of the scattering profiles with varying hydration shell conditions in *CRYSOL*. Linear fits including a constant offset of theoretical scattering profiles calculated with *CRYSOL* with contrast values of the hydration shell of 0.06 $e^-/Å^3$ (black dashed line), 0.12 $e^-/Å^3$ (orange line) and 0.25 $e^-/Å^3$ (green line) (solvent density = 0.334 $e^-/Å^3$ for all three profiles), with a solvent density value of 0.344 $e^-/Å^3$ and default contrast (blue line) and with a solvent density value of 0.344 $e^-/Å^3$ setting the contrast value to 0.25 $e^-/Å^3$ (yellow dashed line). **b** Data from **a** in Kratky representation.

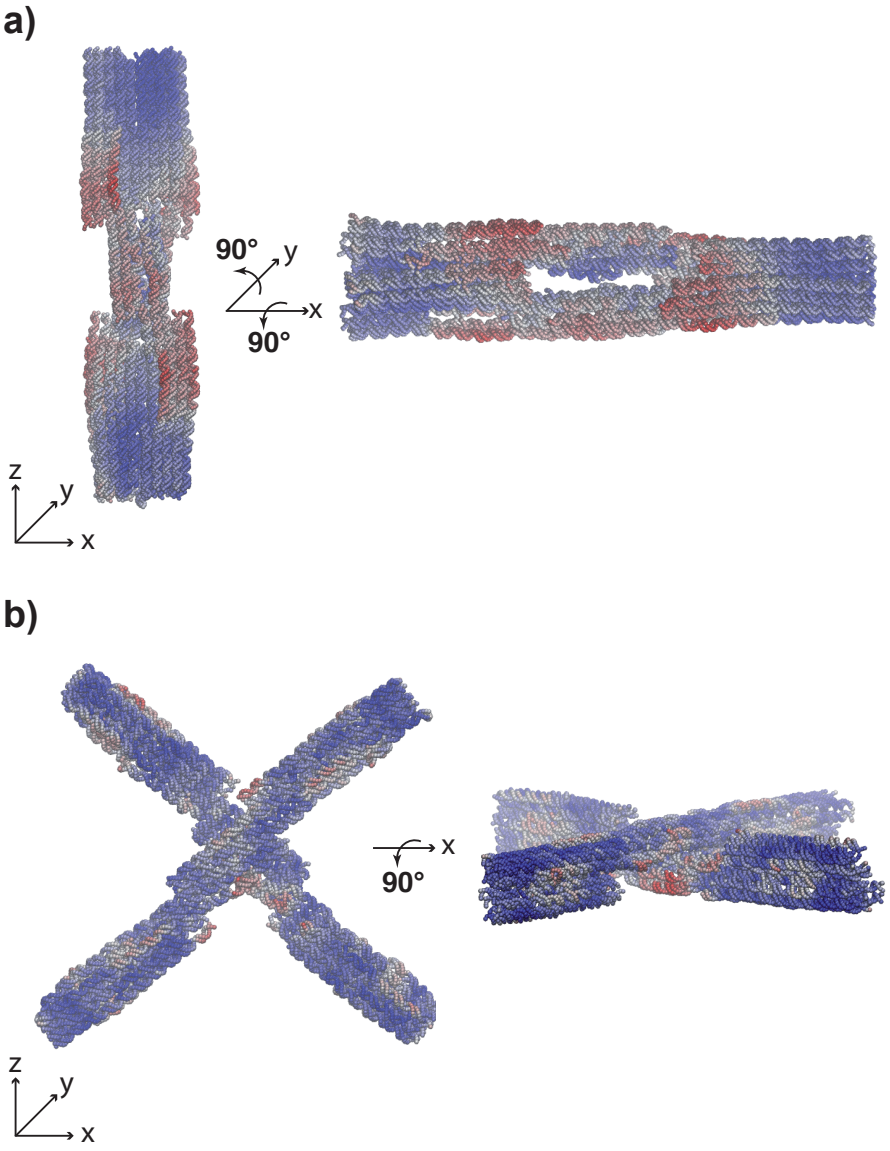

Figure 4.18: Visualization of the switch deformations from the normal mode refinement. **a** Local deformations for switch C (defined as RMSD against the initial CanDo derived structure) are indicated by the colored code where blue and red areas correspond to minimal and maximal deformations, respectively. **b** Local deformations for switch O, same color code as in **a**.

Chapter 5

Time-Resolved SAXS Reveals Millisecond Transitions of a DNA Origami Switch

Summary

We use time-resolved small-angle X-ray scattering to monitor large-scale conformational transitions of a two-state DNA origami switch in free solution. We show that the DNA device switches from its open to its closed conformation upon addition of $MgCl_2$ in milliseconds, which is close to the theoretical diffusive speed limit. Measurements on the dimerization kinetics of a DNA origami brick system suggests that kinetics depend on local concentration and molecular alignment.

5.1 Introduction

The programmable self-assembly of DNA molecules is a new paradigm for creating structures at the nm-μm scale with potential for diagnostic, therapeutic, and engineering applications [133, 250, 251]. Moving beyond static two- and three dimensional structures [102, 124] toward building complex devices will require implementing and controlling reversible mechanical movements in DNA objects, which remains a challenging aspect in the field.

So far, most switchable DNA devices have been triggered by the addition of DNA single strands and toehold-mediated strand exchange, where transitions occur on times scales of minutes [137, 252]. Conformational transitions initiated by changes in ionic strength, pH, temperature, or light can be faster, and have been demonstrated to occur within seconds [108, 145]. However, an experimentally unexplored aspect is how quickly conformational changes of synthetic 5 MDa-sized DNA structures can actually occur. Friction with the solvent and energy barriers in junctions or pivots could pose fundamental speed limits for switching dynamics, similar to what is observed for folding of naturally occurring RNAs due to their rugged free energy landscapes (Supplementary Fig. 5.3).

This Chapter is based on a manuscript by Bruetzel *et al.* [3] (*submitted*). Author contributions: All authors designed the study and contributed to writing the manuscript; T.G. assembled and purified samples; L.K.B. and P.W. performed SAXS measurements and analyzed the data.

5.2 Results and Discussion

To address this question, we employ time-resolved small-angle X-ray scattering (trSAXS) to monitor conformational transitions in a unimolecular (two-state) DNA origami switch and in a bimolecular DNA origami reaction system. SAXS can monitor the conformational transitions of macromolecules and their assemblies in free solution under virtually arbitrary solution conditions [8, 30, 31, 253]. SAXS does not require any labeling and directly probes the global conformation in solution. By using a stopped-flow kinetic mixer to trigger conformational changes by rapid changes in $MgCl_2$ concentration and a high-flux synchrotron beamline for fast data acquisition [254], we achieved a time resolution of 25 ms. We applied trSAXS to study the dynamics of a DNA origami switch (switchD16) [112] consisting of two ~100 nm long rigid arms connected by a Holliday junction at the center that allows for reversible transitions between an open and a closed conformation (Fig. 5.1a,b). Shape-complementary patterns of blunt-ended double helical protrusions and recessions are arranged on both arms that can form 16 basepair stacking interactions in the closed conformation of the switch. Electrostatic repulsion counteracts the stacking contacts, such that at low cation concentration the open conformation is favored.

We have previously demonstrated that SAXS can monitor and quantify the $MgCl_2$-dependent unimolecular equilibrium of the switchD16 device [2] and determined the midpoint of the open-to-close transition at ~10 mM $MgCl_2$ (see Fig. 5.1b and Materials and Methods (5.4)). In the trSAXS measurements, we started with DNA switch devices dissolved in 5 mM $MgCl_2$ where the open conformation is predominantly populated (fraction closed < 4%) [2]. Using the stopped-flow mixer (see Materials and Methods (5.4)), we then rapidly (within ≤ 1 ms) added $MgCl_2$ to final concentrations of 15, 25, and 35 mM (where in equilibrium f_{closed} = 90%, 98%, and 99%, respectively) and monitored the subsequent conformational changes.

For the 15 mM $MgCl_2$ condition the transition from the open to the closed state is resolved and well described by a first-order kinetic model (Fig. 5.1c,d and Supplementary Fig. 5.4) with a closing rate constant k_{close} = 22 s^{-1} and an opening rate constant k_{open} = 2.4 s^{-1}. For the 25 and 35 mM $MgCl_2$ conditions, the transition to the closed state occurs essentially within the dead time of our instrument (25 ms). Analysis of the data suggests a lower limit on the closing rate constants of k_{close} = 150 s^{-1} (Fig. 5.1d and Supplementary Fig. 5.5). The measured closing times of $\tau_{close} = k_{close}^{-1} \leq 7$ ms are at most 1-2 orders of magnitude slower than a simple estimate of the time scale for the diffusive motion of the two arms from the open into the closed state of $\tau_{diff} \sim 100$ μs (see Supplementary Text in section 5.5 and Supplementary Fig. 5.6), suggesting that the DNA switch closes near the diffusive speed limit. Residual energy barriers, if any, for closing must be lower than $\ln(\tau_{close}/\tau_{diff}) \sim 4$ k_BT, where k_BT is the thermal energy.

As a reference construct, we studied the kinetics of a bimolecular reaction system consisting of two separate monomeric DNA origami bricks that dimerize via shape-complementary basepair stacking interactions, similar to the switch device (Fig. 5.2a). The SAXS profiles at 20 mM $MgCl_2$ show pronounced differences between the monomer and dimer scattering patterns (Fig. 5.2b). In particular, the scattering profile of the dimeric complex exhibits a pronounced peak at $q \approx 0.28$ nm^{-1} (Fig. 5.2b), which corresponds to a length scale of $2\pi/q \approx$ 23 nm that matches the cross-section of the dimer (22 nm × 24 nm) (Fig. 5.2a). This strong interference peak is largely missing in the monomeric profile due to the asymmetric cross sectional area (11 nm × 24 nm) (Fig. 5.2a).

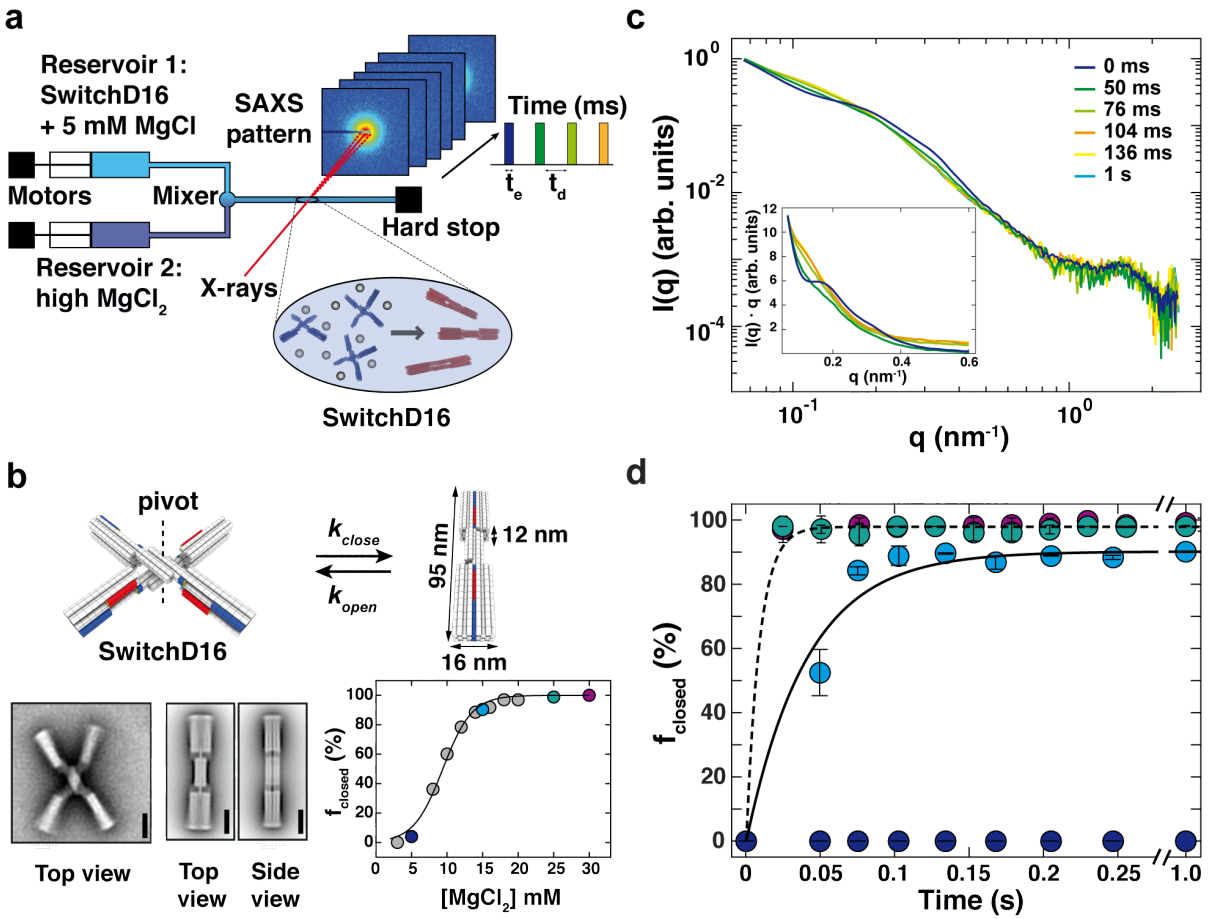

Figure 5.1: Time-resolved SAXS reveals the conformational kinetics of a DNA origami switch device. **a** Schematic of the stopped-flow mixing device coupled to the high brilliance beamline ID02 at the ESRF. The mixing reservoirs 1 and 2 contain the switchD16 device in 5 mM $MgCl_2$ and buffer with high $MgCl_2$ concentrations, respectively. After turbulent mixing, the mixture is directed to a capillary and the flow is stopped. The beam hits the sample in a specific acquisition pattern defined by the exposure time (t_e) and a delay time (t_e) (see Materials and Methods (5.4)). **b** (Top) Schematic view of the switchD16, which changes from an open to a closed conformation upon the addition of $MgCl_2$. The closed state is stabilized by 16 basepair stacking interactions occurring at the interface of shape-complementary double helical protrusions (red) and recessions (blue). (Bottom, left) Negative-stain TEM micrographs of switchD16 particles in the presence of 5 mM and 25 mM $MgCl_2$. (Scale bars, 20 nm). (Bottom, right) Fraction of closed switchD16 devices as a function of $MgCl_2$ determined by SAXS and two-state based thermodynamic model (black line). **c** SwitchD16 scattering profiles for selected time points after increasing the $MgCl_2$ concentration to 15 mM. The inset shows a zoom of the data represented as $I(q) \cdot q$ vs. q. **d** Fraction of switchD16 devices in the closed conformation vs. time after changing to $MgCl_2$ concentrations of: 5 mM (blue circles), 15 mM (cyan circles), 25 mM (green circles) and 35 mM (magenta circles). Symbols and error bars are the mean and standard deviation from two independent repeats of each condition. The solid black line and dashed black line represent a reversible unimolecular first-order reaction fit to the data at 15 mM and 25 mM $MgCl_2$ see Materials and Methods (5.4).

Based on a two-state model we determined the fraction of dimers at each time point (Fig. 5.2c,d, Supplementary Fig. 5.3 and Materials and Methods (5.4)). As expected for a bimolecular system, we find concentration dependent assembly kinetics. From a fit of a bimolecular reaction kinetics model to the data we obtain a negligible dissociation rate constant k_{off} and an estimate of an association rate constant k_{on} of $1.7 \cdot 10^4$ $M^{-1} \cdot s^{-1}$. A simple estimate for the time scale of

diffusive reaction that takes into account the global dimensions of the bricks yields a diffusion-limited reaction rate constant k_{diff} of $\sim 2.5 \cdot 10^8$ $M^{-1} \cdot s^{-1}$ (see Materials and Methods (5.4)).

Hence, the brick system reacts much slower than the diffusive speed limit, which points to the existence of additional barriers, including electrostatics and the correct alignment of the brick monomers [255], that slow down the reaction. Taken together, these data suggest that the very rapid closing transition of the DNA switch device is due to the fact that the central Holliday junction links the two arms and orients them favourably to form the 16 basepair stacking interactions that stabilize the closed state. Therefore, the central pivot link creates a high effective concentration (estimated to be $k_{close}/k_{on} \sim 1.4$ mM) of the two arms enabling them to interact on the millisecond timescale.

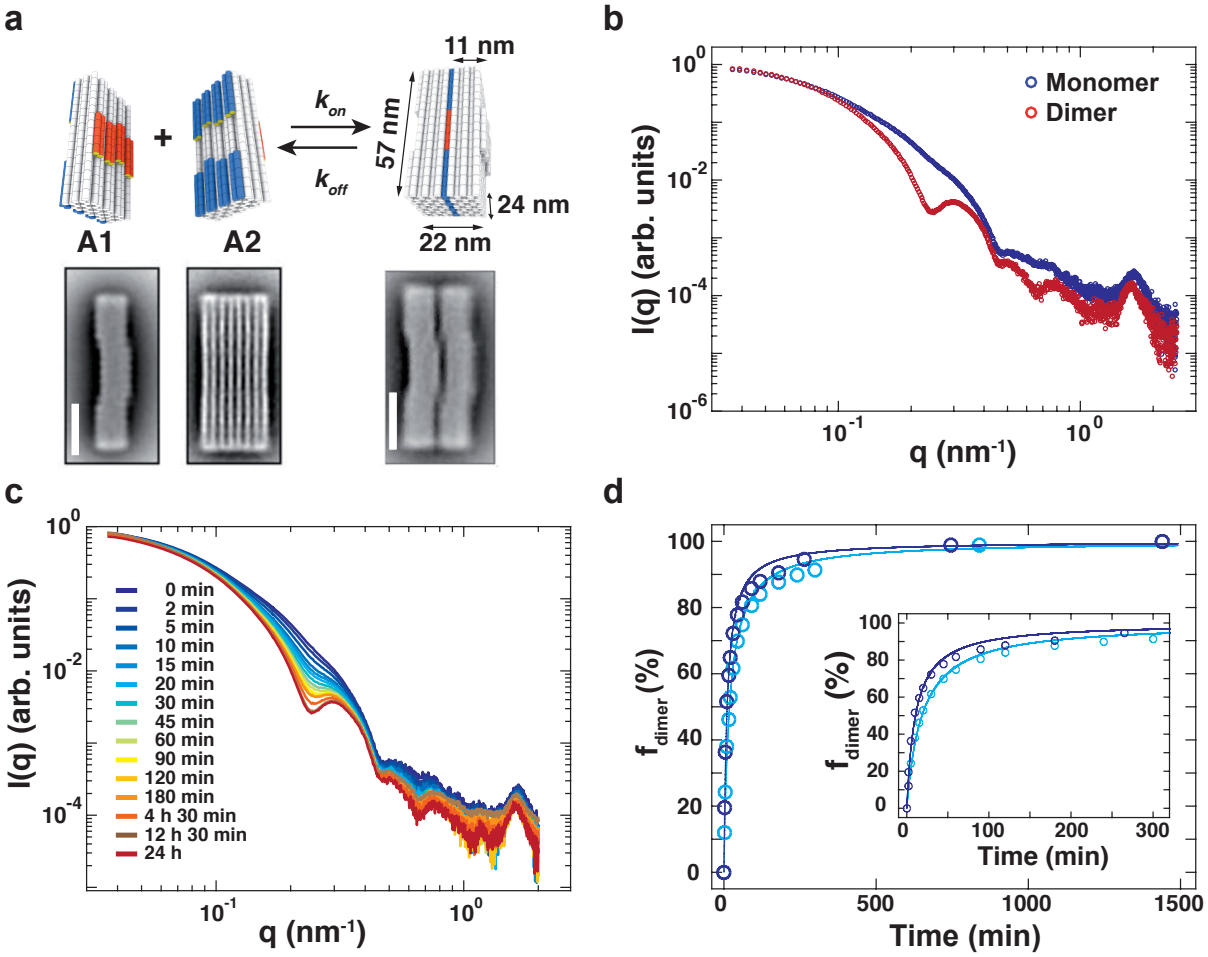

Figure 5.2: Time-resolved SAXS measurements on dimerization kinetics of DNA origami bricks. **a** (Top) Schematic of DNA origami brick monomers with double helical protrusions and recessions (indicated in red and blue) allowing for the formation of a dimeric brick in the presence of 20 mM $MgCl_2$. (Bottom) TEM micrographs of DNA origami monomers and dimers. Scale bar: 20 nm. **b** Experimental scattering profiles of DNA origami monomers (blue circles) and dimers (red circles) at a sample concentration of 100 nM in 20 mM $MgCl_2$. **c** Time evolution of scattering profiles after 1:1 mixing of monomeric brick samples at an initial concentration of 100 nM. **d** Fraction of dimeric brick particles as a function of time determined from a two-state model for initial monomer concentrations of 100 nM (blue circles) and 50 nM (cyan circles). Solid lines represent fits of an irreversible bimolecular reaction rate model (see Equation 5.7) yielding an average association reaction rate constant of 1.7×10^4 $M^{-1} \cdot s^{-1}$. The inset shows a close up of the early time points.

5.3 Conclusion

In conclusion, we have demonstrated that ~5 MDa DNA origami devices can undergo fast conformational dynamics on the millisecond timescale, suggesting that such devices could be employed for switching and sensing molecular capabilities with fast response times. Our work establishes trSAXS as a powerful tool to monitor large-scale conformational changes of DNA origami objects on timescales from milliseconds to hours without the need for labeling or surface immobilization. In the future, a combination of continuous-flow mixing in appropriate microfluidics with microfocus X-ray sources has the potential to push the time-resolution even into the μs-regime [256], which would allow us to probe conformational transitions at the molecular speed limit.

5.4 Materials and Methods

5.4.1 DNA origami assembly and purification

The scaffold DNA (p8064) was prepared as previously described [245]. Staple DNA strands were synthesized by solid-phase chemical synthesis (Eurofins Genomics GmbH, Ebersberg, Germany; HPSF purification). DNA origami objects were designed using caDNAno v.02 [128] and prepared as described previously [2, 112]. Objects were self-assembled by subjecting the one-pot reaction mixture to a thermal annealing ramp using a thermal cycling device (TETRAD; MJ Research – now Biorad) [121]. The reaction mixture contained 50 nM scaffold DNA (p8064), 200 nM of each staple DNA strand, folding buffer (1 mM EDTA, 5 mM TrisBase, 5 mM NaCl; pH 8), and 20 mM $MgCl_2$.

DNA origami switch device

All 16 basepair stacking interactions are active in the dynamic switch variant switchD16 (Supplementary Figure 5.8). After a 15 min thermal denaturation step at 65 °C, the thermal annealing ramp covered the temperature interval [58 – 55 °C] with a rate of 1 °C/90 min. Excess staple DNA strands were removed from the reaction mixture by performing two rounds of polyethylene glycol (PEG) precipitation [123]. The resulting pellet was dissolved in folding buffer (1 mM EDTA, 5 mM TrisBase, 5 mM NaCl; pH 8) containing 5 mM $MgCl_2$. To allow for equilibration, all samples were incubated at 40 °C and 400 rpm overnight. Residual PEG was removed from the samples by performing three rounds of ultrafiltration (30K Amicon Ultra-0.5ml from Merck Millipore). Filters were equilibrated by adding 500 μl folding buffer containing 5 mM $MgCl_2$ at 2000 x g and 25 °C for 2 minutes. Then, 50 μl sample was mixed with 450 μl folding buffer and centrifuged at 8000 x g and 25°C for 15 minutes. The flow-throw was discarded and 480 μl of folding buffer was added to the recovered sample.

DNA origami bricks

We used a self-complementary DNA origami brick where the protrusions on its front face can click into correspondingly shaped recessions on its back face. Two samples were prepared: in brick A_1 protrusions are active and recessions were permanently deactivated (Supplementary Figure 5.9) and in brick A_2 recessions are active and protrusions were permanently deactivated

(Supplementary Figure 5.10). Blunt end contacts were permanently deactivated by using 10-thymine-long overhangs. After a 15 min thermal denaturation step at 65 °C, the thermal annealing ramp covered the temperature interval [56 – 50 °C] with a rate of 1 °C/60 min. Excess staple DNA strands were removed from the reaction mixture by performing one round of polyethylene glycol (PEG) precipitation [123]. The resulting pellets were dissolved in HPLC buffer (1 mM EDTA, 5 mM TrisBase, 200 mM NaCl; pH 8) containing 5 mM $MgCl_2$. Then, we subjected the sample to HPLC (Agilent Technologies 1260/1290 Infinity) using the column (Agilent Bio SEC-5: 5 μm; 2000A; 21.2 × 300 mm) at a flow rate of 2 ml/min and collected fractions of the monomer peak (29.5 – 33.5 minutes). Due to dilution of the sample, we used ultrafiltration (30K Amicon Ultra-15mL from Merck Millipore) to concentrate the sample and to exchange the buffer to folding buffer (1 mM EDTA, 5 mM TrisBase, 5 mM NaCl; 5 mM $MgCl_2$; pH 8). Filters were equilibrated by adding 15 ml folding buffer containing 5 mM $MgCl_2$ at 7000 × g and 25 °C for 5 minutes. Then, 15 ml sample was added and centrifuged at 7000 × g and 25 °C for 7 minutes. The flow through was discarded. This step was repeated until the entire volume of the sample was centrifuged in the same filter. Then, the sample was mixed with 15 ml folding buffer and centrifuged at 7000 × g and 25 °C for 7 minutes. This step was repeated three times. The concentration of all DNA origami samples was determined using a spectrophotometer (NanoDrop 8000; Thermo Scientific). All SAXS experiments were performed on SwitchD16 and brick samples dissolved in folding buffer (1 mM EDTA, 5 mM TrisBase, 5 mM NaCl; pH 8) containing varying $MgCl_2$ concentrations.

5.4.2 SAXS data acquisition

SAXS measurements were performed at beamline P12, DESY, Hamburg [246] and the high brilliance SAXS beamline ID02, ESRF [254], Grenoble.

P12. SAXS measurements at beamline P12 were performed at an X-ray wavelength λ of 1.2 Å and a sample-to-detector distance of 3.0 m, resulting in a q-range of 0.03 to 5 nm^{-1} (with $q = 4\pi sin(\theta)/\lambda$, where 2θ is the total scattering angle). For data acquisition we used a Pilatus 2M detector. For each sample condition 40 frames with an exposure time of 45 ms in 'flow' mode were conducted at room temperature. Buffer samples were measured using identical procedures before and after each sample measurement. Static profiles of monomeric and heterodimeric brick constructs were measured in buffer with 20 mM $MgCl_2$ at sample concentrations of 50 nM and 100 nM, respectively. Time-resolved (tr) SAXS measurements on dimerization kinetics were performed by manual mixing of 50 nM and 100 nM monomer concentrations in a 1:1 mixing ratio.

ID02. SAXS experiments were performed at an X-ray wavelength λ of 0.99 Å. Static experiments at beamline ID02 on switchD16 samples and DNA origami brick monomer and dimer samples were performed in a temperature controlled flow through capillary operated in air using the Rayonix MX-170HS detector (Rayonix L.L.C., USA) with a sample-to-detector distance of 5 m resulting in a q-range of 0.015 nm^{-1} to 1.5 nm^{-1}. Data acquisition was performed with an exposure time of 10 ms including 50 repeats and a delay time of 0.5 s in order to reduce radiation damage. The measurements were conducted at room temperature. SwitchD16 samples were measured at a final sample concentration of 100 nM.

TrSAXS experiments on switchD16 samples were conducted using a stopped-flow device (SFM-400, Bio-Logic, Claix, France) consisting of four motorized syringes coupled through

three mixers. The last mixer is coupled to a quartz capillary with a diameter of 1.5 mm that serves as the observation volume where the sample is exposed to the X-ray beam at a constant position (Figure 5.1). A hard-stop is placed at the end of the flow line and is activated at the end of the mixing sequence in order to stop the flow. The net dead time (~ 1 ms) including the mixing time and the time to transfer the mixture to the beam crossing point in the capillary was determined as described elsewhere [254]. For each trSAXS measurement 150 μl each of buffer and switchD16 samples were prepared in the syringes for mixing and subsequently mixed at equal volumes. For stopped-flow based SAXS experiments the sample-to detector distance was set to 2.5 m covering a q-range of 0.04 nm^{-1} to 3.0 nm^{-1}. For each run 30 to 50 frames were recorded with an exposure time of 10 ms and a delay time t_d = (16× 1.05i) ms (where i denotes the actual frame number) between consecutive frames in order to prevent radiation damage. For trSAXS experiments switchD16 samples at a concentration of 200 nM were dissolved in 5 mM $MgCl_2$ buffer. Buffer solutions with $MgCl_2$ concentrations of 65 mM, 45 mM, 25 mM, and 5 mM were prepared to achieve final $MgCl_2$ concentrations after mixing of 35 mM, 25 mM, 15 mM and 5 mM, respectively. Prior to each stopped-flow experiment static profiles of switchD16 samples (c = 100 nM) at 5 mM, 15mM, 25 mM and 35 mM $MgCl_2$ concentrations and corresponding buffer profiles were recorded with the exposure time set to 10 ms and the number of frames to 10. For each $MgCl_2$ concentration two independent trSAXS repeats were conducted.

5.4.3 SAXS data processing

Data reduction was carried out using custom written scripts in Matlab (Matlab 2015, The MathWorks Inc., Natick, MA, USA). Scattering data were normalized to the intensity at zero angles (*I(0)*) by performing Guinier analysis of the data [29].

Static SAXS measurements. For static SAXS experiments performed at beamline P12 and ID02, sample and buffer data from each run were analyzed for radiation damage, which was not observed in any of the measurement. Matching sample and buffer profiles were averaged and buffer profiles were subtracted for background correction.

Stopped-flow based SAXS measurements. For each $MgCl_2$ concentration scattering profiles at each acquisition point were checked for consistency and radiation damage; no damage was observed in any of the measurements. Matching averaged buffer profiles from static SAXS experiments were subtracted from each single frame for background correction.

5.4.4 SAXS data analysis

SwitchD16. For trSAXS data, the scattering profile at each acquisition point (*I(q,t)*) can be described by a superposition of the scattering profiles of the sample conformation at the initial solution condition ($I_i(q,t_0)$) before mixing and the scattering profile of the final state at equilibrium after mixing ($I_f(q,t_{eq})$):

$$I(q) = f_i \cdot I_i(q, t_0) + f_f \cdot I_f(q, t_{eq}) \tag{5.1}$$

where the coefficients f_i and f_f are fractional occupancies of the initial and final states. For stopped-flow experiments we used static reference profiles of switchD16 samples acquired at 5 mM $MgCl_2$ and 15 mM, 25 mM and 35 mM $MgCl_2$ concentrations for I_i and I_f, respectively. For some frames, portions of the scattering curves deemed unreliable at the lowest q-values

due to parasitic scattering and at high q-values because of low signal-to-noise ratio resulting in an utilizable q-range of 0.08 nm^{-1} to 2.5 nm^{-1} for fitting. The fraction of closed particles was determined from two independent SAXS measurements at each $MgCl_2$ concentration and time point and the mean and the standard deviation were calculated and reported in Figure 5.1d. Fraction of closed particles were normalized to the portion of closed switchD16 particles in steady state for each $MgCl_2$ concentration (i.e. 0%, 90%, 98% and 99% for 5 mM, 15 mM, 25 mM and 35 mM $MgCl_2$ concentrations, respectively), derived from previous SAXS measurements [2]. To evaluate the goodness of the two-state fits, *chi*-squared values (χ^2) were calculated for each fit according to the following equation:

$$\chi^2 = \sum_i \frac{\left[I_{exp}(q_i,t) - I_{fit}(q_i,t)\right]^2}{\sigma_i^2} \tag{5.2}$$

where I_{exp} is the experimental SAXS profile, I_{fit} the best two-state fit profile, and σ the experimental error of I_{exp}.

Bricks. Two-state fits for dimerization kinetics of DNA origami bricks were performed using Equation 5.1, where the initial and final state are given by the scattering profiles of the monomer at the respective starting concentration and the dimer at equilibrium. Each fit was evaluated according to Equation 5.2. To determine the fraction of dimers, we used the q-range from 0.1 nm^{-1} to 2.5 nm^{-1}.

5.4.5 Kinetic fits for folding and assembly

SwitchD16. The (intramolecular) conformational change between the open and the closed state of the switchD16 sample was modeled as a reversible first-order reaction:

$$\mathrm{O} \underset{k_{open}}{\overset{k_{close}}{\rightleftharpoons}} \mathrm{C}$$

where O and C denote the open and closed state of switchD16 particles and k_{close} and k_{open} describe the closing and opening rate constants. Assuming that all objects (with an initial concentration of c_0) adopt an open conformation at t_0, the time dependent relative concentrations of particles in the open and closed state are given by:

$$\frac{c_O(t)}{c_0} = \frac{k_{open} + k_{close} \cdot e^{-(k_{close}+k_{open})\cdot t}}{k_{close} + k_{open}} \tag{5.3}$$

$$\frac{c_C(t)}{c_0} = \frac{k_{close} - k_{close} \cdot e^{-(k_{close}+k_{open})\cdot t}}{k_{close} + k_{open}} \tag{5.4}$$

The equilibrium constant K_{eq} of the reaction is defined as:

$$K_{eq} = \frac{k_{close}}{k_{open}} = exp\left(\frac{\Delta G}{k_B T}\right) \tag{5.5}$$

where k_B is the Boltzmann constant and ΔG denotes the Gibbs free energy between the open and the closed state. To estimate the closing rate constants for the 25 mM and 35 mM $MgCl_2$

data, we calculated the fraction of closed particles following Equation 5.4 for different closing rate constants (20 $s^{-1} < k_{close} < 300\ s^{-1}$) with $k_{open} = 0$ (as at $MgCl_2$ concentrations of 25 mM and 35 mM the closed fractions in equilibrium are ~98% and ~99%, respectively, suggesting that the opening rate constant is essentially negligible) and calculated the reduced χ^2-values for each closing rate constant given by:

$$\chi^2_{red} = \frac{1}{N}\left(\sum_i \frac{\left[f^{exp}_{closed}(t_i) - f^{theo}_{closed}(t_i)\right]^2}{\sigma_i^2}\right) \tag{5.6}$$

where N denotes the number of data points, f^{exp} corresponds to the experimentally determined fraction of closed particles, f^{theo} corresponds to the fraction of closed particles given by Equation 5.4 for each k_{close} value. The errors σ used in the calculation of the reduced χ^2-value are from repeat measurements, with an additional global error of 1%. All fitting procedures were performed with custom written Matlab (Matlab 2015, The MathWorks Inc., Natick, MA, USA) scripts using 'fminsearch' as optimization function.

Bricks. Heterodimerization kinetics of the DNA origami bricks were modeled as an irreversible bimolecular reaction:

$$A_1 + A_2 \xrightarrow{k_{on}} B$$

where A_1 and A_2 correspond to the brick monomer variants where either the protruding stacking pattern (1) or the recessed stacking pattern (2) had been activated, B denotes the dimer state and k_{on} describes the association reaction rate constant in $M^{-1} \cdot s^{-1}$. For our experimental conditions with an equimolar mixing ratio of A_1 and A_2 (with an initial concentration of A_0) and in the absence of dimers B at $t_0 = 0$, the time dependent relative concentrations of heterodimeric bricks as a function of time is given by:

$$\frac{B(t)}{A_0} = 1 - \frac{1}{1 + A_0 \cdot k_{on} \cdot t} \tag{5.7}$$

The model defined by Equation 5.7 was used to fit the fraction of dimers derived from the SAXS data for initial monomer concentrations ($A_1(t_0) = A_2(t_0) = A_0$) of 50 nM and 100 nM. We obtained an association rate constant k_{on} of $1.8 \times 10^4\ M^{-1} \cdot s^{-1}$ and $1.6 \times 10^4\ M^{-1} \cdot s^{-1}$ for a monomer concentration of 50 nM and 100 nM, respectively, and hence a mean value of $1.7 \times 10^4\ M^{-1} \cdot s^{-1}$. We also applied a bimolecular reaction model fit including the dissociation reaction rate constant for different final states of dimer fractions varying between 90% and 100% where a value of 100% dimers resulted in the lowest χ^2-value and a negligible small value for the dissociation reaction rate constant in line with previous experiments [112]. Assuming 100% dimers, we tested different k_{off} rates, yielding that the fit results are insensitive towards the off-rate for $k_{off} < 10^{-6}$. Larger k_{off} values resulted in increasing χ^2-values.

To compare these values with a reaction, only limited by the diffusion dynamics of the monomeric bricks, we calculated the theoretical diffusion-limited association rate constant k_{diff} of the bricks [257]:

$$k_{diff} = 4 \cdot \pi \cdot R \cdot D \cdot N_A \tag{5.8}$$

with R as distance within the two monomers react and form a dimer and can be assumed to be ~2 nm [255], D is the diffusion coefficient according to Equation 5.9 and N_A as the Avogadro constant.

5.5 Supplementary Material

5.5.1 Supplementary Text

Estimation of the timescales involved in the conformational transition from the open to the closed conformation of switchD16 samples.

We estimate the timescales for several processes involved in the conformational transition from the open to the closed state of the switch device. Specifically, we obtain rough, order-of-magnitude, estimates for the timescales of i) the diffusional motion of the two arms from the open to the closed conformation, ii) the formation of DNA basepair stacking interactions, and iii) the local conformational transitions of the central Holliday junction.

Diffusion of the switchD16 arms. After introducing a sufficiently high salt concentration to screen the (long-range) electrostatic repulsion that causes the switchD16 device to adopt the open conformation at low salt, we expect the transition from the open to the closed state to be fundamentally limited by diffusion of the arms, since the favourable stacking interactions that keep the switchD16 device in the closed conformation are short-range in nature [255] (with a range of $\leq$ 2.5 nm) and will only form once the arms are in sufficiently close proximity. Therefore, the timescale for diffusive motion of the two arms is expected to set the ultimate speed limit for closing of the switch device, similar to what has been observed for proteins [258, 259]. To assess the order of magnitude of the timescale for diffusive motion of the arms from the open to the closed state of switchD16, we applied a simple model based on rotational and translational diffusion. Each arm was considered as a rigid rod with a length L = 95 nm and a diameter of D = 16 nm (Supplementary Figure 5.6) and the translational (D_t) and rotational (D_r) diffusion coefficients were calculated following Lehner *et al.*[260]:

$$D_t = \frac{k_B T}{3\pi\eta L}\left[ln\left(\frac{2L}{D}\right) - \xi\right] \tag{5.9}$$

$$D_r = \frac{k_B T}{3\pi\eta L^3}\left[ln\left(\frac{2L}{D}\right) - \gamma\right] \tag{5.10}$$

where k_B is the Boltzmann constant, T the temperature in Kelvin (300 K), η the viscosity of the solvent (1 mPa·s) and ξ and γ are correction factors for the end terms taken from Tirado *et al.* [261]. The distance d each arm has to travel depends on the opening angle Θ, which has a mean value of $\sim 50^\circ$ (Supplementary Figure 5.6) [112]. Translational (t_{trans}) and rotational (t_{rot}) diffusion times for each arm are given by:

$$t_{trans} = \frac{d^2}{4D_t} \tag{5.11}$$

$$t_{rot} = \frac{d^2}{4D_r} \tag{5.12}$$

We find values for t_{rot} in the range of 20 to 70 μs for opening angles Θ between 50° to 90°. The estimate based on translational diffusion gives similar values, again varying the opening angle between 50° and 90°.

Formation of DNA stacking interactions. In the closed state, the two arms of the switchD16 device are held together by DNA stacking interactions. The timescale for the formation of nucleobase stacking interactions was investigated recently by force spectroscopy and molecular dynamics simulations [255]. The results suggest that formation of stacking interactions occurs on a timescale of 2.40×10^{-5} s under conditions similar to our experiments. This implies that once the arms are positioned to form stacking interactions, the formation of the short-range stacking interactions is very fast and essentially negligible compared to the timescale for diffusion of the arms or to the overall rate of closing.

Conformational changes of the central Holliday junction. The single Holliday junction that represents the pivot point for the rotational degree of freedom of the switch object could also influence the dynamics. Dependent on the ion concentration Holliday junctions in isolation can assume multiple conformations: an open conformation at low salt conditions and two stacked conformations at high salt conditions [262, 263]. While there are several studies on the kinetics of the conformational transitions between the two possible stacked conformations of a Holliday junction [262, 264], to the best of our knowledge there exist no experimental rate constants for the transition between the open and the stacked conformations. However, MD simulations yielded transition times in the $\sim \mu$s regime, which again is much faster than the timescales for diffusional motion or overall closing and suggests that the structural dynamics of the Holliday junction are not a rate limiting factor [265, 266].

5.5.2 Supplementary Figures

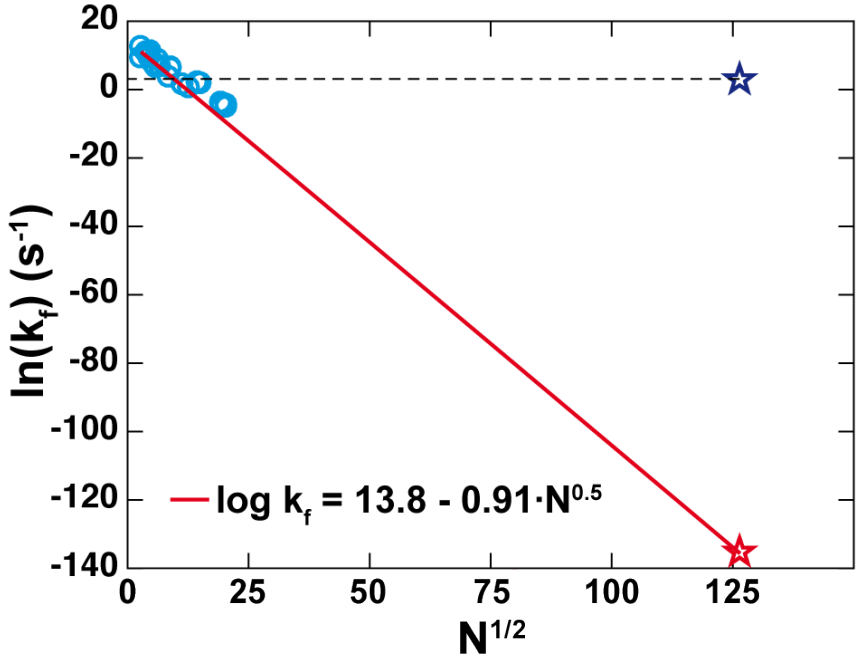

Figure 5.3: Scaling relationship for nucleic acid folding rate constants. Experimentally determined folding rate constants of a range of RNA molecules (cyan circles) as a function of the square root of the number of nucleotides and the corresponding fit of a scaling relationship using $ln(k_{fold}) = ln(k_0) - aN^b$ with a, b, and k_0 as fit parameters; both the data and the fit are from Hyeon *et al.* [267]. The red star indicates the folding rate constant predicted for the switchD16 device by the fitted scaling relationship. In contrast, the blue star corresponds to the experimentally determined folding rate constant for the transition of switchD16 from the open to the closed state at 15 mM $MgCl_2$.

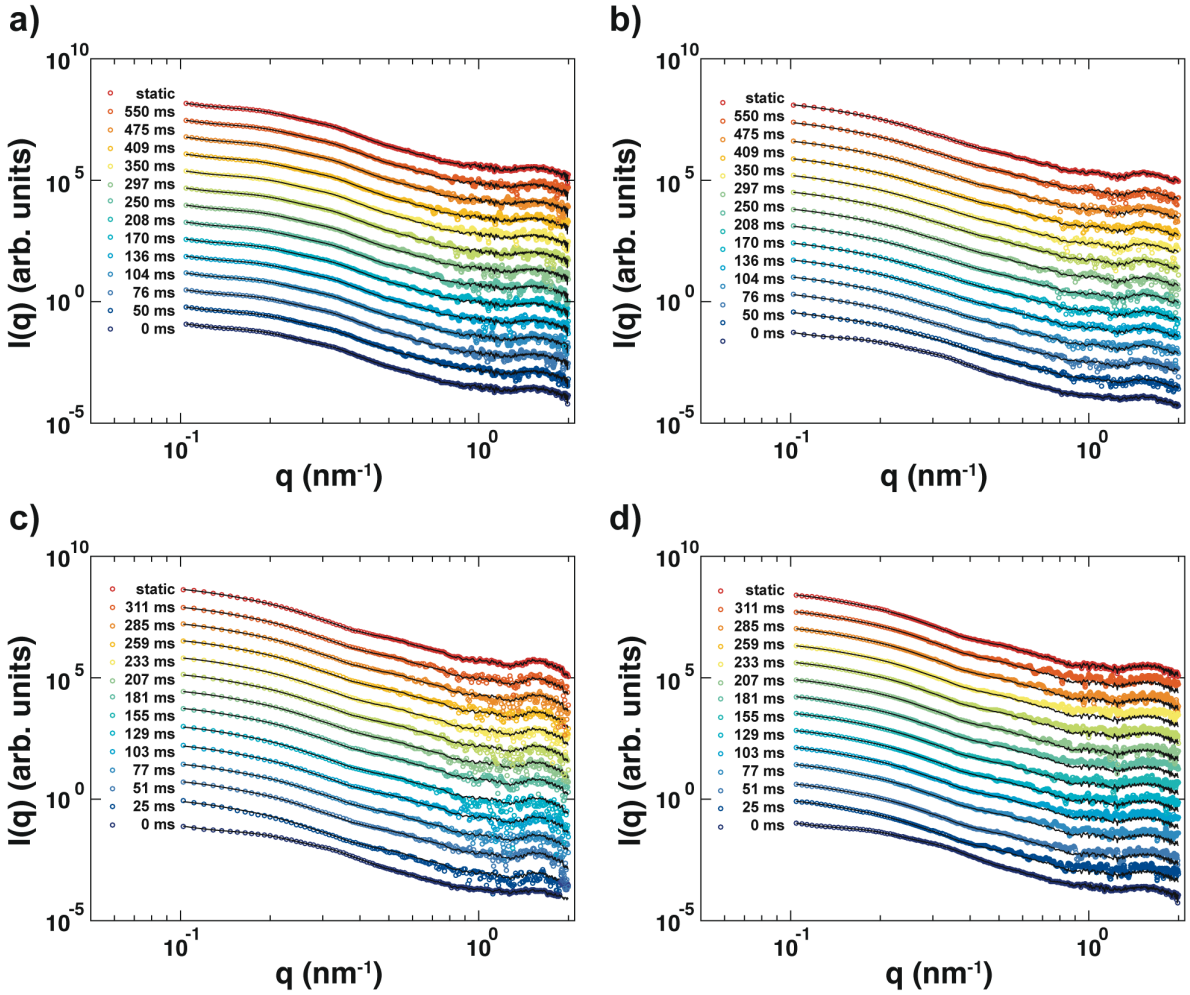

Figure 5.4: Time-dependent scattering profiles for switchD16 and two-state fits. Time-dependent scattering profiles of switchD16 samples upon mixing with varying $MgCl_2$ concentrations and corresponding fitted profiles from a two-state model (black lines) (see main text). **a** Evolution of scattered intensity upon equimolar mixing of switchD16 samples with 5 mM $MgCl_2$ at different time points indicated in the legend. SAXS curves at the bottom (dark blue circles) and at the top (red circles) correspond to static reference profiles of switchD16 samples at the initial and final $MgCl_2$ concentrations (here: 5 mM). **b** Scattering profiles for switchD16 samples diluted into a final concentration of 15 mM $MgCl_2$ at subsequent timepoints acquired after mixing. SAXS profiles at the bottom (dark blue circles) and at the top (red circles) are obtained from static SAXS measurements of switchD16 samples diluted in 5 mM and 15 mM $MgCl_2$, respectively. **c** Scattering profiles of switchD16 samples diluted into a final concentration of 25 mM $MgCl_2$ buffer. SAXS profiles at the bottom (dark blue circles) and at the top (red circles) are obtained from static SAXS measurements of switchD16 samples diluted in 5 mM and 25 mM $MgCl_2$, respectively. **d** Time-dependent SAXS data obtained from switchD16 samples after equimolar mixing with $MgCl_2$ buffer resulting in a final concentration of 35 mM $MgCl_2$. SAXS curves at the bottom (dark blue circles) and at the top (red circles) are obtained from static SAXS measurements of switchD16 samples diluted in 5 mM and 35 mM $MgCl_2$, respectively. Data are vertically offset for clarity. Data from trSAXS experiments with final $MgCl_2$ concentrations of 5 and 35 mM after mixing contain twice the number of data points as compared to the 15 and 25 mM $MgCl_2$ data due to interpolation to the q-bin size of static reference profiles, which where recorded with half of the bin size as stopped-flow SAXS experiments

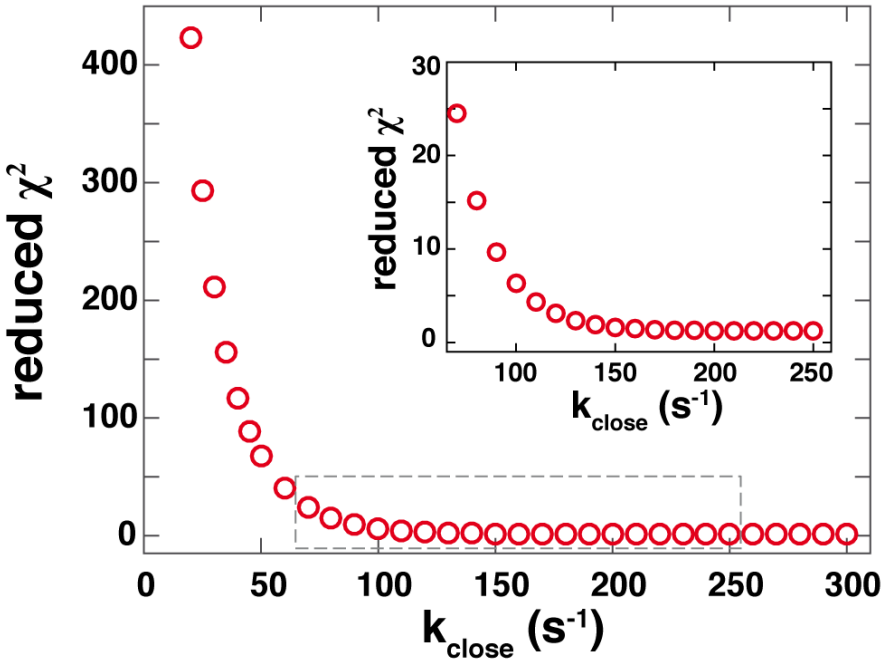

Figure 5.5: Estimate of the closing reaction rate constant of SwitchD16 particles for a final $MgCl_2$ concentration of 25 mM after mixing. We used Equation 5.4 and calculated the reduced χ^2–value for different closing rate constants while setting the opening rate constant to zero (as at a $MgCl_2$ concentration of 25 mM the closed fraction in equilibrium is ~ 98%, suggesting that the opening rate constant is essentially negligible). The data are well described for k_{close} values equal or greater ~ 150 s^{-1} (see inset graph corresponding to the data range indicated by the grey frame). We found an identical trend for the 35 mM $MgCl_2$ data.

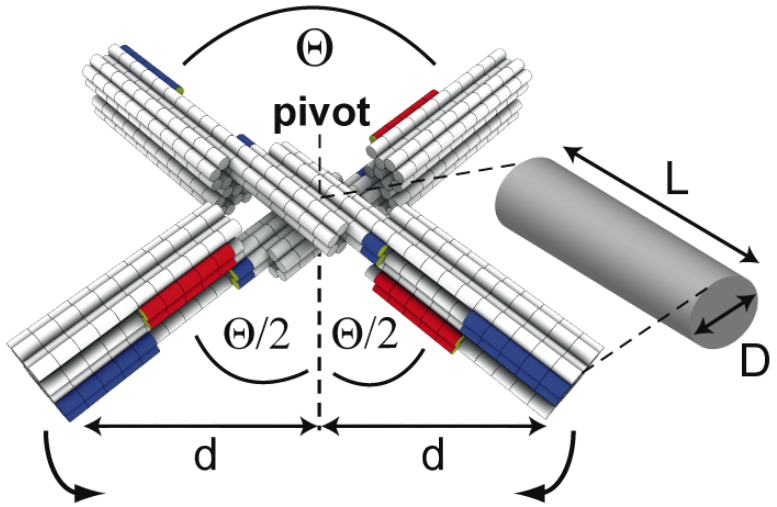

Figure 5.6: Schematic model and length scales to estimate the diffusion time of each arm of switchD16 required to changing from the open conformation (shown here) to the closed conformation.

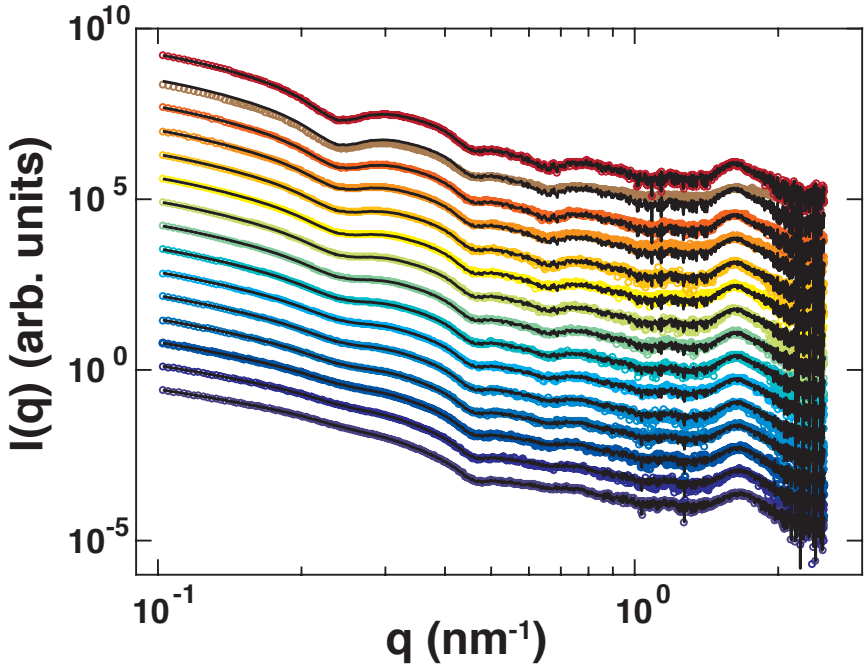

Figure 5.7: Time evolution of scattering profiles from DNA origami dimerization kinetics after 1:1 mixing of monomeric brick samples at a initial concentration of 100 nM: 0 min (dark blue circles, bottom), 2 min, 5 min, 10 min, 15 min, 20 min, 30 min 45 min, 60 min, 90 min, 2 h, 3 h, 4 h 30 min, 12h 30 min and 24 h (red circles, top). Black lines correspond to fits from a two-state model following Equation 5.1.

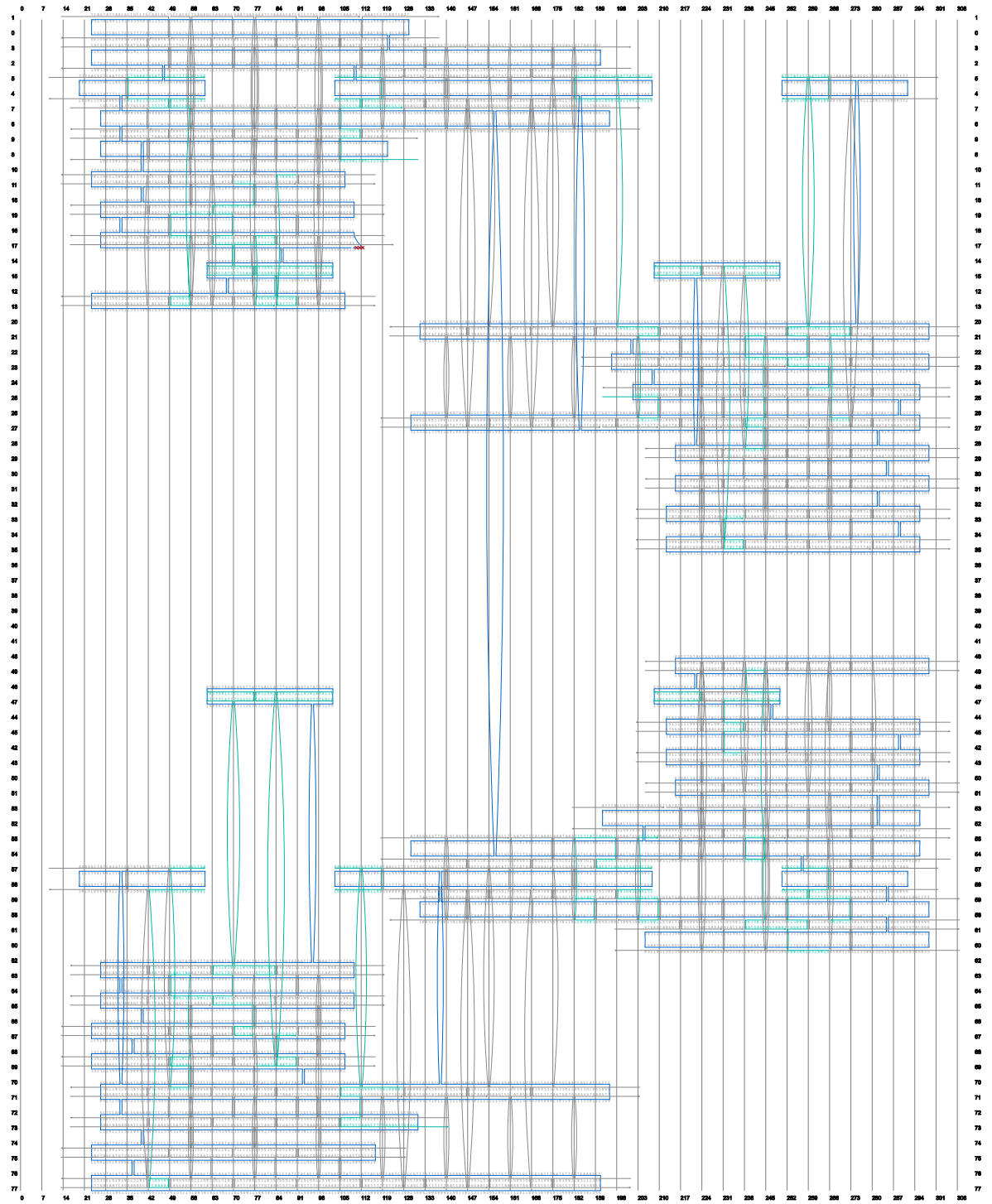

Figure 5.8: Strand diagram of the dynamic switchD16 variant. Scaffold (shown in blue) and staple layout of the dynamic switch variant with 16 activated stacking interactions. Cyan: stacking activated. Generated with caDNAno v0.2.

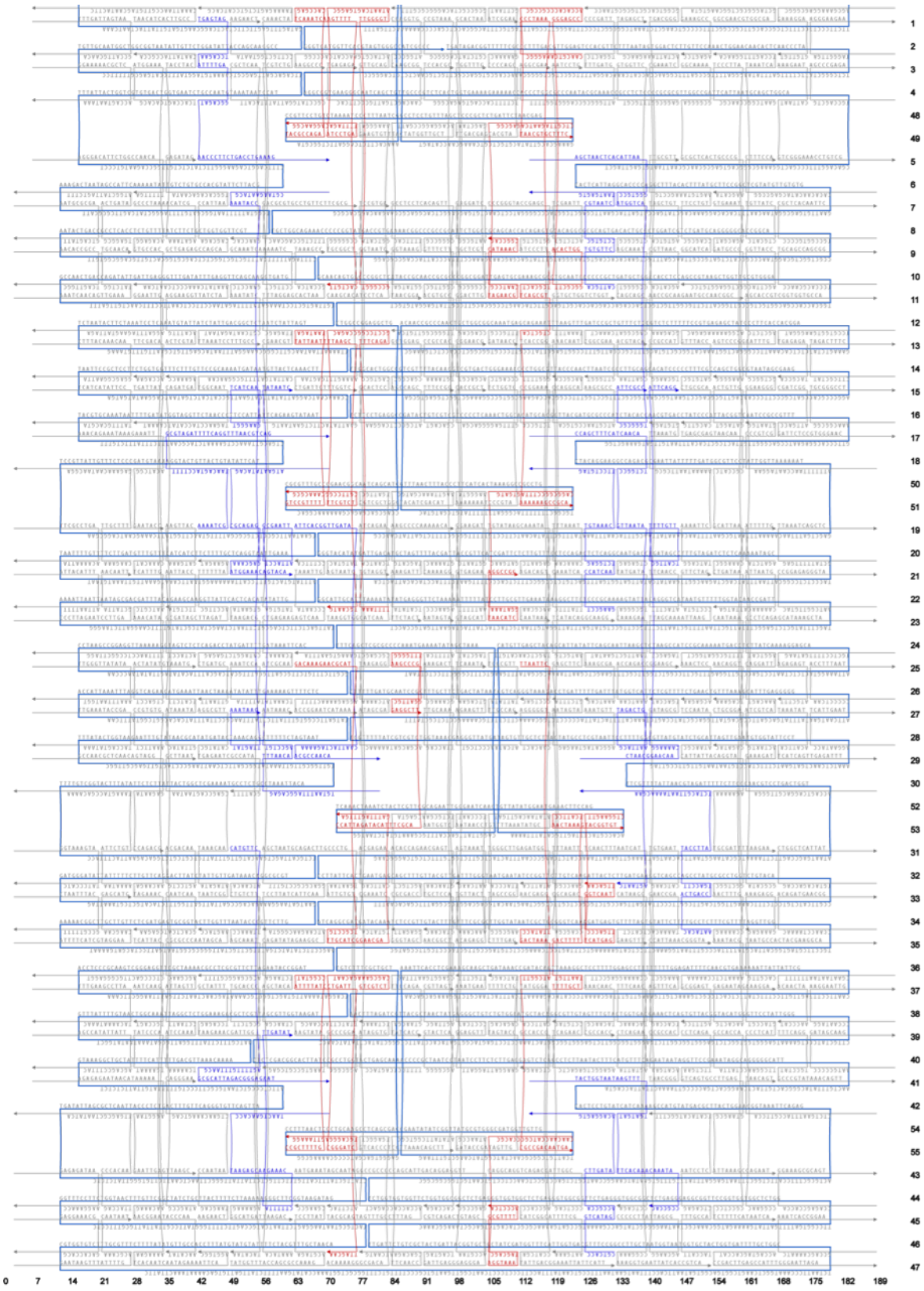

Figure 5.9: Stand diagram of brick monomer A_1 generated with caDNAno v0.2.

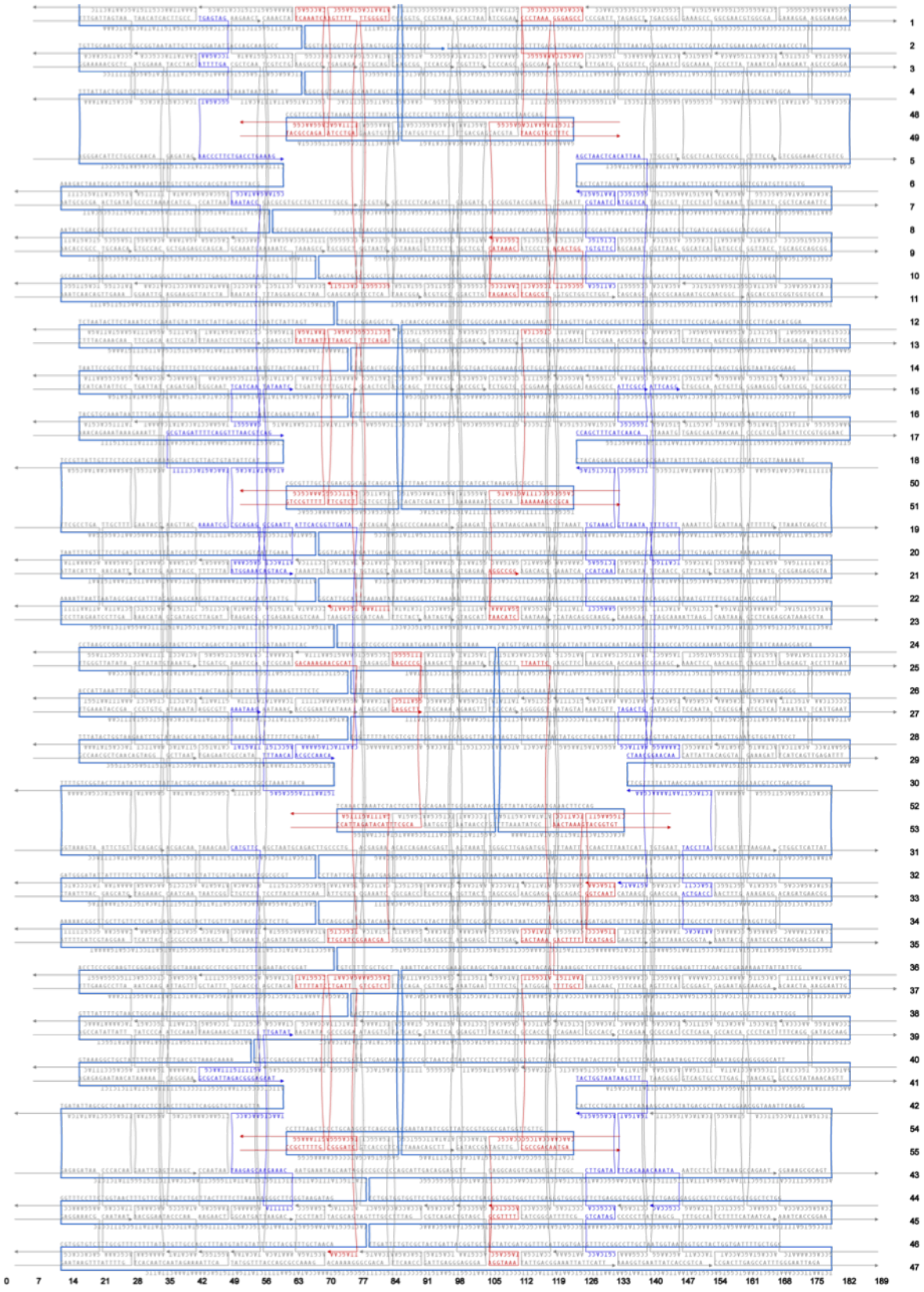

Figure 5.10: Stand diagram of brick monomer A_2 generated with caDNAno v0.2.

Chapter 6

Tracing Dimerization Kinetics of DNA Origami Bricks for Varying Solution Conditions by SAXS

Summary

In chapter 5 a DNA origami brick system that consists of two monomeric brick variants featuring shape-complementary double helical patterns allowing for dimerization was introduced. Dimer assembly and disassembly can be triggered by cation concentration and solution temperature. However, quantitative experimental characterization of the temporal dynamics for varying solution conditions is currently missing. Here, we employ time-resolved SAXS to study the dimerization kinetics of the DNA origami brick system as a function of monomer concentration, salt, and temperature using time-resolved small-angle X-ray scattering based on manual mixing. The results implicate structural deformations of the internal honeycomb lattice structure of monomeric and dimeric DNA origami brick objects in response to changes in ionic strength and ion species. We find concentration dependent dimerization kinetics proceeding on much slower timescales than the diffusion limit. In addition, we observe faster dimer assembly kinetics in the presence of monovalent ions compared to divalent ions, while a change in temperature yields only minor effects on the temporal dynamics.

6.1 Introduction

The rapidly advancing field of structural DNA nanotechnology has allowed for creating versatile structures at the nanometer scale that show great promise for a variety of applications such as nano-engineering [268, 269], material science [145, 270] or drug delivery systems in cancer therapy [213, 271]. A fundamental challenge of DNA nanotechnology is to design even larger DNA objects ($\sim \mu$m) with high spatial control and addressability. These superstructures can facilitate protein crystallography, where 3D DNA origami lattices enable to host and orient many copies of a molecule, such as proteins or nanoparticles, without the need for the often cumbersome process of protein crystallization. In addition, they are promising candidates for

synthetic nanomachines that can mimic macromolecular machines and carry out biological functions.

Molecular self-assembly with scaffolded DNA origami, where a long single-stranded viral genome (scaffold strand) is folded into predefined shapes by hundreds of short synthetic oligonucleotides (staple strands), has become an established method towards this goal. The attainable global dimensions of the resulting DNA origami structures are currently limited by the length of the scaffold strand (~7000 - 8000 bp). Recently, different strategies for scaling up DNA origami size have been suggested, including the use of longer scaffolds [272] or selective structural connections such as sticky-ends [152] to connect individual DNA origami components. These approaches still face some obstacles, such as low assembly yields, loss of unique addressability and preservation of structural integrity.

A promising approach towards designing larger complex DNA origami nanostructures is to employ nucleobase stacking interactions for assembly. This was first presented by Woo *et al.* [273] creating planar 2D DNA origami patches on a surface. Gerling *et al.* [112] established a framework for robust 3D DNA origami objects that exhibit discrete double helical interfaces of shape-complementary protrusions and recessions that can precisely click into each other based on nucleobase stacking interactions. The mechanism was illustrated for a dynamic DNA origami switch device, whose structural properties and dynamics are discussed in chapter 4 and chapter 5. In addition, they designed self-complementary multilayer DNA origami objects that can form more complex structures as recently demonstrated for a nanoscale rotary apparatus [274] or assemble into rigid micron-scale filament architectures [112].

For the multilayer objects, the subunits are formed by two different DNA origami brick variants with shape-complementary patterns that fit precisely into each other (Figure 6.1a). Brick assembly and disassembly can be triggered by changes in ionic strength or temperature, similar to the DNA origami switch device (see chapters 4, 5). However, quantitative experimental characterization of the temporal dynamics in solution is currently lacking. Particularly, how global parameters such as cation valency or temperature influence the dimer assembly kinetics of DNA origami bricks. Here, we study the dimerization kinetics of DNA origami brick objects as a function of monomer concentration, salt, and temperature using time-resolved small-angle X-ray scattering based on manual mixing. Previous work [112] could show that dimerization is possible in the presence of both monovalent and divalent ions as well as at elevated temperatures. We performed time-resolved SAXS measurements on brick dimer assembly in the presence of 20 mM $MgCl_2$ and 2 M NaCl, respectively, and at temperatures of 20 °C and 40 °C. In addition, we investigated whether DNA origami brick samples show structural changes for varying solution conditions based on static SAXS experiments of monomeric and dimeric DNA origami bricks.

6.2 SAXS reveals salt dependent structural characteristics of DNA origami brick samples

The brick system includes two different monomeric variants (A_1 and A_2), where in each variant either double helical protrusions or recessions are permanently deactivated to inhibit further polymerization, respectively (Figure 6.1a). For structural characterization, we analyzed scattering data of DNA origami brick monomers and dimers in the presence of $MgCl_2$ or NaCl and

at two different temperatures, which also serve as reference profiles for time-resolved SAXS studies on dimerization kinetics. For solution conditions containing either 20 mM $MgCl_2$ or 2 M NaCl, scattering profiles of monomeric and dimeric brick samples are clearly distinguishable (Figure 6.1b). SAXS curves of the dimeric complex exhibit a very pronounced peak at a momentum transfer value $q \approx 0.28$ nm^{-1} corresponding to a length scale $d = 2\pi/q \approx 23$ nm, which can be attributed to the cross-section of the dimer (22 nm x 24 nm) (Figure 6.1a). This peak is missing in both monomeric profiles, due to their asymmetric cross sectional area (11 nm x 24 nm) (Figure 6.1a). However, for higher q-values, corresponding to smaller length scales, the scattering profiles of brick monomers and dimers largely coincide, reflecting their identical internal honeycomb lattice structure. For instance, a highly pronounced intensity peak is noticeable at $q \approx 1.6$ nm^{-1} (d $\approx$ 3.9 nm) matching interhelical distances within the honeycomb lattice. In contrast to the SAXS profiles of brick samples dissolved in 20 mM $MgCl_2$, the 2 M NaCl data display a higher noise level due to the 100 fold higher ion concentration resulting in a stronger reduction in contrast. This effect is attributed to the quadratic relation between scattering intensity and the difference in electron density between sample and buffer solution.

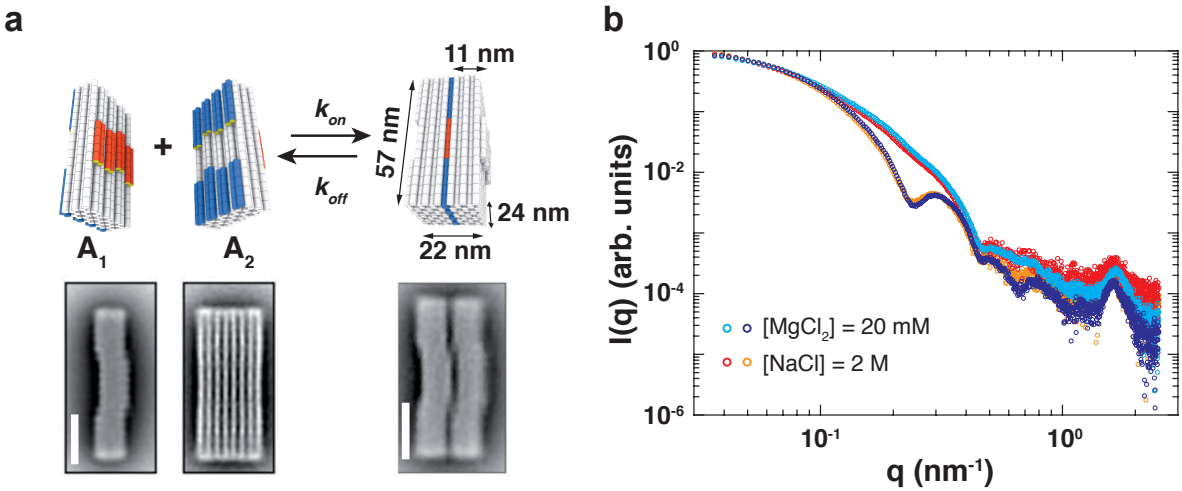

Figure 6.1: Schematic of the DNA origami brick system and corresponding SAXS profiles in the presence of 20 mM $MgCl_2$ and 2 M NaCl. **a** Illustration of DNA origami brick monomer variants (A_1 and A_2) that can form a dimeric complex in the presence of 20 mM $MgCl_2$ or 2 M NaCl (top). Shape-complementary protrusions and recessions, indicated by the red and blue DNA double helical domains, respectively, allow for nucleobase stacking interactions. (Bottom) TEM micrographs of brick monomers and dimers. Scale bar: 20 nm. **b** Static SAXS profiles of monomeric brick samples (only A_1) measured in 20 mM $MgCl_2$ (cyan) and 2 M NaCl (red) and SAXS data from brick dimers (A_1 + A_2) in the presence of 20 mM $MgCl_2$ (blue) and 2 M NaCl (orange). Sample concentrations are 100 nM. Profiles are scaled by a constant factor.

Next, we analyzed the influence of the ion species, ion concentration and temperature on the DNA origami brick structure based on SAXS data. The structure and dynamics of double-stranded DNA are known to be highly influenced by their environment, i.e. salt or temperature [53, 275–277]. A few reports have shown that also DNA origami objects may differ from their idealized internal geometries and do not necessarily exhibit the same properties as DNA (see also chapter 4) [2, 156, 157, 207, 232, 233, 278]. For instance, DNA origami junctions are known to be under mechanical stress, associated with an average intrahelical distance that is larger than the one in a B-DNA duplex [232]. Further, electrostatic repulsion between the

negatively charged phosphate atoms in the DNA backbone along with entropic effects can generate a bowing out of double helical domains between cross-overs [207], which has also been discussed in chapter 4. These internal structural changes might also be affected by salt concentration and temperature, and are crucial for nucleobase stacking interactions where a correct helical alignment of participating double helices is a key prerequisite.

Scattering profiles of brick monomer variant A_1 dissolved in 20 mM $MgCl_2$ exhibit no identifiable temperature dependency, which is also observable in the presence of 2 M NaCl (Figure 6.2). However, for both salt conditions we find smaller radii of gyration (R_g) for monomeric brick samples at a temperature of 40 °C compared to 20 °C, where a rational explanation remains tentative and will require additional measurements for verification. When the $MgCl_2$ concentration was changed to 5 mM, only minor shifts of intensity peaks towards smaller q-values are observable. For instance, the intensity peak at $q \sim 1.6$ nm^{-1} (Figure 6.2a), which is related to distances within the honeycomb lattice, is shifted by $\Delta q \sim 0.5$ Å towards a smaller q-value, implying an increase of interhelical distances by $\sim$ 1 Å, consistent with previous studies from Fischer *et al.* [156]. This effect is even more pronounced for monomeric brick samples measured in the presence of 2 M and 0.5 M NaCl, where the shift of the intensity peak at $q \sim 1.6$ nm^{-1} results in an increase in interhelical distances by $\sim$ 2.5 Å (i.e. from 3.9 nm (2 M NaCl) to 4.1 nm (0.5 M NaCl)). For both salt conditions, the reduced ionic strength associated with an increase in the Debye length (by a factor of two for both salts) reflects the lower screening ability of the electrostatic repulsion between negatively charged phosphate groups resulting in larger interhelical distances.

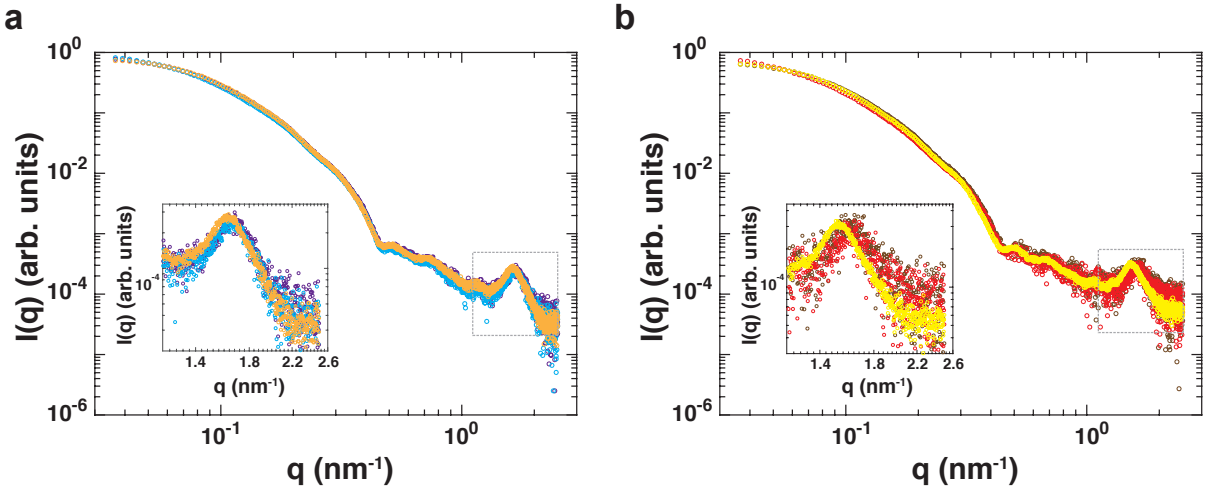

Figure 6.2: Scattering profiles of monomeric DNA origami bricks for different solution conditions. **a** SAXS curves of monomeric bricks (c = 100 nM) dissolved in 20 mM $MgCl_2$ at temperatures of 20°C (cyan) and 40°C (purple), and for a $MgCl_2$ concentration of 5 mM (brick concentration c = 200 nM) at a temperature of 20°C (orange). The inset shows a close up of the intensity peak related to interhelical distances within the honeycomb lattice of the DNA origami bricks. **b** SAXS profiles of monomeric bricks (c = 100 nM) dissolved in 2 M NaCl at temperatures of 20°C (red) and 40°C (brown), and for a NaCl concentration of 0.5 M (brick concentration c = 200 nM) at a temperature of 20°C (yellow). The inset corresponds to a zoom in of the area indicated by the grey lines and includes the intensity peak related to interhelical distances within the honeycomb lattice of the DNA origami bricks.

We obtained a smaller radius of gyration (R_g) for brick monomers dissolved in 5 mM $MgCl_2$ than for monomers dissolved in 20 mM $MgCl_2$ (Table 6.1). The brick monomer concentration was 200 nM at 5 mM $MgCl_2$, which is twice as high as for 20 mM $MgCl_2$ measurements. Thus, a reduction in the R_g presumably results from interparticle interference effects due to repulsive interactions between brick objects (see section 1.3.1 in chapter 1), which become more dominant at lower $MgCl_2$ concentrations and higher sample concentrations. Similar results were obtained from NaCl data (Table 6.1). In general the calculated R_g-values seem reasonable in comparison to theoretical values derived from approximating the monomeric brick objects as rectangular beams ($R_g^{theo} = \frac{1}{3}\left[(\frac{W}{2})^2 + (\frac{H}{2})^2 + (\frac{L}{2})^2\right]^{\frac{1}{2}}$, where W, H and L are the width, height and length of the object, respectively). Here, the R_g-values are in the range of 18-19 nm depending on the diameter used for a DNA double helix, which can vary between 2-2.6 nm [279], but which does not include any salt effects.

In comparison to the $MgCl_2$ data, both internal and overall dimensions of DNA origami bricks are extended by a few Ångstroms in the presence of NaCl suggesting a lower screening ability for monovalent ions.

Structural analysis of brick dimers at lower salt concentrations was not possible, as these structures would disassemble. Scattering profiles of dimeric brick samples for temperatures of 20°C and 40°C revealed no clearly identifiable differences (see Figure 6.8 in section 6.6), for both 20 mM $MgCl_2$ and 2 M NaCl, implying no evidence for disassembly, which is in line with previous work [112]. As already observed for the monomeric brick samples, we find smaller R_g-values for brick dimers at a temperature of 40°C (Table 6.1), which needs to be clarified in future experiments.

Sample	**R_g (nm) (T = 20°C)**	**R_g (nm) (T = 40°C)**	**R_g^{theo} (nm)**
Brick monomer	-	-	18.0-19.2
Brick dimer	-	-	19.0-20.4
Brick monomer ([$MgCl_2$] = 5 mM)	18.3	-	-
Brick monomer ([$MgCl_2$] = 20 mM)	20.0 (± 0.2)	19.4 (±0.3)	-
Brick dimer ([$MgCl_2$] = 20 mM)	22.5 (± 0.1)	20.8 (± 0.1)	-
Brick monomer ([NaCl] = 0.5 M)	19.7	-	-
Brick monomer ([NaCl] = 2 M)	22.3 (± 0.0)	19.5 (± 0.0)	-
Brick dimer ([NaCl] = 2 M)	24.8 (± 0.2)	22.5 (± 0.8)	-

Table 6.1: Comparison of the radius of gyration (R_g) of monomeric and dimeric brick samples at sample concentrations of 100 nM dissolved in different $MgCl_2$ and NaCl concentrations at ambient temperatures of 20°C and 40°C. For monomeric brick samples dissolved in 5 mM $MgCl_2$ and 0.5 M NaCl sample concentrations were 200 nM. For Guinier analysis the fitting range $q_{max}R_g < 1.6$ was used. Theoretical R_g-values were determined by approximating the brick objects as rectangular beams (see main text for details) with dimensions given in Figure 6.1a.

6.2.1 Comparison of experimental SAXS data to theoretical scattering profiles

We compared our experimental scattering data of monomeric and dimeric DNA origami brick samples to their corresponding theoretical scattering profiles based on idealized atomistic models generated by *CanDo* [228] (see Materials and Methods (6.5)). Double helical protrusions and recessions were missing in the atomistic models, which should have only a minor impact on the computation of the theoretical SAXS profile. The computed profiles roughly describe the overall shape of the experimental SAXS curves reproducing structural characteristic peaks, including the specific dimer peak ($q \approx 0.28$ nm^{-1}) and the peak related to the internal honeycomb lattice structure (Figure 6.3).

However, the theoretical curves are shifted towards higher q-values (corresponding to smaller dimensions), which has also been observed for DNA origami structures discussed in chapter 4. Moreover, we obtain smaller R_g-values for monomeric (R_g = 16.5 nm) and dimeric brick samples (R_g = 17.6 nm) from the theoretical SAXS data than from experimentally derived values. Combined, these differences suggest that the conformations of the DNA origami brick objects in solution deviate from the atomistic models generated by *CanDo*. Structural refinement approaches, as presented in chapter 4 would allow for determining structural deformations and flexibility in more detail.

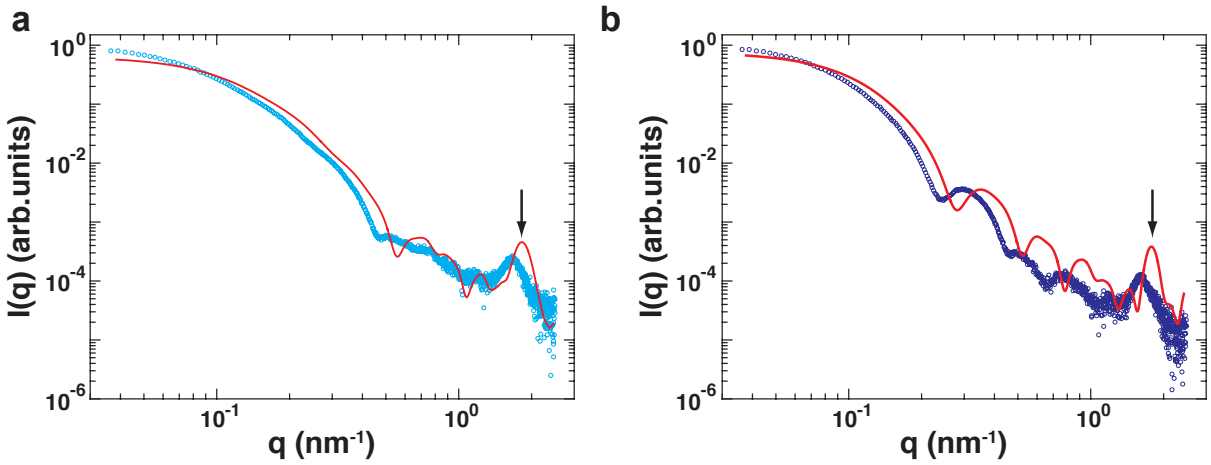

Figure 6.3: Comparison of scattering profiles of DNA origami bricks and theoretical scattering profiles obtained from the software *CRYSOL* based on their atomistic models. **a** Experimental SAXS profile of the monomeric DNA origami brick sample dissolved in 20 mM $MgCl_2$ (cyan circles) and theoretical scattering profiles (red line) of the corresponding atomistic model that were predicted from the software *CanDo*. **b** Experimental SAXS profile of the dimeric DNA origami brick sample dissolved in 20 mM $MgCl_2$ (blue circles) and theoretical scattering profiles (red line) of the corresponding atomistic model that were predicted from the software *CanDo*. Arrows indicate the q-value corresponding to internal distances within the honeycomb lattice structure of the DNA origami brick objects.

6.3 Dimerization kinetics of DNA origami bricks

In the previous section essential structural features of DNA origami brick samples were characterized for varying solution conditions. Here, we studied the dimerization kinetics of the DNA origami brick system as a function of initial monomer concentrations (i.e. 50 nM and 100 nM), ion species (i.e. 20 mM $MgCl_2$ and 2 M NaCl) and temperature (i.e. 20°C and 40°C) using time-resolved SAXS based on manual mixing (see Materials and Methods (6.5)).

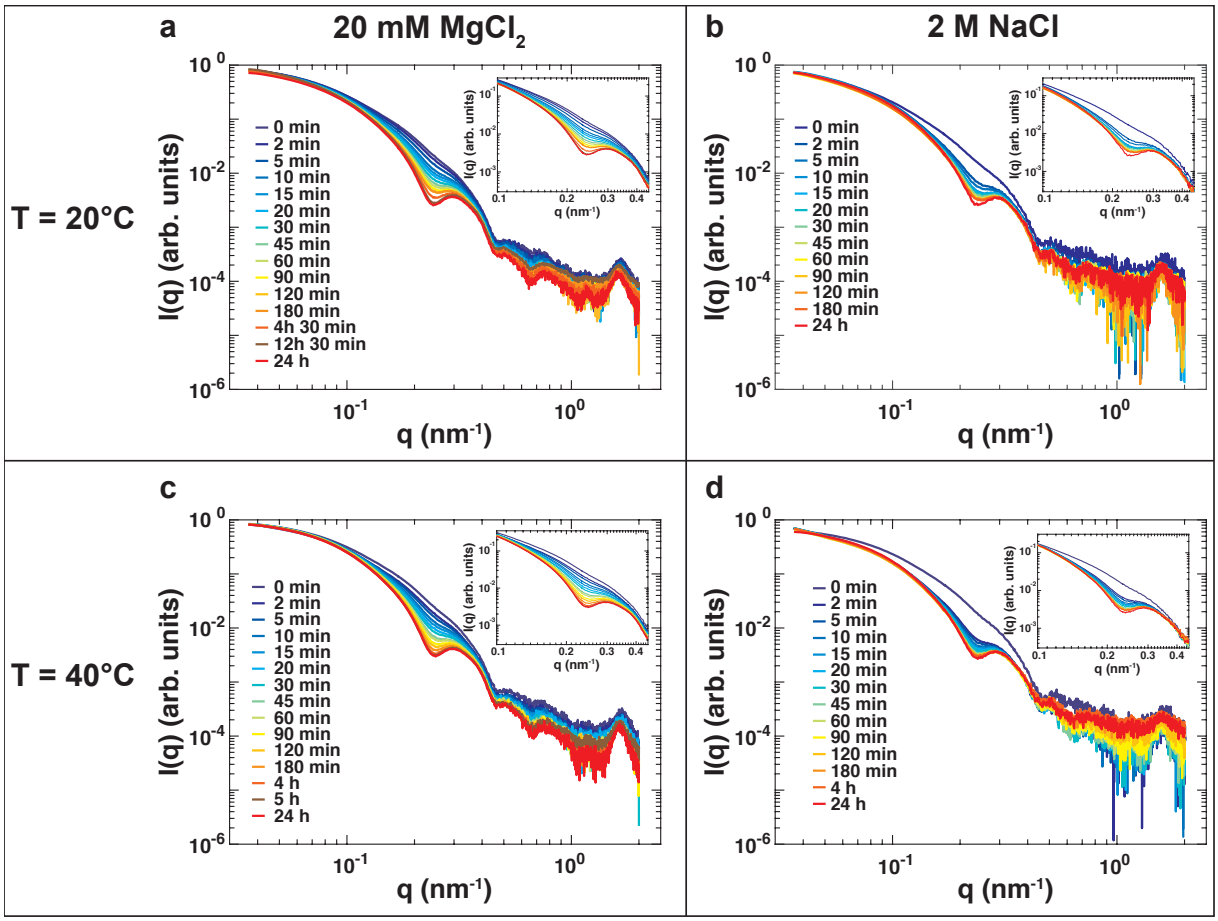

Figure 6.4: Representative scattering profiles of DNA origami brick dimerization kinetics for varying solution conditions. **a** Time evolution of scattering profiles after 1:1 mixing of monomeric brick samples at an initial concentration of 100 nM each dissolved in 20 mM $MgCl_2$ and a temperature of 20°C. **b** Time-resolved scattering profiles after 1:1 mixing of monomeric brick samples at an initial concentration of 100 nM each dissolved in 2 M NaCl and a temperature of 20°C. **c** Time evolution of scattering profiles for sample conditions described in **a** but at a temperature of 40°C. **d** Time evolution of scattering profiles for sample conditions described in **b** but at a temperature of 40°C. Scattering profiles for t = 0 min correspond to static SAXS profiles of monomeric brick samples for each measurement condition.

Representative time courses of scattering profiles of brick dimerization in the presence of 20 mM $MgCl_2$ and a temperature of 20°C (Figure 6.4a) reveal a continuously increasing dimer peak at $q \approx 0.28$ nm^{-1}. SAXS curves of brick dimerization kinetics in the presence of 2 M NaCl display a similar time evolution. However, an fast change of the intensity profiles from t = 0 min to t = 2 min is observable in the 2 M NaCl data, which is not noticeable in the 20 mM $MgCl_2$ data suggesting faster dimerization kinetics in the presence of monovalent ions. This effect is

even more pronounced for time courses of scattering profiles from brick dimerization kinetics in the presence of 2 M NaCl and a temperature of 40°C (Figure 6.4d). In contrast, corresponding scattering profiles for brick dimerization kinetics in the presence of 20 mM $MgCl_2$ still display a rather continuous time course (Figure 6.4c). In comparison to the scattering data obtained at T = 20°C, we find no significant deviations of SAXS profiles acquired at T = 40°C, implying no disassembly due to the higher temperature, in line with previous work [112].

6.3.1 Singular value decomposition

To test whether the brick dimer assembly is well-described by a two-state process or whether there are detectable intermediate states, we performed a singular value decomposition (SVD) analysis of the time-resolved data for each measurement condition (see Materials and Methods (6.5)). In this method the scattering profile at each time point is represented by a different linear combination of a set of orthogonal basis functions. To apply a SVD, time-dependent scattering profiles are compiled into a matrix, *A(q,k)*, where the rows correspond to different momentum transfer values q_i and the columns are the intensity profile for a certain timepoint denoted by the index k (i.e. $A(q,k) = I(q, t_k)$). The matrix A is decomposed into a set of orthogonal basis functions [280]:

$$A(q,k) = u(q,k)sv^T \tag{6.1}$$

For N discrete q-values and k time points, A is an $N \times K$ matrix. The columns of the $N \times K$ matrix *u(q,k)* are the orthogonal basis functions $U_k(q_i)$, where a linear superposition of these functions describes the scattering profile at each timepoint. The diagonal components of the $K \times K$ matrix s contain the so-called singular values (w_k), which are ordered such that $w_1 \geq w_2 \geq w_3 \geq \ldots \geq w_k$. The product sv^T determines the time-dependent weight applied to the individual basis functions when constructing the scattering profiles. The scattering profile at each time point during dimerization can be approximated by [280]:

$$I(q,t_k) = \sum_{j=1}^{L} w_j v_{kj} U_j(q) = \sum_{j=1}^{L} w_j b_j^k U_j(q) \tag{6.2}$$

where L is the minimum number of components necessary to adequately reconstruct the scattering profiles and $b_j^k = v_{kj}$ describe the basis coefficient j at each time-point.

The number of significant SVD components reveals the number of distinct conformational states involved in the DNA origami brick dimerization process. In order to determine the number of significant components, we followed the selection criteria of Henry *et al.* [281], which employ the noise level in the basis functions (*U(q)*), the size of the singular values (S_i) and computation of the autocorrelation of basis functions (C_i) to identify the set of linear independent basis functions (see Materials and Methods (6.5)). Figure 6.5 displays the first four basis components *U(q)* obtained from the SVD of the scattering data for dimerization kinetics upon 1:1 mixing of DNA origami brick monomers (c = 100 nM) in the presence of 20 mM $MgCl_2$ or 2 M NaCl (T = 20°C). Comparison of the shape of the basis functions suggests that only the first two components contain significant signal. This finding is corroborated by the values of the weighted singular values (S_i), which are $< 10^{-2}$ for the last two components, and the values of the autocorrelations which are >90% only for the first two components.

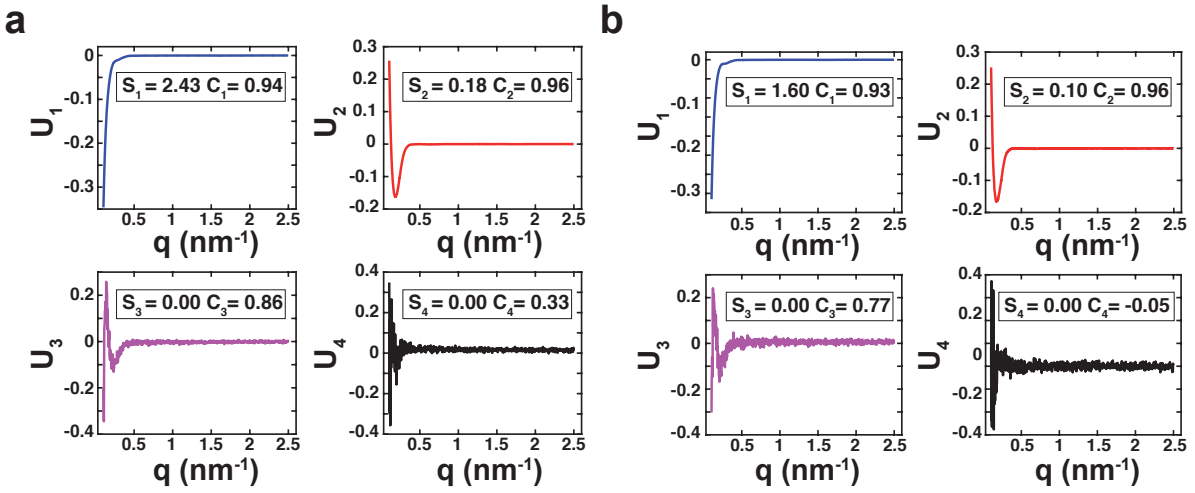

Figure 6.5: The first four basis functions $U_i(q)$ from an SVD of time-resolved SAXS data of DNA origami brick dimerization kinetics. S_i are the weighted singular values and C_i denotes the autocorrelation (see main text for details).

Similar results were obtained for dimerization kinetics of brick samples with initial monomer concentrations of 50 nM and at a temperature of 40°C. Description of the dimerization process of DNA origami bricks by two independent states (i.e. monomeric and dimeric conformation) is consistent with a bimolecular reaction system, as a third or fourth component corresponding to physically phenomena as the existence of an intermediate state [282] or interparticle interference effects [283] are very unlikely. An intermediate state seems very improbable due to geometrical constraints and interparticle interference effects such as repulsion were not observed in any of the measurement conditions for SAXS measurements on dimerization kinetics.

6.3.2 Two-state model fits

Based on the results obtained from the SVD analysis we applied a two-state model to the brick dimerization SAXS data, where the SAXS profile at each time point is described by a linear superposition of the monomeric and dimeric brick scattering profiles (see Materials and Methods (6.5)). The two-state fits provide an overall good description of the experimental data for dimerization kinetics in the presence of 20 mM $MgCl_2$ or 2 M NaCl at a temperature of 20°C (Figure 6.6) with reduced χ^2-values in the range of 1.0 and 2.0. Similar results were obtained for SAXS measurements on brick dimerization at a temperature of 40°C and for measurements with initial monomer concentrations of 50 nM.

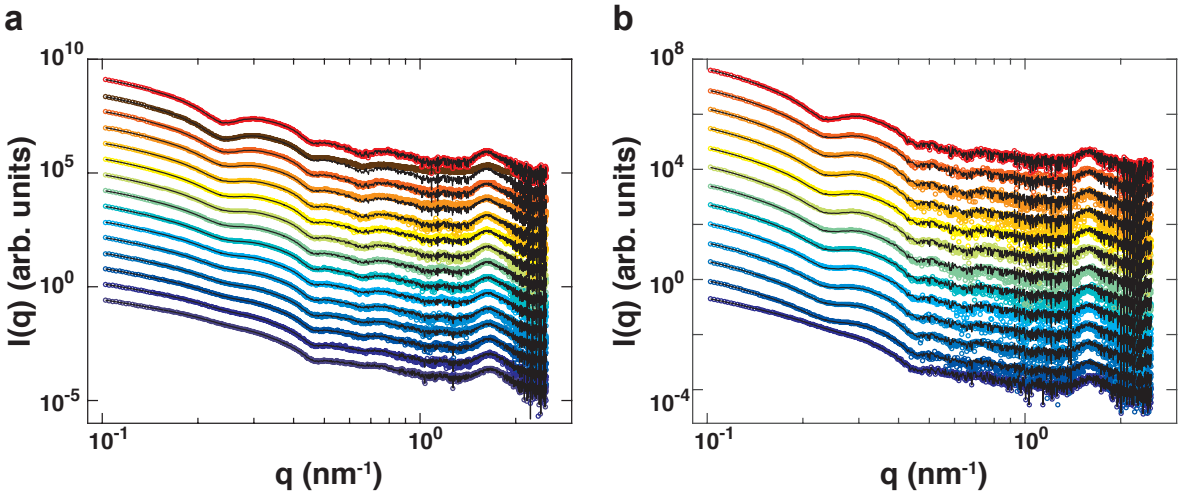

Figure 6.6: Time-dependent scattering profiles of DNA origami brick dimerization kinetics and two-state fits. **a** Evolution of scattered intensity upon 1:1 mixing of DNA origami brick monomers (c = 100 nM) in the presence of 20 mM $MgCl_2$ at a temperature of 20°C for subsequent time points (from blue to red): 0 min, 2 min, 5 min, 10 min, 15 min, 20 min, 30 min, 45 min, 60 min, 90 min, 120 min, 180 min, 4h 30 min, 12 h 30 min and 24 h. Black lines correspond to fitted profiles from a two-state model. **b** Time course of scattering profiles upon 1:1 mixing of DNA origami brick monomers (c = 100 nM) in the presence of 2 M NaCl at a temperature of 20°C for subsequent time points (from blue to red): 0 min, 2 min, 5 min, 10 min, 15 min, 20 min, 30 min, 45 min, 60 min, 90 min, 120 min, 180 min, and 24 h. Black lines correspond to fitted profiles from a two-state model. Data are vertically offset for clarity.

6.3.3 Bimolecular reaction model fit

From the two-state fits we were able to define the fraction of dimers at each measurement time point, which are displayed in Figure 6.7. In order to determine the association- (k_{on}) and dissociation rate constants (k_{off}) of the brick dimerization process, we fitted a bimolecular reaction kinetics model to the data (see Materials and Methods (6.5)). As expected for a bimolecular system, we find concentration dependent assembly kinetics for both salt conditions (Table 6.2). In addition, dimerization kinetics proceed slightly faster at a temperature of 40°C, where the relative change of the association rate constant is slightly larger for brick assembly kinetics in the presence of 20 mM $MgCl_2$ than for 2 M NaCl.

Remarkably, we observe significantly faster dimerization kinetics at 2 M NaCl with a half-life of $\tau_{1/2} \approx 1$ min than at 20 mM $MgCl_2$, where $\tau_{1/2} \approx 10$ min, for T = 20°C. This is still the case for DNA origami brick dimerization in the presence of 1 M NaCl yielding a half-life of $\tau_{1/2} \approx 6$ min (data were obtained from previous SAXS measurements). For dimerization dynamics at a temperature of T = 40°C the half-lives reduce by 10 % and ~ 20 % in the presence of 2 M NaCl or 20 mM $MgCl_2$, respectively.

Moreover, we derive non-negligeable values for the dissociation rate constants for 2 M NaCl (and 1 M NaCl), whereas fit results for 20 mM $MgCl_2$ are insensitive towards the off-rate for $k_{off} \leq 10^{-6}s^{-1}$ (Table 6.2). Thus, the $MgCl_2$ data can be also described by an irreversible bimolecular reaction fit (see Materials and Methods (6.5) and Table 6.2) yielding similar association rate constants, whereas the irreversible fit applied to the NaCl data provides slight deviations for the association rate constants.

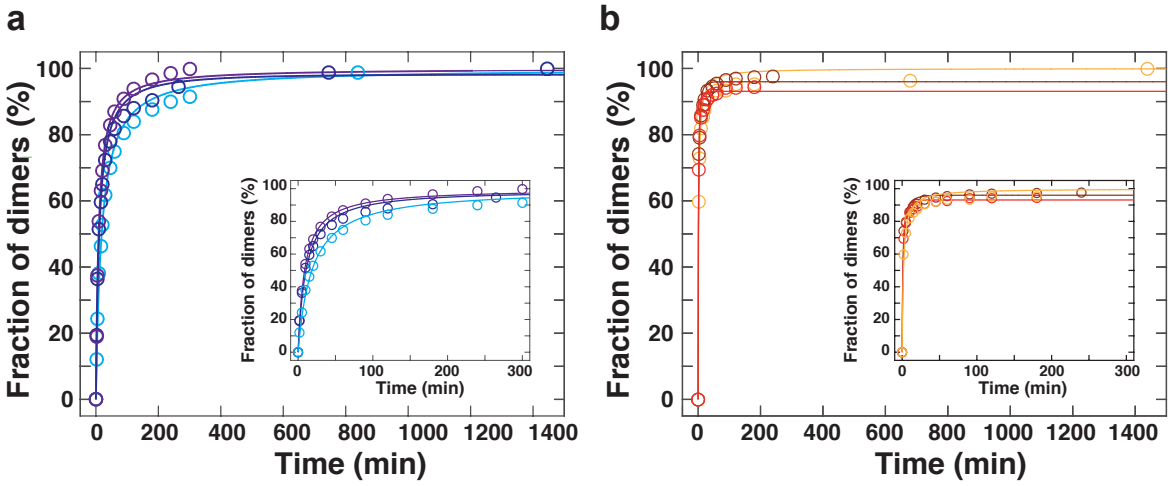

Figure 6.7: Fraction of dimeric DNA origami brick objects as a function of time, determined from a two-state model for varying initial monomer concentrations and solution conditions. **a** Dimer fractions derived from a two-state fit of SAXS data on DNA origami brick dimerization kinetics performed at 20 mM $MgCl_2$ for inital monomer concentrations of 50 nM each (cyan circles), 100 nM each (blue circles) at T = 20°C, and for initial monomer concentrations of 100 nM at T = 40°C (purple circles). Solid lines represent a reversible bimolecular reaction fit to the data. The inset shows a zoom of the data and corresponding fits for a selected time range. **b** Dimer fractions derived from a two-state fit of SAXS data on DNA origami brick dimerization performed at 2 M NaCl for inital monomer concentrations of 50 nM each (orange circles), 100 nM each (red circles) at T = 20°C, and for initial monomer concentrations of 100 nM at T = 40°C (brown circles). Solid lines represent a reversible bimolecular reaction fit to the data. The inset shows a zoom of the data and corresponding fits for a selected time range.

Measurement conditions	$\mathbf{k_{on}(10^{-4} \cdot Ms)^{-1}}$	$\mathbf{k_{off}(10^{5} \cdot s)^{-1}}$	$\mathbf{k_{on}^{irr}(10^{-4} \cdot Ms)^{-1}}$
$[NaCl]$ = 2 M, c_0 = 50 nM, T = 20°C	19.8 (15.9, 23.7)	3.1 (0, 6.4)	18.3 (14.2, 22.5)
$[NaCl]$ = 2 M, c_0 = 100 nM, T = 20°C	16.0 (11.7, 20.3)	8.2 (1, 15)	13.7 (9.1, 18.2)
$[NaCl]$ = 2 M, c_0 = 100 nM, T = 40°C	17.6 (12.6, 22.7)	3.0 (0, 7.4)	16.4 (11.6, 21.1)
$[NaCl]$ = 1 M, c_0 = 80 nM, T = 20°C	3.6 (2.5, 4.8)	1.4 (0, 3.6)	3.4 (2.2, 4.5)
$[MgCl_2]$ = 20 mM, c_0 = 50 nM, T = 20°C	1.8 (1.7, 1.9)	$\leq 10^{-6}$	1.8 (1.7, 1.9)
$[MgCl_2]$ = 20 mM, c_0 = 100 nM, T = 20°C	1.6 (1.4, 1.7)	$\leq 10^{-6}$	1.6 (1.4, 1.7)
$[MgCl_2]$ = 20 mM, c_0 = 100 nM, T = 40°C	1.9 (1.8, 2.0)	$\leq 10^{-6}$	1.9 (1.8, 2.0)

Table 6.2: Reaction rate constants of dimerization kinetics of DNA origami bricks for different salt and temperature conditions. Measurement conditions involve salt concentration, initial concentration c_0 of each brick monomer prior to mixing, and the temperature T. The reaction rate constants k_{on} and k_{off} are derived by fitting a reversible bimolecular reaction rate model (see Materials and Methods (6.5)) to the experimentally determined dimer fractions. For $MgCl_2$ data fit results are insensitive towards the off-rate for $k_{off} \leq 10^{-6}s^{-1}$. k_{on}^{irr} corresponds to a fit of an irreversible bimolecular reaction model. Number in brackets indicate values for a 95% confidence interval.

Combined, these results imply a considerable sensitivity of DNA origami brick dimer formation to the presence of mono- or divalent ions suggesting the existence of salt dependent energy barriers. The existence of energy barriers is further corroborated by calculations of the diffusion-limited reaction rate constant k_{diff} of 2.5×10^8 M^{-1} s^{-1} for the DNA origami brick samples (see Materials and Methods (6.5)), showing that the brick system reacts much slower than the diffusive speed limit. Additional barriers, such as overcoming electrostatic repulsion and correct alignment of shape-complementary protrusions and recessions at the double helical interfaces of the brick monomers required for dimer formation, should result in an effective energy barrier lower than $\ln(k_{on}^{-1}/k_{diff}^{-1})$. For 2 M NaCl we obtained a value of ~7 k_bT and for 20 mM $MgCl_2$ a value of ~9 k_bT, where k_bT is the thermal energy. Moreover, the brick system displays much slower kinetics than the DNA origami switch device ($\tau_{1/2} \sim$ min vs. $\tau_{1/2} \sim$ ms) (see chapter 5). This highlights the accelerating effect of a constrained pre-alignment of shape-complementary interfaces, as it is realized in the switch device by a central pivot connection, on the kinetics.

It appears somewhat counterintuitive that dimer assembly kinetics occur on faster timescales at 2 M NaCl than at 20 mM $MgCl_2$ considering the empirical rule that for DNA-ion interactions, ~ 10 mM $MgCl_2$ gives similar behavior of DNA duplex stability as ~ 1 M NaCl [53]. Also, single-molecule studies of DNA stacking interactions of individual base-pair stacks revealed salt dependent association (and dissociation) rates yielding higher values for the association rate constant for measurements in $MgCl_2$ compared to those conducted in NaCl [255].

However, these aspects should not compromise the obtained results. Structural analysis of the DNA origami brick monomers yielded slightly more extended structures in 2 M NaCl compared to brick monomers dissolved in 20 mM $MgCl_2$ (see section 6.2). These extensions possibly facilitate the formation of nucleobase stacking interactions at the brick interfaces, while brick structures dissolved in 20 mM $MgCl_2$ appear to be too small resulting in slower dimer assembly kinetics. In addition, other ion related effects will be relevant for dimer assembly, in particular the influence of the ion atmosphere surrounding the DNA origami brick objects in solution. While properties of the ion atmosphere, containing dissolved cations and (to a lesser extent) anions, cannot yet be accurately predicted from theory [53], various studies on nucleic acid-ion interactions indicate that the composition and energetics of the ion atmosphere have a major impact on nucleic acid structure and dynamics [54, 55, 249, 284, 285]. For instance, when Mg^{2+} ions compete with Na^+ ions around double-stranded DNA, the concentration of Mg^{2+} in proximity to the DNA surface was shown to be much greater than that of Na^+ [55] and Mg^{2+} ions displayed stronger adsorption to the DNA surface. These tightly bound Mg^{2+} ions form a condensed layer around the DNA where additional effects such as local density fluctuations and inter-ion correlation occur [231, 286–288]. The latter is weak for monovalent ions, but strong for divalent ions and is highly relevant for an adequate description of nucleic acid-ion interactions [289]. Regarding the DNA origami brick system, the layer of immobile magnesium ions featuring strong ion-ion correlations might be considered as a barrier making correct alignment of the shape-complementary protrusions and recessions more difficult. In addition, these effects might also explain the much smaller value of the dissociation rate constants (k_{off}) at 20 mM $MgCl_2$ than that at 2 M NaCl. Once the dimers are formed the dense and compact Mg^{2+} ion layer stabilizes the dimer complex much stronger than the more diffusive Na^+ ion layer inhibiting the disassembly of the dimeric conformation.

In addition, other nucleic acid systems display faster kinetics in the presence of NaCl than for $MgCl_2$. For instance, studies on RNA folding reveal faster folding rates for NaCl than for $MgCl_2$ [290]. Similar results were found for ribozyme folding, which was faster in the presence of $\sim$ 1 M Na^+ (k >50 s^{-1}) than in 10 mM Mg^{2+} (k $\sim$ 2 - 0.2s^{-1}) [291]. Moreover, conformational transitions of a Holliday junction, which is a four-way DNA junction and a common structural motif applied in DNA origami structures, occur on faster timescales in the presence of Na^+ ions [262, 263].

6.4 Conclusion and Outlook

We have shown the ability for SAXS to sensitively reveal structural conformations of DNA origami brick objects under varying salt and temperature conditions and to trace their dimerization kinetics. Structural analysis of brick monomers and dimers unveiled slightly larger extensions of both internal and overall dimensions of the brick objects in the presence of NaCl concentrations in the molar range compared to solution conditions containing only millimolar concentrations of $MgCl_2$. Temperatures of 40°C did not cause any significant conformational deviations for both salt conditions, implying no disassembly of the DNA origami bricks. Time-resolved SAXS experiments on dimer assembly kinetics of DNA origami brick objects based on manual mixing of brick monomers demonstrate $\sim$ 10 times faster dimerization kinetics in the presence of 2 M NaCl than for 20 mM $MgCl_2$, while a temperature of 40°C yields only slightly faster kinetics than for 20°C. Although further experiments including computational approaches would be helpful to get a better understanding of the underlying molecular mechanisms, these results highlight the sensitivity of DNA origami structures to the presence of mono- or divalent ions and related structural changes should be considered in (future) DNA origami design concepts, such as the choice of the number of crossovers.

In addition, structural deformations of the DNA origami lattice will also influence the performance of dynamic DNA origami devices, especially those applied as drug delivery systems or precision rulers in super-resolution microscopy, where deformations may lead to leakage of the payload or imprecise calibrations, respectively. Thus, ion related effects on DNA origami structures may be prevented by an adequate choice of salt. In conclusion, supplementing DNA origami solutions with specific ion species can be a useful tool to both optimize DNA origami designs and to tune the kinetics of dynamic DNA origami nanodevices.

6.5 Materials and Methods

6.5.1 DNA origami assembly and purification

DNA origami brick folding and purification is described in detail in the Materials and Methods section of chapter 5.

6.5.2 SAXS data acquisition and processing

SAXS measurements were performed at beamline P12 at an X-ray wavelength λ of 1.2 Å and a sample-to-detector distance of 3.0 m. The resulting q-range was 0.03 to 5 nm^{-1} (with $q = 4\pi sin(\theta)/\lambda$, where 2θ is the total scattering angle). We used a Pilatus 2M detector for data acquisition. 40 frames with an exposure time of 45 ms in 'flow' mode were conducted at room temperature for each sample condition. For temperatures performed at 40°C, both the sample loader and the capillary were heated to 40°C. Buffer samples were measured using identical procedures before and after each sample measurement.

All SAXS experiments were performed on DNA origami brick samples dissolved in folding buffer (1 mM EDTA, 5 mM TrisBase, 5 mM NaCl; pH 8) containing varying $MgCl_2$ and NaCl concentrations. Static profiles of monomeric and dimeric brick constructs were measured at sample concentrations of 50 nM and 100 nM, respectively. Static reference SAXS profiles of dimeric brick samples were obtained in reaction equilibrium for at least 48 h after 1:1 mixing of monomeric brick variants A_1 and A_2.

Time-resolved SAXS experiments on dimerization kinetics of DNA origami bricks in buffer solutions containing either 20 mM $MgCl_2$ or 2 M NaCl were performed by manual mixing of 50 nM and 100 nM monomer concentrations in a 1:1 mixing ratio. For time-resolved SAXS measurements at temperatures of 40°C, DNA origami brick samples were stored in a heat bath at T ≈ 40°C for ∼ 2 h prior to the first SAXS experiment and during waiting times between the different acquisition runs of each measurement.

6.5.3 SAXS data analysis

Scattering profiles from both static and time-resolved measurements were checked for consistency and radiation damage; no damage was observed in any of the measurements. For some measurements, slight deviations between scattering profiles of repeat runs were observable which is probably related to different mixing ratios due to inaccurate pipetting.

Guinier analysis

We performed Guinier analyses [29] to obtain radii of gyrations (R_g) for all measured DNA origami brick objects, by fitting the logarithm of the scattering intensity as a function of q^2 to a straight line within a fitting range criterion of $q_{max}R_g < 1.6$ [192]. R_g-values shown in Table 6.1 correspond to mean R_g-values of monomeric and dimeric brick samples, respectively, measured at sample concentrations of 50 nM and 100 nM. Errors correspond to the standard deviation. For solution conditions containing either 5 mM $MgCl_2$ or 0.5 M NaCl, we performed SAXS measurements for only one concentration (i.e. 200 nM) so that no mean and standard deviation

could be calculated. Scattering data from each sample were normalized to the intensity at zero angles (*I(0)*) obtained from the Guinier analysis.

Computation of theoretical scattering profiles using *CRYSOL*

The atomistic models for the DNA origami brick monomer object was generated with the software *CanDo* assuming idealized DNA helix and junction geometries [228]. Double helical protrusions and recessions are not included in the model. The atomistic model for the dimer brick was created based on two brick monomer models which were arranged in a dimeric geometry using a custom written MATLAB script (The MathWorks, Inc., MA, USA). We used the program *CRYSOL* [46] for calculation of the theoretical scattering curves from the atomistic models. *CRYSOL* was run in interactive mode, setting the order of harmonics to the maximum value of 50 and the order of the Fibonacci grid to 18. The number of points in the theoretical curve was fixed to 900 within a q-range from 0 - 2.5 nm^{-1}. Remaining parameters were set to default values, without fitting the theoretical curve to the experimental data.

Singular value decomposition

SVD analysis was performed using the 'SVD' command in MATLAB (The MathWorks, Inc., MA, USA). For each measurement condition, scattering profiles obtained at each measurement time point were used for a q-range of 0.1 - 2.5 nm^{-1}. The autocorrelation of each of the basis functions, which gives an estimate on the noise level, is calculated as follows:

$$C_i = \sum_{i=1}^{L-1} U_i(q_i) \cdot U_i(q_{i+1}) \tag{6.3}$$

According to Henry *et al.* [281] SVD components containing appreciable signal have autocorrelations close to 1.0 (>0.9), whereas components that correspond to noise tend to have C_i values < 0.8.

Two-state model fits

Two-state fits for dimerization kinetics of DNA origami bricks were performed describing the scattering profile at each acquisition point by a linear combination of the brick monomer conformation ($I_i(q,t_0)$) and the scattering profile of the dimer at equilibrium ($I_f(q,t_{eq})$):

$$I(q) = f_i \cdot I_i(q, t_0) + f_f \cdot I_f(q, t_{eq}) \tag{6.4}$$

where the coefficients f_i and f_f are fractional occupancies of the initial and final states, respectively. To evaluate the quality of the two-state fits, *chi*-squared values (χ^2) were calculated for each fit according to the following equation:

$$\chi^2 = \sum_i \frac{\left[I_{exp}(q_i, t) - I_{fit}(q_i, t)\right]^2}{\sigma_i^2} \tag{6.5}$$

with σ_i as standard deviation of the scattering intensity at each scattering vector q_i. To determine the fraction of dimers, we used a q-range from 0.1 nm^{-1} - 2.5 nm^{-1}.

Time dependent bimolecular reaction kinetic fit for DNA origami brick dimerization

Dimerization kinetics of the DNA origami brick system was modeled as a reversible bimolecular reaction:

$$\mathrm{A}_1 + \mathrm{A}_2 \underset{k_{off}}{\overset{k_{on}}{\rightleftharpoons}} \mathrm{B}$$

where A_1 and A_2 correspond to the brick monomer variants having either the protruding stacking pattern (1) or the recessed stacking pattern (2) activated, and B is the dimer state; k_{on} describes the association reaction rate constant in $\mathrm{M}^{-1}\ \mathrm{s}^{-1}$ and k_{off} is the dissociation reaction rate constant in s^{-1}. For our experimental conditions with an equimolar mixing ratio of A_1 and A_2 (with initial concentrations $c_0(A_1) = c_0(A_2)$) and in the absence of dimers B at $t_0 = 0$, the time dependent concentrations of dimeric bricks as a function of time are given by [112]:

$$B(t) = \frac{1}{2} \cdot \frac{(\beta - \eta) \cdot e^{\beta \cdot (k_{on} \cdot t + z)} + (\beta + \eta)}{1 - e^{\beta \cdot (k_{on} \cdot t + z)}} \tag{6.6}$$

with:

$$\eta = K_D + c_0(A_1) + c_0(A_2) \tag{6.7}$$

$$\beta = \sqrt{\eta^2 - 4 \cdot c_0(A_1) \cdot c_0(A_2)} \tag{6.8}$$

$$z = \frac{1}{\beta} \left(\frac{2 \cdot c_0(B) - \eta - \beta}{2 \cdot c_0(B) - \eta + \beta} \right) \tag{6.9}$$

Thereby, c_0 denotes the concentration of brick monomer variants A_1 and A_2 and of the dimers B at t = 0, which where either 50 nM or 100 nM for both monomer variants and 0 nM for dimeric brick samples. K_D is the dissociation constant of the dimerization reaction in units (M). Experimentally determined time-dependent dimer fractions were multiplied with respective initial monomer concentrations (i.e. 50 nM and 100 nM) and fitted using Equation 6.6.

We also applied the reversible bimolecular reaction model fit for different final dimer fractions varying between 90 % and 100 %, where a value of 100 % dimers resulted in the lowest χ^2-value.

For an irreversible bimolecular reaction kinetics fit we used the following equation:

$$\frac{B(t)}{c_0(A_1)} = 1 - \frac{1}{(1 + c_0(A_1) \cdot k_{on}^{irr} \cdot t)} \tag{6.10}$$

Diffusion-limited association rate

To compare experimentally derived association rate constants with a reaction that is only limited by the diffusion of the monomeric bricks, we calculated the theoretical diffusion-limited association rate constant k_{diff} of the brick samples [257]:

$$k_{diff} = 4 \cdot \pi \cdot R \cdot D \cdot N_A \tag{6.11}$$

where R denotes the distance within the two monomers can react and form a dimer, which can be assumed to be ~ 2 nm [255], N_A is the Avogadro constant, and D is the diffusion coefficient defined as:

$$D = \frac{k_b T}{3\pi\eta L}\left[ln\left(\frac{2L}{D}\right) - \xi\right] \tag{6.12}$$

where k_B is the Boltzmann constant, T the temperature in Kelvin (300 K), η the viscosity of the solvent (1 mPa· s) and ξ is the correction factor for the end terms taken from Tirado *et al.* [261].

6.6 Supplementary Material

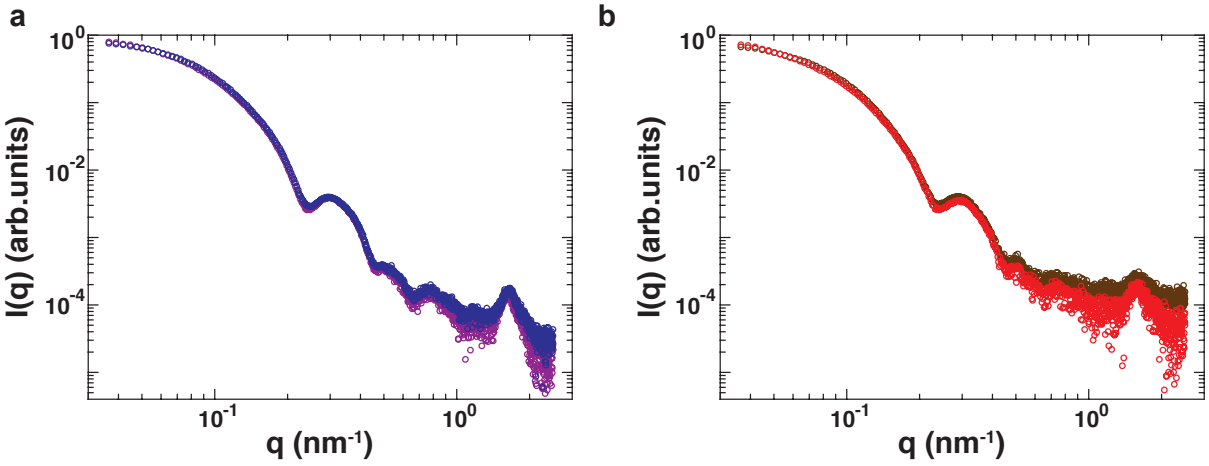

Figure 6.8: SAXS profiles of DNA origami brick dimers at temperatures of T = 20°C and T = 40°C. **a** SAXS profiles of DNA origami brick dimers (c = 100 nM) at temperatures of T = 20°C and T = 40°C dissolved in 20 mM $MgCl_2$. **b** SAXS profiles of DNA origami brick dimers (c = 100 nM) at temperatures of T = 20°C and T = 40°C dissolved in 2 M NaCl.

Part III

Conclusion and Outlook

Chapter 7
Conclusion and Outlook

The function of biological macromolecules and their complexes is governed by their three-dimensional structure and conformational dynamics. To create synthetic objects that can perform user-defined tasks and mimic biological functions, which is a major goal in DNA nanotechnology, we need to obtain information about structure and dynamics of designed objects in order to assure a precise functionality. To study macromolecular conformations under a broad range of solution conditions, small-angle X-ray scattering (SAXS) has been established as a powerful technique.

Within this thesis I have contributed to the construction of an in-house SAXS instrument. Further, I established synchrotron-based SAXS measurements on 3D DNA origami objects.

The build up of the in-house SAXS setup included state-of-the-art components, such as scatterless slits, a hybrid pixel detector, and the implementation of a custom-made temperature-controlled sample stage. In contrast to most common in-house SAXS setups that are based on copper (Cu) anodes, we employed a molybdenum (Mo)-microfocus-anode-based source. Although the Mo-based X-ray tube provides a ten times lower flux compared to Cu-anodes, the system allows for structural studies on biological macromolecules with different scattering properties and sizes up to ~ 30 nm in solution. SAXS measurements on a set of well characterized molecules including proteins, a 24 bp DNA duplex, and detergent micelles, at sample concentrations comparable to synchrotron-based SAXS measurements, could be performed within 2 h. The data were of adequate quality to derive basic geometric parameters, such as the radius of gyration (R_g) or the maximum particle dimension (D_{max}), and were in good agreement with previous measurements. Moreover, we could perform *ab initio* reconstructions to determine the 3D low resolution macromolecular shapes. Combined, our Mo-anode-based in-house setup provides an attractive alternative to other commercially available setups or synchrotron facilities. However, future upgrades might involve the replacement of the microfocus anode by a liquid-metal-jet anode, operating at similar energies as our Mo-anode but providing higher flux, in order to reduce the required exposure times from hours to minutes.

The main part of this thesis focuses on the structural analysis of conformational states and transitions of DNA origami objects, which are based on shape-complementarity and nucleobase stacking interactions, using SAXS. So far structural characterization of DNA origami objects has almost exclusively relied on surface-based techniques such as AFM or negative-stain TEM imaging. In this thesis, solution-based SAXS could be established as a powerful complementary structural analysis approach.

It was shown, that SAXS can sensitively monitor conformational states of a dynamic DNA origami switch device that reversibly changes from an x-shaped open to a rectangular shaped closed state as a function of ionic strength. Experimentally it was found that transitions between the open and closed state are well described by a two-state process.

Moreover, considerable flexibility and deformations for the switch structure deviating from predicted atomistic models were observed. Using a normal mode approach based on an elastic network model, we were able to refine the switch model structures against our experimental SAXS data. We found root-mean-square deviation (RMSD) values of 22.3 Å and 8.4 Å between the initial atomistic models and the refined structures for the closed and open conformation, respectively. These findings highlight the great potential of combined small-angle X-ray scattering experiments and refinement approaches that might be especially relevant for evaluating new design strategies of DNA origami objects.

A key finding of this thesis was the ability to resolve conformational kinetics of the DNA origami switch device as a function of ionic strength using time-resolved SAXS. Rapid turbulent mixing of switch particles with different magnesium chloride concentrations revealed cation concentration dependent transitions from the open to the closed state of the switch object on the millisecond time scale. These exceptional rapid dynamics proceed close to the theoretical diffusive speed limit and are in stark contrast to conformational kinetics of recent dynamic DNA origami devices, which were found to occur on timescales of minutes or seconds. These results emphasize the high potential of the design principle realized in the switch device that offers a promising framework to create reconfigurable molecular machines that might ultimately carry out enzymatic reactions or transmit cellular signals requiring dynamics in the (sub-) millisecond regime.

Furthermore, a heteromultimeric DNA origami brick system, consisting of two monomeric brick variants that can form a dimer via a shape-complementary recognition scheme, was investigated for varying salt and temperature conditions using SAXS. Solution scattering data yielded structural deformations of a few Ångstroms of the brick objects depending on the ion species and ion concentration. Thereby, the presence of Na^+ ions induced slightly larger deformations than the presence of Mg^{2+} ions. In addition, time-resolved SAXS experiments on brick dimerization kinetics showed ~ 10 times faster kinetics in the presence of monovalent ions compared to divalent ions, while an increase in temperature yielded only slightly faster kinetics. In contrast to the switch device, where shape-complementary interfaces are already pre-aligned by a single flexible Holliday junction, dimer assembly kinetics occur on much slower time scales, i.e. in the order of minutes to hours. Combined, these findings implicate the existence of additional barriers, such as electrostatic interactions and correct alignment of shape-complementary interfaces, that influence the dynamics of related DNA origami objects.

However, these effects can be utilized in a positive direction, where appropriate salt conditions can promote desired conformations and allow for tuning conformationl dynamics of DNA origami objects. This is particularly relevant for DNA origami devices used as potential therapeutics and diagnostics, where both structural stability and precise spatial organization are essential prerequisites to assure a targeted delivery of their molecular payload without any prior leakages due to structural deformations of the origami structure.

In brief, to optimize and extend current DNA origami design principles and to get a better understanding of structure-function relationships of synthetic objects, interdisciplinary approaches are indispensable. As I have successfully demonstrated in this thesis, SAXS will undoubtedly contribute to future exciting studies on DNA origami objects.

The combination of SAXS data and computational methods provides a promising platform to refine and validate atomistic models of DNA origami objects, still with room for improvement. Considering recent advances in cryo-EM, particularly the continuous improvement of the achievable resolution, it would be interesting to compare SAXS-refined structures to cryo-EM structures and molecular dynamics or coarse-grained simulations.

Moreover, regarding the ambition for creating even larger objects in the giga dalton regime SAXS offers a great structural analysis tool as it is not limited in size and can be used complementary to cryo-EM studies. Thereby, the use of time-resolved SAXS will be a powerful approach to characterize assembly and disassembly kinetics of higher order structures under varying solution conditions. The design of sample cells that can be used in combination with heat sources such as laser devices would allow to study also conformational kinetics induced by temperature jumps. Finally, the recent commissioning of free electron lasers, delivering extremely brilliant, femtosecond X-ray pulses, might also open new research opportunities in DNA origami technology.

Bibliography

[1] Linda K Bruetzel, Stefan Fischer, Annalena Salditt, Steffen M Sedlak, Bert Nickel, and Jan Lipfert. A Mo-anode-based in-house source for small-angle X-ray scattering measurements of biological macromolecules. *Review of Scientific Instruments*, 87(2):025103, February 2016.

[2] Linda K Bruetzel, Thomas Gerling, Steffen M Sedlak, Philipp U Walker, Wenjun Zheng, Hendrik Dietz, and Jan Lipfert. Conformational Changes and Flexibility of DNA Devices Observed by Small-Angle X-ray Scattering. *Nano Letters*, 16(8):4871–4879, August 2016.

[3] Linda K Bruetzel, Philipp U Walker, Thomas Gerling, Hendrik Dietz, and Jan Lipfert. Time-resolved SAXS reveals millisecond transitions of a DNA origami switch. *submitted*.

[4] Chengdong Huang and Charalampos G Kalodimos. Structures of Large Protein Complexes Determined by Nuclear Magnetic Resonance Spectroscopy. *Annual review of biophysics*, 46:317–336, May 2017.

[5] Giuseppe Zanotti. Cryo-EM and X-Ray Crystallography: Complementary or Alternative Techniques? *NanoWorld Journal*, 2(2), 2016.

[6] Moritz Pfreundschuh, David Martinez-Martin, Estefania Mulvihill, Susanne Wegmann, and Daniel J Muller. Multiparametric high-resolution imaging of native proteins by force-distance curve-based AFM. *Nature Protocols*, 9(5):1113–1130, April 2014.

[7] Christopher D Putnam, Michal Hammel, Greg L Hura, and John A Tainer. X-ray solution scattering (SAXS) combined with crystallography and computation: defining accurate macromolecular structures, conformations and assemblies in solution. *Quarterly Reviews of Biophysics*, 40(3):191–285, August 2007.

[8] Greg L Hura, Angeli L Menon, Michal Hammel, Robert P Rambo, Farris L Poole II, Susan E Tsutakawa, Francis E Jenney Jr, Scott Classen, Kenneth A Frankel, Robert C Hopkins, Sung-jae Yang, Joseph W Scott, Bret D Dillard, Michael W W Adams, and John A Tainer. Robust, high-throughput solution structural analyses by small angle X-ray scattering (SAXS). *Nature Methods*, 6(8):606–612, August 2009.

[9] Jens Als-Nielsen and Des McMorrow. *Elements of Modern X-ray Physics*. Als-Nielsen/Elements. John Wiley & Sons, Inc., Hoboken, NJ, USA, March 2011.

[10] Michel H J Koch, Patrice Vachette, and Dmitri I Svergun. Small-angle scattering: a view on the properties, structures and structural changes of biological macromolecules in solution. *Quarterly Reviews of Biophysics*, 36(2):147–227, May 2003.

[11] Dmitri I Svergun, Michel H J Koch, Peter A Timmins, and Roland P May. *Small Angle X-Ray and Neutron Scattering from Solutions of Biological Macromolecules*. International Union of Crystallography Texts on Crystallography. Oxford University Press, 2013.

[12] Greg L Hura, Chi-Lin Tsai, Shelley A Claridge, Marc L Mendillo, Jessica M Smith, Gareth J Williams, Alexander J Mastroianni, A Paul Alivisatos, Christopher D Putnam, Richard D Kolodner, and John A Tainer. DNA conformations in mismatch repair probed in solution by X-ray scattering from gold nanocrystals. *Proceedings of the National Academy of Sciences*, 110(43):17308–17313, October 2013.

[13] Victor M Balcão and Marta M D C Vila. Structural and functional stabilization of protein entities: state-of-the-art. *Advanced drug delivery reviews*, 93:25–41, October 2015.

[14] Cameron Neylon. Small angle neutron and X-ray scattering in structural biology: recent examples from the literature. *European Biophysics Journal*, 37(5):531–541, January 2008.

[15] David A Jacques and Jill Trewhella. Small-angle scattering for structural biology-Expanding the frontier while avoiding the pitfalls. *Protein Science*, 19(4):642–657, April 2010.

[16] Xiangyun Qiu, Lisa W Kwok, Hye Yoon Park, Jessica S Lamb, Kurt Andresen, and Lois Pollack. Measuring inter-DNA potentials in solution. *Physical review letters*, 96(13): 138101, April 2006.

[17] A Tardieu, A Le Verge, M Malfois, F Bonnete, S Finet, M Riès-Kautt, and L Belloni. Proteins in solution: from X-ray scattering intensities to interaction potentials. *Journal of Crystal Growth*, 196(2-4):193–203, January 1999.

[18] Cy M Jeffries, Melissa A Graewert, Dmitri I Svergun, and Clément E Blanchet. Limiting radiation damage for high-brilliance biological solution scattering: practical experience at the EMBL P12 beamline PETRAIII. *Journal of synchrotron radiation*, 22(2):273–279, February 2015.

[19] Shigeo Kuwamoto, Shuji Akiyama, and Tetsuro Fujisawa. Radiation damage to a protein solution, detected by synchrotron X-ray small-angle scattering: dose-related considerations and suppression by cryoprotectants. *Journal of synchrotron radiation*, 11(6):462–468, October 2004.

[20] Jan Lipfert, Daniel Herschlag, and Sebastian Doniach. Riboswitch conformations revealed by small-angle X-ray scattering. *Methods in molecular biology (Clifton, N.J.)*, 540:141–159, 2009.

[21] Luca Costa, Alexander Andriatis, Martha Brennich, Jean-Marie Teulon, Shu-Wen W Chen, Jean-Luc Pellequer, and Adam Round. Combined small angle X-ray solution scattering with atomic force microscopy for characterizing radiation damage on biological macromolecules. *BMC structural biology*, 16(1):18, October 2016.

[22] Jesse B Hopkins and Robert E Thorne. Quantifying radiation damage in biomolecular small-angle X-ray scattering. *Journal of Applied Crystallography*, 49(Pt 3):880–890, June 2016.

[23] Jonathan C Brooks-Bartlett, Rebecca A Batters, Charles S Bury, Edward D Lowe, Helen Mary Ginn, Adam Round, and Elspeth F Garman. Development of tools to automate quantitative analysis of radiation damage in SAXS experiments. *Journal of synchrotron radiation*, 24(Pt 1):63–72, January 2017.

[24] Daniel Franke, Cy M Jeffries, and Dmitri I Svergun. Correlation Map, a goodness-of-fit test for one-dimensional X-ray scattering spectra. *Nature Methods*, 12(5):419–422, April 2015.

[25] Vincent Vagenende, Miranda G S Yap, and Bernhardt L Trout. Mechanisms of Protein Stabilization and Prevention of Protein Aggregation by Glycerol. *Biochemistry*, 48(46): 11084–11096, November 2009.

[26] Mark C Alliegro. Effects of dithiothreitol on protein activity unrelated to thiol-disulfide exchange: for consideration in the analysis of protein function with Cleland's reagent. *Analytical Biochemistry*, 282(1):102–106, June 2000.

[27] John A V Butler, A B Robins, and Joseph Rotblat. The Inactivation of Formula-Chymotrypsin by Ionizing Radiations. *Proceedings of the Royal Society of London A: Mathematical, Physical and Engineering Sciences*, 256(1284):1–14, May 1960.

[28] Steve P Meisburger, Matthew Warkentin, Huimin Chen, Jesse B Hopkins, Richard E Gillilan, Lois Pollack, and Robert E Thorne. Breaking the radiation damage limit with Cryo-SAXS. *Biophysical Journal*, 104(1):227–236, January 2013.

[29] André Guinier. La diffraction des rayons X aux tres petits angles : applications a l'etude de phenomenes ultramicroscopiques. *Annales de physique*, (11. Sér. 12), 1939.

[30] Dmitri I Svergun and Michel H J Koch. Small-angle scattering studies of biological macromolecules in solution. *Reports on Progress in Physics*, 66(10):1735–1782, October 2003.

[31] Jan Lipfert and Sebastian Doniach. Small-angle X-ray scattering from RNA, proteins, and protein complexes. *Annual review of biophysics and biomolecular structure*, 36(1), 2007.

[32] Haydyn D T Mertens and Dmitri I Svergun. Structural characterization of proteins and complexes using small-angle X-ray solution scattering. *Journal of Structural Biology*, 172 (1):128–141, October 2010.

[33] Otto Glatter. A new method for the evaluation of small-angle scattering data. *Journal of Applied Crystallography*, 10(5):415–421, October 1977.

[34] Peter B Moore. Small-angle scattering. Information content and error analysis. *Journal of Applied Crystallography*, 13(2):168–175, April 1980.

[35] Dimitri I Svergun. Mathematical methods in small-angle scattering data analysis. *Journal of Applied Crystallography*, 24(5):485–492, October 1991.

[36] Otto Kratky and Otto Glatter. Small Angle X-Ray Scattering. *Academic Press, London*, 1982.

[37] Anne T Tuukkanen and Dmitri I Svergun. Weak protein-ligand interactions studied by small-angle X-ray scattering. *The FEBS journal*, 281(8):1974–1987, April 2014.

[38] Rick Russell, Ian S Millett, Mark W Tate, Lisa W Kwok, Bradley Nakatani, Sol M Gruner, Simon G J Mochrie, Vijay Pande, Sebastian Doniach, Daniel Herschlag, and Lois Pollack. Rapid compaction during RNA folding. *Proceedings of the National Academy of Sciences of the United States of America*, 99(7):4266–4271, April 2002.

[39] Florian Praetorius and Hendrik Dietz. Self-assembly of genetically encoded DNA-protein hybrid nanoscale shapes. *Science*, 355(6331):eaam5488–10, March 2017.

[40] Michal Hammel. Validation of macromolecular flexibility in solution by small-angle X-ray scattering (SAXS). *European Biophysics Journal*, 41(10):789–799, October 2012.

[41] Robert P Rambo and John A Tainer. Bridging the solution divide: comprehensive structural analyses of dynamic RNA, DNA, and protein assemblies by small-angle X-ray scattering. *Current Opinion in Structural Biology*, 20(1):128–137, February 2010.

[42] Martina Palamini, Anselmo Canciani, and Federico Forneris. Identifying and Visualizing Macromolecular Flexibility in Structural Biology. *Frontiers in Molecular Biosciences*, 3: e14874–17, September 2016.

[43] Frédéric Poitevin, Henri Orland, Sebastian Doniach, Patrice Koehl, and Marc Delarue. AquaSAXS: a web server for computation and fitting of SAXS profiles with non-uniformally hydrated atomic models. *Nucleic Acids Research*, 39(Web Server issue): W184–9, July 2011.

[44] Dina Schneidman-Duhovny, Michal Hammel, and Andrej Sali. FoXS: a web server for rapid computation and fitting of SAXS profiles. *Nucleic Acids Research*, 38(Web Server issue):W540–4, July 2010.

[45] Krishnakumar M Ravikumar, Wei Huang, and Sichun Yang. Fast-SAXS-pro: A unified approach to computing SAXS profiles of DNA, RNA, protein, and their complexes. *The Journal of Chemical Physics*, 138(2), 2013.

[46] Dimitri Svergun, Claudio Barberato, and Michel H J Koch. CRYSOL - a program to evaluate X-ray solution scattering of biological macromolecules from atomic coordinates. *Journal of Applied Crystallography*, 28(6):768–773, December 1995.

[47] Kasper Stovgaard, Christian Andreetta, Jesper Ferkinghoff-Borg, and Thomas Hamelryck. Calculation of accurate small angle X-ray scattering curves from coarse-grained protein models. *BMC bioinformatics*, 11(1):429, August 2010.

[48] Jouko Juhani Virtanen, Lee Makowski, Tobin R Sosnick, and Karl F Freed. Modeling the hydration layer around proteins: applications to small- and wide-angle x-ray scattering. *Biophysical Journal*, 101(8):2061–2069, October 2011.

[49] Vladimir Makarov, B Montgomery Pettitt, and Michael Feig. Solvation and hydration of proteins and nucleic acids: a theoretical view of simulation and experiment. *Accounts of Chemical Research*, 35(6):376–384, June 2002.

[50] Dimitri I Svergun, Stephane Richard, Michel H Koch, Z Sayers, S Kuprin, and G Zaccai. Protein hydration in solution: experimental observation by x-ray and neutron scattering. *Proceedings of the National Academy of Sciences of the United States of America*, 95(5): 2267–2272, March 1998.

[51] Henry S Kim, Anne Martel, Eric Girard, Martine Moulin, Michael Härtlein, Dominique Madern, Martin Blackledge, Bruno Franzetti, and Frank Gabel. SAXS/SANS on Supercharged Proteins Reveals Residue-Specific Modifications of the Hydration Shell. *Biophysical Journal*, 110(10):2185–2194, May 2016.

[52] Damien Laage, Thomas Elsaesser, and James T Hynes. Water Dynamics in the Hydration Shells of Biomolecules. *Chemical reviews*, 117(16):10694–10725, August 2017.

[53] Jan Lipfert, Sebastian Doniach, Rhiju Das, and Daniel Herschlag. Understanding nucleic acid-ion interactions. *Annual Review of Biochemistry*, 83(1), 2014.

[54] Rhiju Das, Thalia T Mills, Lisa W Kwok, Gregory S Maskel, Ian S Millett, Sebastian Doniach, Kenneth D Finkelstein, Daniel Herschlag, and Lois Pollack. Counterion distribution around DNA probed by solution X-ray scattering. *Physical review letters*, 90(18): 188103, May 2003.

[55] Jejoong Yoo and Aleksei Aksimentiev. Competitive binding of cations to duplex DNA revealed through molecular dynamics simulations. *The Journal of Physical Chemistry B*, 116(43):12946–12954, November 2012.

[56] Dina Schneidman-Duhovny, Michal Hammel, John A Tainer, and Andrej Sali. Accurate SAXS profile computation and its assessment by contrast variation experiments. *Biophysical Journal*, 105(4):962–974, August 2013.

[57] Heinrich B Stuhrmann. Ein neues Verfahren zur Bestimmung der Oberflächenform und der inneren Struktur von gelösten globulären Proteinen aus Röntgenkleinwinkelmessungen. *Zeitschrift für Physikalische Chemie*, 72(46):177–184, December 1970.

[58] Pablo Chacón, Frederico Morán, J F Díaz, E Pantos, and Jose M Andreu. Low-Resolution Structures of Proteins in Solution Retrieved from X-Ray Scattering with a Genetic Algorithm. *Biophysical Journal*, 74(6):2760–2775, June 1998.

[59] Dimitri I Svergun. Restoring Low Resolution Structure of Biological Macromolecules from Solution Scattering Using Simulated Annealing. *Biophysical Journal*, 76(6):2879–2886, June 1999.

[60] Dirk Walther, Fred E Cohen, and Sebastian Doniach. Reconstruction of low-resolution three-dimensional density maps from one-dimensional small-angle X-ray solution scattering data for biomolecules. *Journal of Applied Crystallography*, 33(2):350–363, April 2000.

[61] Daniel Franke and Dmitri I Svergun. DAMMIF, a program for rapid ab-initio shape determination in small-angle scattering. *Journal of Applied Crystallography*, 42(2):342–346, April 2009.

[62] Dmitri I Svergun, Maxim V Petoukhov, and Michel H J Koch. Determination of Domain Structure of Proteins from X-Ray Solution Scattering. *Biophysical Journal*, 80(6):2946–2953, June 2001.

[63] Willy Wriggers, Ronald A Milligan, and J Andrew McCammon. Situs: A Package for Docking Crystal Structures into Low-Resolution Maps from Electron Microscopy. *Journal of Structural Biology*, 125(2-3):185–195, April 1999.

[64] Anne T Tuukkanen, Alessandro Spilotros, and Dmitri I Svergun. Progress in small-angle scattering from biological solutions at high-brilliance synchrotrons. *IUCrJ*, 4(5):518–528, September 2017.

[65] Maxim V Petoukhov and Dmitri I Svergun. Applications of small-angle X-ray scattering to biomacromolecular solutions. *International Journal of Biochemistry and Cell Biology*, 45(2):429–437, February 2013.

[66] Michael B Kozin and Dimitri I Svergun. Automated matching of high- and low-resolution structural models. *Journal of Applied Crystallography*, 34(1):33–41, February 2001.

[67] Vladimir V Volkov and Dimitri I Svergun. Uniqueness of ab initio shape determination in small-angle scattering. *Journal of Applied Crystallography*, 36(3):860–864, April 2003.

[68] Christian Gorba and Florence Tama. Normal Mode Flexible Fitting of High-Resolution Structures of Biological Molecules Toward SAXS Data. *Bioinformatics and biology insights*, 4, 2010.

[69] Wenjun Zheng and Mustafa Tekpinar. Accurate flexible fitting of high-resolution protein structures to small-angle x-ray scattering data using a coarse-grained model with implicit hydration shell. *Biophysical Journal*, 101(12):2981–2991, December 2011.

[70] Florence Tama and Yves H Sanejouand. Conformational change of proteins arising from normal mode calculations. *Protein engineering*, 14(1):1–6, January 2001.

[71] Marc Delarue and Philippe Dumas. On the use of low-frequency normal modes to enforce collective movements in refining macromolecular structural models. *Proceedings of the National Academy of Sciences of the United States of America*, 101(18):6957–6962, May 2004.

[72] Willy Wriggers and Pablo Chacón. Using Situs for the registration of protein structures with low-resolution bead models from X-ray solution scattering. *Journal of Applied Crystallography*, 34(6):773–776, November 2001.

[73] Jan Lipfert, Jonathan Ouellet, David G Norman, Sebastian Doniach, and David M J Lilley. The Complete VS Ribozyme in Solution Studied by Small-Angle X-Ray Scattering. *Structure*, 16(9):1357–1367, September 2008.

[74] Nikolai B Suslov, Saurja DasGupta, Hao Huang, James R Fuller, David M J Lilley, Phoebe A Rice, and Joseph A Piccirilli. Crystal structure of the Varkud satellite ribozyme. *Nature Chemical Biology*, 11(11):840–848, September 2015.

[75] Mark Wells, Henning Tidow, Trevor J Rutherford, Phineus Markwick, Malene Ringkjobing Jensen, Efstratios Mylonas, Dmitri I Svergun, Martin Blackledge, and Alan R Fersht. Structure of tumor suppressor p53 and its intrinsically disordered N-terminal transactivation domain. *Proceedings of the National Academy of Sciences*, 105(15):5762–5767, April 2008.

[76] Helen M Berman, John Westbrook, Zukang Feng, Gary Gilliland, T N Bhat, Helge Weissig, Ilya N Shindyalov, and Philip E Bourne. The Protein Data Bank. *Nucleic Acids Research*, 28(1):235–242, January 2000.

[77] Jeff Perry, Perry Jefferson, and John A Tainer. Developing advanced X-ray scattering methods combined with crystallography and computation. *Methods (San Diego, Calif.)*, 59(3):363–371, March 2013.

[78] Maxim V Petoukhov and Dimitri I Svergun. Global rigid body modeling of macromolecular complexes against small-angle scattering data. *Biophysical Journal*, 89(2):1237–1250, August 2005.

[79] Kevin Wiehe, Matthew W Peterson, Brian Pierce, Julian Mintseris, and Zhiping Weng. *Protein-protein docking: overview and performance analysis.*, volume 413. Methods in molecular biology (Clifton, N.J.), Bioinformatics Program, Boston University, Boston, MA, USA., 2008.

[80] Brian Jiménez-García, Carles Pons, Dmitri I Svergun, Pau Bernado, and Juan Fernández-Recio. pyDockSAXS: protein–protein complex structure by SAXS and computational docking. *Nucleic Acids Research*, 43(W1):W356–W361, June 2015.

[81] Christina E M Schindler, Sjoerd J de Vries, Alexander Sasse, and Martin Zacharias. SAXS Data Alone can Generate High-Quality Models of Protein-Protein Complexes. *Structure/Folding and Design*, 24(8):1387–1397, August 2016.

[82] Oscar Hemberg, Mikael Otendal, and Hans M Hertz. Liquid-metal-jet anode electron-impact x-ray source. *Applied Physics Letters*, 83(7):1483–1485, August 2003.

[83] V Honkimäki, J Sleight, and P Suortti. Characteristic X-ray flux from sealed Cr, Cu, Mo, Ag and W tubes. *Journal of Applied Crystallography*, 23(5):412–417, October 1990.

[84] Jan S Pedersen. A flux- and background-optimized version of the NanoSTAR small-angle X-ray scattering camera for solution scattering. *Journal of Applied Crystallography*, 37 (3):369–380, June 2004.

[85] Tadeusz Skarzynski. Collecting data in the home laboratory: evolution of X-ray sources, detectors and working practices. *Acta Crystallographica Section D: Biological Crystallography*, 69(Pt 7):1283–1288, July 2013.

[86] Paul Allé, Emmanuel Wenger, Slimane Dahaoui, Dominik Schaniel, and Claude Lecomte. Comparison of CCD, CMOS and Hybrid Pixel x-ray detectors: detection principle and data quality. *Physica Scripta*, 91(6):063001–16, May 2016.

[87] M Schuster and H Gobel. Parallel-beam coupling into channel-cut monochromators using curved graded multilayers. *Journal of Physics D: Applied Physics*, 28(4A):A270–A275, April 1995.

[88] Tomi Tuohimaa, J Ewald, M Schlie, J M Fernández-Varea, Hans M Hertz, and Ulrich Vogt. A microfocus x-ray source based on a nonmetal liquid-jet anode. *Applied Physics Letters*, 92(23):233509–4, June 2008.

[89] George D Wignall, Jiao S Lin, and S Spooner. Reduction of parasitic scattering in small-angle X-ray scattering by a three-pinhole collimating system. *Journal of Applied Crystallography*, 23(4):241–245, August 1990.

[90] Youli Li, Roy Beck, Tuo Huang, Myung C Choi, and Morito Divinagracia. Scatterless hybrid metal–single-crystal slit for small-angle X-ray scattering and high-resolution X-ray diffraction. *Journal of Applied Crystallography*, 41(6):1134–1139, December 2008.

[91] Beat Henrich, Anna Bergamaschi, Christian Broennimann, Roberto Dinapoli, Eric F Eikenberry, I Johnson, Miroslav Kobas, Philipp Kraft, Aldo Mozzanica, and Bernd Schmitt. PILATUS: A single photon counting pixel detector for X-ray applications. *Nuclear Instruments and Methods in Physics Research Section A: Accelerators, Spectrometers, Detectors and Associated Equipment*, 607(1):247–249, August 2009.

[92] Philip Willmott. *An Introduction to Synchrotron Radiation.* Techniques and Applications. John Wiley & Sons, Ltd, Chichester, UK, July 2011.

[93] Robin L Owen, Jordi Juanhuix, and Martin Fuchs. Current advances in synchrotron radiation instrumentation for MX experiments. *Archives of Biochemistry and Biophysics*, 602:21–31, July 2016.

[94] Antonella Balerna and Settimio Mobilio. Introduction to Synchrotron Radiation. In *Synchrotron Radiation*, pages 3–28. Springer Berlin Heidelberg, Berlin, Heidelberg, August 2014.

[95] Petra Pernot, Adam Round, Ray Barrett, Alejandro De Maria Antolinos, Alexandre Gobbo, Elspeth Gordon, Julien Huet, Jerôme Kieffer, Mario Lentini, Muriel Mattenet, Christian Morawe, Christoph Mueller-Dieckmann, Staffan Ohlsson, Werner Schmid, John Surr, Pascal Theveneau, Louiza Zerrad, and Sean McSweeney. Upgraded ESRF BM29 beamline for SAXS on macromolecules in solution. *Journal of synchrotron radiation*, 20(Pt 4): 660–664, July 2013.

[96] Adam Round, Franck Felisaz, Lukas Fodinger, Alexandre Gobbo, Julien Huet, Cyril Villard, Clément E Blanchet, Petra Pernot, Sean McSweeney, Manfred Roessle, Dmitri I Svergun, and Florent Cipriani. BioSAXS Sample Changer: a robotic sample changer for rapid and reliable high-throughput X-ray solution scattering experiments. *Acta Crystallographica Section D: Biological Crystallography*, 71(Pt 1):67–75, January 2015.

[97] Richard P Feynman. There's plenty of room at the bottom. *Engineering and Science*, 23 (5), 1960.

[98] Kim E Drexler. *Engines of Creation.* Engines of Creation. Fourth Estate, 1986.

[99] Nadrian C Seeman. Nucleic Acid Junctions and Lattices. *Journal of theoretical biology*, 99(2):237–247, November 1982.

[100] Junghuei Chen and Nadrian C Seeman. Synthesis from DNA of a molecule with the connectivity of a cube. *Nature*, 350(6319):631–633, April 1991.

[101] Yuwen Zhang and Nadrian C Seeman. Construction of a DNA-Truncated Octahedron. *Journal of the American Chemical Society*, 116(5):1661–1669, March 1994.

[102] Paul W K Rothemund. Folding DNA to create nanoscale shapes and patterns. *Nature*, 440(7082):297–302, March 2006.

[103] Vivek V Thacker, Lars O Herrmann, Daniel O Sigle, Tao Zhang, Tim Liedl, Jeremy J Baumberg, and Ulrich F Keyser. DNA origami based assembly of gold nanoparticle dimers for surface-enhanced Raman scattering. *Nature Communications*, 5:3448, March 2014.

[104] Francesca Cella Zanacchi, Carlo Manzo, Angel S Alvarez, Nathan D Derr, Maria F Garcia-Parajo, and Melike Lakadamyali. A DNA origami platform for quantifying protein copy number in super-resolution. *Nature Methods*, 14(8):789–792, August 2017.

[105] Honglu Zhang, Jie Chao, Dun Pan, Huajie Liu, Yu Qiang, Ke Liu, Chengjun Cui, Jianhua Chen, Qing Huang, Jun Hu, Lianhui Wang, Wei Huang, Yongyong Shi, and Chunhai Fan. DNA origami-based shape IDs for single-molecule nanomechanical genotyping. *Nature Communications*, 8:14738, April 2017.

[106] Jonas J Funke and Hendrik Dietz. Placing molecules with Bohr radius resolution using DNA origami. *Nature Nanotechnology*, 11(1):47–52, January 2016.

[107] Jonas J Funke, Philip Ketterer, Corinna Lieleg, Sarah Schunter, Philipp Korber, and Hendrik Dietz. Uncovering the forces between nucleosomes using DNA origami. *Science advances*, 2(11):e1600974–e1600974, November 2016.

[108] Arivazhagan Rajendran, Masayuki Endo, Kumi Hidaka, and Hiroshi Sugiyama. Direct and Real-Time Observation of Rotary Movement of a DNA Nanomechanical Device. *Journal of the American Chemical Society*, 135(3):1117–1123, January 2013.

[109] Florian Praetorius and Hendrik Dietz. Self-assembly of genetically encoded DNA-protein hybrid nanoscale shapes. *Science*, 355(6331):eaam5488–10, March 2017.

[110] Shawn M Douglas, Ido Bachelet, and George M Church. A Logic-Gated Nanorobot for Targeted Transport of Molecular Payloads. *Science*, 335(6070), 2012.

[111] Robert Schreiber, Jaekwon Do, Eva-Maria Roller, Tao Zhang, Verena J Schüller, Philipp C Nickels, Jochen Feldmann, and Tim Liedl. Hierarchical assembly of metal nanoparticles, quantum dots and organic dyes using DNA origami scaffolds. *Nature Nanotechnology*, 9 (1):74–78, January 2014.

[112] Thomas Gerling, Klaus F Wagenbauer, Andrea M Neuner, and Hendrikha Dietz. Dynamic DNA devices and assemblies formed by shape-complementary, non-base pairing 3D components. *Science*, 347(6229):1446–1452, March 2015.

[113] Nicholas Stephanopoulos, Minghui Liu, Gary J Tong, Zhe Li, Yan Liu, Hao Yan, and Matthew B Francis. Immobilization and One-Dimensional Arrangement of Virus Capsids with Nanoscale Precision Using DNA Origami. *Nano Letters*, 10(7):2714–2720, July 2010.

[114] Nandhini Ponnuswamy, Maartje M C Bastings, Bhavik Nathwani, Ju Hee Ryu, Leo Y T Chou, Mathias Vinther, Weiwei Aileen Li, Frances M Anastassacos, David J Mooney, and William M Shih. Oligolysine-based coating protects DNA nanostructures from low-salt denaturation and nuclease degradation. *Nature Communications*, 8:1–9, May 2017.

[115] Verena J Schüller, Simon Heidegger, Nadja Sandholzer, Philipp C Nickels, Nina A Suhartha, Stefan Endres, Carole Bourquin, and Tim Liedl. Cellular immunostimulation by CpG-sequence-coated DNA origami structures. *ACS Nano*, 5(12):9696–9702, December 2011.

[116] Isaac Gállego, Brendan Manning, Joan Daniel Prades, Mònica Mir, Josep Samitier, and Ramon Eritja. DNA-Origami-Driven Lithography for Patterning on Gold Surfaces with Sub-10 nm Resolution. *Advanced materials (Deerfield Beach, Fla.)*, 29(11), March 2017.

[117] Gaëtan Bellot, Mark A McClintock, James J Chou, and William M Shih. DNA nanotubes for NMR structure determination of membrane proteins. *Nature Protocols*, 8(4):755–770, April 2013.

[118] Katharine Sanderson. Bioengineering: What to make with DNA origami. *Nature Publishing Group*, 464(7286):158–159, March 2010.

[119] Pengfei Wang, Travis A Meyer, Victor Pan, Palash K Dutta, and Yonggang Ke. The Beauty and Utility of DNA Origami. *Chem*, 2(3):359–382, March 2017.

[120] Thomas G Martin and Hendrik Dietz. Magnesium-free self-assembly of multi-layer DNA objects. *Nature Communications*, 3:1103, October 2012.

[121] Jean-Philippe J Sobczak, Thomas G Martin, Thomas Gerling, and Hendrik Dietz. Rapid folding of DNA into nanoscale shapes at constant temperature. *Science*, 338(6113): 1458–1461, December 2012.

[122] Klaus F Wagenbauer, Floris A S Engelhardt, Evi Stahl, Vera K Hechtl, Pierre Stömmer, Fabian Seebacher, Letizia Meregalli, Philip Ketterer, Thomas Gerling, and Hendrik Dietz. How We Make DNA Origami. *Chembiochem : a European journal of chemical biology*, 440:297–14, August 2017.

[123] Evi Stahl, Thomas G Martin, Florian Praetorius, and Hendrik Dietz. Facile and Scalable Preparation of Pure and Dense DNA Origami Solutions. *Angewandte Chemie*, 126(47): 12949–12954, November 2014.

[124] Shawn M Douglas, Hendrik Dietz, Tim Liedl, Björn Högberg, Franziska Graf, and William M Shih. Self-assembly of DNA into nanoscale three-dimensional shapes. *Nature Publishing Group*, 459(7245):414–418, May 2009.

[125] Yonggang Ke, Luvena L Ong, William M Shih, and Peng Yin. Three-Dimensional Structures Self-Assembled from DNA Bricks. *Science*, 338(6111), 2012.

[126] Anton Kuzyk, Kimmo T Laitinen, and Päivi Törmä. DNA origami as a nanoscale template for protein assembly. *Nanotechnology*, 20(23):235305, June 2009.

[127] Niels V Voigt, Thomas Torring, Alexandru Rotaru, Mikkel F Jacobsen, Jens B Ravnsbæk, Ramesh Subramani, Wael Mamdouh, Jørgen Kjems, Andriy Mokhir, Flemming Besenbacher, and Kurt Vesterager Gothelf. Single-molecule chemical reactions on DNA origami. *Nature Nanotechnology*, 5(3):200–203, March 2010.

[128] Shawn M Douglas, Adam H Marblestone, Surat Teerapittayanon, Alejandro Vazquez, George M Church, and William M Shih. Rapid prototyping of 3D DNA-origami shapes with caDNAno. *Nucleic Acids Research*, 37(15):5001–5006, August 2009.

[129] Hendrik Dietz, Shawn M Douglas, and William M Shih. Folding DNA into twisted and curved nanoscale shapes. *Science*, 325(5941):725–730, August 2009.

[130] Dongran Han, Suchetan Pal, Yang Yang, Shuoxing Jiang, Jeanette Nangreave, Yan Liu, and Hao Yan. DNA gridiron nanostructures based on four-arm junctions. *Science*, 339 (6126):1412–1415, March 2013.

[131] Dongran Han, Suchetan Pal, Jeanette Nangreave, Zhengtao Deng, Yan Liu, and Hao Yan. DNA Origami with Complex Curvatures in Three-Dimensional Space. *Science*, 332(6027): 342–346, April 2011.

[132] Nicholas A W Bell and Ulrich F Keyser. Nanopores formed by DNA origami: A review. *FEBS letters*, 588(19):3564–3570, June 2014.

[133] Jürgen J Schmied, Andreas Gietl, Phil Holzmeister, Carsten Forthmann, Christian Steinhauer, Thorben Dammeyer, and Philip Tinnefeld. Fluorescence and super-resolution standards based on DNA origami. *Nature Methods*, 9(12):1133–1134, December 2012.

[134] Robert Schreiber, Jaekwon Do, Eva-Maria Roller, Tao Zhang, Verena J Schüller, Philipp C Nickels, Jochen Feldmann, and Tim Liedl. Hierarchical assembly of metal nanoparticles, quantum dots and organic dyes using DNA origami scaffolds. *Nature Nanotechnology*, 9 (1):74–78, December 2013.

[135] Anton Kuzyk, Robert Schreiber, Zhiyuan Fan, Günther Pardatscher, Eva-Maria Roller, Alexander Högele, Friedrich C Simmel, Alexander O Govorov, and Tim Liedl. DNA-based self-assembly of chiral plasmonic nanostructures with tailored optical response. *Nature Publishing Group*, 483(7389):311–314, April 2013.

[136] Palash K Dutta, Reji Varghese, Jeanette Nangreave, Su Lin, Hao Yan, and Yan Liu. DNA-Directed Artificial Light-Harvesting Antenna. *Journal of the American Chemical Society*, 133(31):11985–11993, August 2011.

[137] David Yu Zhang and Georg Seelig. Dynamic DNA nanotechnology using strand-displacement reactions. *Nature chemistry*, 3(2):103–113, February 2011.

[138] Bernard Yurke, Andrew J Turberfield, Allen P Mills, Friedrich C Simmel, and Jennifer L Neumann. A DNA-fuelled molecular machine made of DNA. *Nature*, 406(6796):605–608, August 2000.

[139] Ebbe S Andersen, Mingdong Dong, Morten M Nielsen, Kasper Jahn, Ramesh Subramani, Wael Mamdouh, Monika M Golas, Bjoern Sander, Holger Stark, Cristiano L P Oliveira, Jan Skov Pedersen, Victoria Birkedal, Flemming Besenbacher, Kurt V Gothelf, and Jørgen Kjems. Self-assembly of a nanoscale DNA box with a controllable lid. *Nature*, 459(7243): 73–76, May 2009.

[140] Andre V Pinheiro, Dongran Han, William M Shih, and Hao Yan. Challenges and opportunities for structural DNA nanotechnology. *Nature Publishing Group*, 6(12):763–772, November 2011.

[141] Veikko Linko and Hendrik Dietz. The enabled state of DNA nanotechnology. *Current opinion in biotechnology*, 24(4):555–561, August 2013.

[142] Michael W Hudoba, Yi Luo, Angelita Zacharias, Michael G Poirier, and Carlos E Castro. Dynamic DNA Origami Device for Measuring Compressive Depletion Forces. *ACS Nano*, 11(7):6566–6573, July 2017.

[143] Yukiko Kamiya and Hiroyuki Asanuma. Light-Driven DNA Nanomachine with a Photoresponsive Molecular Engine. *Accounts of Chemical Research*, 47(6):1663–1672, June 2014.

[144] Robert Schreiber, Ngoc Luong, Zhiyuan Fan, Anton Kuzyk, Philipp C Nickels, Tao Zhang, David M Smith, Bernard Yurke, Wan Kuang, Alexander O Govorov, and Tim Liedl. Chiral plasmonic DNA nanostructures with switchable circular dichroism. *Nature Communications*, 4, 2013.

[145] Anton Kuzyk, Yangyang Yang, Xiaoyang Duan, Simon Stoll, Alexander O Govorov, Hiroshi Sugiyama, Masayuki Endo, and Na Liu. A light-driven three-dimensional plasmonic nanosystem that translates molecular motion into reversible chiroptical function. *Nature Communications*, 7:10591, February 2016.

[146] Kalle Gehring, Jean-Louis Leroy, and Maurice Guéron. A tetrameric DNA structure with protonated cytosine.cytosine base pairs. *Nature*, 363(6429):561–565, June 1993.

[147] Fritz M Pohl and Thomas M Jovin. Salt-induced co-operative conformational change of a synthetic DNA: equilibrium and kinetic studies with poly (dG-dC). *Journal of molecular biology*, 67(3):375–396, June 1972.

[148] Dongsheng Liu and Shankar Balasubramanian. A Proton-Fuelled DNA Nanomachine. *Angewandte Chemie International Edition*, 42(46):5734–5736, December 2003.

[149] Samantha M Reilly, Daniel F Lyons, Sara E Wingate, Robert T Wright, John J Correia, David M Jameson, and Randy M Wadkins. Folding and Hydrodynamics of a DNA i-Motif from the c-MYC Promoter Determined by Fluorescent Cytidine Analogs. *Biophysical Journal*, 107(7):1703–1711, October 2014.

[150] Mahmoud Moradi, Volodymyr Babin, Christopher Roland, and Celeste Sagui. Reaction path ensemble of the B-Z-DNA transition: a comprehensive atomistic study. *Nucleic Acids Research*, 41(1):33–43, December 2012.

[151] Alexandria N Marchi, Ishtiaq Saaem, Briana N Vogen, Stanley Brown, and Thomas H LaBean. Toward larger DNA origami. *Nano Letters*, 14(10):5740–5747, October 2014.

[152] Zhao Zhao, Yan Liu, and Hao Yan. Organizing DNA Origami Tiles into Larger Structures Using Preformed Scaffold Frames. *Nano Letters*, 11(7):2997–3002, July 2011.

[153] Daniel Schiffels, Veronika A Szalai, and J Alexander Liddle. Molecular Precision at Micrometer Length Scales: Hierarchical Assembly of DNA–Protein Nanostructures. *ACS Nano*, 11(7):6623–6629, July 2017.

[154] Xiao-Chen Bai, Thomas G Martin, Sjors H W Scheres, and Hendrik Dietz. Cryo-EM structure of a 3D DNA-origami object. *Proceedings of the National Academy of Sciences*, 109(49):20012–20017, December 2012.

[155] Takayuki Kato, Russell P Goodman, Christoph M Erben, Andrew J Turberfield, and Keiichi Namba. High-Resolution Structural Analysis of a DNA Nanostructure by cryoEM. *Nano Letters*, 9(7):2747–2750, July 2009.

[156] Stefan Fischer, Caroline Hartl, Kilian Frank, Joachim O Rädler, Tim Liedl, and Bert Nickel. Shape and Interhelical Spacing of DNA Origami Nanostructures Studied by Small-Angle X-ray Scattering. *Nano Letters*, 16(7):4282–4287, July 2016.

[157] Christopher Maffeo, Jejoong Yoo, and Aleksei Aksimentiev. De novo reconstruction of DNA origami structures through atomistic molecular dynamics simulation. *Nucleic Acids Research*, 44(7):3013–3019, April 2016.

[158] Steven D Perrault and William M Shih. Virus-Inspired Membrane Encapsulation of DNA Nanostructures To Achieve In VivoStability. *ACS Nano*, 8(5):5132–5140, May 2014.

[159] Dimitri I Svergun. Determination of the Regularization Parameter in Indirect-Transform Methods Using Perceptual Criteria. *Journal of Applied Crystallography*, 25(4), 1992.

[160] Daniel Herschlag, Rick Russell, Ian S Millett, and Sebastian Doniach. Small angle X-ray scattering reveals a compact intermediate in RNA folding. *Nature Structural Biology*, 7 (5):367–370, May 2000.

[161] Adelene Y L Sim, Jan Lipfert, Daniel Herschlag, and Sebastian Doniach. Salt dependence of the radius of gyration and flexibility of single-stranded DNA in solution probed by small-angle x-ray scattering. *Physical Review E*, 86(2):021901, August 2012.

[162] Pau Bernado, Efstratios Mylonas, Maxim V Petoukhov, Martin Blackledge, and Dmitri I Svergun. Structural Characterization of Flexible Proteins Using Small-Angle X-ray Scattering. *Journal of the American Chemical Society*, 129(17):5656–5664, May 2007.

[163] Jan Lipfert, Vincent B Chu, Yu Bai, Daniel Herschlag, and Sebastian Doniach. Low-resolution models for nucleic acids from small-angle X-ray scattering with applications to electrostatic modeling. *Journal of Applied Crystallography*, 40:s229–s234, February 2007.

[164] Alexander Grishaev, Justin Wu, Jill Trewhella, and Ad Bax. Refinement of multidomain protein structures by combination of solution small-angle X-ray scattering and NMR data. *Journal of the American Chemical Society*, 127(47), 2005.

[165] Gulnahar B Mortuza, Tommaso Cavazza, Maria Flor Garcia-Mayoral, Dario Hermida, Isabel Peset, Juan G Pedrero, Nekane Merino, Francisco J Blanco, Jeppe Lyngsø, Marta Bruix, Jan Skov Pedersen, Isabelle Vernos, and Guillermo Montoya. XTACC3-XMAP215 association reveals an asymmetric interaction promoting microtubule elongation. *Nature Communications*, 5, 2014.

[166] Daniel M Dupont, Cathrine K Thuesen, Kenneth A Bøtkjær, Manja A Behrens, Karen Dam, Hans P Sørensen, Jan S Pedersen, Michael Ploug, Jan K Jensen, and Peter A Andreasen. Protein-Binding RNA Aptamers Affect Molecular Interactions Distantly from Their Binding Sites. *PloS one*, 10(3):e0119207–22, March 2015.

[167] W Vogel. X-ray structure investigation of electron evaporated Cu C and W C multilayers. *Surface Science*, 156(0):420–425, June 1985.

[168] Toshiyuki Takamuku, Atsushi Yamaguchi, Daisuke Matsuo, Masaaki Tabata, Toshio Yamaguchi, Toshiya Otomo, and Tomohiro Adachi. NaCl-Induced Phase Separation of 1,4-Dioxane–Water Mixtures Studied by Large-Angle X-ray Scattering and Small-Angle Neutron Scattering Techniques. *The Journal of Physical Chemistry B*, 105(41):10101–10110, October 2001.

[169] Masaru Matsugami, Toshiyuki Takamuku, Toshiya Otomo, and Toshio Yamaguchi. Thermal properties and mixing state of ethylene glycol-water binary solutions by calorimetry, large-angle X-ray scattering, and small-angle neutron scattering. *The Journal of Physical Chemistry B*, 110(25):12372–12379, June 2006.

[170] Naoto Metoki, Wolfgang Donner, and Hartmut Zabel. Grazing-incidence x-ray-scattering study of (001)-oriented high-quality epitaxial Co/Cr superlattices. *Physical Review B*, 49 (24):17351–17359, June 1994.

[171] Michele Cianci, John R Helliwell, David Moorcroft, Andrzej Olczak, James Raftery, and Pierre J Rizkallah. The role of wavelength and source in the search for sulfur-atom positions evaluated in two case studies: lysozyme at room temperature and cryo apocrustacyanin A1. *Journal of Applied Crystallography*, 37(4):555–564, July 2004.

[172] Thorsten Mühge, Thomas Zeidler, Qing Q Wang, Christian Morawe, Naoto Metoki, and H Zabel. Structural and magnetic studies of FexCo1–x(001) alloy films on MgO(001) substrates. *Journal of Applied Physics*, 77(3):1055–1060, February 1995.

[173] Shigeo Sato, Tsuyoshi Nishi, Eiichiro Matsubara, Muneyuki Imafuku, Nobuyuki Nishiyama, Yoshio Waseda, and Akihisa Inoue. Development of in-house fast X-ray diffraction apparatus and its application to the supercooled liquid Pd 40Ni 10Cu 30P 20alloy. *Science and Technology of Advanced Materials*, 3(2):69–73, July 2008.

[174] Annette Rösler, Harm-Anton Klok, Ian W Hamley, Valeria Castelletto, and Oleksandr O Mykhaylyk. Nanoscale structure of poly(ethylene glycol) hybrid block copolymers containing amphiphilic beta-strand peptide sequences. *Biomacromolecules*, 4(4):859–863, July 2003.

[175] Anne Martel, Manfred Burghammer, Richard J Davies, Emanuela Di Cola, Charlotte Vendrely, and Christian Riekel. Silk fiber assembly studied by synchrotron radiation SAXS/WAXS and Raman spectroscopy. *Journal of the American Chemical Society*, 130 (50):17070–17074, December 2008.

[176] Jasmina A Sichert, Yu Tong, Niklas Mutz, Mathias Vollmer, Stefan Fischer, Karolina Z Milowska, Ramon García Cortadella, Bert Nickel, Carlos Cardenas-Daw, Jacek K Stolarczyk, Alexander S Urban, and Jochen Feldmann. Quantum Size Effect in Organometal Halide Perovskite Nanoplatelets. *Nano Letters*, 15(10):6521–6527, October 2015.

[177] Alexander Bergmann, Doris Orthaber, Günther Scherf, and Otto Glatter. Improvement of SAXS measurements on Kratky slit systems by Göbel mirrors and imaging-plate detectors. *Journal of Applied Crystallography*, 33(3):869–875, June 2000.

[178] Jan Lipfert, Ian S Millett, Sönke Seifert, and Sebastian Doniach. Sample holder for small-angle x-ray scattering static and flow cell measurements. *Review of Scientific Instruments*, 77(4):046108, April 2006.

[179] B L Henke, Eric M Gullikson, and J C Davis. X-Ray Interactions: Photoabsorption, Scattering, Transmission, and Reflection at E = 50-30,000 eV, Z = 1-92. *Atomic data and nuclear data tables*, 54(2):181–342, July 1993.

[180] Philipp Kraft, Anna Bergamaschi, Christian Broennimann, Roberto Dinapoli, Eric F Eikenberry, Beat Henrich, I Johnson, Aldo Mozzanica, Christian M Schlepuetz, Philip R Willmott, and Bernd Schmitt. Performance of single-photon-counting PILATUS detector modules. *Journal of synchrotron radiation*, 16(Pt 3):368–375, May 2009.

[181] T N Blanton, T C Huang, H Toraya, C R Hubbard, S B Robie, D Louër, H E Göbel, G Will, R Gilles, and T Raftery. JCPDS—International Centre for Diffraction Data round robin study of silver behenate. A possible low-angle X-ray diffraction calibration standard. *Powder Diffraction*, 10(02):91–95, June 1995.

[182] Fan Zhang, Jan Ilavsky, Gabrielle G Long, John P G Quintana, Andrew J Allen, and Pete R Jemian. Glassy Carbon as an Absolute Intensity Calibration Standard for Small-Angle Scattering. *Metallurgical and Materials Transactions A*, 41(5):1151–1158, August 2009.

[183] Yu Bai, Rhiju Das, Ian S Millett, Daniel Herschlag, and Sebastian Doniach. Probing counterion modulated repulsion and attraction between nucleic acid duplexes in solution. *Proceedings of the National Academy of Sciences of the United States of America*, 102(4): 1035–1040, January 2005.

[184] Jan Ilavsky. Nika: software for two-dimensional data reduction. *Journal of Applied Crystallography*, 45(2):324–328, March 2012.

[185] Xiang Jun Lu and Wilma K Olson. 3DNA: a software package for the analysis, rebuilding and visualization of three-dimensional nucleic acid structures. *Nucleic Acids Research*, 31 (17):5108–5121, September 2003.

[186] Maxim V Petoukhov, Daniel Franke, Alexander V Shkumatov, Giancarlo Tria, Alexey G Kikhney, Michal Gajda, Christian Gorba, Haydyn D T Mertens, Petr V Konarev, and Dmitri I Svergun. New developments in the ATSAS program package for small-angle scattering data analysis. *Journal of Applied Crystallography*, 45(2):342–350, April 2012.

[187] William Humphrey, Andrew Dalke, and Klaus Schulten. VMD: Visual molecular dynamics. *Journal of molecular graphics*, 14(1):33–38, February 1996.

[188] Shuji Akiyama, Satoshi Takahashi, Tetsunari Kimura, Koichiro Ishimori, Isao Morishima, Yukihiro Nishikawa, and Tetsuro Fujisawa. Conformational landscape of cytochrome c folding studied by microsecond-resolved small-angle x-ray scattering. *Proceedings of the National Academy of Sciences*, 99(3):1329–1334, February 2002.

[189] D J Segel, A Bachmann, J Hofrichter, K O Hodgson, S Doniach, and T Kiefhaber. Characterization of transient intermediates in lysozyme folding with time-resolved small-angle X-ray scattering. *Journal of molecular biology*, 288(3), 1999.

[190] Efstratios Mylonas and Dmitri I Svergun. Accuracy of molecular mass determination of proteins in solution by small-angle X-ray scattering. *Journal of Applied Crystallography*, 40(s1):S245–S249, April 2007.

[191] Pablo Chacón, J Fernando Dıaz, Federico Morán, and José M Andreu. Reconstruction of protein form with X-ray solution scattering and a genetic algorithm. *Journal of molecular biology*, 299(5):1289–1302, June 2000.

[192] Michal Hammel, Yaping Yu, Brandi L Mahaney, Brandon Cai, Ruiqiong Ye, Barry M Phipps, Robert P Rambo, Greg L Hura, Martin Pelikan, Sairei So, Ramin M Abolfath, David J Chen, Susan P Lees-Miller, and John A Tainer. Ku and DNA-dependent Protein Kinase Dynamic Conformations and Assembly Regulate DNA Binding and the Initial Non-homologous End Joining Complex. *Journal of Biological Chemistry*, 285(2), 2010.

[193] M le Maire, P Champeil, and J V Moller. Interaction of membrane proteins and lipids with solubilizing detergents. *Biochimica et biophysica acta*, 1508(1-2):86–111, November 2000.

[194] Sebastian Hiller, Robert G Garces, Thomas J Malia, Vladislav Y Orekhov, Marco Colombini, and Gerhard Wagner. Solution structure of the integral human membrane protein VDAC-1 in detergent micelles. *Science*, 321(5893):1206–1210, August 2008.

[195] Annela M Seddon, Paul Curnow, and Paula J Booth. Membrane proteins, lipids and detergents: not just a soap opera. *Biochimica et biophysica acta*, 1666(1-2):105–117, November 2004.

[196] Linda Columbus, Jan Lipfert, Kalyani Jambunathan, Daniel A Fox, Adelene Y L Sim, Sebastian Doniach, and Scott A Lesley. Mixing and matching detergents for membrane protein NMR structure determination. *Journal of the American Chemical Society*, 131(21): 7320–7326, June 2009.

[197] J Bowie. Stabilizing membrane proteins. *Current Opinion in Structural Biology*, 11(4): 397–402, August 2001.

[198] Sow-Hsin Chen. Small Angle Neutron Scattering Studies of the Structure and Interaction in Micellar and Microemulsion Systems. *Annual Review of Physical Chemistry*, 37(1): 351–399, October 1986.

[199] Ruitian Zhang, Palma Ann Marone, P Thiyagarajan, and David M Tiede. Structure and Molecular Fluctuations of n-Alkyl-β- d-glucopyranoside Micelles Determined by X-ray and Neutron Scattering. *Langmuir : the ACS journal of surfaces and colloids*, 15(22): 7510–7519, October 1999.

[200] Camille Dupuy, X Auvray, and C Petipas. Anomeric effects on the structure of micelles of alkyl maltosides in water. *Langmuir : the ACS journal of surfaces and colloids*, 13(15), 1997.

[201] Jan Lipfert, Linda Columbus, Vincent B Chu, Scott A Lesley, and Sebastian Doniach. Size and shape of detergent micelles determined by small-angle X-ray scattering. *The Journal of Physical Chemistry B*, 111(43):12427–12438, November 2007.

[202] Linda Columbus, Jan Lipfert, Heath Klock, Ian Millett, Sebastian Doniach, and Scott A Lesley. Expression, purification, and characterization of Thermotoga maritima membrane proteins for structure determination. *Protein Science*, 15(5):961–975, May 2006.

[203] Ryan C Oliver, Jan Lipfert, Daniel A Fox, Ryan H Lo, Sebastian Doniach, and Linda Columbus. Dependence of micelle size and shape on detergent alkyl chain length and head group. *PloS one*, 8(5), 2013.

[204] A George and W W Wilson. Predicting protein crystallization from a dilute solution property. *Acta Crystallographica Section D: Biological Crystallography*, 50(Pt 4):361–365, July 1994.

[205] Nadrian C Seeman. DNA in a material world. *Nature*, 421(6921):427–431, January 2003.

[206] Erik Winfree, Furong Liu, Lisa A Wenzler, and Nadrian C Seeman. Design and self-assembly of two-dimensional DNA crystals. *Nature*, 394(6693):539–544, August 1998.

[207] Carlos Ernesto Castro, Fabian Kilchherr, Do-Nyun Kim, Enrique Lin Shiao, Tobias Wauer, Philipp Wortmann, Mark Bathe, and Hendrik Dietz. A primer to scaffolded DNA origami. *Nature Methods*, 8(3):221–229, March 2011.

[208] Erik Benson, Abdulmelik Mohammed, Johan Gardell, Sergej Masich, Eugen Czeizler, Pekka Orponen, and Björn Högberg. DNA rendering of polyhedral meshes at the nanoscale. *Nature*, 523(7561), 2015.

[209] Anton Kuzyk, Robert Schreiber, Hui Zhang, Alexander O Govorov, Tim Liedl, and Na Liu. Reconfigurable 3D plasmonic metamolecules. *Nature Materials*, 13(9):862–866, September 2014.

[210] Minghui Liu, Jinglin Fu, Christian Hejesen, Yuhe Yang, Neal W Woodbury, Kurt Gothelf, Yan Liu, and Hao Yan. A DNA tweezer-actuated enzyme nanoreactor. *Nature Communications*, 4, July 2013.

[211] Alexander E Marras, Lifeng Zhou, Hai-Jun Su, and Carlos E Castro. Programmable motion of DNA origami mechanisms. *Proceedings of the National Academy of Sciences of the United States of America*, 112(3):713–718, January 2015.

[212] Akinori Kuzuya and Yuichi Ohya. Nanomechanical Molecular Devices made of DNA Origami. *Accounts of Chemical Research*, 47(6):1742–1749, June 2014.

[213] Yong-Xing Zhao, Alan Shaw, Xianghui Zeng, Erik Benson, Andreas M Nyström, and Björn Högberg. DNA origami delivery system for cancer therapy with tunable release properties. *ACS Nano*, 6(10):8684–8691, October 2012.

[214] Fei Zhang, Shuoxing Jiang, Siyu Wu, Yulin Li, Chengde Mao, Yan Liu, and Hao Yan. Complex wireframe DNA origami nanostructures with multi-arm junction vertices. *Nature Nanotechnology*, 10(9):779–784, September 2015.

[215] Ali Aghebat Rafat, Tobias Pirzer, Max B Scheible, Anna Kostina, and Friedrich C Simmel. Surface-assisted large-scale ordering of DNA origami tiles. *Angewandte Chemie (International ed. in English)*, 53(29):7665–7668, July 2014.

[216] Martin Langecker, Vera Arnaut, Thomas G Martin, Jonathan List, Stephan Renner, Michael Mayer, Hendrik Dietz, and Friedrich C Simmel. Synthetic Lipid Membrane Channels Formed by Designed DNA Nanostructures. *Science*, 338(6109), 2012.

[217] Robert P Rambo and John A Tainer. Super-resolution in solution X-ray scattering and its applications to structural systems biology. *Annual review of biophysics*, 42(1):415–441, 2013.

[218] David Eliezer, Patricia A Jennings, Peter E Wright, Sebastian Doniach, Keith O Hodgson, and Hirotsugu Tsuruta. The radius of gyration of an apomyoglobin folding intermediate. *Science*, 270(5235):487–488, October 1995.

[219] Xingwang Fang, Kenneth Littrell, Xiao-jing Yang, Stephen J Henderson, Sonke Siefert, P Thiyagarajan, Tao Pan, and Tobin R Sosnick. Mg 2+-Dependent Compaction and Folding of Yeast tRNA Pheand the Catalytic Domain of the B. subtilisRNase P RNA Determined by Small-Angle X-ray Scattering †. *Biochemistry*, 39(36):11107–11113, September 2000.

[220] Nicholas J Bessman, Atrish Bagchi, Kathryn M Ferguson, and Mark A Lemmon. Complex relationship between ligand binding and dimerization in the epidermal growth factor receptor. *Cell reports*, 9(4):1306–1317, November 2014.

[221] Robert P Rambo and John A Tainer. Improving small-angle X-ray scattering data for structural analyses of the RNA world. *RNA*, 16(3):638–646, March 2010.

[222] Jan Lipfert, Rhiju Das, Vincent B Chu, Madhuri Kudaravalli, Nathan Boyd, Daniel Herschlag, and Sebastian Doniach. Structural transitions and thermodynamics of a glycine-dependent riboswitch from Vibrio cholerae. *Journal of molecular biology*, 365(5), 2007.

[223] Mona Ali, Jan Lipfert, Soenke Seifert, Daniel Herschlag, and Sebastian Doniach. The ligand-free state of the TPP riboswitch: a partially folded RNA structure. *Journal of molecular biology*, 396(1):153–165, February 2010.

[224] Steve P Meisburger, Julie L Sutton, Huimin Chen, Suzette A Pabit, Serdal Kirmizialtin, Ron Elber, and Lois Pollack. Polyelectrolyte properties of single stranded DNA measured using SAXS and single-molecule FRET: Beyond the wormlike chain model. *Biopolymers*, 99(12):1032–1045, December 2013.

[225] Xiaobing Zuo, Guanglei Cui, Kenneth M Merz, Ligang Zhang, Frederick D Lewis, and David M Tiede. X-ray diffraction "fingerprinting" of DNA structure in solution for quantitative evaluation of molecular dynamics simulation. *Proceedings of the National Academy of Sciences of the United States of America*, 103(10):3534–3539, March 2006.

[226] Thang K Chiu and Richard E Dickerson. 1 A crystal structures of B-DNA reveal sequence-specific binding and groove-specific bending of DNA by magnesium and calcium. *Journal of molecular biology*, 301(4):915–945, August 2000.

[227] Joachim Frank. Single-particle imaging of macromolecules by cryo-electron microscopy. *Annual review of biophysics and biomolecular structure*, 31(1), 2002.

[228] Keyao Pan, Do-Nyun Kim, Fei Zhang, Matthew R Adendorff, Hao Yan, and Mark Bathe. Lattice-free prediction of three-dimensional structure of programmed DNA assemblies. *Nature Communications*, 5:5578–7, December 2014.

[229] Lois Pollack. SAXS studies of ion-nucleic acid interactions. *Annual review of biophysics*, 40(1), 2011.

[230] Steve P Meisburger, Suzette A Pabit, and Lois Pollack. Determining the Locations of Ions and Water around DNA from X-Ray Scattering Measurements. *Biophysical Journal*, 108 (12):2886–2895, June 2015.

[231] Sergei Gavryushov and Piotr Zielenkiewicz. Electrostatic potential of B-DNA: effect of interionic correlations. *Biophysical Journal*, 75(6):2732–2742, December 1998.

[232] Jejoong Yoo and Aleksei Aksimentiev. In situ structure and dynamics of DNA origami determined through molecular dynamics simulations. *Proceedings of the National Academy of Sciences*, 110(50):20099–20104, December 2013.

[233] Do-Nyun Kim, Fabian Kilchherr, Hendrik Dietz, and Mark Bathe. Quantitative prediction of 3D solution shape and flexibility of nucleic acid nanostructures. *Nucleic Acids Research*, 40(7):2862–2868, April 2012.

[234] Reza Sharifi Sedeh, Keyao Pan, Matthew Ralph Adendorff, Oskar Hallatschek, Klaus-Jürgen Bathe, and Mark Bathe. Computing Nonequilibrium Conformational Dynamics of Structured Nucleic Acid Assemblies. *Journal of chemical theory and computation*, 12 (1):261–273, January 2016.

[235] Osamu Miyashita, Christian Gorba, and Florence Tama. Structure modeling from small angle X-ray scattering data with elastic network normal mode analysis. *Journal of Structural Biology*, 173(3):451–460, March 2011.

[236] José Ramón López-Blanco, Osamu Miyashita, Florence Tama, and Pablo Chacón. *Normal Mode Analysis Techniques in Structural Biology*. John Wiley & Sons, Ltd, Chichester, UK, May 2001.

[237] Marc Delarue. Dealing with structural variability in molecular replacement and crystallographic refinement through normal-mode analysis. *Acta Crystallographica Section D: Biological Crystallography*, 64(Pt 1):40–48, January 2008.

[238] Konrad Hinsen. Analysis of domain motions by approximate normal mode calculations. *Proteins*, 33(3):417–429, November 1998.

[239] Florence Tama, Mikel Valle, Joachim Frank, and Charles L Brooks. Dynamic reorganization of the functionally active ribosome explored by normal mode analysis and cryo-electron microscopy. *Proceedings of the National Academy of Sciences of the United States of America*, 100(16):9319–9323, August 2003.

[240] Gunnar F Schröder, Michael Levitt, and Axel T Brunger. Super-resolution biomolecular crystallography with low-resolution data. *Nature*, 464(7292):1218–1222, April 2010.

[241] Alejandro Panjkovich and Dmitri I Svergun. Deciphering conformational transitions of proteins by small angle X-ray scattering and normal mode analysis. *Physical Chemistry Chemical Physics*, 18(8), 2016.

[242] Javier Pérez, Patrice Vachette, Daniela Russo, Michel Desmadril, and Dominique Durand. Heat-induced unfolding of neocarzinostatin, a small all-beta protein investigated by small-angle X-ray scattering. *Journal of molecular biology*, 308(4):721–743, May 2001.

[243] Lois Pollack. Time resolved SAXS and RNA folding. *Biopolymers*, 95(8):543–549, August 2011.

[244] Nathan J Baird, Eric Westhof, Hong Qin, Tao Pan, and Tobin R Sosnick. Structure of a Folding Intermediate Reveals the Interplay Between Core and Peripheral Elements in RNA Folding. *Journal of molecular biology*, 352(3):712–722, September 2005.

[245] Benjamin Kick, Florian Praetorius, Hendrik Dietz, and Dirk Weuster-Botz. Efficient Production of Single-Stranded Phage DNA as Scaffolds for DNA Origami. *Nano Letters*, 15(7):4672–4676, June 2015.

[246] Clément E Blanchet, Alessandro Spilotros, Frank Schwemmer, Melissa A Graewert, Alexey Kikhney, Cy M Jeffries, Daniel Franke, Daniel Mark, Roland Zengerle, Florent Cipriani, Stefan Fiedler, Manfred Roessle, and Dmitri I Svergun. Versatile sample environments and automation for biological solution X-ray scattering experiments at the P12 beamline (PETRA III, DESY). *Journal of Applied Crystallography*, 48(Pt 2):431–443, April 2015.

[247] Claude E Shannon. A Mathematical Theory of Communication. *Bell System Technical Journal*, 27(4):623–656, July 2013.

[248] Iradwikanari Waluyo, Congcong Huang, Dennis Nordlund, Uwe Bergmann, Thomas M Weiss, Lars G M Pettersson, and Anders Nilsson. The structure of water in the hydration shell of cations from x-ray Raman and small angle x-ray scattering measurements. *Journal of Chemical Physics*, 134, 2011.

[249] Kurt Andresen, Rhiju Das, Hye Y Park, H Smith, Lisa W Kwok, Jessica S Lamb, Earl J Kirkland, Daniel Herschlag, Kenneth D Finkelstein, and Lois Pollack. Spatial distribution of competing ions around DNA in solution. *Physical review letters*, 93, 2004.

[250] Mahsa Siavashpouri, Christian H Wachauf, Mark J Zakhary, Florian Praetorius, Hendrik Dietz, and Zvonimir Dogic. Molecular engineering of chiral colloidal liquid crystals using DNA origami. *Nature Materials*, 16(8):849–856, May 2017.

[251] Patrick D Halley, Christopher R Lucas, Emily M McWilliams, Matthew J Webber, Randy A Patton, Comert Kural, David M Lucas, John C Byrd, and Carlos E Castro. Daunorubicin-Loaded DNA Origami Nanostructures Circumvent Drug-Resistance Mechanisms in a Leukemia Model. *Small*, 12(3):308–320, November 2015.

[252] Jing Pan, Feiran Li, Tae-Gon Cha, Haorong Chen, and Jong Hyun Choi. Recent progress on DNA based walkers. *Current opinion in biotechnology*, 34:56–64, August 2015.

[253] Lois Pollack and Sebastian Doniach. *Chapter 12 - Time-Resolved X-ray Scattering and RNA Folding*, volume 469. Elsevier Inc., 1 edition, 2009.

[254] Pierre Panine, Stephanie Finet, Thomas M Weiss, and Theyencheri Narayanan. Probing fast kinetics in complex fluids by combined rapid mixing and small-angle X-ray scattering. *Advances in Colloid and Interface Science*, 127(1):9–18, November 2006.

[255] Fabian Kilchherr, Christian Wachauf, Benjamin, Matthias Rief, Martin Zacharias, and Hendrik Dietz. Single-molecule dissection of stacking forces in DNA. *Science*, 353(6304): aaf5508–aaf5508, September 2016.

[256] Rita Graceffa, R Paul Nobrega, Raul A Barrea, Sagar V Kathuria, Srinivas Chakravarthy, Osman Bilsel, and Thomas C Irving. Sub-millisecond time-resolved SAXS using a continuous-flow mixer and X-ray microbeam. *Journal of synchrotron radiation*, 20(Pt 6): 820–825, November 2013.

[257] Peter William Atkins and Julio de Paula. *Atkins' Physical Chemistry*. Oxford University Press, USA, 2002.

[258] Wei Yuan Yang and Martin Gruebele. Folding at the speed limit. *Nature*, 423(6936): 193–197, May 2003.

[259] Jan Kubelka, James Hofrichter, and William A Eaton. The protein folding 'speed limit'. *Current Opinion in Structural Biology*, 14(1):76–88, February 2004.

[260] Dieter Lehner, Helmut Lindner, and Otto Glatter. Determination of the translational and rotational diffusion coefficients of rodlike particles using depolarized dynamic light scattering. *Langmuir : the ACS journal of surfaces and colloids*, 16(4):1689–1695, 2000.

[261] M Mercedes Tirado, Carmen López Martínez, and José García de la Torre. Comparison of theories for the translational and rotational diffusion coefficients of rod-like macromolecules. Application to short DNA fragments. *Journal of Chemical Physics*, 81(4): 2047–2052, August 1984.

[262] Sean A McKinney, Anne-Cécile Déclais, David M J Lilley, and Taekjip Ha. Structural dynamics of individual Holliday junctions. *Nature Structural Biology*, 10(2):93–97, February 2003.

[263] Chirlmin Joo, Sean A McKinney, David M J Lilley, and Taekjip Ha. Exploring Rare Conformational Species and Ionic Effects in DNA Holliday Junctions Using Single-molecule Spectroscopy. *Journal of molecular biology*, 341(3):739–751, August 2004.

[264] Franc J Overmars and Cornelis Altona. NMR study of the exchange rate between two stacked conformers of a model Holliday junction. *Journal of molecular biology*, 273(3): 519–524, October 1997.

[265] Jin Yu, Taekjip Ha, and Klaus Schulten. Conformational model of the Holliday junction transition deduced from molecular dynamics simulations. *Nucleic Acids Research*, 32(22): 6683–6695, 2004.

[266] Wujie Wang, Laura M Nocka, Brianne Z Wiemann, Daniel M Hinckley, Ishita Mukerji, and Francis W Starr. Holliday Junction Thermodynamics and Structure: Coarse-Grained Simulations and Experiments. *Scientific Reports*, 6(1):22863, March 2016.

[267] Changbong Hyeon and D Thirumalai. Chain Length Determines the Folding Rates of RNA. *Biophysical journal*, 102(3):L11–L13, February 2012.

[268] Yonggang Ke, Travis Meyer, William M Shih, and Gaëtan Bellot. Regulation at a distance of biomolecular interactions using a DNA origami nanoactuator. *Nature Communications*, 7:10935, March 2016.

[269] Jonas J Funke, Philip Ketterer, Corinna Lieleg, Philipp Korber, and Hendrik Dietz. Exploring Nucleosome Unwrapping Using DNA Origami. *Nano Letters*, 16(12):7891–7898, December 2016.

[270] Anastasiya Puchkova, Carolin Vietz, Enrico Pibiri, Bettina Wünsch, María Sanz Paz, Guillermo P Acuna, and Philip Tinnefeld. DNA Origami Nanoantennas with over 5000-fold Fluorescence Enhancement and Single-Molecule Detection at 25 μM. *Nano Letters*, 15(12):8354–8359, December 2015.

[271] Jiang Li, Chunhai Fan, Hao Pei, Jiye Shi, and Qing Huang. Smart Drug Delivery Nanocarriers with Self-Assembled DNA Nanostructures. *Advanced Materials*, 25(32):4386–4396, June 2013.

[272] Honglu Zhang, Jie Chao, Dun Pan, Huajie Liu, Qing Huang, and Chunhai Fan. Folding super-sized DNA origami with scaffold strands from long-range PCR. *Chemical communications (Cambridge, England)*, May 2012.

[273] Sungwook Woo and Paul W K Rothemund. Programmable molecular recognition based on the geometry of DNA nanostructures. *Nature chemistry*, 3(8):620–627, August 2011.

[274] Philip Ketterer, Elena M Willner, and Hendrik Dietz. Nanoscale rotary apparatus formed from tight-fitting 3D DNA components. *Science advances*, 2(2):e1501209, February 2016.

[275] Isabelle Morfin, Ferenc Horkay, Peter J Basser, Françoise Bley, Anne-Marie Hecht, Cyrille Rochas, and Erik Geissler. Adsorption of divalent cations on DNA. *Biophysical Journal*, 87(4):2897–2904, October 2004.

[276] Zhi-Jie Tan and Shi-Jie Chen. Nucleic Acid Helix Stability: Effects of Salt Concentration, Cation Valence and Size, and Chain Length. *Biophysical Journal*, 90(4):1175–1190, February 2006.

[277] Sam Meyer, Daniel Jost, Nikos Theodorakopoulos, Michel Peyrard, Richard Lavery, and Ralf Everaers. Temperature dependence of the DNA double helix at the nanoscale: structure, elasticity, and fluctuations. *Biophysical Journal*, 105(8):1904–1914, October 2013.

[278] Scott Michael Slone, Chen-Yu Li, Jejoong Yoo, and Aleksei Aksimentiev. Molecular mechanics of DNA bricks: in situstructure, mechanical properties and ionic conductivity. *New Journal of Physics*, 18(5):055012, May 2016.

[279] Marshal Mandelkern, John G Elias, Don Eden, and Donald M Crothers. The dimensions of DNA in solution. *Journal of molecular biology*, 152(1):153–161, October 1981.

[280] Daniel J Segel, Anthony L Fink, Keith O Hodgson, and Sebastian Doniach. Protein Denaturation: A Small-Angle X-ray Scattering Study of the Ensemble of Unfolded States of Cytochrome c†. *Biochemistry*, 37(36):12443–12451, September 1998.

[281] Eric R Henry and James Hofrichter. Singular value decomposition: Application to analysis of experimental data. *Methods in Enzymology*, 210:129–921, December 1992.

[282] Lingling Chen, Keith O Hodgson, and Sebastian Doniach. A lysozyme folding intermediate revealed by solution X-ray scattering. *Journal of molecular biology*, 261(5):658–671, September 1996.

[283] J Lipfert, L Columbus, V B Chu, S Doniach, and IUCr. Analysis of small-angle X-ray scattering data of protein–detergent complexes by singular value decomposition. *Journal of Applied Crystallography*, 40(s1):s235–s239, April 2007.

[284] Feng Pan, Christopher Roland, and Celeste Sagui. Ion distributions around left- and right-handed DNA and RNA duplexes: a comparative study. *Nucleic Acids Research*, 42 (22):13981–13996, December 2014.

[285] A Yu Grosberg, T T Nguyen, and B I Shklovskii. Colloquium: The physics of charge inversion in chemical and biological systems. *Rev. Mod. Phys.*, 74(2), 2002.

[286] Vincent B Chu, Yu Bai, Jan Lipfert, Daniel Herschlag, and Sebastian Doniach. Evaluation of ion binding to DNA duplexes using a size-modified Poisson-Boltzmann theory. *Biophysical Journal*, 93(9):3202–3209, November 2007.

[287] Maria L Sushko, Dennis G Thomas, Suzette A Pabit, Lois Pollack, Alexey V Onufriev, and Nathan A Baker. The Role of Correlation and Solvation in Ion Interactions with B-DNA. *Biophysical Journal*, 110(2):315–326, January 2016.

[288] Zaven Ovanesyan, Bharat Medasani, Marcia O Fenley, Guillermo Iván Guerrero-García, Mónica Olvera de la Cruz, and Marcelo Marucho. Excluded volume and ion-ion correlation effects on the ionic atmosphere around B-DNA: Theory, simulations, and experiments. *Journal of Chemical Physics*, 141(22):225103–17, December 2014.

[289] Zhi-Jie Tan and Shi-Jie Chen. Electrostatic correlations and fluctuations for ion binding to a finite length polyelectrolyte. *Journal of Chemical Physics*, 122(4):44903, January 2005.

[290] M S Rook, D K Treiber, and J R Williamson. An optimal Mg(2+) concentration for kinetic folding of the tetrahymena ribozyme. *Proceedings of the National Academy of Sciences of the United States of America*, 96(22):12471–12476, October 1999.

[291] Inna Shcherbakova, Sayan Gupta, Mark R Chance, and Michael Brenowitz. Monovalent ion-mediated folding of the Tetrahymena thermophila ribozyme. *Journal of molecular biology*, 342(5):1431–1442, October 2004.

List of Figures

List of Tables

Danksagung

Ich möchte mich bei einigen Leuten bedanken, ohne die diese Arbeit nicht möglich gewesen wäre und die mich während meiner Promotion sehr unterstützt haben:

Jan Lipfert, der mir die Gelegenheit gegeben hat mich während meiner Promotion mit verschiedensten Gebieten der Biophysik zu befassen.

Danke, dass du mich bei allen Projekten stets unterstützt hast und somit erheblich zu meiner wissenschaftlichen Weiterentwicklung beigetragen hast. Mit deiner offenen, freundlichen und diskussionsbereiten Art hast du eine sehr angenehme Arbeitsatmosphäre geschaffen und neben der Wissenschaft blieb auch immer Zeit für lustige Lab-Aktivitäten. Zudem habe ich es sehr genossen, dass ich an vielen Konferenzen sowie dem JNN-Austausch teilnehmen durfte.

Hendrik Dietz, für die hervorragende Kollaboration und die spannenden Projekte.

Bert Nickel, für seine Unterstützung beim Aufbau der SAXS Anlage sowie die vielen aufschlussreichen Diskussionen.

Wenjun Zheng, für die zuverlässige Zusammenarbeit und die vielen 'refinement runs' für den Switch.

Hermann Gaub, für die herzliche und inspirierende Arbeitsatmosphäre und die Großzügigkeit sowohl auf wissenschaftlicher Ebene als auch bei den vielen schönen Lehrstuhl-Aktivitäten.

Thomas Gerling, für die gute Zusammenarbeit, die vielen Origami Proben, die ich messen durfte und seine stete Unterstützung.

Stefan Fischer, für seine unglaubliche Hilfsbereitschaft, die gute Zusammenarbeit, die intensiven Diskussionen sowie die vielen lustigen Stunden im Röntgenlabor. Die Bier und Burger Tradition sollten wir auch weiterhin pflegen!

Philipp Walker, für die tolle Zusammenarbeit bei den gemeinsamen SAXS Projekten sowie den guten und intensiven Diskussionen (insbesondere zu Reaktionsraten). Insbesondere möchte ich mich für deine Ausdauer, Konzentration und trotz allem dem Humor am Synchrotron (vor allem an der ID02 !) bedanken. Danke auch fürs Korrekturlesen.

Franziska Kriegel, für die zuverlässige, vertrauensvolle, motivierende, hilfsbereite, loyale und humorvolle Art. Ich bin unheimlich dankbar für die gemeinsame Zeit. Du hast mich immer unterstützt und bestärkt und ich habe die Atmosphäre in unserem Büro stets genossen. Du bist einfach die beste Kollegin, die man haben kann!

Magnus Bauer, für seine Hilfsbereitschaft sei es seine Bereitschaft zweimal mit auf Strahlzeit nach Grenoble (den Kessel) zu fahren oder seine Hilfe mit Python-Skripten und seine Offenheit und Diskussionsbereitschaft gegenüber jeglichen (un-) physikalischen Fragen. Danke auch für die zuverlässige Freundschaft, deine gutes Zuhören, und die vielen fröhlichen und lustigen gemeinsamen Abende mit Timon.

Timon Funk, für die vielen weiterführenden Antworten bei Fragen zu DNA Origami Themen, die erfolgreichen CD-Messungen, die vielen lustigen Stadt-Land-Fluss Abende und die gute langjährige Freundschaft.

Thomas Zettl, für seine Hilfe bei allen IT-Problemen und den vielen Diskussionen insbesondere zu DNA Origami Themen.

Jochen Müller und Achim Löf, für die tolle Zusammenarbeit beim von Willebrand Faktor' Projekt. Danke, dass ich mitmachen konnte!

Steffen Sedlak, für die gute Zusammenarbeit und die Unterstützung in der Anfangsphase.

Constantin Schöler, für die vielen Mittagessen (Nudeln mit Pesto), die guten Gespräche und einfach die lustige und schöne gemeinsame Zeit.

Fabian Baumann, für die diskussionsfreudige und lustige Atmosphäre in unserem Büro.

Manu, für seine fröhliche Art mit der er uns gerne im Büro besucht hat, die vielen aufmunternden Kaffeepausen, und die gemeinsamen work-outs.

Philip und Flo, für eure lustige und humorvolle Art mit der ihr jede schlechte Laune vertreibt und für die tolle Zeit in Venedig.

Sylvia und **Angelika**, für die netten morgendlichen Gespräche und die besten Smoothies der Welt. Bei Sylvia möchte ich mich vor allem für die Hilfe bei allen organisatorischen und bürokratischen (insbesondere den französischen!) Angelegenheiten bedanken.

CeNS und **NIM** Mitarbeitern, für die Realisierung der ganzen Events und Aktivitäten für Doktoranden und für die gute Zusammenarbeit im Rahmen des NIM student boards.

Des Weiteren danke ich allen Mitarbeitern der **AG Lipfert** und der **AG Nickel** sowie des **Lehrstuhl Gaubs** für die angenehme Arbeitsatmosphäre, die Hilfsbereitschaft und Offenheit gegenüber Fragen und den Spaß.

Es gibt eine Menge anderer Menschen, die mich während meines Studiums und meiner Promotion begleitet haben. Besonderer Dank gebührt: Meinen Eltern, meiner Oma, Jan, Jens, Georg, Jasmin und Jule. Danke für eure Unterstützung und eure Motivation. Ihr wart immer für mich da, habt mir zugehört und vor allem Rückhalt gegeben, wenn die Wissenschaft mal wieder frustrierend war.